

**Damage Tolerance of Thermoset Composites with  
Thermoplastic Fibres and Graphene Nanocomposite Fibres**

**A thesis submitted to the University of Manchester for the degree of**

**Doctor of Philosophy**

**in the Faculty of Science and Engineering**

**2021**

**Jinseong Park**

**Robotics and Textile Composites Group**

**School of Natural Sciences**

**Department of Materials**

**The University of Manchester**

---

---

## Table of Contents

<b>Table of Contents .....</b>	<b>2</b>
<b>List of Figures .....</b>	<b>6</b>
<b>List of Tables .....</b>	<b>12</b>
<b>List of Abbreviations .....</b>	<b>14</b>
<b>Abstract.....</b>	<b>15</b>
<b>Declaration .....</b>	<b>16</b>
<b>Copyright Statement .....</b>	<b>17</b>
<b>Acknowledgements.....</b>	<b>18</b>
<b>Chapter 1. Introduction .....</b>	<b>20</b>
1.1 Background .....	20
1.2 Problem definition and research approach.....	21
1.3 Research aims and objectives .....	22
1.4 Thesis layout .....	24
1.5 Summary .....	25
<b>Chapter 2. Literature Review.....</b>	<b>27</b>
2.1 Mechanics of fibre reinforced polymer composites .....	27
2.2 Impact damage behaviour of fibre reinforced polymer composites .....	28
2.2.1 Impact damage behaviour by low energy impact.....	28
2.2.2 Failure of UD, 2D and 3D preform structure composites .....	29
2.2.3 Polymer matrix modification .....	30
2.3 Improving the impact damage tolerance of composites.....	31
2.3.1 Preform structures development.....	31
2.3.2 Reinforced fibre modification.....	35
2.4 Fibre hybridisation process and hybrid yarn composites .....	36
2.4.1 Commingling .....	36
2.4.2 Wrapping.....	39
2.5 Increase mechanical properties of thermoplastic fibres by drawing process....	40
2.6 Industrial robotic systems and automated fibre placement .....	41
2.6.1 General robot structures .....	41
2.6.2 System control .....	43
2.6.3 Commercial automated fibre placement .....	43

---

2.6.4	Continuous dry fibre placement .....	44
2.7	Summary and critical discussion .....	45
<b>Chapter 3. Development of Automatic Hybrid Yarns Manufacturing Process .....</b>		<b>48</b>
3.1	Background .....	48
3.2	Machine development process .....	48
3.3	Development of fibre hybridisation process .....	49
3.4	Hardware design and assembly .....	51
3.4.1	Drawing zone .....	51
3.4.2	Wrapping zone .....	52
3.4.3	Commingling zone .....	54
3.4.4	Let off zone .....	55
3.4.5	Winding zone .....	57
3.4.6	Machine assembly and safety guard .....	57
3.5	Electrical network and PLC based controller .....	59
3.5.1	Electrical network system .....	59
3.5.2	PLC assembly .....	62
3.6	Software design .....	63
3.6.1	System initializing .....	64
3.6.2	Motor programming .....	64
3.6.3	Heater and pneumatics programming .....	65
3.6.4	MHI touch screen .....	65
3.7	Discussion .....	66
<b>Chapter 4. Materials and Experimental Procedures .....</b>		<b>67</b>
4.1	Materials .....	67
4.1.1	Commingled and wrapped yarn .....	67
4.1.2	High thermal performance thermoplastic hybrid yarn .....	67
4.1.3	Micro wrapped yarn .....	68
4.2	Methods .....	69
4.2.1	Hybrid yarn manufacturing .....	69
4.2.2	Polypropylene fibre drawing .....	74
4.2.3	Carbon fibre tow splitting .....	76
4.2.4	Preforming .....	76

---

---

4.2.5	Composites manufacturing .....	80
4.3	Testing .....	84
4.3.1	Fibre tensile testing .....	84
4.3.2	Composites tensile test .....	85
4.3.3	Short beam strength test .....	86
4.3.4	Drop-weight impact test .....	87
4.3.5	Compression testing .....	87
4.3.6	Inspection of impact damaged area .....	88
<b>Chapter 5. Impact Damage Tolerance of Thermoset Composites with Carbon and PP Multifilament Hybrid Yarn .....</b>		<b>89</b>
5.1	Introduction .....	89
5.2	Results and discussion .....	89
5.2.1	Morphology of hybrid yarn .....	89
5.2.2	Polypropylene fibre tensile properties .....	91
5.2.3	Comparison of impact resistance of hybrid yarn composites .....	92
5.2.4	CAI test of commingled and wrapped yarn .....	94
5.2.5	Impact damage tolerance of wrapped yarn composites at different manufacturing conditions .....	95
5.2.6	UD vs 3D structure hybrid wrapped yarn composites .....	98
5.3	Discussion .....	105
<b>Chapter 6. Hybrid Composites with Higher Thermal Performance Thermoplastic Fibres .....</b>		<b>107</b>
6.1	Introduction .....	107
6.2	Results and discussion .....	107
6.2.1	PA6/Graphene hybrid wrapped yarn composites .....	107
6.2.2	CF/PEI thermoset composites .....	113
6.3	Discussion .....	122
<b>Chapter 7. Study of Impact Damage Tolerance with Micro-wrapped Carbon Fibres and Polypropylene/Graphene Nanocomposite Fibres .....</b>		<b>124</b>
7.1	Introduction .....	124
7.2	Results and discussion .....	125
7.2.1	Dimension of PP/Graphene fibres .....	125

---

---

7.2.2	Fibre tensile test .....	126
7.2.3	Composites tensile tests .....	133
7.2.4	Short beam strength test .....	136
7.2.5	Composites impact tests .....	138
7.2.6	Inspection of the impact damaged area with C-Scan .....	141
7.2.7	Compression test .....	143
7.3	Discussion .....	147
<b>Chapter 8. Conclusion and Future Work.....</b>		<b>149</b>
8.1	Conclusion .....	149
8.1.1	Hybrid yarn manufacturing machine development .....	149
8.1.2	Thermoplastic fibre drawing.....	149
8.1.3	Graphene loaded fibre .....	150
8.1.4	Micro wrapped yarn composites.....	150
8.1.5	Impact damage tolerance of hybrid yarn composites.....	150
8.1.6	UD vs 3D structure composites .....	151
8.1.7	Development of the hybrid yarn manufacturing systems .....	151
8.1.8	Hybrid wrapped yarns at different wrapping conditions .....	152
8.1.9	CF and high-temperature engineering thermoplastic composites ..	152
8.1.10	Micro wrapped yarn with graphene nanocomposite fibres .....	153
8.2	Future work .....	153
8.2.1	Enhancing interface properties of nanocomposites fibres .....	153
8.2.2	Improve micro wrapped yarn.....	154
8.2.3	Expansion of research with new air nozzle.....	154
8.2.4	Hybrid yarn manufacturing depends on machine setting.....	154
8.2.5	Improving the impact behaviour of thermoset composites.....	155
<b>References.....</b>		<b>156</b>
<b>Appendix A. Tensile Test Simulation of Thermoset Composites.....</b>		<b>171</b>
<b>Appendix B. Programing .....</b>		<b>177</b>
<b>Appendix C. PLC Electrical Schematics .....</b>		<b>188</b>
<b>Appendix D. New Air Nozzle Design .....</b>		<b>202</b>

**Word count: 36,905**

---

## List of Figures

Figure 2-1 Typical stress-strain behaviour of polymers [16] .....	27
Figure 2-2 Strain-stress curves of FRP composites and steel [19].....	28
Figure 2-3 Typical impact damage in fibre reinforced polymer composites [21].....	28
Figure 2-4 Micrographic of fibre fracture and delamination at cross-ply structure fibre composite [30].....	29
Figure 2-5 (a) Delamination crack and z-binder bridging, and (b) fracture of 3D woven structural composites in mode I test [31] .....	29
Figure 2-6 Impact damage resistance of 3D structure composites by increased z-binder content [31].....	32
Figure 2-7 Types of 3D preform structures .....	34
Figure 2-8 Hybrid yarn structures [61] .....	36
Figure 2-9 (a) General commingling process and (b) Twintex commingling process [13], [65].....	37
Figure 2-10 Typical structure of commingled yarn that is produced by an air nozzle [67] .....	38
Figure 2-11 Fibre wrapping process [13].....	39
Figure 2-12 Yarn structure of singly (S twist) and doubly (S and Z twist) wrapped yarns [51].....	40
Figure 2-13 The different types of robots architecture; (a) Articulated, (b) SCARA, (c) Cartesian, (d) Delta (d), and (e) Cylindrical [77].....	42
Figure 2-14 Commercial robotic tow placement [79], [80].....	43
Figure 2-15 Boeing AFP machine to produce the monolithic carbon fibre composites of fuselage section [81] .....	44
Figure 2-16 Gantry automated fibre placement at the University of Manchester .....	45
Figure 2-17 Robotic fibre placement developed by the University of Manchester [90]	45
Figure 3-1 Commingling production line at The University of Manchester [14], [95] ..	48
Figure 3-2 Machine development process .....	49
Figure 3-3 Schematic typical wrapping, commingling, and fibre drawing processes ....	50
Figure 3-4 Schematic design for specially developed fibre hybridisation process .....	50

---

---

Figure 3-5 Initial 3D design of the fibre wrapping process.....	51
Figure 3-6 3D design of fibre drawing device (a), and assembled drawing device (b) ..	52
Figure 3-7 3D CAD design of wrapping zone.....	52
Figure 3-8 CF/PP wrapped yarn manufacturing process .....	53
Figure 3-9 Schematic diagram of bobbin holder and motor pulley .....	53
Figure 3-10 Side view and cross section view of previous air nozzle design .....	54
Figure 3-11 Commingling zone.....	55
Figure 3-12 PP fibre tension control in the let-off zone .....	56
Figure 3-13 Schematic bobbin stand with 2kg carbon fibre.....	56
Figure 3-14 (a) helical winding of wrapped yarn, and (b) hoop winding of PP fibre.....	57
Figure 3-16 Assembled fibre hybridisation machine .....	58
Figure 3-17 Assembled protective panels and the gap for air circulation. ....	59
Figure 3-18 Electrical network block diagram of motors, heaters and pneumatics for fibre hybridisation process .....	60
Figure 3-19 Arrangement of PLC devices .....	63
Figure 3-20 Back and front view of installed five digital temperature controllers, reset button, and e-stop button on the PLC .....	63
Figure 3-21 (a) display design and function setting for each button in the software and (b) the corresponding display operation mode after uploading the program.....	65
Figure 4-1 Commingling process of CF/PP fibre on the developed machine .....	70
Figure 4-2 CAD design of multifilament single and double wrapping yarn structure....	71
Figure 4-3 Wrapped yarn manufacturing process; (a) wrapping, and (b) winding process .....	71
Figure 4-4 Geometric definition of wrapped yarn.....	72
Figure 4-5 manufacturing process of micro wrapped yarn with split carbon fibre and mono PP fibres.....	73
Figure 4-6 Optical microscope images of micro wrapped yarn at a cross- and lateral- section.....	74
Figure 4-7 Schematic fibre drawing systems on the developed machine .....	75
Figure 4-8 Fibre drawing process on the developed machine .....	75
Figure 4-9 Tow splitting setting for carbon fibre .....	76
Figure 4-10 Manufactured hybrid yarn 3D structure preforms .....	77

---

---

Figure 4-11 Cross-ply [0/90] structure preforming on robotic tow placement developed by the University of Manchester .....	78
Figure 4-12 Wrapped yarn 3D structure preform with PP/Graphene mono fibre through-thickness binders .....	78
Figure 4-13 PEI veil and carbon fibre lay-up process on the Cartesian coordinate robot; PEI 3D structure of (a) 10mm width, and (b) 200mm width .....	79
Figure 4-14 Vacuum bagging set-up.....	80
Figure 4-15 Paper card dimension to prepare specimens of single fibre tensile test .....	84
Figure 4-16 Single fibre tensile test set-up on the Instron 3344 with 100N load cell ....	85
Figure 4-17 Experimental tensile test set-up on DIC normal images .....	86
Figure 4-18 (a), (b) Test set-up during the test, and (c) Schematic representation of short beam shear test set-up.....	87
Figure 4-19 Systems of drop weight impact test on a CEAST 9350 machine .....	88
Figure 4-20 CAI test set-up with specimen fixture .....	88
Figure 5-1 Typical stress-strain curves of PP multifilament at 1, 10, 1000 mm/min loading speed .....	92
Figure 5-2 Typical force-displacement curves of (a) commingled yarn, (b) developed commingled yarn, (c) single wrapped yarn, and (d) double wrapped yarn composites at 10J impact energy .....	93
Figure 5-3 Typical force-displacement curves of (a) commingled yarn, (b) developed commingled yarn, (c) single wrapped yarn, and (d) double wrapped yarn composites at 25J impact energy .....	93
Figure 5-4 Compressive strength of 3D structure hybrid yarn after 0J, 10J and 25J impact test .....	95
Figure 5-5 Force - displacement and energy - time curve from 10J weight drop test of wrapped yarn composites manufactured at 50, 75, 100, 125w/m.....	96
Figure 5-6 Force - displacement and energy -time curve from 10J weight drop test of wrapping yarn composites manufactured by 1PP, 2PP and 3PP yarns .....	97
Figure 5-7 Compressive stress versus impact energy curve at different the number of PP multifilament after drop weight impact test .....	98
Figure 5-8 Impact test results of UD and 3D structure composites at (a), (c), (e) 10J and (b), (d), (f) 25J .....	99

---



---

Figure 5-9 Dent depth of UD structure composites at 10J impact.....	101
Figure 5-10 3D digital microscopy images of impact depth of UDCF and UDCF-50-2PP composites at 10J impact.....	101
Figure 5-11 CF and wrapped yarn composite specimens after impact test at 10J and 25J energy .....	103
Figure 5-12 C-scan image of carbon fibre and wrapped yarn composites between UD and 3D structure at 10J and 25J .....	103
Figure 5-13 Damaged area of UD and 3D structure composites at 10J and 25J.....	104
Figure 5-14 Compression strength of UDCF and UDCF-50-2PP composites at different impact energies.....	105
Figure 6-1 PA6 and PA6/Graphene multifilament tensile test results at (a)1 mm/min, (b)10 mm/min, (c)1000 mm/min load speed.....	108
Figure 6-2 Force-time, force-displacement, and force-displacement curves of PA6 and PA6/G wrapped yarn composites at (a), (c), (e) 10J and (b), (c), (f) 25J impact test .....	110
Figure 6-3 C-scan image of UD structure PA6 and PA6/Graphene wrapped yarn composites at 10J and 25J .....	111
Figure 6-4 (a) Dent depth and (b) damaged are after drop weight impact test of UD structure CF/polyamide 6 hybrid yarn composites .....	111
Figure 6-5 Compression strength of UDCF, UDCF-1PA6-SW50, and UDCF-1PA6/G-SW50 composites at different impact energies .....	112
Figure 6-6 3D digital microscopy images of UDCF, UDCF-1PA6-SW50, and UDCF-1PA6/G-SW50 composites at 10J impact and external surface after CAI test at 10J and 25J.....	112
Figure 6-7 PEI veil tensile test at 1, 10, 1000mm/min load speed.....	113
Figure 6-8 Force-time, force-displacement, and force-displacement curves of CF/PEI hybrid composites at (a), (c), (e) 10J and (b), (c), (f) 25J impact test .....	115
Figure 6-9 Typical c-scan images of UDCF-Tape-PEI and UDCF-Film-PEI composites for UD structure at 10J and 25J.....	116
Figure 6-10 (a) Dent depth and (b) damaged area of UD structure PEI composites after 10J and 25J impact test.....	117

---

---

Figure 6-11 Dent depth of (a) UDCF- PEI-200 and (b) UDCF-PEI-10 composites at 10J energy impact .....	117
Figure 6-12 Compression strength of UDCF, UDCF-PEI-10, and UDCF-PEI-200 composites at different impact energy .....	118
Figure 6-13 Force-time, force-displacement and energy-time curves of 10mm and 200 width PEI veil composites at 10J and 25J .....	120
Figure 6-14 C-scan image of 3DCF-Tape-PEI and 3DCF-Film-PEI composites for 3D structure at 10J and 25J .....	120
Figure 6-15 (a) Dent depth and (b) damaged area of 3D structure PEI composites after 10J and 25J impact test.....	121
Figure 6-16 Compression strength of 3DCF, 3DCF-PEI-10, and 3DCF-PEI-200 composites at different impact energy .....	121
Figure 6-17 Damaged area of 3D structure composites after CAI test with 10J impact energy; (a) 3DCF-PEI-10, and (b) 3DCF- PEI-200.....	122
Figure 7-1 Stress-strain curves of drawn fibres at 10 mm/min loading speed .....	128
Figure 7-2 Stress-strain curves of drawn fibres at 1000 mm/min loading speed .....	129
Figure 7-3 Failure surface of polypropylene at different magnifications (a) and (b) at 250mm/min, and (c) and (d) 1000mm/min loading speed tensile tests [127].....	130
Figure 7-4 Variation of tensile stress, Young's modulus, and failure strain of the PP/Graphene nanocomposites fibres as a function of Graphene content at 10mm/min and 1000 mm/min loading speed .....	131
Figure 7-5 Agglomerated graphene particles (black dots) in PPG1 fibres of (a) 300µm (undrawn fibre), (b) 120 µm, (c) 100 µm, and (d) 90 µm diameter drawn by the supplier .....	132
Figure 7-6 Schematic tensile properties of PP/Graphene nanocomposite fibres at the low and high loading speed .....	132
Figure 7-7 Typical stress-strain curves of composites: (a) CF, (b) CF/PP, (c) CF/PPG1.0, and (d) CF/PPG1.0/TT.....	133
Figure 7-8 General images of CF, CF/PP, CF/PPG1.0, and CF/PPG1.0/TT composite specimens at failure .....	134

---

---

Figure 7-9 Image of DIC method of cross-ply structure composites specimens at maximum load; (a) CF, (b) CF/PP, (c) CF/PPG1.0, and (d) CF/PPG1.0/TT binder composites .....	135
Figure 7-10 Typical force-displacement curves of carbon fibre and PP/Graphene wrapped yarn composites in the short beam strength test .....	136
Figure 7-11 Composites specimens after short beam shear test.....	137
Figure 7-12 Typical force-displacement curves of (a) CF composites, (b) CF/PP composites, (c) CF/PPG1.0 composites, and (d) CF/PPG1.0/TT composites at 10J impact energy .....	138
Figure 7-13 Typical force-displacement curves of (a) CF composites, (b) CF/PP composites, (c) CF/PPG1.0 composites, and (d) CF/PPG1.0/TT composites at 20J impact energy .....	139
Figure 7-14 Typical energy-time curves of composites at (a) 10J and (b) 20J impact energy .....	139
Figure 7-15 C-Scan images of cross-ply and 3D structure composite samples at 10J and 20J impact energy .....	141
Figure 7-16 Impact damaged area of composites samples after 20J impact test.....	142
Figure 7-17 Damaged area and dent depth of cross-ply structure and 3D structure composite at (a) 10J and at (b) 20J impact energy.....	143
Figure 7-18 Comparison of DIC images of 20J post-impact cross-ply and 3D structure composites during the CAI test .....	144
Figure 7-19 Load-extension curves of the hybrid yarn reinforced composites obtained from compression tests .....	145
Figure 7-20 (a) Peak compression stress of cross-ply and 3D structure composites samples after 0J, 10J and 20J impact test and (b) normalised data.....	146

---

## List of Tables

Table 2-1 Mechanical properties of carbon fibre composite and steel. ....	31
Table 2-2 The parameters of commingled yarn manufacture [66].....	37
Table 2-3 Commingling yarn depending on researchers .....	38
Table 3-1 Variables for pulley belt length calculation.....	53
Table 3-2 List of the main hardware .....	61
Table 4-1 Specification of carbon fibre and thermoplastic.....	67
Table 4-2 Specification of carbon fibre and thermoplastic.....	68
Table 4-3 Specification of carbon fibre and extruded PP/Graphene fibre.....	68
Table 4-4 Optical microscope image of PP fibre samples .....	69
Table 4-5 Processing parameters for single wrapped yarn manufacturing.....	71
Table 4-6 Specification of wrapping yarn samples at 50w/m .....	72
Table 4-7 Geometric properties of wrapped yarns.....	73
Table 4-8 Specification of wrapping yarn samples at 50w/m .....	73
Table 4-9 Mono fibres drawing conditions of temperature, tension and speed .....	75
Table 4-10 Carbon fibre linear density after and before splitting .....	76
Table 4-11 Specification of hybrid yarn of PEI veil and carbon fibre.....	79
Table 4-12 Details of sample codes .....	81
Table 4-13 Physical properties of composite samples .....	83
Table 5-1 Cross and lateral section photo-microscopy images of wrapping yarn .....	89
Table 5-2 Specification of hybrid yarn samples.....	90
Table 5-3 Tensile properties data for PP multifilament .....	91
Table 5-4 Summary of impact test results of 3D structure composites with hybrid yarns at 10J and 25J impact energy .....	94
Table 5-5 Summary of impact test results of wrapped yarn UD structure composites at different wrapping density at 10J impact energy .....	96
Table 5-6 Summary of impact test results of UD structure wrapped yarn composites at different the number of PP fibres .....	98
Table 5-7 Dent depth of UD structure composites with different PP contents at 10J ..	100

---

---

Table 6-1 Tensile properties data for PA6 and PA6/Graphene multifilament. ....	108
Table 6-2 Summary of dynamic impact parameters of CF, PA6, PA6/Graphene wrapped yarn composites at 10J and 25J impact energy .....	109
Table 6-3 Tensile properties of thermoplastic fibres and veils at 1, 10, 1000mm/min loading speed.....	113
Table 6-4 Summary of dynamic impact parameters of CF and PEI veil hybrid UD composites at 10J and 25J impact energy.....	114
Table 6-5 Summary of impact dynamic parameters of CF and PEI veil hybrid 3D composites at 10J and 25J impact energy.....	119
Table 7-1 Optical microscope images and fibre diameters of the undrawn and drawn PP/Graphene fibres .....	126
Table 7-2 Tensile properties of polypropylene/graphene fibres at the different loading speed .....	127
Table 7-3 Summary of tensile test results of composites .....	134
Table 7-4 Summary of dimensions, maximum load and interlaminar shear strength of composites specimens in short beam strength test.....	136
Table 7-5 Summary of impact test results for cross-ply and 3D structure composites at 10J and 20J impact energy .....	140
Table 7-6 Summary of experimental and normalised compressive stress data of hybrid yarn reinforced composites .....	147

---

## List of Abbreviations

<b>2D</b>	<b>Two dimensional</b>
<b>3D</b>	<b>Three dimensional</b>
<b>AFRP</b>	<b>Aramid fibre reinforced polymer</b>
<b>C</b>	<b>Commingled yarn</b>
<b>CAI</b>	<b>Compression after impact test</b>
<b>CF</b>	<b>Carbon fibres</b>
<b>CFRP</b>	<b>Carbon fibre reinforced polymer</b>
<b>G</b>	<b>Graphene nanoparticles</b>
<b>GFRP</b>	<b>Glass fibre reinforced polymer</b>
<b>GNP</b>	<b>Graphene nanoplatelets</b>
<b>MW</b>	<b>Micro wrapped yarn</b>
<b>PA6</b>	<b>Polyamide</b>
<b>PEI</b>	<b>Polyetherimide</b>
<b>PP</b>	<b>Polypropylene</b>
<b>UD</b>	<b>Unidirectional</b>
<b>W</b>	<b>Wrapped yarn</b>

## Abstract

Fibre-reinforced polymer composites as low-density materials as an alternative to steel are widely used in markets, especially in the automotive and aerospace industries, due to their superior mechanical performance and light weight construction. However, the main disadvantage of thermoset composites is their brittleness. Therefore, there has been growing interest in impact damage tolerance of thermoset composites recently.

The aim of this research is to improve the impact damage tolerance of carbon fibre thermoset composites by incorporating thermoplastic fibres. Hybrid CF/thermoplastic fibres are initially manufactured through the conventional comingling method. However, producing homogeneous comingled yarn with enhanced mechanical properties is challenging due to fibre damage by an air pressure nozzle. Hence the micro wrapping of the finer sub-bundles has been developed as a way of introducing intra-tow toughness without fibre damage. A tow-splitting technique has been developed in order to produce 1.5k carbon fibre tows that are prohibitively expensive and not easily available commercially. Initially, wrapped yarn with polypropylene multifilament was studied at different wrap densities and number of filaments. Furthermore, PP/Graphene nanocomposite fibres have been used to study the impact performance.

A novel machine for comingling, micro-wrapping and thermoplastic filament drawing has been developed from the first principles. This system consists of heating, stretching, wrapping/comingling stages, and final winding all controlled through the Triomotion software platform. This system has online tension and image acquisition capability. These hybridised yarns have been used for producing unidirectional (UD), cross-ply (2D), and three-dimensional (3D) preforms using a robotic tow placement system. The thermoset composites were prepared through a vacuum bagging process. The impact damage tolerance of these composites has been mainly assessed by the drop weight impact and compression after impact (CAI) tests. Furthermore, an ultrasonic C-scanning has been used for quantifying the damaged areas.

Results showed that the impact damage tolerance of 3D preform structure thermoset composites with hybrid yarn was increased by 14% by wrapped yarn and decreased by 21% by comingled yarn after the 25 J impact test. Micro wrapped yarn composites also showed increased impact damage tolerance by 34% after the 20 J impact test. However, there was no significant improvement in impact damage tolerance between PP and PP/graphene fibres hybrid yarn composites.

## **Declaration**

No portion of the work referred to in the thesis has been submitted in support of an application for another degree or qualification of this or any other university or other institute of learning;



## Copyright Statement

- I. The author of this thesis (including any appendices and/or schedules to this thesis) owns certain copyright or related rights in it (the “Copyright”), and he has given The University of Manchester certain rights to use such Copyright, including for administrative purposes.
  
- II. Copies of this thesis, either in full or in extracts and whether in hard or electronic copy, may be made only in accordance with the Copyright, Designs and Patents Act 1988 (as amended) and regulations issued under it or, where appropriate, in accordance with licensing agreements which the University has from time to time. This page must form part of any such copies made.
  
- III. The ownership of certain Copyright, patents, designs, trademarks and other intellectual property (the “Intellectual Property”) and any reproductions of copyright works in the thesis, for example, graphs and tables (“Reproductions”), which may be described in this thesis, may not be owned by the author and may be owned by third parties. Such Intellectual Property and Reproductions cannot and must not be made available for use without the prior written permission of the owner(s) of the relevant Intellectual Property and/or Reproductions.
  
- IV. Further information on the conditions under which disclosure, publication and commercialisation of this thesis, the Copyright and any Intellectual Property and/or Reproductions described in it may take place is available in the University IP Policy (see <http://documents.manchester.ac.uk/DocuInfo.aspx?DocID=487>), in any relevant Thesis restriction declarations deposited in the University Library, The University Library’s regulations (see <http://www.manchester.ac.uk/library/aboutus/regulations>) and in The University’s policy on Presentation of Theses.

## **Acknowledgements**

Firstly, I would like to sincerely thank my supervisor, Prof. Prasad Potluri, for his constant support, tolerance, and guidance. Most of all, he has provided me with various and invaluable research experiences. Secondly, I am deeply grateful to Dr Vivek Koncherry for his continuous support and encouragement. He always supports students to find a solution. My special thanks go to Prof. David Lloyd, who always made time to support me. Especially during the lockdown period due to COVID-19, he constantly gave me feedback for my PhD thesis through a virtual meeting.

I am also grateful for the funding and industrial experience from EPSRC (Engineering and Physical Sciences Research Council), Alvant, BAE Systems, Advanced Medical Solutions, Petronas, and Alva Industries. They provided me with invaluable research experience and knowledge.

Last but not least, I would like to express my thanks to the Robotics and Textile Composites groups and the school of natural sciences staff for their contributions to my research.

**This thesis is dedicated to my parents.**

For their endless encouragement, support and love

# Chapter 1.

## Introduction

### 1.1 Background

Fibre-reinforced polymer composites have become competitive with steel because of their light weight, superb fatigue strength and stiffness, ease of fabrication, corrosion resistance and flexibility in design [1]. These characteristics of composites are suitable for load-bearing structures and are mainly applied to high-performance vehicles, such as aircraft and marine vessels. Therefore, because the complex shape of composites has been required to apply to various applications, thermoset matrix as low viscosity material is widely used in industry. However, thermoset composites are brittle due to their high cross-linking density [2]. Once composites can be damaged as they hit or collide with other objects, these impacts cause matrix cracking, fibre fracture, delamination, and denting in the composites [1].

Many scientists have been examining to increase impact damage tolerance of thermoset composites by preform architecture, toughened matrix, modified reinforcement, interleaving material, and stitching [1], [3]–[7]. Most of all, because thermoplastic composites have better delamination resistance and less matrix cracking than thermoset composites, thermoplastics as a type of hybrid yarns [8], [9], nanoparticles [10], veils [11], and films [12] are used with thermoset composites to improve impact damage tolerance. However, thermoplastic matrix composites are expensive to manufacture and have problems such as creep; hence their use is restricted to non-structural composites. High-performance thermoplastic composites, such as PEEK based, are excessively expensive. As a result, thermoset composites with improved damage tolerance through the incorporation of inexpensive thermoplastic fibres have the potential to provide damage tolerance at an affordable cost. This work investigates hybrid yarns containing mainly reinforcing fibres combined with a very small quantity of thermoplastic fibres. The hybrid yarns are made of high-performance materials such as carbon, glass, Kevlar fibres and low-cost thermoplastic fibres such as PP. Hybrid composites produced through low-cost

---

resin-infused out-of-autoclave manufacturing processes could be used in primary airframes and automotive chassis.

Previously, commingling, schapped and kemafil technologies were used for manufacturing hybrid yarns for thermoplastic matrix composites [13]. These hybrid yarns have around 50% by volume reinforcing fibres and the rest thermoplastic fibres. In contrast, only a small proportion of thermoplastic fibres (10%) are required for toughened thermoset composites. Among these technologies, the commingling process is the simplest and cheapest way to produce hybrid yarns with continuous multifilament without adding twists. Furthermore, commingled yarn can be presented on fast impregnation of fibre reinforcement fibres. Hybrid yarns are developed to produce thermoplastic composites initially. However, serious fibre damage is caused by air pressure applied to the yarns during the manufacturing process, and low fibre distribution is shown. Those factors decrease the mechanical properties of composites.

This study developed a fibre hybridisation process and manufacturing machine to minimise fibre damage and increase impact damage tolerance of carbon fibre thermoset composites. Previous studies on wrapping were conducted on glass fibres [9]. As carbon fibres are the principal reinforcing fibres for high-performance composites, there is a need to develop hybrid micro-wrapped yarns with carbon fibres. As this technology does not exist, novel manufacturing concepts a) tow splitting and b) micro-wrapping have been investigated in this work. As there are no commercially available machines, the main focus of this work has been to develop machines from the first principles.

## **1.2 Problem definition and research approach**

This project addresses the issue of lack of impact damage tolerance in thermoset composites, especially produced with low-cost resin infusion technology. Matrix toughening solutions are currently available only in expensive prepreg systems used in the aerospace industry. Toughened resins are difficult to infuse and require expensive manufacturing machines, often involving in-line heating. As a result, thermoplastic fibres incorporated in fibre preforms prior to resin infusion offer a cost-effective damage tolerance solution. Standard resin infusion equipment could be used for manufacturing these toughened composites.

Currently, comingling is the primary method for hybridising thermoplastic fibres with reinforcing fibres. However, comingling does not produce uniform fibre distribution, causing a lot of fibre distortion and damage. As a result, there is a significant loss in strength and stiffness of the composites. Here, fibre hybridisation technology is needed for the uniform distribution of thermoplastic fibres without excess fibre distortion or damage. The research approach is explained below to solve the research problems.

- Commingled yarns made of glass fibres and polypropylene fibres could decrease impact damage and increase impact damage tolerance [14]. However, because comingled yarns are manufactured through an air nozzle, fibre breakages and non-homogeneous fibre distribution were caused. Therefore, the wrapping process was introduced to decrease fibre damage and increase fibre distribution. Initially, PP multifilament was used to wrap 6K carbon fibres at different wrap densities and the number of filaments; then, micro-wrapped yarns were produced to obtain homogeneous fibre distribution. To compare with previous research, the present study initially used PP fibre to investigate the damage tolerance of hybrid yarn composites.
- The impact damage of composites, such as delamination, matrix cracking, fibre and matrix debonding and fibre fracture, can be decreased depending on preform architecture for composites [15]. Therefore, UD and 3D structure preform composites were manufactured with hybrid yarns and their impact behaviours and damage tolerance were compared and analysed with neat carbon fibre composites.
- Manufacturing machine for comingling, micro wrapping and fibre drawing is not available in the market. To develop a hybrid yarn manufacturing process and use conductive fibres such as carbon fibres, a bespoke machine was designed and developed. Because carbon fibre as conductive material can cause electric shocks on a machine, machine development was needed in this study (see Chapter 3).

### **1.3 Research aims and objectives**

The aim of this research is to improve the impact damage tolerance of carbon fibre thermoset composites by using low-cost thermoplastic fibre through a hybridisation

---

process that distributes thermoplastic fibres uniformly within a carbon fibre tow with minimum distortion or damage. This may be achieved through the development of a novel manufacturing machine from the first principles.

In order to realise this aim, the following objectives have been identified:

- Investigate the limitations of comingled hybrid yarn systems to decrease fibre damage and develop a hybrid yarn manufacturing process to increase impact damage tolerance of thermoset composites.
- Develop a concept for micro-wrapping thermoplastic fibres on sub-scale carbon fibre tows to produce automatically.
- Develop a concept for splitting larger carbon fibre tows into finer tows in order to facilitate micro-wrapping as a means to distribute thermoplastic fibres uniformly within a large carbon fibre tow.
- Develop very fine thermoplastic fibres through a controlled drawing process to increase carbon fibre volume fraction.
- Incorporate nanomaterials such as graphene nanoplatelets (GNP) in thermoplastic fibres in order to investigate the potential of nanomaterials on damage tolerance of thermoset composites.
- Develop a novel computer-controlled fibre drawing, comingling and micro wrapping all in one machine from the first principles. This may provide a research platform for composites beyond this project.
- Investigate impact damage performance of micro-wrapped composites and compare with comingled yarn composites.
- Investigate post-impact residual strength through compression after impact (CAI) test to analyse the impact damage tolerance of thermoset composites with hybrid yarns.

## **1.4 Thesis layout**

This thesis has been organised into the following eight chapters: (1) introduction, (2) literature review, (3) development of automatic hybrid yarns manufacturing process, (4) materials and experimental procedure, (5) impact damage tolerance of thermoset composites with carbon and PP multifilament hybrid yarn, (6) hybrid composites with higher thermal performance thermoplastic fibres, (7) study of impact damage tolerance with micro-wrapped carbon fibres and polypropylene/graphene nanocomposite fibres, and (8) conclusion and future works.

Chapter 1 explains the direction of this research and why it was conducted. The research problem, objectives, and approach for solving the problem are specifically discussed.

Chapter 2 explains the different fracture types of composites caused by impact and methods to improve the impact damage tolerance of composites from previous research. In addition, this chapter discusses traditional hybrid yarn manufacturing methods (with a view to developing an updated manufacturing process) and currently developed robotic tow placement for preforming.

Chapter 3 presents the machine development process for fibre hybridisation and fibre drawing. The machine was assembled based on a designed 3D CAD drawing and is operated by a programmable logic controller which can control five motors, two limit sensors, five heaters, and three pneumatics.

Chapter 4 presents the specification of materials for CF and thermoplastics. This study used thermoplastic fibres, veils, and graphene nanocomposite fibres to manufacture hybrid yarn. The manufactured hybrid yarn on the developed machine produced UD, 2D and 3D preform structures on a robotic tow placement. Their composites were manufactured through the resin infusion process. Lastly, testing methods for analysing the characteristics of the samples are presented.

Chapter 5 presents the hybrid yarn development process, the impact damage tolerance of CF/PP multifilament wrapped yarn composites at different wrap densities, the number of PP filaments, and the preform structure (UD vs 3D).



Chapter 6 analyses hybrid CF thermoset composites with stable thermal thermoplastic and PA6 and PEI veils to study impact damage tolerance. PA6 multifilaments and PA6/graphene nanocomposite multifilaments were prepared and investigated, and PEI veils were applied to thermoset composites using different insertion methods.

Chapter 7 analyses the mechanical properties of micro-wrapped yarn composites with PP/graphene nanocomposite mono fibres. The improved wrapped yarn structure, called micro-wrapped yarn, is explained. The fibre drawing process increased the mechanical properties of PP and graphene nanocomposite fibres; these fibres were then applied to the hybrid yarn composites.

Chapter 8 summarises the main findings of this research and discusses their implications with respect to future research on developing manufacturing processes and improving the mechanical properties of CF thermoset composites.

## **1.5 Summary**

Thermoplastic hybrid yarns improve the impact damage tolerance of thermoset composites. Thermoplastic composites have better delamination resistance and less matrix cracking than thermoset composites. Thermoplastics are blended with thermosets to improve impact damage tolerance by previous researchers. In this study, a hybrid yarn manufacturing process was developed to overcome the current limitations of the traditional commingling process, which causes fibre damage and poor fibre distribution.

Extruded PP/graphene nanocomposite fibres are used to produce micro-wrapped yarn after the fibre drawing process to increase carbon fibre volume fraction and impact damage tolerance of composites. Since improvement in the mechanical properties of thermoplastic and graphene nanocomposites has been demonstrated by many researchers, it is expected that the impact damage resistance and tolerance of thermoset composites could also be improved by using PP/graphene nanocomposites fibres.

PP multifilament and monofilament are used to produce a hybrid yarn in order to compare the damage tolerance of composites for different hybrid yarn structures. The impact damage tolerance of a composite can be determined using composite materials and preform architecture. Composite preforms for the UD, 2D cross-ply and 3D structure are

produced using hybrid yarn on an automatic tow placement developed by the University of Manchester. The impact behaviour of hybrid yarn thermoset composites was estimated by the CAI test.

## Chapter 2.

### Literature Review

#### 2.1 Mechanics of fibre reinforced polymer composites

Material properties can be characterised by Young's modulus, which is calculated from a tensile test or equation of classical lamination theory. The engineering constants are calculated through the equations and provide information on mechanical properties, including elasticity, brittleness, ductility, and the toughness of the material. These obtained engineering constants can also be used in testing by simulations to predict the mechanical behaviour and property of materials (Appendix A).

Typical polymer stress-strain curves are shown in Figure 2-1. The thermoset presents a high modulus and low elongation from the tensile test because of its brittleness. On the other hand, thermoplastic shows low modulus and high elongation due to ductility [16]. Fibre-reinforced polymer composites are stronger and lighter than steel. However, impact damage resistance of composite is low, and delamination or cracks are caused easily by the impact due to their inherent brittleness (Figure 2-2). Therefore, a lot of studies for the anti delamination of composite have been studied by resin modification, development of fabric architectures, and interleaving thermoplastic to improve impact damage tolerance and resistance [17], [18].

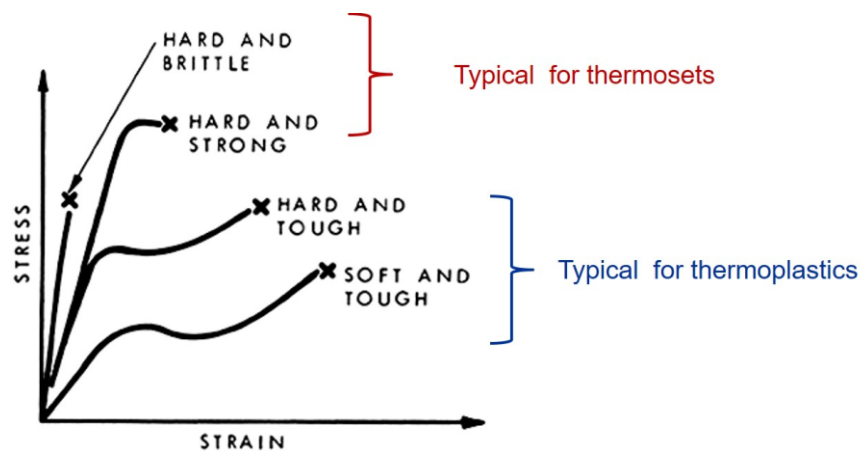


Figure 2-1 Typical stress-strain behaviour of polymers [16]

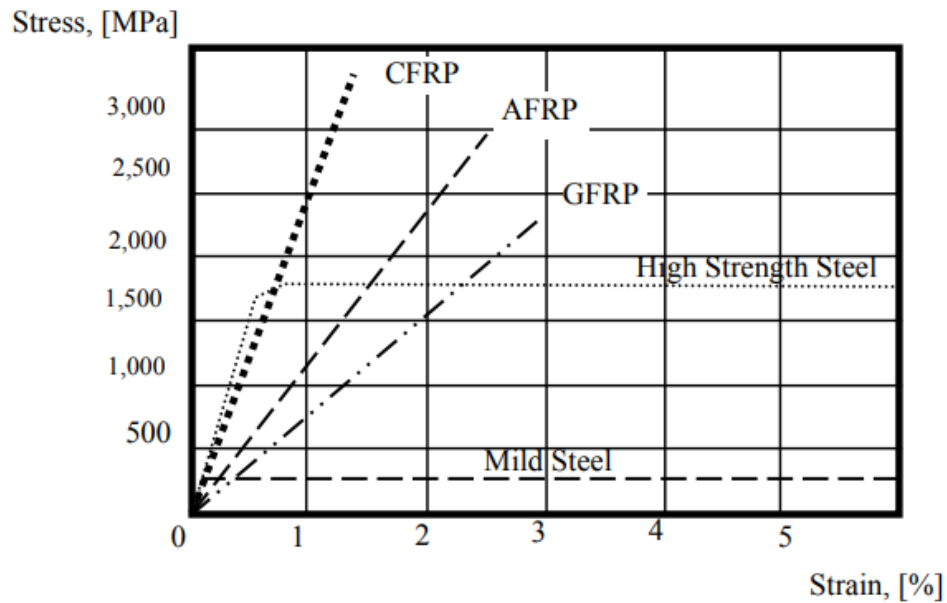


Figure 2-2 Strain-stress curves of FRP composites and steel [19]

## 2.2 Impact damage behaviour of fibre reinforced polymer composites

### 2.2.1 Impact damage behaviour by low energy impact

Figure 2.3 shows the typical fracture types of composites for low-energy impacts, which do not cause penetration of the composites [20]. Delamination, matrix cracks, fibre breakages and surface deformation are generally observed. These defects are easily generated by voids and resin-rich or resin-starved areas [21].

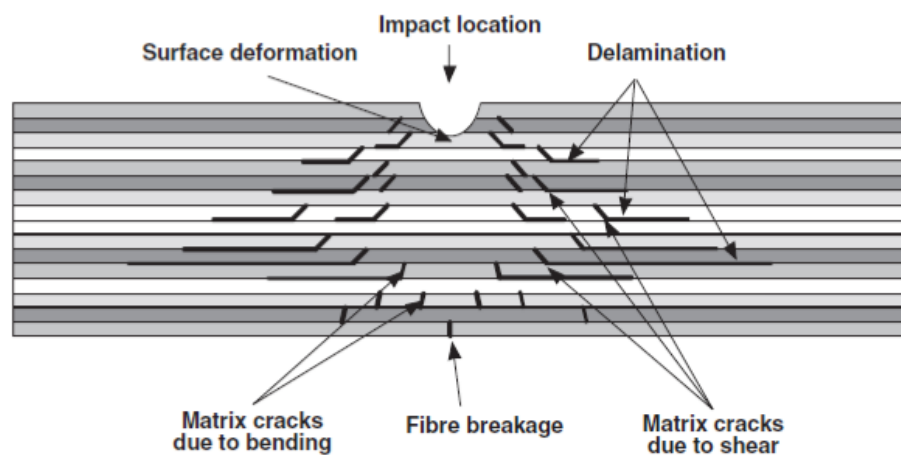


Figure 2-3 Typical impact damage in fibre reinforced polymer composites [21]

Compatibility between matrix and fibres is also one of the causes of creating fractures in the composites. Those fractures were observed at both thermoset and thermoplastic fibre composites. However, the thermoplastic composites show better impact damage tolerance than thermoset composites in the compression after impact (CAI) test and simulation of impact test [22], [23].

### 2.2.2 Failure of UD, 2D and 3D preform structure composites

Damage to UD composites occurs easily along with the fibre direction at low-velocity impact. Cross-ply structure composites occur the typical fibre breakage, delamination, and matrix cracks which are generated via shear stress on the laminate surface [24], [25] (Figure 2-4.). Previous studies have demonstrated that 3D orthogonal woven composites are degraded in the early stage of fatigue [26], [27]. The defects are generated at polymer-rich regions, fibre crimps, and surface segments of z-binders [28]. When the binder tow is placed in the surface layers, the strain is concentrated in this area. It is why cracking occurs along with composite interface debonding. Furthermore, Figure 2-5 shows that binder tows contribute to preventing the failure of composites [29].

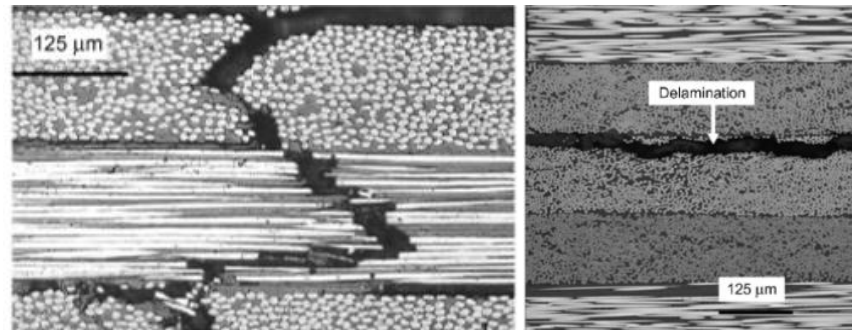


Figure 2-4 Micrographic of fibre fracture and delamination at cross-ply structure fibre composite [30]



Figure 2-5 (a) Delamination crack and z-binder bridging, and (b) fracture of 3D woven structural composites in mode I test [31]

3D weave preform structures can be classified as orthogonal, angle-interlock, layer-to-layer, and layer-to-layer weave, depending on the z-binder structure. The orthogonal weave composites structure has shown transverse matrix cracks spanning resin-rich channels in the early stage of fatigue [32]. In an angle-interlocked binder, transverse cracks grow on every side through the weft yarns. The angle interlock specimen has a higher crack density than the modified layer-to-layer sample [32]. The layer-to-layer composite having a weave pattern at the top and bottom layers show debonding cracks or delamination along with the interface between the binder yarns and the surrounding material. However, the angle interlocked laminates have the highest compression strength values after impact compared to orthogonal and layer-to-layer weave because of less crimp [33]. Therefore, non-crimp preform structures are considered to decrease the propagation of cracks and debonding in the composites [32].

### **2.2.3 Polymer matrix modification**

Semi-crystalline thermoplastic composites, which can be melted and reused, have superior impact resistance and the manufacturing cycle time of thermoplastic composites is short compared to thermoset composites. The producing process of thermoplastic composites includes melting the matrix, shaping, consolidation, and cooling. However, a disadvantage of this process is that it requires high pressure due to the high melt viscosity of the thermoplastic, in contrast to thermoset [34].

On the other hand, thermoset resin matrix composites exhibit higher tensile strength and modulus than metals or thermoplastic composites, as shown in Table 2.1 [35]. In addition, the advantages of thermoset composites are low viscosity and high thermal stability. The low viscosity resin is appropriate for vacuum infusion because the reinforcement is well-immersed in resin at room temperature [35]. Carbon fibre thermoset composites are also used in areas where high-temperature resistance is required [36]–[38]. Therefore, thermoset resins are widely used and created to produce composites of complex shape structures.

Table 2-1 Mechanical properties of carbon fibre composite and steel.

Material type	Density (kg/m <sup>3</sup> )	Tensile strength (MPa)	Elastic Modulus (GPa)	Breaking Length (km)	Ref.
Carbon fibre (standard)	1760	3530	230	205	[39]
Steel (S355)	7850	500	210	6	

However, thermoset composites are brittle and lack toughness due to their high crosslink density [35],[40]. It causes decreased impact damage tolerance of thermoset composites. On the other hand, because thermoplastic presents superior impact damage tolerance, the thermoset composites are manufactured with thermoplastic and increased mechanical properties. Other researchers accomplished these studies, and they added thermoplastic or rubber to thermoset resins to overcome brittleness [35].

Furthermore, nanoparticles obstruct cracking and improve the adhesion of fibres and resin [41]. These nanoparticles can be mixed with resin to produce fibre-reinforced polymer composites. Nanoparticles are generally agglomerated because of Van der Waals forces through the covalent and non-covalent functionalisation effect [42]. To disperse the nanoparticles evenly, researchers commonly employ ultrasonic mixing because ultrasonic waves can break up particle agglomerates [43]. Even with this technique, it remains difficult to disperse the nanoparticles in the resin. One method for achieving good dispersion and bonding between the resin and the nanoparticles is to control the quantity of nanoparticles. The particles show better dispersion when graphene oxide is used at less than 1 wt% to manufacture epoxy/graphene oxide composites; higher amounts cause particle agglomeration [44]. Composite manufacturing with nanoparticles needs to be assessed for particle dispersion and interfacial strength [45].

## 2.3 Improving the impact damage tolerance of composites

### 2.3.1 Preform structures development

The preform structure of a composite is a critical factor to improve mechanical properties. The fibre reinforced polymer (FRP) composite basically has a UD, 2D, and 3D preform

structure. When a load is applied to FRP composites, the generated growth direction of a crack tip is the same as that of the fibre alignment [24], [25]. Therefore, impact damage tolerance is dropped depending on fibre alignment and applied force direction. Because of this reason, 3D structure composites have shown better impact damage resistance and tolerance than UD and 2D structure composites.

The advantages of a 3D composite structure are high stiffness and high strength because z-binders are used through the z-direction [31]. In addition, it provides superior delamination resistance and superior impact damage tolerance. Figure 2-6 shows that impact damage resistance in 3D composite structures improves with increasing z-binder content. Although the fibre volume fraction of z-binder material is usually less than 0.5–1.0%, such composites can have significantly increased delamination toughness and damage resistance compared to non-z-binders composites [31]. The most common types of 3D structure composite are produced by weaving, stitching, z-pinning, 3D knitting, braiding, and tufting [31], as shown in Figure 2-7.

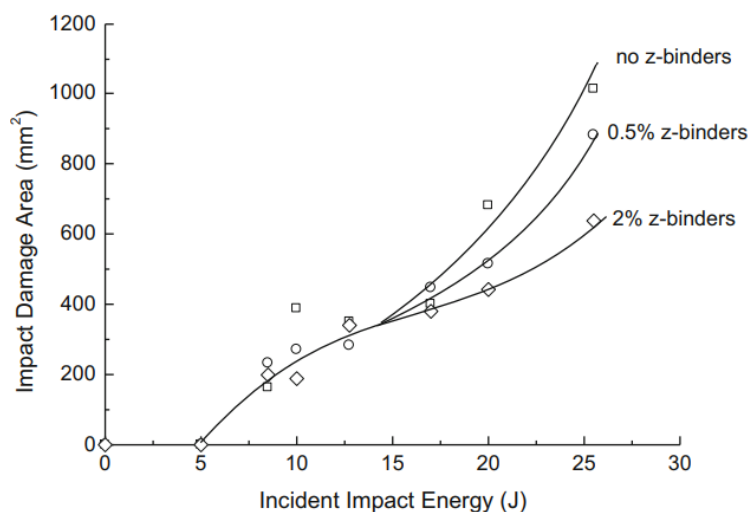


Figure 2-6 Impact damage resistance of 3D structure composites by increased z-binder content [31]

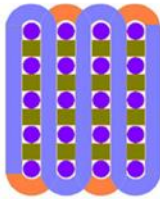
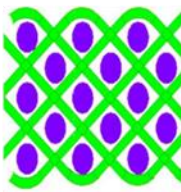

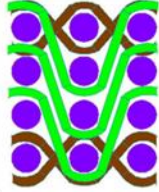
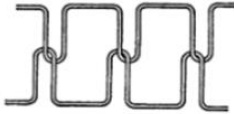


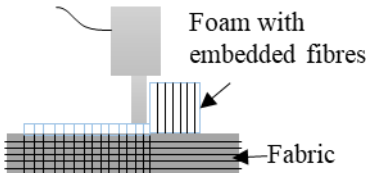
Depending on their binder structures, 3D woven preform structures can be categorised as orthogonal, angle interlock, layer-to-layer and modified layer-to-layer weave. The binder of a through-thickness interlock penetrates through the entire thickness of the composite. When the interlacing angle between the binder and the weft yarns is other than  $90^\circ$ , it is called an angle interlock. An interlacing angle of  $90^\circ$  is classified as an orthogonal



interlock. The binder in a layer-to-layer structure holds adjacent layers together [46]. Lastly, the modified layer-to layer weave structure especially has the plain weave on the top and bottom, as shown in Figure 2-7 [33].

The stitching process on a stack of plies consists of penetrating and binding by needle and threads. The standard stitching types are lock and chain, but modified lock stitch is more popular. The modified lock stitch minimises in-plane fibre distortion because the knots linking needle and bobbin threads are formed at one side of the laminate [47]. Stitching is also one of the most common ways to lessen impact damage in composite laminates. The delamination resistance and bending strength are improved by the stitching process [48]. In addition, researchers have discovered that a smaller stitching gap distance lowers the number of debonding areas in a composite structure [49].

In the z-pinning process, reinforcement fibres coated with cured resin are embedded into a thermoplastic foam. This foam is applied to dry composite fabrics, and the thermoplastic foams are melted. The reinforced fibres are pushed into the fabrics by heat and pressure produced by vacuum bagging [50].

	3D structures				
Weaving					[33]
	Orthogonal	Angle interlock	Layer-to-layer	Modified layer-to-layer	
Stitching					[47]
	Lock	Chain	Modified lock		
Z-pinning					[50]

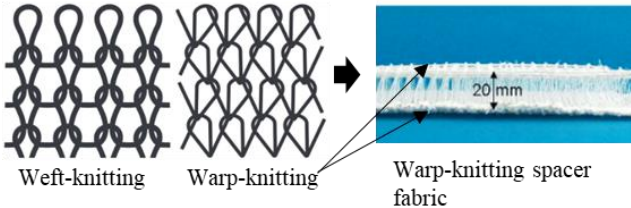
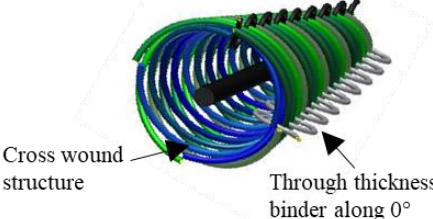
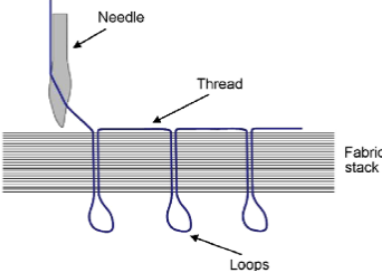
Knitting	 <p>Weft-knitting    Warp-knitting    Warp-knitting spacer fabric</p>	[51]
Braiding	 <p>Cross wound structure    Through thickness binder along 0°</p>	[52]
Tufting	 <p>Needle    Thread    Fabric stack    Loops</p>	[53]

Figure 2-7 Types of 3D preform structures

Knitted fabrics experience frequent fibre damage during manufacturing because the process of loop-forming exposes the fibres to tensile and bending forces [51]. However, the advantages of this structure are that knitted fabrics can cover a complex shape without wrinkling. 3D knitted structures are produced by both weft-knitting and warp-knitting. Warp-knitted spacer fabric, in particular, is used for 3D textiles in structural applications. Two warp-knitted laminates are manufactured and connected by another yarn to form a 3D structure [18].

3D braided structures are produced with through-thickness reinforcement fibres. These binders are guided by braider bobbins moving in helical directions [52]. Finally, 3D tufted preforms are manufactured by inserting a threaded needle into fabrics to make thread loops. This technique weakens the mechanical strength of composites by damaging the fibres in the fabric stack [53].

The structure of a 3D woven composite can be manufactured using various weaving patterns and different binders. The through-thickness component of a 3D composite is created by stitching, tufting, or z-pinning. These methods have production limitations due

to their slow production rate. [48], [53]. However, a 3D composite structure with through-thickness z-binder yarns can efficiently obstruct the spread of delaminations [54]–[58]. In addition, the merits of 3D woven composites are smaller damaged areas and higher impact damage resistance and interlaminar fracture toughness than UD and 2D structure composites.

### **2.3.2 Reinforced fibre modification**

To enhance the impact damage tolerance of thermoset composite, reinforcement fibre can be modified as using a third phase or increasing the functional group of carbon fibre. The use of nanoparticles such as graphene, carbon nanotubes, and graphite nanoparticles can raise fracture behaviour and the electrical and thermal characteristics of composites [59]. Recently, carbon black nanoparticles are mixed with a non-ionic surfactant, and then carbon fibres are dipped in this solution to achieve a well-distributed coating [41]. Another method to coat nanoparticles on carbon fibres is that the hydroxyl groups of modified carbon fibres react with isopropylidene malonate to create the carboxyl functionalised groups [60]. Carboxylic and alcohol groups increase the surface adhesive strength between nanoparticles, fibres, and resin. According to this research [60], the interfacial strength between the matrix and reinforcement fibre is critical for improving impact damage tolerance.

A hybrid yarn using third phase material is a mix of reinforcement and thermoplastic fibres to improve impact damage tolerance of thermoset composites. Hybrid yarns can be made by various techniques, such as commingling, cospinning, cowrapping, and cotwisting (Figure 2-8). Commingled yarns blend two or three different types of fibres using an air nozzle; this is the most common and straightforward method. Cospun threads are made as continuous reinforcing fibres cover spun fibres. Moreover, cowrapped threads, which are wrapped by matrix fibres, produce high-performance yarns [13]. Cotwisted yarns are made by twisting matrix and reinforcement fibres together, as shown in Figure 2-8.

Among the yarn structures, commingled yarn theoretically has the most homogeneous fibre distribution. Researchers have explained that the commingling process could improve fibre impregnation in contrast to side-by-side structures [61], [62]. Commingled

---

yarns (COM) produce composites with a higher crack resistance and fracture toughness than side-by-side (SBS) yarns; their tensile modulus is also approximately four times higher than that of a composite with a side-by-side yarn structure [63].



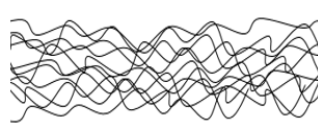
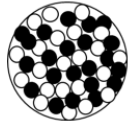
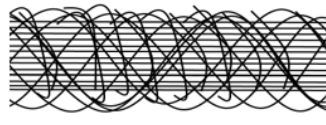
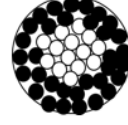
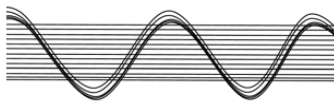
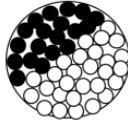

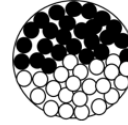
Category	Idealised yarn structure	
Side by side yarn		
Commingled yarn		
Cospun yarn		
Cowrapped yarn		
Cotwisted yarns		

Figure 2-8 Hybrid yarn structures [61]

## 2.4 Fibre hybridisation process and hybrid yarn composites

### 2.4.1 Commingling

Commingled yarn can be defined as two or more different filaments entangled as a single strand of yarn using an air nozzle. This traditional commingling process (Figure 2-9.a) has been developed through various methods because it is difficult to obtain a homogeneous fibre distribution by using an air nozzle. Saint-Gobain Vetrotex [64] created the commercial commingling process for thermoplastic fibres and glass fibres (Figure 2-9.b). These commingled yarns are manufactured through melt-spinning processes, and this created commingled yarn shows excellent stiffness properties.

Table 2-2 shows the parameters for commingled yarn manufacture. Air pressure facilitates the mingling process for the opening and blending of filaments. Air pressure is usually required to be up to 3 bar. Previous researchers used an air nozzle to obtain compact sections (nip) and the opened filament sections by air stream impacts during the commingling process (Figure 2-10). The nip frequency was increased with increasing air pressure however, if air pressure is applied with overpressure, the number of nips is dramatically decreased with poor fibre distribution [68]. Fibre tension is also crucial for commingling fibres because the nips can be eliminated if over tension is applied [66].

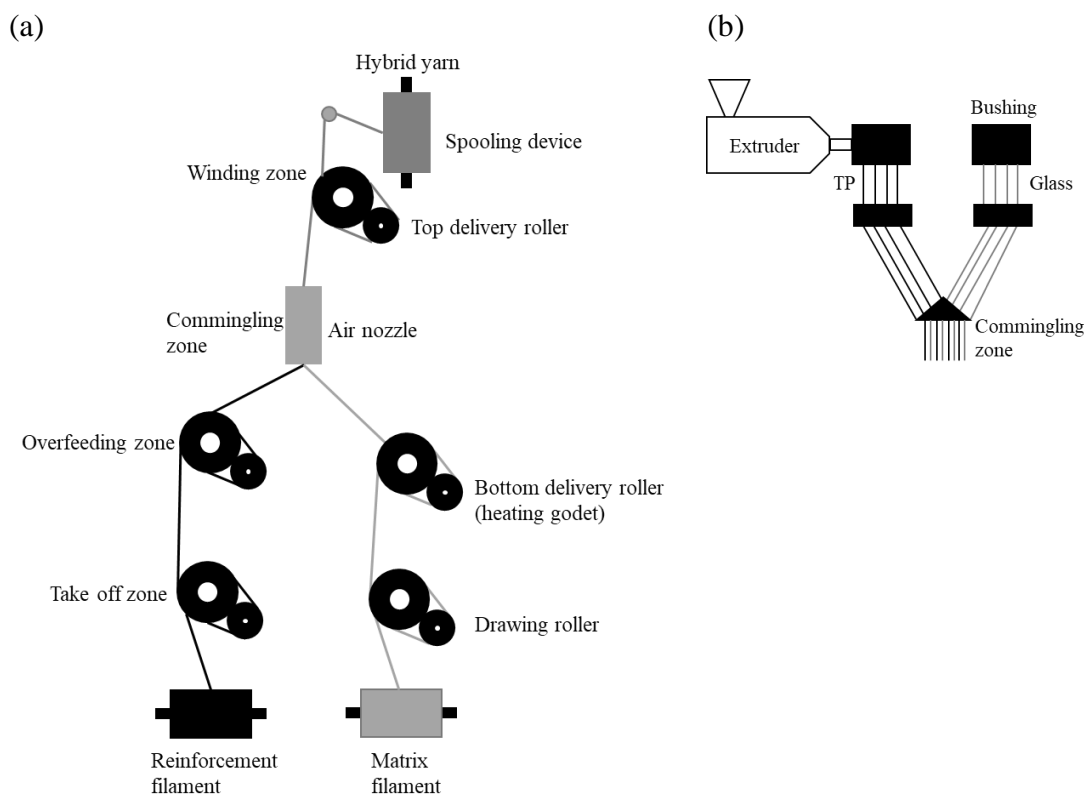


Figure 2-9 (a) General commingling process and (b) Twintex commingling process [13], [65].

Table 2-2 The parameters of commingled yarn manufacture [66]

<b>Categorisation</b>	<b>Parameters</b>
Raw material parameters	filament denier, number of filaments, cross-sectional shape of fibres, and filament rigidity
Processing parameters	air pressure, overfeed, and process speed
Machine parameters	nozzle design and machine configuration

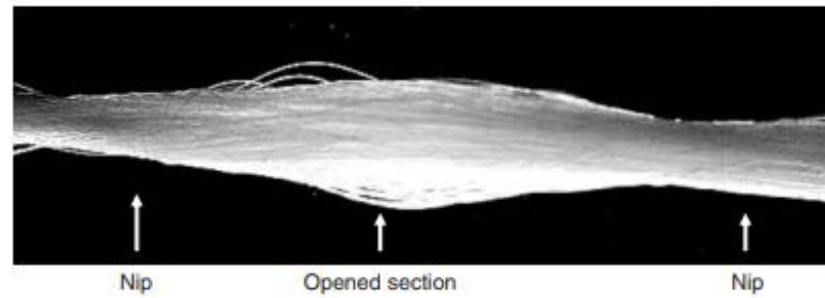


Figure 2-10 Typical structure of commingled yarn that is produced by an air nozzle [67]

Table 2-3 Commingling yarn depending on researchers

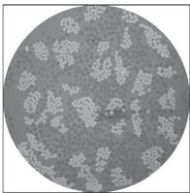
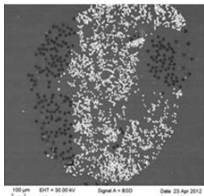
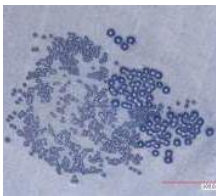
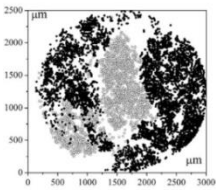
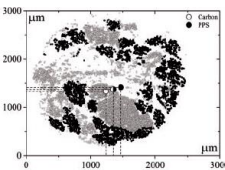
no.	Cross-section	Fibre	Method	Degree of overfeeding (%)	Production speed (m/min)	Ref.
1		Glass/PP, Twintex	Spinning	-	-	[69]
2		Glass/PP (600/33tex)	Nozzle (1-4 bar)	7	-	[14]
3		Glass/PP (33/17tex)	Nozzle & Winding (1-4bar)	7	-	[70]
4		Glass/PP (1200/800tex)	Nozzle (3-9bar)	1,3,4,8	50, 100	[66]
5		Carbon/PPS (800/800tex)	Nozzle (5-6bar)	4, 6	50, 100	[71]

Table 2-3 shows commingled yarn cross section SEM images from previous researchers. Sample no.1, consisting of glass fibre and PP fibre, was manufactured with a spinneret from Twintex; it shows better fibre distribution in the image than the other samples in Table 2-3. Samples no.2–4 also consist of glass fibre and PP fibre, but an air nozzle was used to mingle the fibres; they still require an improvement in fibre distribution. For sample no.3, a rewinding process was added to create a homogeneous commingled yarn; however, it is still non-homogeneous because the alignment of the fibres moved during the manufacturing process [51]. Sample no. 5, made using an air nozzle, consists of carbon fibre (CF) and PP fibre (Table 2-3); although it presented improved fibre distribution, it still requires further improvement.

### 2.4.2 Wrapping

Filament-wrapping processes require a sheath yarn and a core yarn. The sheath yarn wraps the core yarn through spindle rotation. The basic wrapping process involves a feed roller, nip roller, hollow spindle, and winding unit, as shown in Figure 2-11 [13]. The core yarn passes through the centre of the hollow spindle; then, as the spindle is rotated, the sheath yarn (mounted on a spindle) wraps the core yarn in a spiral fashion. The number of wraps per meter is controlled by adjusting the spindle speed and the yarn take-up speed before starting the production of the hybrid yarn.

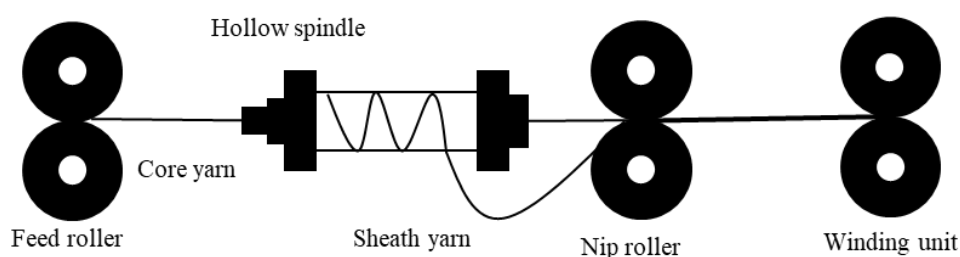


Figure 2-11 Fibre wrapping process [13]

The wrapping direction of sheath yarn can be single wrapping (called an ‘S’ or ‘Z’ twist) and double wrapping (called an ‘SZ’ twist) (Figure 2-12). The letters S and Z signify the rotation direction. The double-wrapping yarn requires two spindles because the two sheaths of yarn rotate in different directions to produce the S and Z twists.

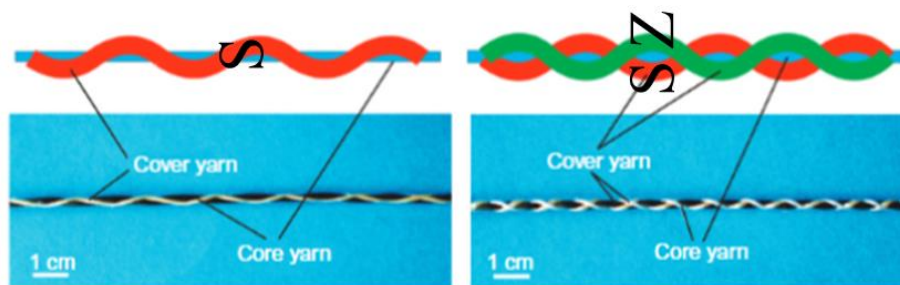


Figure 2-12 Yarn structure of singly (S twist) and doubly (S and Z twist) wrapped yarns [51]

The wrapped yarn is used to manufacture thermoplastic composites mostly. This wrapped yarn thermoplastic composite was produced by PEEK fibres and CF [72], and it improves mechanical properties. An air-textured PLA yarn was wrapped by PLA filaments [73], and flexural strength improved 2 - 3.3 times more and impact strength is increased 2 times higher than neat PLA samples. For thermoset composites, glass fibres and PP fibres were used for micro-wrapped yarns for impact damage tolerance of composites [9]. This research presents better compressive strength in micro-wrapped yarn compared to commingled yarn. Micro-wrapped yarn and commingled yarn composites retain 60-43% and 60-39% of compressive strength at 15-50J impact energy. Currently, almost of all research use wrapped yarn for thermoplastic composites. This research aims to exploit the hybrid yarn technology for improved damage tolerance in thermoset composites. While there has been some work on glass fibre composites, this research aims to investigate hybrid thermoset composites with carbon fibres commonly used fibres in aerospace and automotive structural composites.

## 2.5 Increase mechanical properties of thermoplastic fibres by drawing process

Most polymers have both crystalline and amorphous characteristics. The amorphous region in the polymer fibres can increase crystallinity through the fibre drawing process, and it grows the tensile strength of fibres. The mechanical property is also changed at different fibre draw ratios. The fibre draw ratio (DR) can be calculated from Equation 2-1.  $D_i$  and  $D_f$  are the initial and final diameters of each fibre. When the draw ratio is increased, elastic modulus and stress at the break value of fibre are also increased [74]. Therefore, The increase in DR value corresponds to enhanced strength and toughness of fibres.



---

$$DR = \left(\frac{D_i}{D_f}\right)^2$$

Equation  
2-1

To improve the mechanical properties of polymer fibres, fillers such as fumed silica [74] and single-wall carbon nanotube (SWNT) [75] nanoparticles can be applied to produce nanocomposite fibres. The strain at break value differs depending on the materials used. PP/fumed silica composite fibres with increased DR values demonstrate decreased strain at failure. However, poly L-lactide/SWNT composite fibres increase elongation at failure at a draw ratio of 15 [74].

## **2.6 Industrial robotic systems and automated fibre placement**

According to ISO 8373, an industrial robot is automatically controlled, and it is possible to be reprogrammed [76]. It is a multipurpose manipulator that is programmable in more than three axes. It is fixed in place and can be mobilised for use in industrial automation. Therefore, automation systems can produce products economically. This section outlines the necessary information to understand automatic manufacturing systems and the currently developed robotic tow placement device.

### **2.6.1 General robot structures**

The configuration of industrial robots is categorised as Articulated, SCARA (Selective Compliance Assembly Robot Arm), Cartesian, Delta, and Cylindrical (Figure 2-13). They are used in suitable industries depending on an application because they have different movements and tolerances in load capacity [77].

An articulated or jointed arm is the most common structure and generally has six or four rotation joints (Figure 2-13.a). Articulated arms are used for palletising, packing, and picking up objects [77]. Each joint carries all the weight of the following joints. For example, Joint number 4 carries joints number 5 and 6. SCARA (Figure 2-13.b) has four axes for two horizontal moves, one vertical move and one rotation move. It is generally used at assembly factories for packing, press tending, adhesive dispensing, and other applications [77].

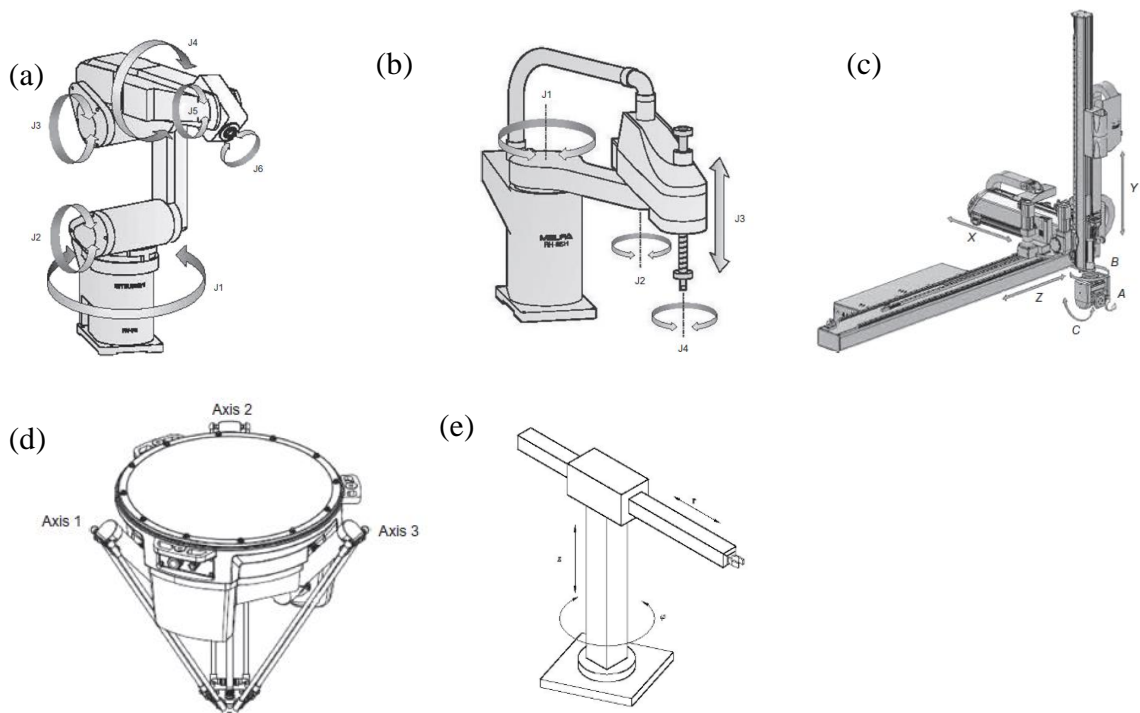


Figure 2-13 The different types of robots architecture; (a) Articulated, (b) SCARA, (c) Cartesian, (d) Delta (d), and (e) Cylindrical [77].

Cartesian robots (Figure 2-13.c) have only linear drives for two (X-Y) or three (X-Y-Z) main axes. Rotary axes can be additionally mounted on the end effector, and this robot is applied to assembly, plastic moulding, handling, and palletising tasks [77]. Cartesian robots are similar to gantry machines, but gantry uses two X-axes, and Cartesian have one X-axis. Hence, the gantry can have much longer stroke lengths and carry heavy loads. Furthermore, it is safe due to the clear limited work area.

Delta or Parallel robots have concurrent prismatic or rotary joints (Figure 2-13.d). This robot is an overhead mounted machine with three motors and an end effector. They are each linked to the other to move the robot arm. This robot can decrease arm weight and increase acceleration and speed to a very high level. However, it has a low payload capacity, generally under 8 kg. Therefore, its application areas are picking, packing for food, and assembling [77].

Lastly, cylindrical robots consist of rotary and linear axes (Figure 2-13.e). The vertical and horizontal linear axis and rotary axis follow the rotation motion at the base of the

robot. The main application is in the electronics industry, especially the room cleaning industry [77].

### 2.6.2 System control

The system control enables the automatic working of a machine or robot. The roles of the system control are providing correct sequence moving, data for manufacturing execution system (MES), error recognition and safety systems. The programmable logic controller (PLC) can handle hundreds of inputs and outputs (I/O), analogue functions and advanced network interfaces such as Profibus and Ethernet. Sensors can also provide different types of information, such as the location of motors and temperatures through the PLC. The robot can set the work conditions through this information. Therefore, a current robot system includes the PLC to control all functions [78]. PLC controller is interfaced with a human-machine interface (HMI) to provide all information, and it shows overall control functions to the operator via a graphical display.

### 2.6.3 Commercial automated fibre placement

Composite materials can make flexible shapes and complex structures on the Automated Fibre Placement (AFP). AFP parts include a computer-controlled robotic arm with a head-end effector used in the lay-up on the mould, as shown in Figure 2-14. The functions of the fibre-placement process include filament winding and tape laying. The tows (untwisted fibres) are unrolled from creels and fed to the fibre-placement head. Many tows are controlled through the tensioner of the robot [79], [80]. The roller compacts the tow by applying heat to the mould surface.

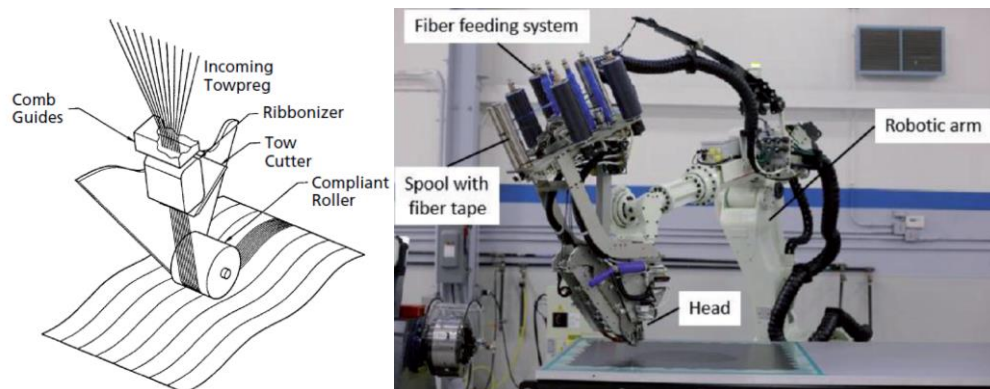


Figure 2-14 Commercial robotic tow placement [79], [80]

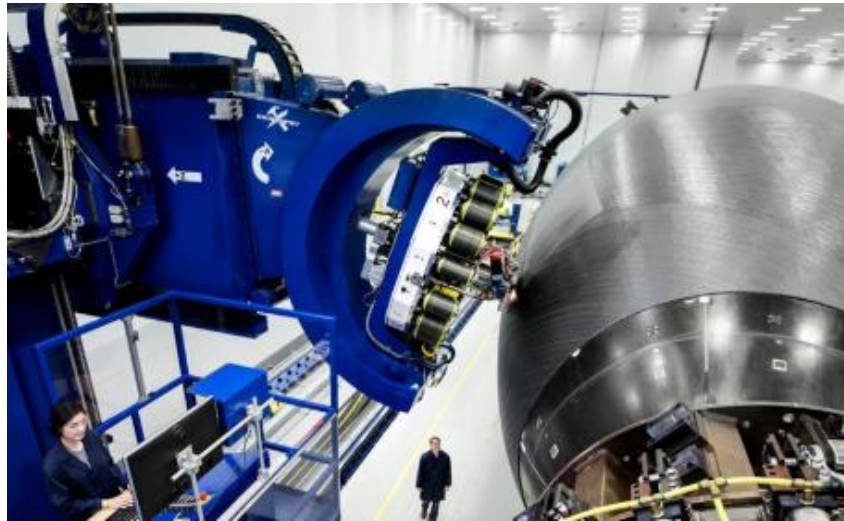


Figure 2-15 Boeing AFP machine to produce the monolithic carbon fibre composites of fuselage section [81]

The roller removes the trapped air between the tows and the mould surface. Low tension is used at 0–2 lb, and compaction pressure is used at 10–400 lb for the lay-up process [82]. This process can produce an optimal composite structure having stiffness laminates with curvilinear fibre paths. It can improve the buckling load [83], [84], the effect of the stress degree [85]–[87], and the notch sensitivity [88]. AFP machine has already been introduced in commercial areas to make composite products (Figure 2-15).

#### 2.6.4 Continuous dry fibre placement

Robotic fibre placement techniques have been developed for the 3D preform process [3] because 3D woven preforms require complex mechanisms and are limited in design. It can also save on cost and cycle time. The advantage of dry robotic tow placement is low manufacturing cost compared to commercial prepreg fibre placement, especially in the aerospace sector [79], [89].

A Gantry robotic system for automated dry fibre placement has been developed at the University of Manchester (Figure 2-16). This robot employs the four axes of freedom, i.e., the X, Y, Z and rotation axes. This machine is automatically operated to make preforms [79]. A new tool was introduced to overcome these limitations. The tool consists of pins that can hold each tow (Figure 2-17). Its advanced dry fibre placement provides a

preform of  $0, 90, \pm \Theta$  degree [90]. Composite panels for this study are also manufactured by using gantry automated tow placement systems [91], as shown in Figure 2-17.



Figure 2-16 Gantry automated fibre placement at the University of Manchester

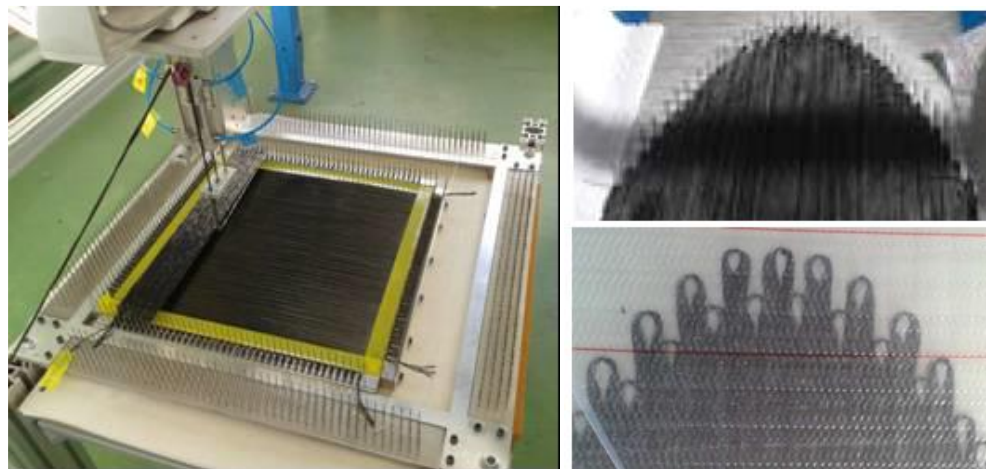


Figure 2-17 Robotic fibre placement developed by the University of Manchester [90]

## 2.7 Summary and critical discussion

The aim of this study was to improve the impact damage tolerance of thermoset composites. The damage tolerance of composites can be improved by tows modification, preform structure development and resin modification. This research chose hybrid yarns

to improve impact damage tolerance and discussed previous hybrid yarn composites studies.

Almost of all previous researchers have used glass and PP fibre commingled yarn to improve fibre distribution and manufacture thermoplastic composites. The other researchers use hybrid yarn especially commingled yarns to improve the impact damage tolerance of thermoset composites. However, the traditional method of using an air nozzle for manufacturing commingled yarn can cause serious fibre damage and low fibre distribution. Furthermore, composite impact damage resistance and tolerance can be dropped compared to neat CF composites. The micro wrapping process is developed with carbon fibres to decrease fibre damage by air nozzle and increase fibre distribution.

Furthermore, traditional commingling equipment is not suitable for conductive materials such as CF, which can cause electrical shock. Therefore, commingled yarn research based on carbon fibre for thermoset composites is valuable in the composites industry. A hybrid yarn manufacturing machine should be developed so that it is protected from carbon fibre dust.

Thermoset is brittle. Moreover, composites fracture is generated as following the fibre alignment by impact. To prevent fracture growing by impact, this research investigates preform structure, hybrid yarn structure or nanoparticles.

Previous researchers used industrial multifilament to produce commingled yarns. Because sizing is applied to industrial filaments, it can be more difficult to obtain homogeneous fibres distribution from the air nozzle. In addition, an air nozzle can generate a lot of fibre breakage and decrease composites' mechanical properties. Therefore, this research initially studied a commingling process, and it was developed with a de-sizing process to improve the mechanical properties of thermoset composites.

The compressive strength of standard composites (non-impacted composites) is difficult to measure through the CAI standard test method [92]. Fracture of composites after impact starts near the impact area during the compression test. On the other hand, standard composites break at the edge area contacted between the compressive fixture and specimen. This gives lower strength values compared to impacted composites. Thus, this

---

research used compressive strength data of standard composites to compare strength between different standard samples.

Many researchers have demonstrated improved impact damage tolerance in 3D structure composites [3], [93]. Therefore, this study manufactured and developed hybrid yarns and these hybrid yarns were used to produce 3D structure composites to increase and evaluate the impact damage tolerance. In addition, all production processes of hybrid yarns were developed and assembled to obtain homogeneous fibre distributions and decreased fibre damage.

## Chapter 3.

### Development of Automatic Hybrid Yarns Manufacturing Process

#### 3.1 Background

This chapter describes the machine development processes for commingling, wrapping, and fibre drawing to improve the fibre distribution of hybrid yarn and impact damage tolerance of hybrid yarn thermoset composites. The developed machine was designed after understanding each production process from previous studies [14], [69], [94].

The previous commingled machine was designed for non-conductive materials, such as glass fibre [14], [95], as shown in Figure 3-1. On the other hand, as a conductive material, carbon fibres can destroy electrical products or cause a power cut on a machine. Hence, the design of the machine in this research was considered to allow it to run safely with carbon fibre.

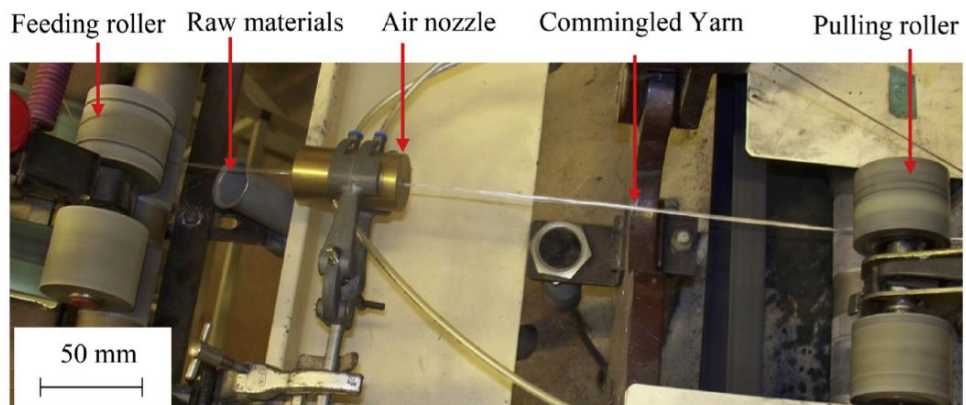


Figure 3-1 Commingling production line at The University of Manchester [14], [95]

#### 3.2 Machine development process

The fibre hybridisation machine was developed over a few stages, as shown in Figure 3-2. Firstly, a manufacturing process was drawn in 2D after understanding the wrapping, commingling, and fibre drawing processes. And then, CAD design on a 3D modelling design software (Dassault systèmes, CATIA v5) enabled a drawing in 3D that was based



on the 2D schematic drawing. The proper sizes and positions of the components were considered at this stage before the actual manufacturing of the customised components. It can save the cost and time associated with positioning errors and wrong part sizing through the virtual assembly.

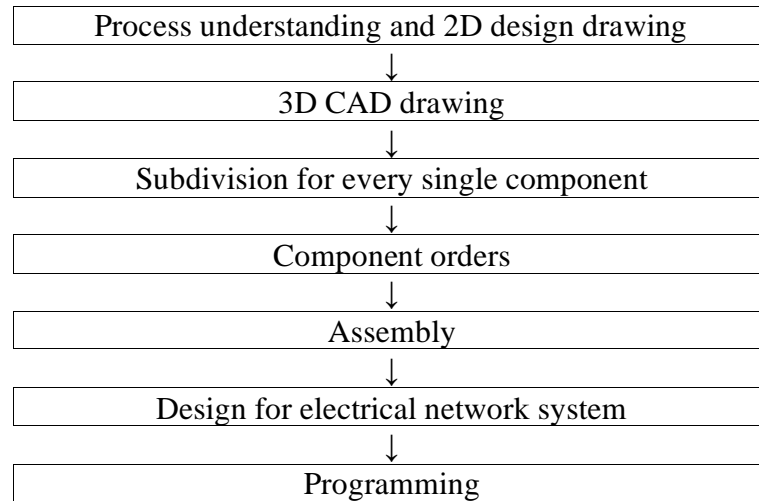


Figure 3-2 Machine development process

Assembly processes are faster now and have become more straightforward, as every specification for the parts, such as bolt sizes, quantities, and thread types, is decided while drawing in 3D. The designed components are made of aluminium and manufactured in the Department of Materials and HPE Ltd. workshops. These manufactured components are set up on the designed aluminium profile structure; the cross-section size of the aluminium profile was 40 x 80 mm.

The electrical network system controls the automatic system using a customised programme once assembly is completed. The PLC (programmable logic controller) was assembled to communicate with each electrical drive, based on the designed electrical network system. Motors, heaters, and pneumatics can be operated automatically through the customised programme on the PLC. The specific information about each step to develop the machine is explained below.

### 3.3 Development of fibre hybridisation process

In this study, the specially developed machine handles wrapping, commingling, and stretching processes. Each traditional production line was reviewed and hybrid yarn

manufacturing machine was designed based on the findings of previous studies [14], [69], [94], as shown in Figure 3-3. The wrapping process consists of a hollow spindle, feeding roller, pulling roller, and winding units; the commingling process involves a feeding roller, pulling roller, air nozzle and winding unit; the stretching process has heating elements, tension controllers, take-up, and winding units. These three different processes are rearranged and combined in a different order for this study, as shown in Figure 3-4.

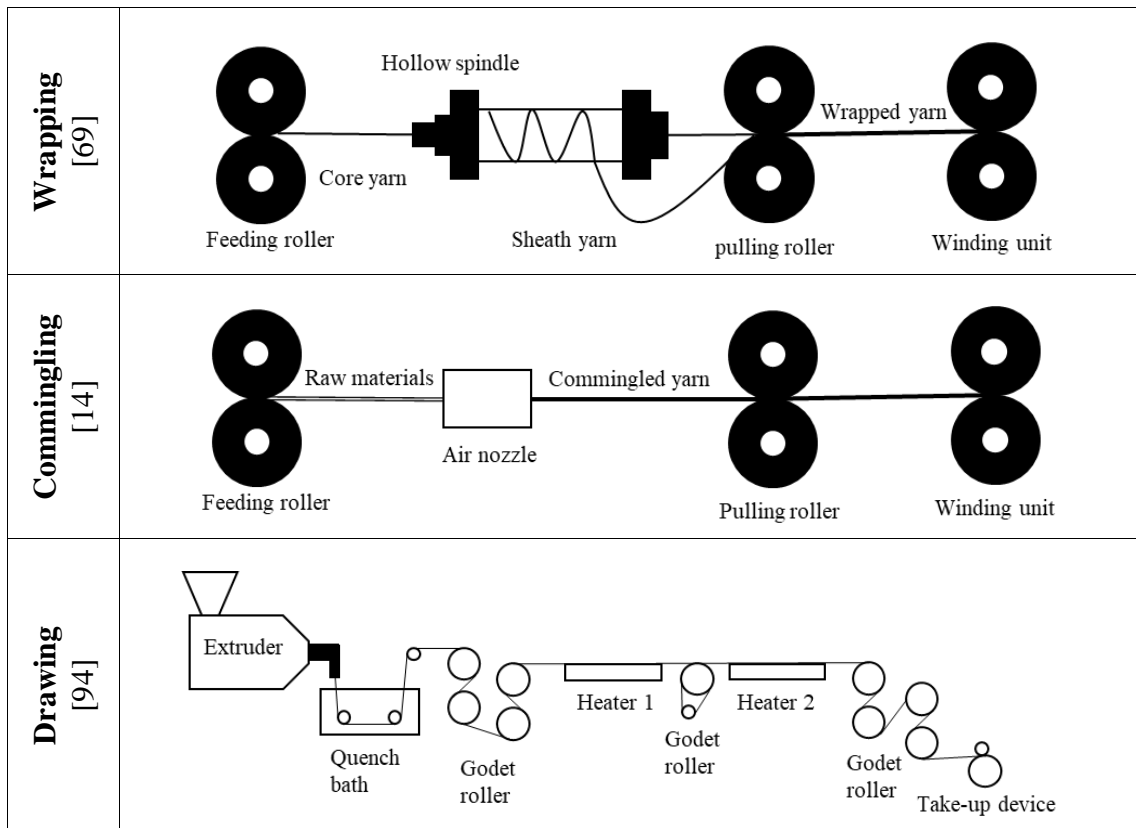


Figure 3-3 Schematic typical wrapping, commingling, and fibre drawing processes

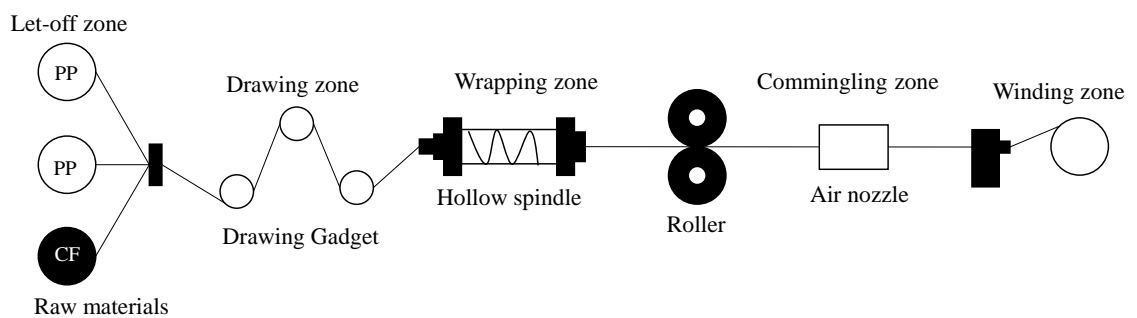


Figure 3-4 Schematic design for specially developed fibre hybridisation process

### 3.4 Hardware design and assembly

The basic aluminium profile structure size is 1500 x 600 x 1800 mm, and this machine can be divided into 5 parts, as shown in Figure 3-5. All single components were considered and designed, and then components manufactured by the workshop were assembled based on the 3D CAD design. A fibre guide was set on the machine, as it helps prevent fibre slippage from the production line and prevents the separation of fibres while the machine is running.

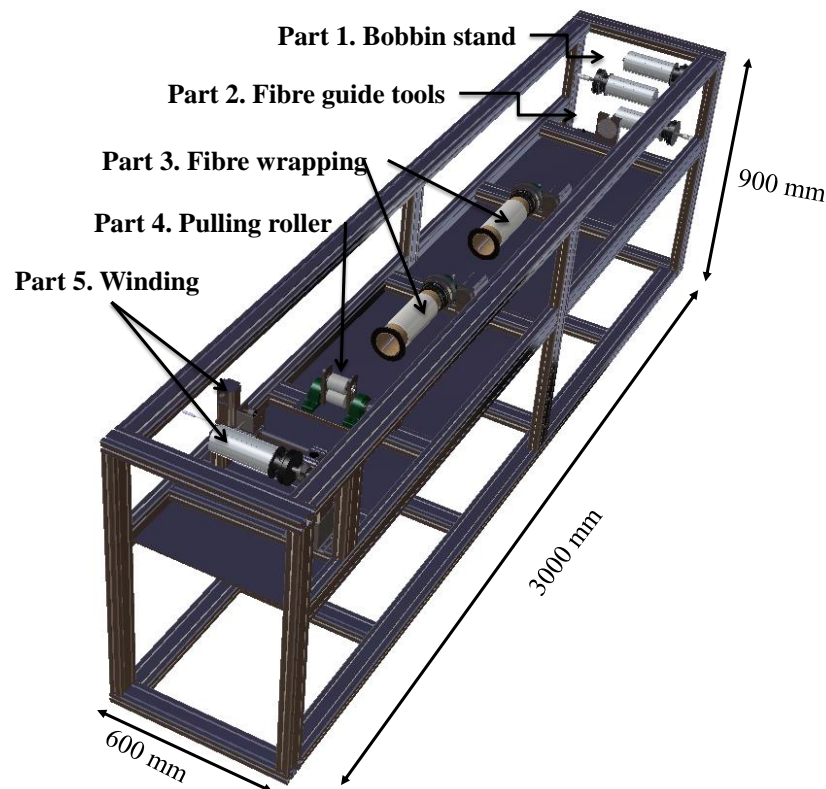


Figure 3-5 Initial 3D design of the fibre wrapping process

#### 3.4.1 Drawing zone

The fibre drawing requires heating elements and applying tension to the fibre as fibre crystallinity changes depending on applied tension and gradient of temperature. The heating element design (Figure 3-6) includes three aluminium tubes, which separately control the temperature. Fibre tension can also be controlled by changing the position of the tube on the heater holder. The heating element and thermocouple are fixed inside aluminium tubes with a 2 mm wall thickness and connected with temperature controllers.

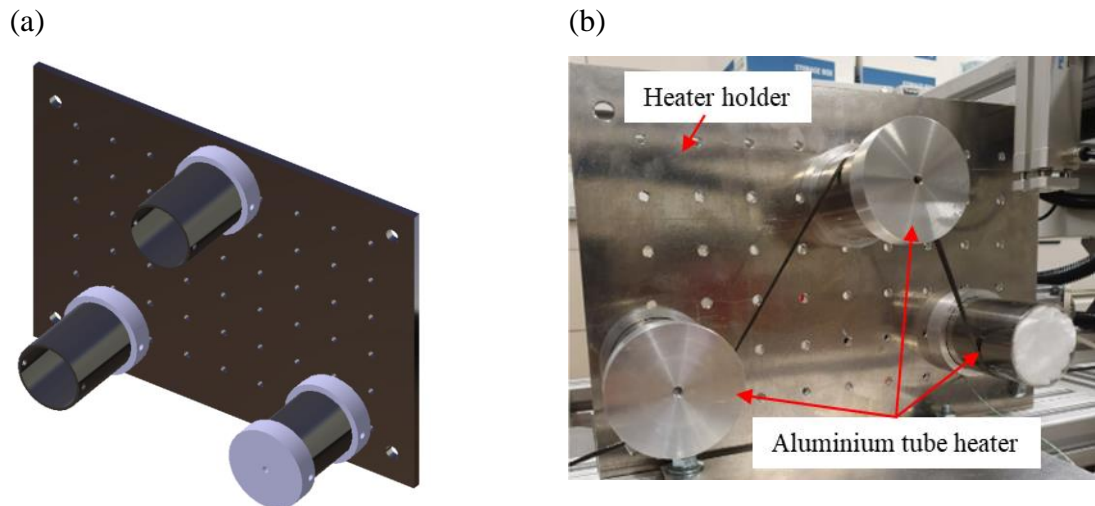


Figure 3-6 3D design of fibre drawing device (a), and assembled drawing device (b)

### 3.4.2 Wrapping zone

The wrapping density of thermoplastic fibres is decided by the rotation speed of the hollow spindle and the take-up speed. Carbon fibre passes through the hollow spindle, where a thermoplastic fibre bobbin is mounted (Figure 3-7 and 3-8). Then thermoplastic fibres wrap the carbon through rotation of the bobbin. This research chooses a pulley and pulley belt to rotate the bobbin by a motor. Its installation cost is cheaper, and the set-up is more manageable than gears.

To decide the length of the pulley belt, the dimensions of the pulley belt connection area on the bobbin holder and the motor pulley must be decided first. The dimensions of the pulley and pitch should be considered because they influence the wrapping speed. The pulley and pulley belt should have the same pitch. This pitch indicates the distance between the centres of one tooth to the centres of the next tooth.

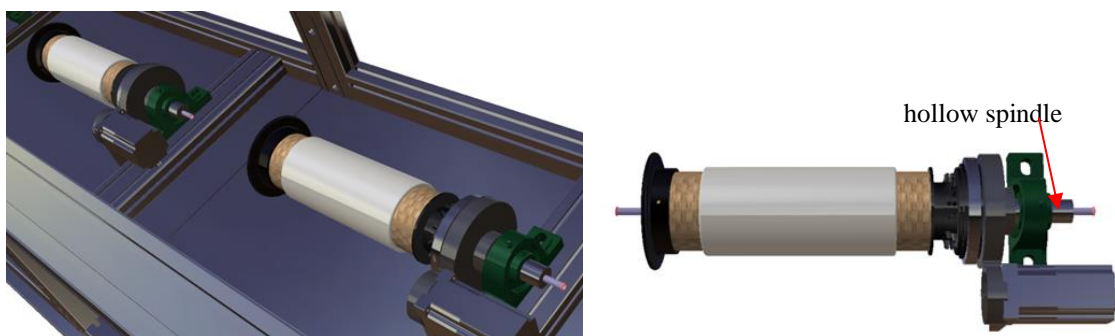


Figure 3-7 3D CAD design of wrapping zone

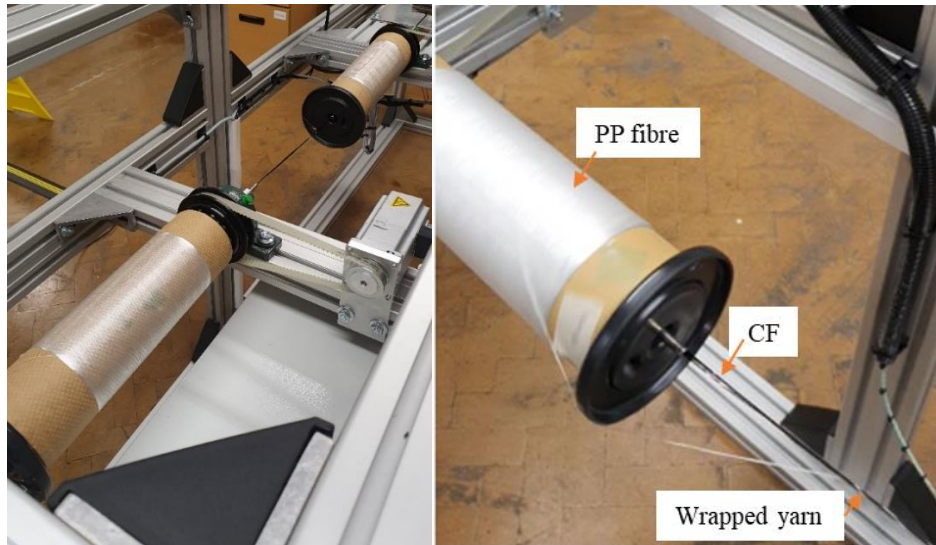


Figure 3-8 CF/PP wrapped yarn manufacturing process

Pulley belt length can be calculated using the pitch diameter of the two pulleys and the pulleys' centre distance, as shown in Equation 3-1 [96]. The pitch diameter means the diameter of the pitch circle, which is the middle point of the height of the tooth around the pulley. The pulley belt length for this study can be predicted using variables as shown in Table 3-1 and Figure 3-9.

Table 3-1 Variables for pulley belt length calculation

	<b>Dimension (mm)</b>
Pitch diameter of the motor pulley ( $D_1$ )	40
Diameter of the bobbin holder ( $D_2$ )	90
Centre distance (C)	190
Belt length (L)	$587.4 \approx 590$

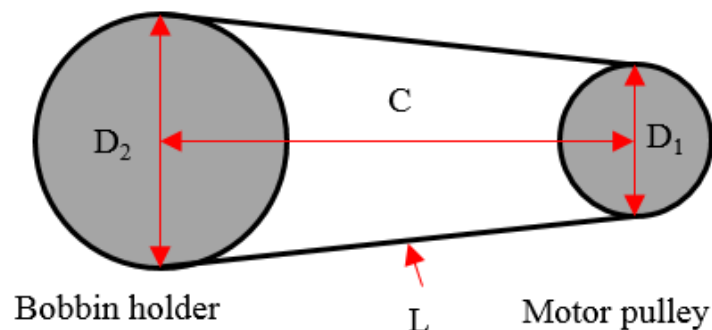


Figure 3-9 Schematic diagram of bobbin holder and motor pulley

The expected belt length is based on the pulley design, and the distance between the two pulleys is calculated as shown in Equation 3-2. The distance between the bobbin and motor pulley is 190mm, and the pulley is chosen for around a 40 mm pitch diameter and 5 mm pitch; this 5 mm pitch should be matched with the pulley belt, resulting in pulley belts that are used for a 590 mm length.

$$L = 2C + \frac{\pi(D_2 + D_1)}{2} + \frac{(D_2 - D_1)^2}{4C} \quad \text{Equation 3-1}$$

$$L = 2 \times 190 + \frac{\pi(90 + 40)}{2} + \frac{(90 - 40)^2}{4 \times 190} \quad \text{Equation 3-2}$$

$$= 587.4 \text{ mm}$$

L = belt length

C = centre distance between two pulleys

D<sub>1</sub> = pitch diameter of a small pulley

D<sub>2</sub> = pitch diameter of a large pulley

### 3.4.3 Commingling zone

Commingled yarn quality is influenced by air nozzle pressure, nozzle shape, yarn tension, and take-up roller speed. Previous researchers [14], [97] have used air nozzles with three air inlets, consisting of one 45-degree and two 90-degree air inlets (Figure 3-10). The 45-degree air inlet opens the bundles of yarn, and the 90-degree air inlet mixes two types of yarns. However, fibre distribution still needs to be enhanced. In this research, the commingling process was developed with the traditional air nozzle. The designed parameters such as air inlet angle, nozzle diameter and length have been adopted from previous literature providing optimum parameters [14], [97]. The orifice diameter of the original nozzle is 1mm, and the yarn channel diameter is 4mm. The air nozzle is required to decrease the fibre damage and increase the quality of the commingled yarn.

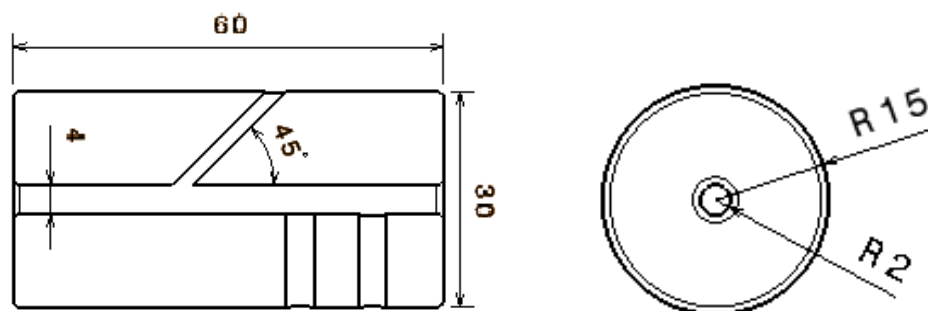


Figure 3-10 Side view and cross section view of previous air nozzle design

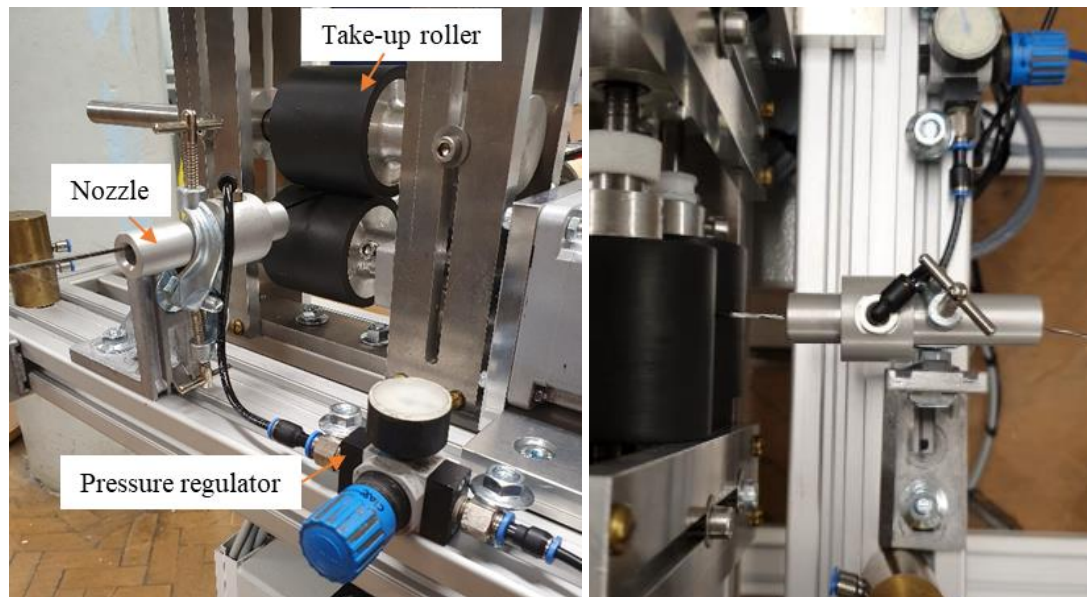


Figure 3-11 Commingling zone

Figure 3-11 presents the feeding roller, and this roller shaft and motor shaft are connected using a coupling. A metal roller is coated in rubber to manufacture a take-up roller. Two metal roller shafts are coated with nitrile rubber (95 shores) to achieve the friction property required at the roller. This surface of the hard rubber roller is polished to A1 class, which is the highest level of surface finish standards noted by the SPI (Society of the Plastics Industry). To use as a feeding and take up roller, A1 Class polishing was appropriated to control the fibres. The final roller has a 60 mm face length and a 58 mm OD- this roller was available from the previous project.

#### 3.4.4 Let off zone

A fibre stand and tension control are installed in the let-off zone, as shown in Figure 3-12. The let-off zone commonly uses commercialised 2 kg bobbins of carbon tow (Toray T300 60E) as the reinforcement fibre. 12 mm diameter and 500 mm length aluminium round bars are used to fix the bobbin holder (Figure 3-13). When 1mm deflection happens, the force can be predicted based on the four-point bending equation [87], as shown in Equation 3-3. Bending stiffness,  $S_b$  is calculated by the 295 MPa minimum tensile strength and the volume of a rod (Equation 3-4). Thus, when 185.6 kgf is mounted, the aluminium rod shows 1 mm deflection (Equation 3-5). The 2kg CF bobbin, which is used in this research, is enough to mount on this aluminium rod because it only has around 0.1mm deflection in this case.

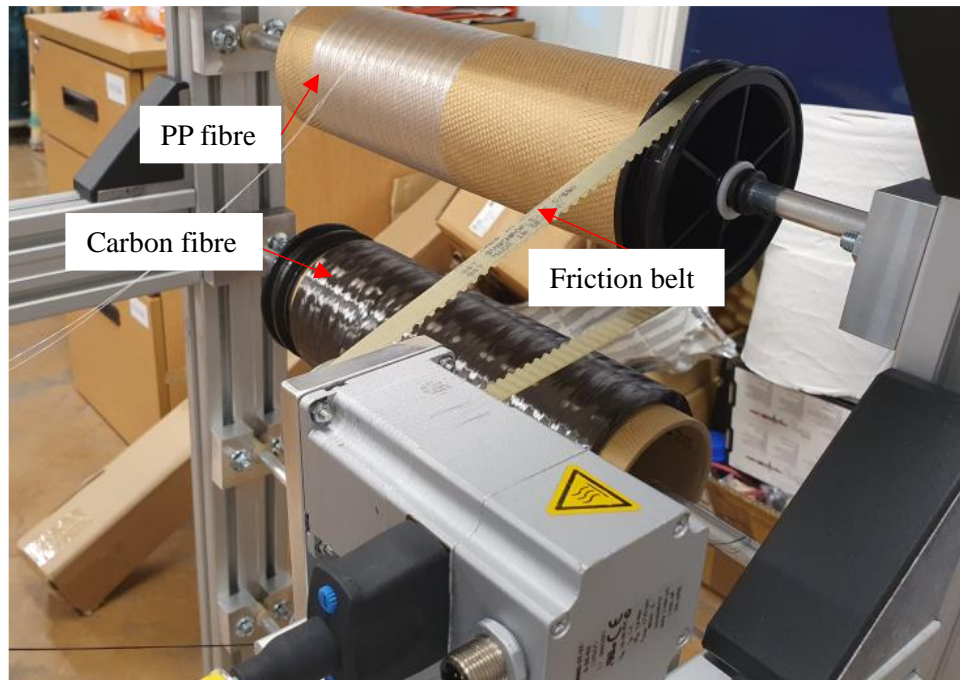


Figure 3-12 PP fibre tension control in the let-off zone

$$S_b = \frac{F}{f} \times \frac{l_1}{8} \times \frac{l_2^2}{b} \quad \text{Equation 3-3}$$

$S_b$  = bending stiffness, N·mm

$F$  = force, N

$f$  = linear deflection, mm

$l_1$  = distance in the four-point method, mm

$l_2$  = bending length in the four-point method, mm

$b$  = test piece width in the direction of the bending axis, mm

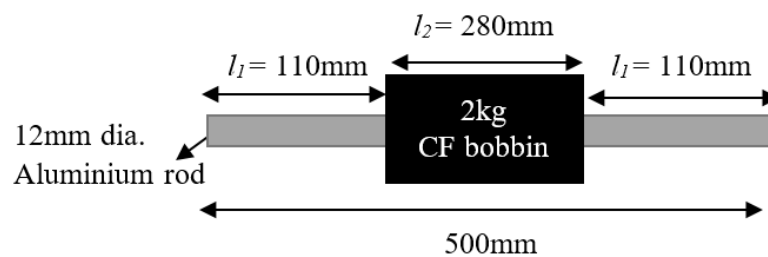


Figure 3-13 Schematic bobbin stand with 2kg carbon fibre

$$S_b = 295 \text{ N/mm}^2 \times 56520 \text{ mm}^3 = 16673400 \text{ N}\cdot\text{mm} \quad \text{Equation 3-4}$$



$$16673400 \text{ N} \cdot \text{mm} = \frac{F}{1\text{mm}} \times \frac{110\text{mm}}{8} \times \frac{280^2\text{mm}}{12} \quad \text{Equation 3-5}$$

$$\therefore F = 185.60\text{N} = 185.60\text{kgf}$$

### 3.4.5 Winding zone

The fibre winding process collects hybrid yarns on the bobbins, as shown in Figure 3-14. The belt-driven linear actuator in the winding system moves forwards and backwards to collect hybrid yarn on a wide area of the bobbin. The winding angle can be changed depending on the position of fibres controlled by winding and oscillatory motion speed.

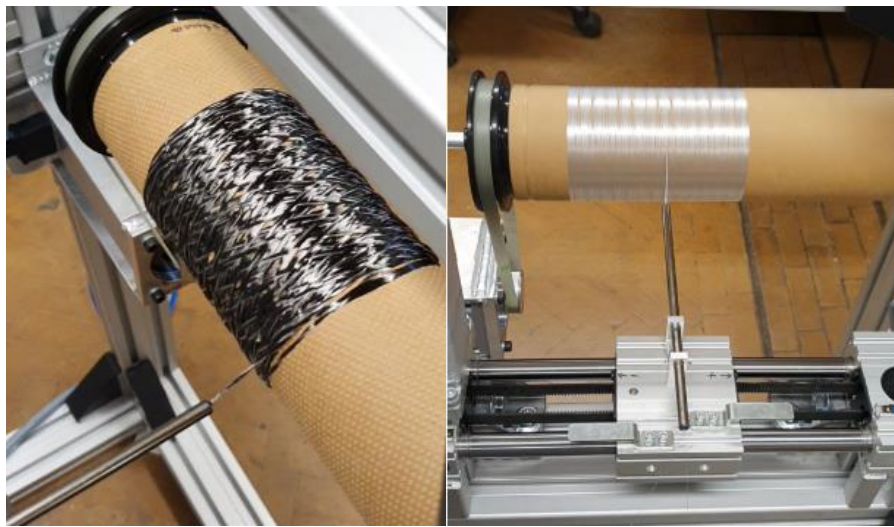


Figure 3-14 (a) helical winding of wrapped yarn, and (b) hoop winding of PP fibre

### 3.4.6 Machine assembly and safety guard

A hybrid yarn manufacturing machine was designed and assembled for wrapping, commingling and fibre stretching, as shown in Figure 3-16. It consists of five motors, five heaters, and three solenoid valves; one of the solenoid valves is used for an air nozzle to manufacture the commingled yarn; the four heaters are used for polypropylene (PP) fibre stretching processes; and the five motors are used for winding, wrapping, and roller drives.

Multiple safety devices are essential for the operation of this machine, as unexpected accidents can happen. Five emergency stop (e-stop) buttons are installed on the machine, as shown in Figure 3-16. Four of them are set on each side of the machine, and the fifth is set on the PLC control box. E-stop buttons cut the power of all electrical devices and

halt their motion using stored programming; even the touch screen does not work after pushing this button. To restart the machine, every e-stop button should be released, and then the reset button must be pressed.

The main materials used in this research are carbon fibres, and these would fly everywhere in the lab while the machine is running. Therefore, protective panels installed as electrical products can be destroyed by carbon fibres. Black PVC (polyvinyl chloride) foam and clear PETG (polyethylene terephthalate glycol) panels are used, at 5 mm and 6 mm thickness, respectively. The black PVC panels are used to block the carbon fibre flying, and the clear PETG panels are used to check processing during the machine running. Hinges and door handles are set up on the PETG panels, and they can be opened and closed by magnetic catches. There is a 2 cm gap that exists between the door and the aluminium profile, which allows heat to escape (Figure 3-17).

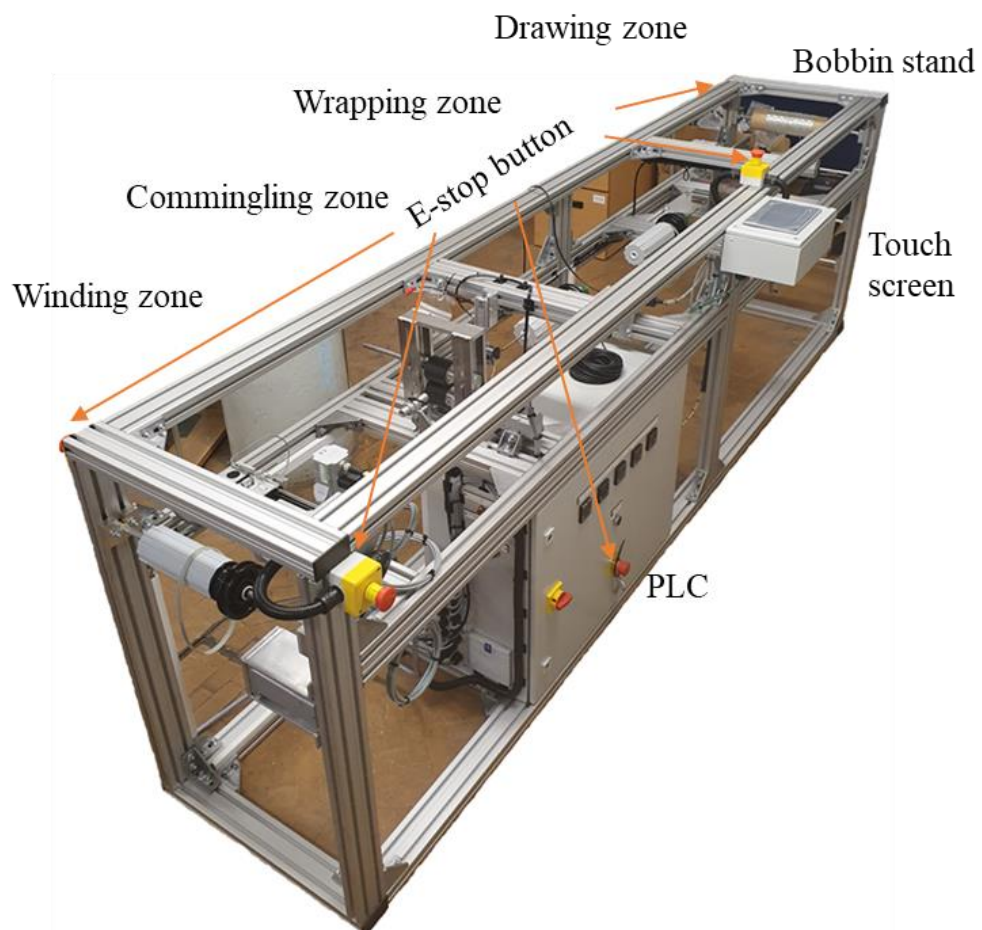


Figure 3-15 Assembled fibre hybridisation machine

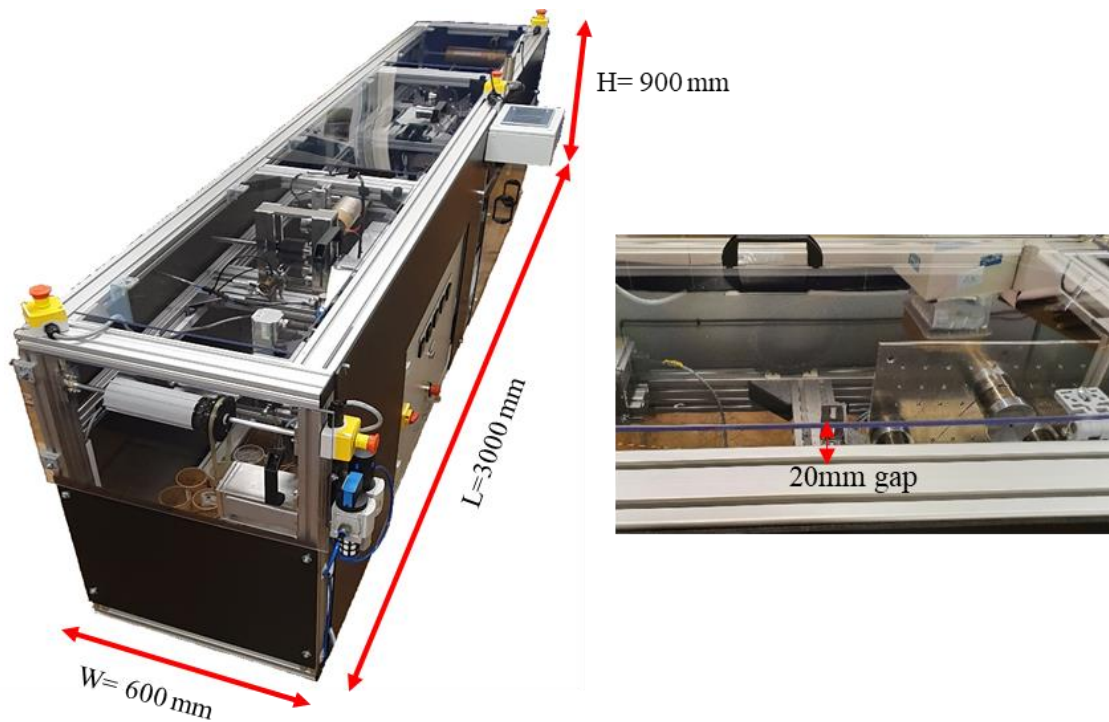


Figure 3-16 Assembled protective panels and the gap for air circulation.

## 3.5 Electrical network and PLC based controller

### 3.5.1 Electrical network system

The electrical network system is designed to upload programs and then run the machine automatically. This system consists of a human-machine interface (HMI), the programmable logic controller (PLC), and electrical devices, such as motors, pneumatic solenoid valves, and heaters.

Figure 3-18 shows how the electrical hardware is connected to communicate in each block. The motion controller (Trio, P600), motor drive (Lam tech. DS10), I/O expansion module (Trio, P371 and P372), and display (Trio, Uniplay 7 in HMI) were purchased from Motor Technology Ltd. The software for programming uses Trio Motion Perfect, V4. Once a program is uploaded on the controller, the user can send an order to the PLC through the HMI, enabling the electrical devices to be run. The choice of electrical devices was decided before the PLC was assembled, as installation of the PLC takes into account the capacity of the power supply based on the selected devices (Table 3-2).

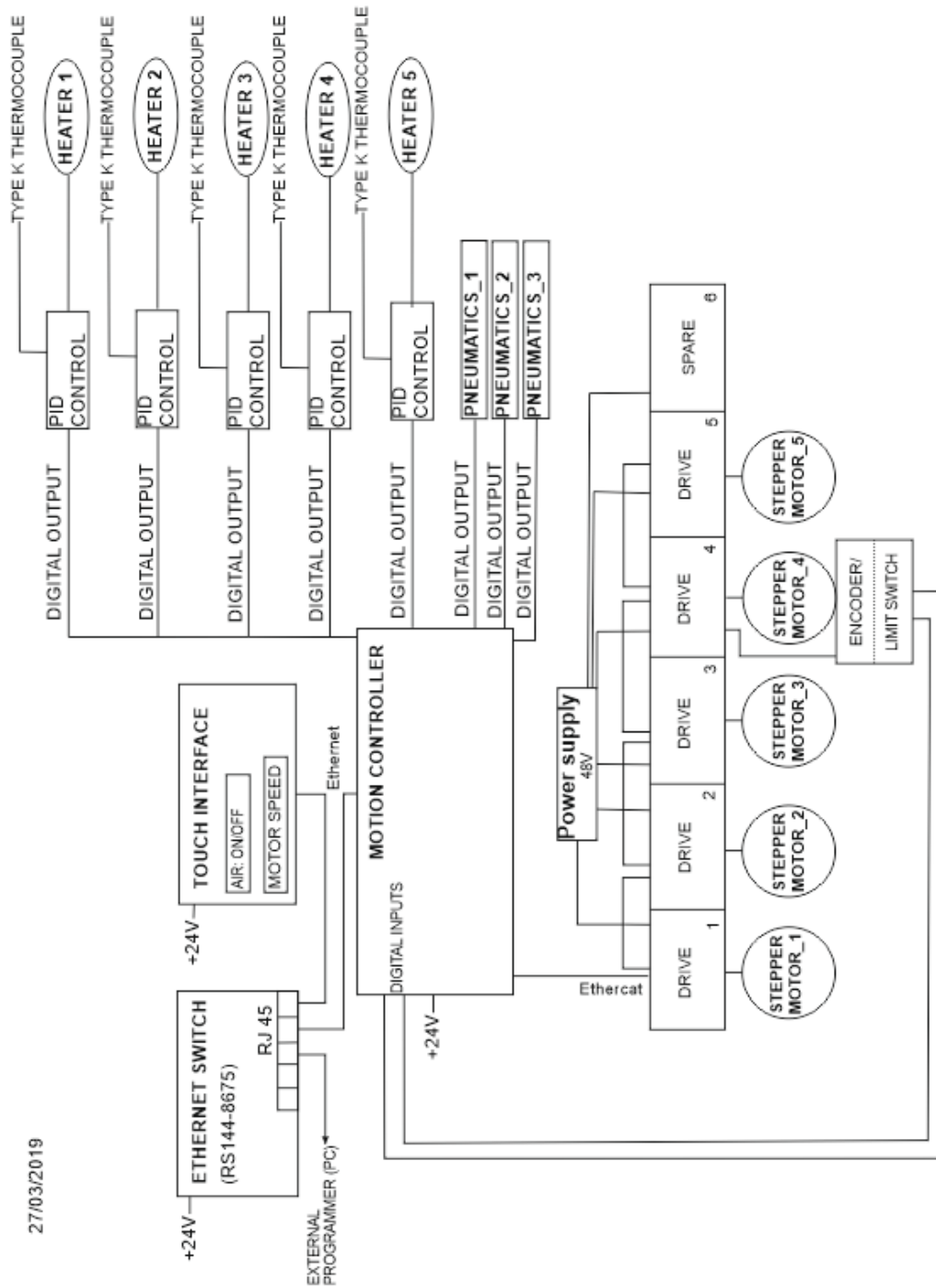


Figure 3-17 Electrical network block diagram of motors, heaters and pneumatics for fibre hybridisation process

Table 3-2 List of the main hardware

FILE NO.	PARTS	MODEL	QUANTITY
1	STEPPER MOTOR_1,5	FESTO, MTR-ST87-48S-AA(48V, 4.7A)	2
2	STEPPER MOTOR_2,3	FESTO, EMMS-ST-57-S-SE-G2(48V, 5A)	2
3	STEPPER MOTOR_4	FESTO, EMMS-ST-57-M-SE(48V, 5A)	1
4	PNEUMATICS_1-3	FESTO,CPE10-M1BH-5L-QS-4(24V)	3
5	HEATER 1 (flexible)	OMEGA, SRFGA-205/10-P (100W, 230V)	1
5	HEATER 2 (flexible)	OMEGA, SRFGA-205/10-P (100W, 230V)	1
5	HEATER 3 (flexible)	OMEGA, SRFGA-205/10-P (100W, 230V)	1
6	HEATER 4 (flexible)	OMEGA, SRFGA-205/10-P (100W, 230V)	1
7	HEATER 5 (flexible)	OMEGA, SRFGA-508/10-P (400W, 230V)	1
8	TOUCH INTERFACE	MC4 display, Uniplay 7inch HMI (24V)	1
9	MOTION CONTROLLER	Triomotion, Flex-6 Nano, P600 (24V)	1
10	3 axis contoller	Triomotion, Flex 3-Axis, P375 (24V)	2
11	Input EXPANSION MODULE	Triomotion, 16-IN PNP Module, P372 (24V)	1
12	Output EXPANSION MODULE	Triomotion, 16-OUT PNP Module, P371(24V)	1
13	DRIVE	LAM Technologies, DS10 (48V)	5
14	LIMIT SWITCH	SIES-8M	2

### **3.5.2 PLC assembly**

The purpose of the PLC is to control the five motors, five heaters, and three air solenoids, along with a touch interface and four e-stop buttons, using digital inputs and outputs. The devices required to assemble the PLC are shown in Figure 3-19. Electrical wiring for the PLC was implemented by the controller installation companies, Manes Controls Ltd. and Motor Technology Ltd. Heaters and pneumatics were able to replace based on the installed electrical schematics provided by manes controls Ltd (Appendix C). The five motors are connected to each drive; these drives are connected with the motion controller. The limit sensors at the winding unit, heaters, and air solenoids are connected with an I/O expansion module, and these modules are also connected with the motion controller.

The temperature of a heater is adjusted by the temperature controller. To maintain the set temperature, power is cut using a heater switching contactor. Then, when the temperature drops down, power is resupplied to maintain the temperature. K type thermocouples measure temperature, and these data are sent to the temperature controller (Figure 3-20). The user can read the temperature on this temperature controller.

This machine uses solenoid valves to supply air to the air nozzle. The solenoid valves are connected in a digital I/O expansion module, and they can be opened and closed using controls on the HMI screen. Lastly, safety systems must be set on the machine in order to prevent accidents. A total of four e-stop buttons are installed, and these are controlled by a safety relay and a contactor.

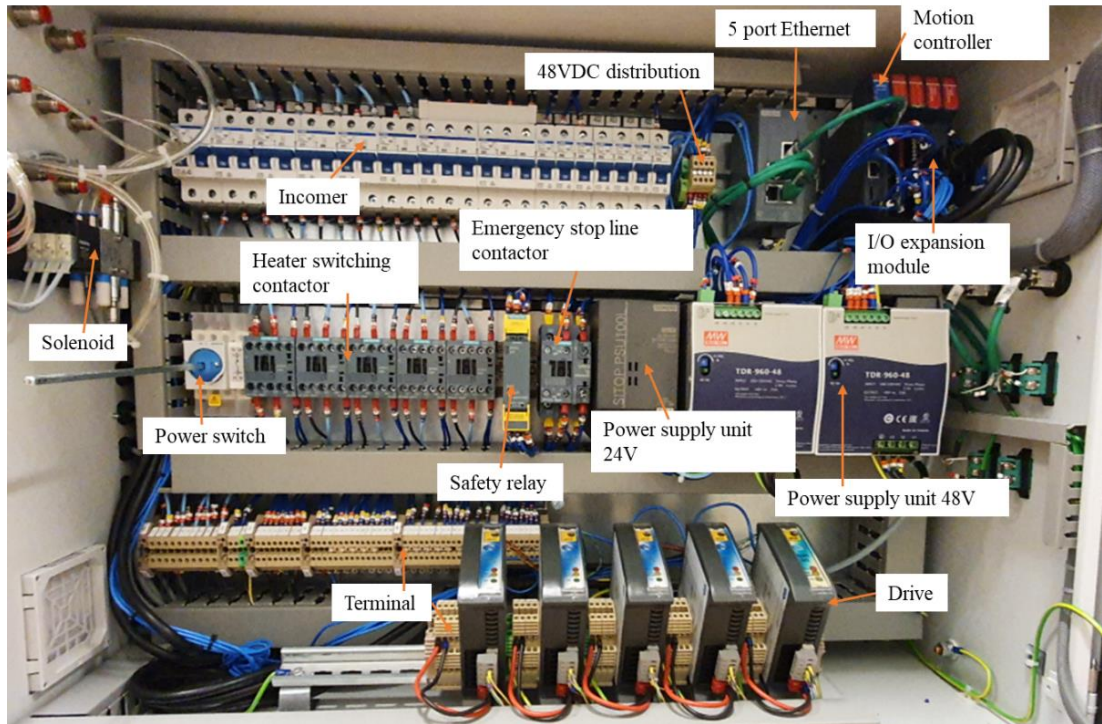


Figure 3-18 Arrangement of PLC devices

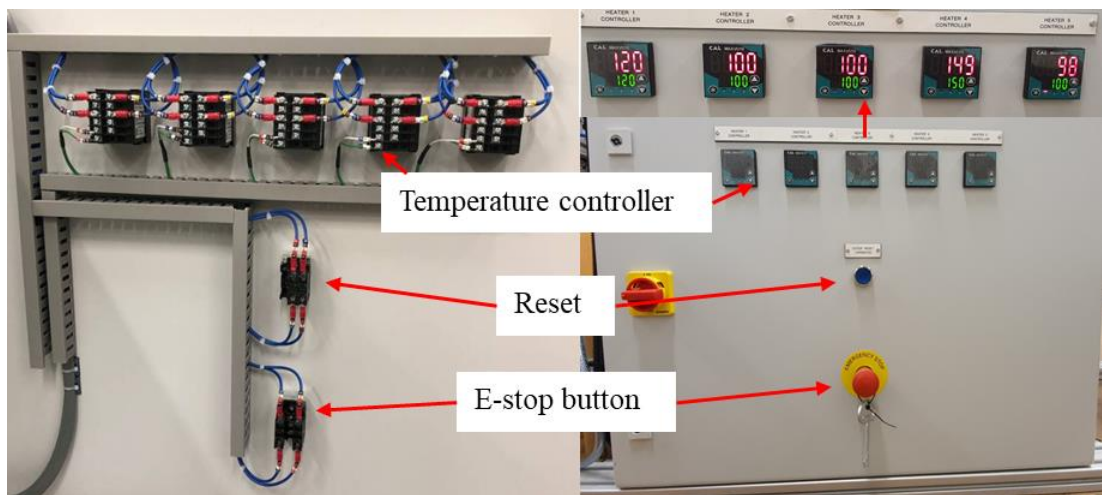


Figure 3-19 Back and front view of installed five digital temperature controllers, reset button, and e-stop button on the PLC

### 3.6 Software design

The mechanics of the machine cannot work without a control program. Control programmes, written in Trio Motion Perfect V4, have been designed with Motor

Technology Ltd after the author received a programming certificate from this company (Appendix B). These programs control motor speed and direction, temperature, and switching the solenoid valves on/off. The electrical devices communicate to send data using analogue or digital I/O. The digital input is ‘on/off’ for the heater, solenoid valve, motor, e-stop buttons, and limit sensor. The digital output is ‘power on’ for the motor, heater, valve, and alarm. The thermocouple is catalogued as an analogue input, and the temperature control and encoder are analogue outputs. Programming is written for system initialising and is logical for each electrical device; every electrical device is ready to run when the machine power is on or is reset. The programming can be uploaded into the PLC using Trio Motion Perfect V4.

### **3.6.1 System initializing**

After the machine’s power is turned on, the machine is ready to run through the initialising programme. The software can reset itself after an error is resolved as the error detection and reset functions are included in the initialising programme. After finishing the check for communication errors of its electrical devices, the acceleration and deceleration of motors are set, and the initial speed is set to zero. Motors can be run from the HMI touch screen using the programmed keypad. Lastly, the emergency stop system with its error routine is implemented for all electrical devices. When an error is generated by pressing the e-stop button, all motors, heaters, solenoid valves, and sensors are stopped. The HMI touch screen does not work and shows only an error message until the systems are reset and initialised.

### **3.6.2 Motor programming**

The five stepper motors for continuous rotation are used as take-up, wrapping, let off, and winding units. The motor program defines values for deceleration and acceleration. Speed value and direction are controlled on the MHI touch screen using the keypad or speed control buttons. The motor for the oscillating motion in the winding zone moves forwards and backwards due to two limit switch sensors. The direction is changed when one of the limit sensors is off. This motor connects to an encoder to control the motion position and speed on the linear stroke. It can also manage the backwards and forwards motion as defined by the position on the programme.

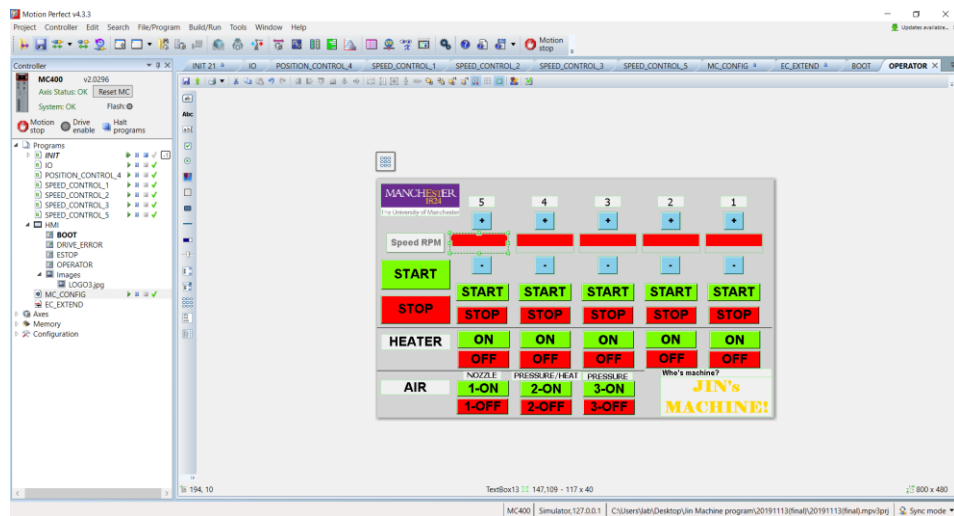


### 3.6.3 Heater and pneumatics programming

In this machine, the motors, heater and solenoid valves deal with digital output processing for the on and off function. Each element is classified using a device number (e.g. op (12)). If users want to turn off device number 12, the controller accepts the order from a PC or HMI touch screen and turns off the device numbered 12.

### 3.6.4 MHI touch screen

(a)



(b)



Figure 3-20 (a) display design and function setting for each button in the software and (b) the corresponding display operation mode after uploading the program

All electrical devices are identified by numbers in the program. These numbers are essential for the programming of the display design. All touch buttons are identified with a device number which is fixed by the author. Therefore, the user can control the electrical devices through these buttons. The display design and the function of each button can be modified directly by the user through the Ethernet connection (Figure 3-21a). Then, this finished design can be seen on a screen after the program is uploaded (Figure 3-21b).

### **3.7 Discussion**

This chapter presents a novel advanced manufacturing machine to produce hybrid yarns with carbon fibre and thermoplastic hybrid yarns. The development of the fibre commingling, wrapping, and drawing process was based on a traditional production-line process, then assembled by an automatic manufacturing machine. Previous studies investigated the use of hybrid yarns for thermoplastic composites for the consolidation process. However, in this study, thermoplastic dry fibres were utilised to improve the impact damage tolerance of thermoset composites. Therefore, the design of the machine took into consideration the fibre distribution of thermoplastic fibres and the mechanical properties of hybrid yarns.

First, further research is needed to design a better manufacturing system. The machine discussed here was designed and programmed primarily to control motor speed, solenoid air valves, and temperature control through the HMI touch screen. However, temperature settings could be changed with a temperature controller, which is mounted on the PLC panel. Thus, the ability to send data from the temperature controller to the touch screen could simplify the manufacturing process. Second, during the development process of the machine in this study, the use of polypropylene fibres was taken into consideration; therefore, due to limitations on the existing heating elements, the elements needed to be replaced in order to run the machine at temperatures greater than 232 °C. Finally, the movement distance of the linear stroke to collect samples was narrow compared to the bobbin size. Sample production could be increased by replacing the current linear stroke with a longer one.

## Chapter 4. Materials and Experimental Procedures

### 4.1 Materials

#### 4.1.1 Commingled and wrapped yarn

The carbon fibre and polypropylene fibre specifications are shown in Table 4-1. T700SC-6000-60E and 50C carbon fibres were purchased from Toray [98]. The carbon fibre with 0.3% low sizing content (CF1) was chosen to manufacture hybrid yarn, and the other carbon fibre with 1% sizing content (CF2) was used as a through-thickness binder (TT). Polypropylene multifilament fibres (DURON CF) were supplied by Drake Extrusion Ltd. [99].

Table 4-1 Specification of carbon fibre and thermoplastic

Material	CF1	CF2	PP
Material type	fibre	fibre	Fibre
Tensile strength (MPa)	4900	4900	302*
Modulus (GPa)	230	230	3.7*
Linear density (Tex)	400	400	16.5
Filament diameter ( $\mu\text{m}$ )	7	7	24
Number of the filament (n)	6000	6000	40
density ( $\text{g}/\text{cm}^3$ )	1.8	1.8	0.9
Binder material	Epoxy	Epoxy	-
Sizing content (wt%)	0.3	1.0	-

\*Measured by the author (see Chapter 5.2)

#### 4.1.2 High thermal performance thermoplastic hybrid yarn

Polyamide 6 multifilament fibres (DT1021-05) and polyamide 6/Graphene multifilament fibres (DT1021-06) were manufactured by Fibre Extrusion Technology [100] and provided by First Graphene ltd [101]. The 10 mm and 200 mm width PEI veils (T2570-28) were supplied by Technical Fibre Products ltd [102]. Table 4-2 shows the specification of carbon fibres and thermoplastics. The tensile properties were obtained

from stress-strain curves tested at 10mm/min loading, and Young's modulus was calculated at an initial slope.

Table 4-2 Specification of carbon fibre and thermoplastic

Material	CF	CF	PA6	PA6/G	PEI
Material type	fibre	fibre	fibre	fibre	veil
Tensile strength (MPa)	4900	4900	449*	325*	8.4* <sup>1</sup>
Modulus (GPa)	230	230	4.5*	4.2*	0.13* <sup>1</sup>
Linear density (Tex)	400	400	23.8*	23.2*	200* <sup>1</sup>
Filament diameter ( $\mu\text{m}$ )	7	7	34*	35*	-
Number of the filament (n)	6000	6000	24	24	-
density ( $\text{g}/\text{cm}^3$ )	1.8	1.8	1.1*	1.0*	1.26
Graphene content (wt%)	-	-	-	0.1	-
GSM ( $\text{g}/\text{m}^2$ )	-	-	-	-	20
Thickness (mm)	-	-	-	-	0.0159
Binder material	Epoxy	Epoxy	-	-	Polyester
Sizing content (%)	0.3	1.0	-	-	10

\*Measured by the author (see Chapter 6.2), <sup>1</sup> only 10mm width of PEI veil

### 4.1.3 Micro wrapped yarn

Tenax<sup>®</sup>-E HTS45 E23 3K carbon fibres are used as reinforcement with 1.2% sizing based on epoxy resin and supplied by Teijin Carbon Europe GmbH [103].

Table 4-3 Specification of carbon fibre and extruded PP/Graphene fibre

	Carbon fibre	Neat PP	PP/ Graphene 0.25%	PP/ Graphene 0.5%	PP/ Graphene 1%
Tensile strength (MPa)	4500	28.9 ( $\pm 4.8$ )*	40.0 ( $\pm 1.3$ )*	33.7 ( $\pm 2.8$ )*	31.8 ( $\pm 1.1$ )*
Modulus (GPa)	245	1.0 ( $\pm 0.5$ )*	1.4 ( $\pm 0.1$ )*	1.3 ( $\pm 0.1$ )*	1.5 ( $\pm 0.2$ )*
Linear density (Tex)	200	58 ( $\pm 1.4$ )*	60 ( $\pm 2.8$ )*	75 ( $\pm 3.2$ )*	76 ( $\pm 7.3$ )*
Filament diameter ( $\mu\text{m}$ )	7	296 ( $\pm 23$ )*	287 ( $\pm 40$ )*	326 ( $\pm 10$ )*	320 ( $\pm 11$ )*
Number of the filament (n)	3000	1*	1*	1*	1*
Density ( $\text{g}/\text{cm}^3$ )	1.8	0.8*	0.9*	0.9*	0.9*
Graphene content (wt%)	-	0	0.25	0.5	1
Binder material	Epoxy	-	-	-	-
Sizing content (%)	1.2	-	-	-	-

\*Measured by the author

The extruded PP and Graphene nanocomposites at different graphene nanoparticles content (0 wt%, 0.25 wt%, 0.5 wt%, and 1 wt%) fibres were provided from First Graphene (Henderson, Australia) [101]. The mechanical specifications of CF, PP and PP/Graphene fibres are shown in Table 4-3. The author analysed the mechanical properties of PP and PP/Graphene fibres in Table 4-3 because the extruded fibres were manufactured by the supplier for this study.

## 4.2 Methods

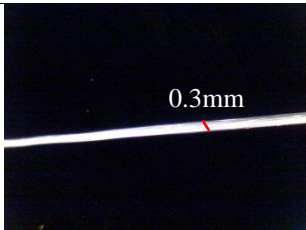
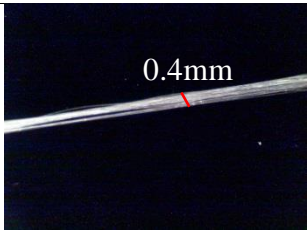
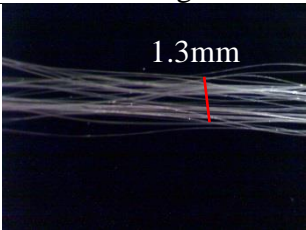
### 4.2.1 Hybrid yarn manufacturing

A key aspect of manufacturing hybrid yarn is improving the impact damage tolerance of carbon fibre reinforced thermoset composites using thermoplastic fibres. The fibre distribution of thermoplastic in the hybrid yarn is one of the critical factors to improve impact tolerance. Thus, a commingling process was developed based on the traditional mingling processes. Furthermore, different hybrid yarn structures, such as wrapped fibres, have been manufactured on the developed machine (see chapter 3), and the mechanical properties were analysed.

#### 4.2.1.1 Improving PP fibre distribution of commingled yarn

The binder materials of PP multifilament were removed to enable the PP filaments to be opened more by air pressure and to improve fibre distribution. A water bath designed by the University of Manchester was used [104] with tap water (24°C) at 1.5N tension. Proper tension during the process helps multifilament opening.

Table 4-4 Optical microscope image of PP fibre samples

	Original PP filaments	Under tenion	Under tenion & De-sizing
Images			
Tex	17 ( $\pm 0.59$ )	12.4 ( $\pm 0.27$ )	12.8 ( $\pm 0.19$ )

After binder removal, an infrared heater (100 °C), a heat gun (120–130°C) and an air cooler were employed to dry the water from PP fibres based on a preliminary trial. Table 4.4 shows PP multifilament under different experimental conditions.

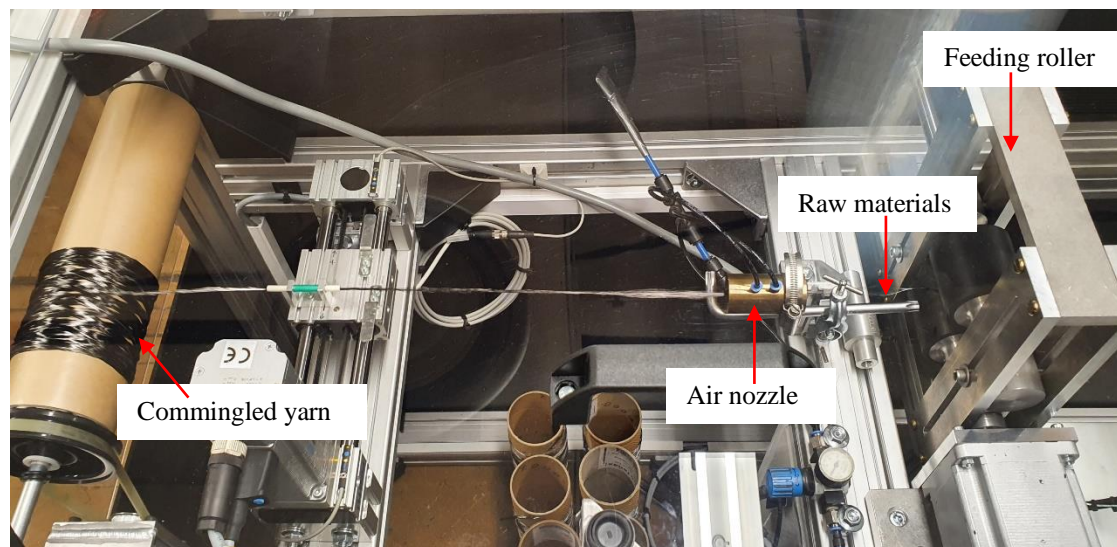


Figure 4-1 Commingling process of CF/PP fibre on the developed machine

Commingled yarns were manufactured with original PP fibre or de-sized PP fibres on the developed machine (Figure 4-1). The CF and PP fibres were wound together to obtain side by side structure, and then they were mingled through the air nozzle. The let-off and production speeds were fixed through the preliminary test at 0.22 m/s and 0.18 m/s. 2 bar air pressure was used because fibre damage was less than with 3 bar air pressure and mingling condition was better than at 1 bar air pressure.

#### 4.2.1.2 Wrapped yarn

Single and double wrapped yarn drawn by 3D CAD are shown in Figure 4-2. The PP multifilaments wrap the core of carbon fibres. It is expected that PP fibre can protect carbon fibres from impact as they surround the carbon fibres. Single-wrapped yarns were manufactured at different wrapping densities, 50, 75, 100, and 125 w/m (wraps per metre), and their manufacturing conditions and sample name are displayed in Table 4-3. The wrapping density was controlled by the rotation speed of the PP fibre bobbin, as shown in Figure 4-3a, and this sample was collected from the winding section (Figure 4-3b) on the developed machine. The double wrapped yarn was also produced at 50 w/m with two hollow spindles. The volume and weight fraction of wrapped yarns depending on the

number of PP fibres are illustrated in Table 4-4. The volume fractions of the single and double wrapped yarn are 86% CF and 14% PP multifilaments. The CF volume fraction of 1PP single wrapped yarn is 92%.

Table 4-5 Processing parameters for single wrapped yarn manufacturing

Sample name	Wrapping per metre	Wrapping speed (rpm)	Pulling roller speed (rpm)	Winding (rpm)	Material
CF-2PP-SW50	50	360	28	25	6K Carbon fibre (400 tex x 1)
CF-2PP-SW75	75	540	28	25	
CF-2PP-SW100	100	720	28	25	PP fibre (17 tex x 2)
CF-2PP-SW125	125	900	28	25	

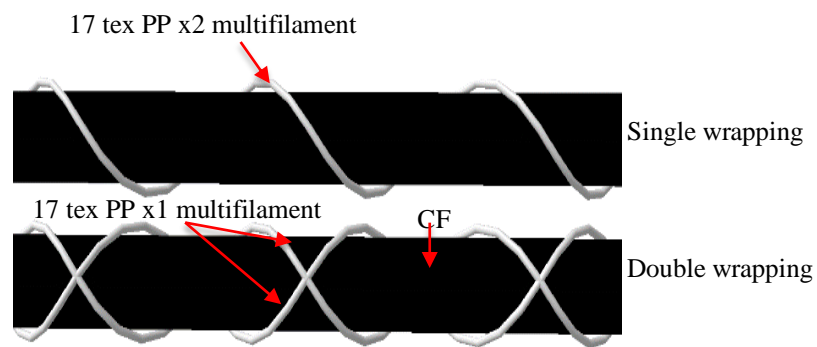


Figure 4-2 CAD design of multifilament single and double wrapping yarn structure

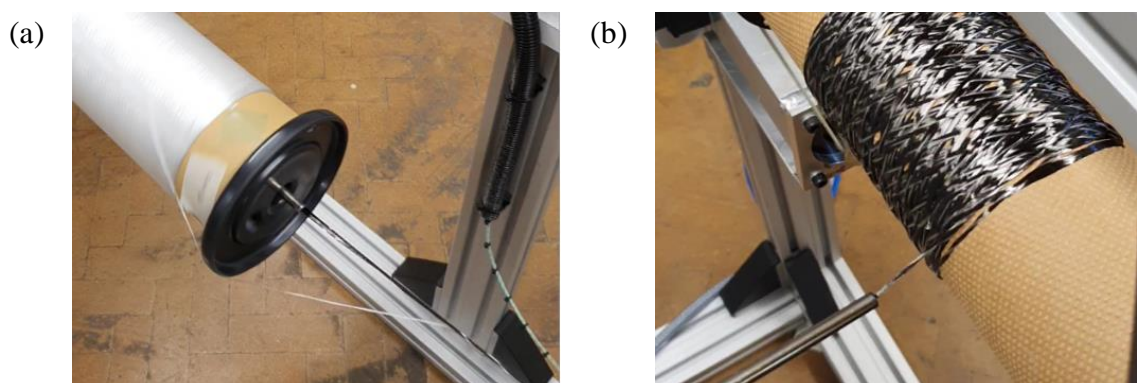


Figure 4-3 Wrapped yarn manufacturing process; (a) wrapping, and (b) winding process

Table 4-6 Specification of wrapping yarn samples at 50w/m

	CF-1PP-SW50	CF-2PP-SW50	CF-2PP-DW50
Carbon fibre (Tex)	400 x1	400 x1	400 x1
Thermoplastic fibre (Tex)	17 x 1	17 x 2	17 x 2
CF weigh fraction	0.96	0.92	0.92
TP weight fraction	0.04	0.08	0.08
CF volume fraction	0.92	0.86	0.86
TP volume fraction	0.08	0.14	0.14

The parameters that explain the geometrical properties of wrapped yarns are explained in Figure 4-4 and are calculated using Equations 4-1 – 4-4 [105]. The helical length of wrapped yarn ( $L$ ) is obtained from Equation 4-1 via Pythagoras's Theorem, and the weight fraction of core yarn ( $W_c$ ) is calculated in Equation 4-2 with the value of  $L$  obtained in Equation 4-1. The weights of the core yarn ( $w_c$ ) and wrapping yarn ( $w_w$ ) can be obtained with Equations 4-3 and 4-4. The weight fractions at different wrapping densities are summarised in Table 4-5, and they show a similar weight fraction at 92%. The specification of manufactured hybrid yarn are shown in Table 4-6.

$W_c$ = weight fraction of core yarn	$d_w$ = wrapping density, w/m
$N_c$ = core yarn tex	$N_w$ = wrapping yarn tex
$w_c$ = weight of core yarn	$w_w$ = weight of wrapping yarn
$L$ = helical length of wrapped yarn	$\lambda$ = cyclic pitch of wrapped yarn
$D_c$ = core yarn diameter	$D_w$ = wrapped yarn diameter

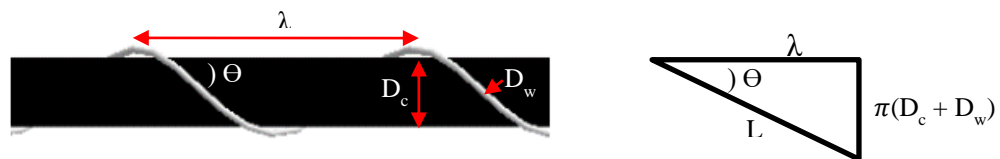


Figure 4-4 Geometric definition of wrapped yarn

$$L = \sqrt{\lambda^2 + (\pi(D_c + D_w))^2} \quad \text{Equation 4-1}$$

$$W_c (\%) = \frac{w_c}{w_c + w_w} \times 100 \quad \text{Equation 4-2}$$

$$w_c = \lambda \times N_c \times d_w \quad \text{Equation 4-3}$$

$$w_w = L \times N_w \times d_w \quad \text{Equation 4-4}$$



Table 4-7 Geometric properties of wrapped yarns

Sample name	Wrap per meter (w/m)	$\lambda$ (cm)	L (cm)	$W_c$ (%)	$W_w$ (%)
CF-2PP-SW50	50	0.020	2.001	92.161	7.839
CF-2PP-SW75	75	0.013	1.335	92.155	7.845
CF-2PP-SW100	100	0.010	1.003	92.147	7.853
CF-2PP-SW125	125	0.008	0.803	92.136	7.864

### 4.2.1.3 Hybrid CF/PA6 wrapped yarn

PA610 and PA610/Graphene multifilaments were used to manufacture single wrapped yarn with carbon fibres at 50 wraps per meter (w/m) on the developed machine (see chapter 3). Fibre weight and volume fraction are summarised in Table 4-8.

Table 4-8 Specification of wrapping yarn samples at 50w/m

	1PA6-SW50	1PA6/G-SW50
Carbon fibre (Tex)	400 x 1	400 x 1
Thermoplastic fibre (Tex)	24 x 1	23 x 1
CF weigh fraction	0.94	0.95
TP weight fraction	0.06	0.05
CF volume fraction	0.91	0.91
TP volume fraction	0.09	0.09

### 4.2.1.4 Micro-wrapping

Microfibre wrapped yarns are manufactured by split carbon fibres and two times drawn PP/Graphene 0 wt% or 1 wt% fibres on the developed wrapping machine with a wrapping density of 50 wraps per meter (w/m).

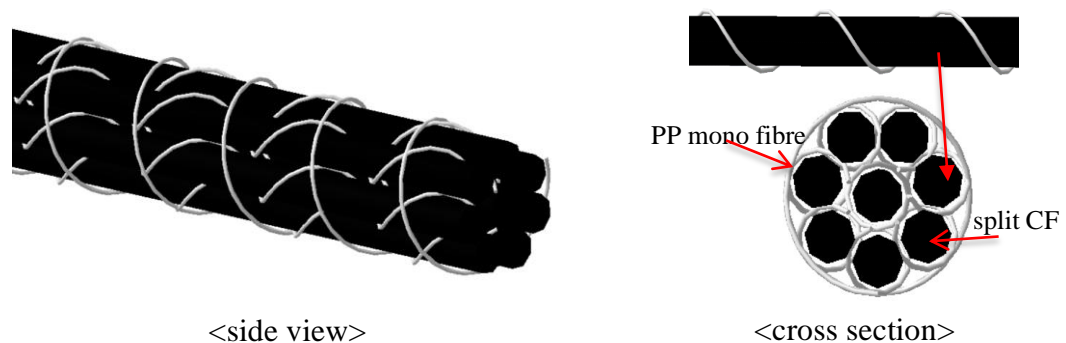


Figure 4-5 manufacturing process of micro wrapped yarn with split carbon fibre and mono PP fibres.

First, drawn PP fibres were wrapped split carbon fibres, and then eight of wrapped yarns were combined and wrapped together again to make one thread, as can be seen in Figure. 4-5. Figure 4-6 presents the digital optical microscope images of hybrid wrapped yarn of CF and PP fibres.

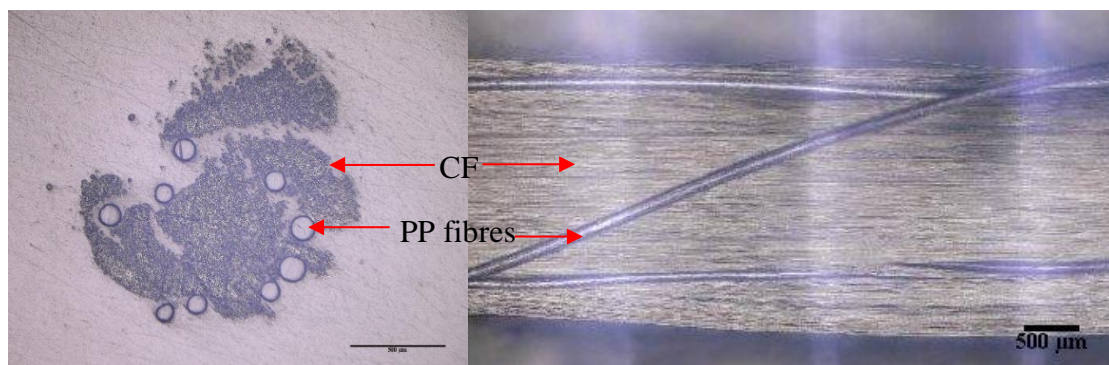


Figure 4-6 Optical microscope images of micro wrapped yarn at a cross- and lateral- section

#### 4.2.2 Polypropylene fibre drawing

The neat PP and binary PP/Graphene mono fibres were drawn from one to three times each sample. The drawing condition is set through preliminary testing, and this condition is summarised in Table 4-9. Tension and wind up speeds were fixed at 1.5N and 1.1m/min, and the initial temperatures of the three heaters were 100, 110, and 115°C, respectively. Because fibres may be degraded/damaged at high temperatures, several trials were conducted to establish safe temperatures for the drawing process. The temperature of all three heaters was increased by ten degrees celsius each at the third drawing. A compensating tensioner (Ascotex Ltd, UK) was used as the fibre tension controller, and tension was measured by an FK 50 tension meter (SAUTER, UK). From this set-up, PP/Graphene fibres were stretched under the specified tension at the heating zone, as shown in Figure 4-7.

Breakage of drawn fibres can sometimes happen during production by an unexpected accident. It is difficult to recognise the fibre breakage unless someone stands and keeps looking at the production line until the fibre drawing is finished. Therefore, the breakage and quality of microfibrils were monitored through the set-up of a USB digital microscope (RS PRO, SPD-8200U-C, UK) with a laptop on the developed machine to save time from an idle machine running, as shown in Figures 4-8.

Table 4-9 Mono fibres drawing conditions of temperature, tension and speed

Drawing frequency	Temperature (°C)			Tension (N)	Wind-up speed (m/min)
	Heater 1	Heater 2	Heater 3		
1	100	110	115	1.5	1.1
2	100	110	115	1.5	
3	110	120	125	1.5	

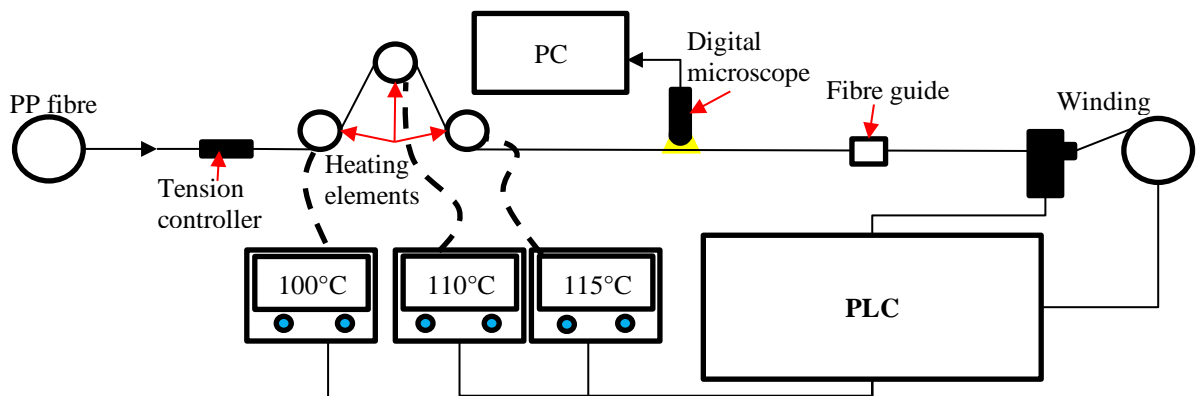


Figure 4-7 Schematic fibre drawing systems on the developed machine

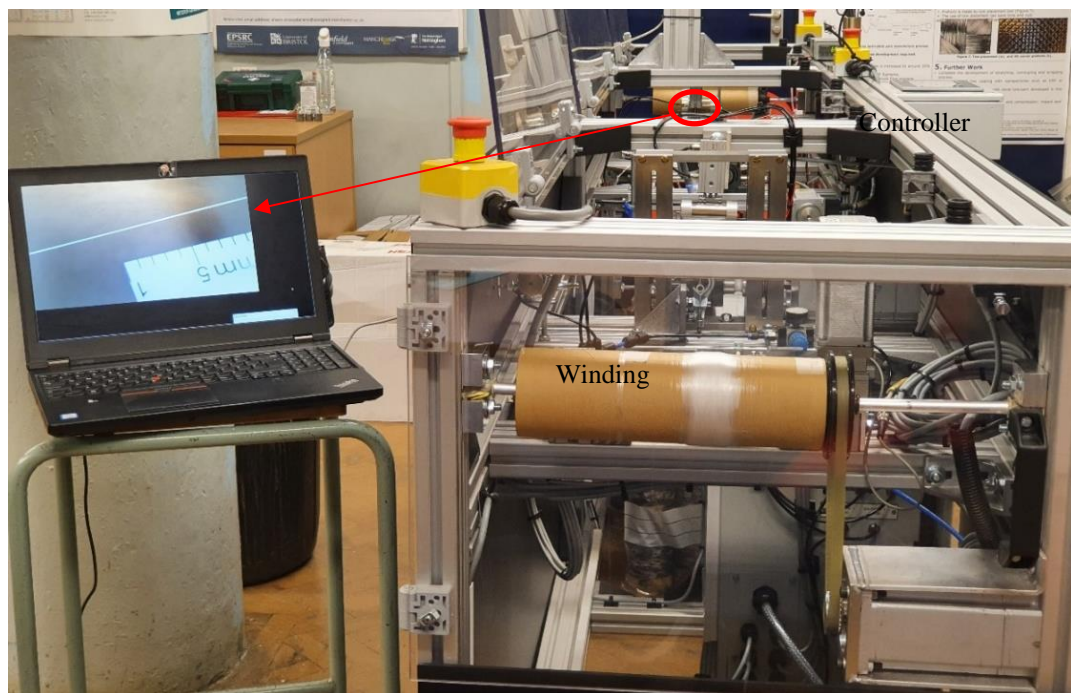


Figure 4-8 Fibre drawing process on the developed machine

### 4.2.3 Carbon fibre tow splitting

Non-twisted Tenax<sup>®</sup>-E HTS45 E23 3k carbon fibres from Teijin were used to split carbon fibres. Carbon fibre splitting systems were set up as shown in Figure 4-9. First, a 1mm diameter needle, which can minimise fibre damage and loss of fibres, halved the 3k carbon fibres (4-9.a). Then, these split tows were wound on two different bobbins on the Model 965 winders (Leesona, USA). Figure 4-9.b shows the set-up of fibre splitting at 13cm/s winding speed. From this fibre splitting process, carbon fibre loss of 4.3% occurred, and the 3K carbon fibres were split into 1.23K and 1.64K (Table 4-10).

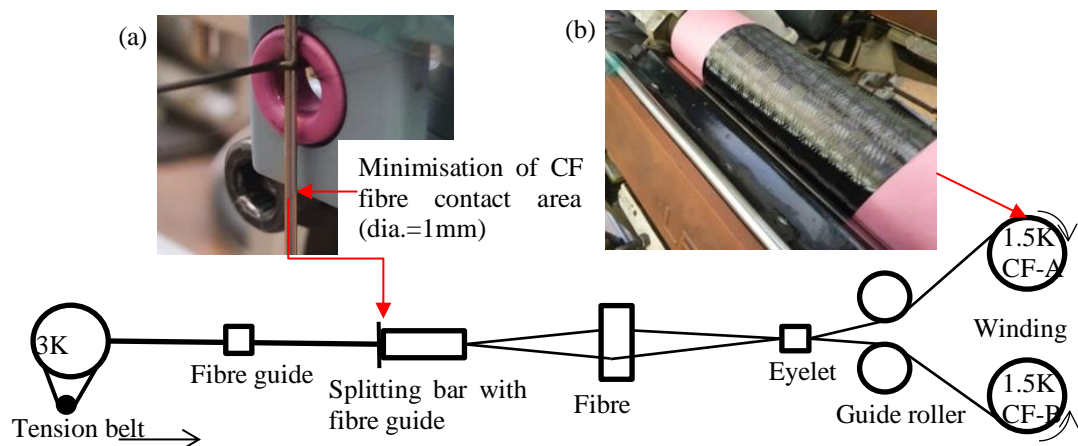


Figure 4-9 Tow splitting setting for carbon fibre

Table 4-10 Carbon fibre linear density after and before splitting

	Before splitting	After splitting-bobbin A	After splitting-bobbin B	Total(=A+B)	Loss
Number of filaments (k)	3	1.23	1.64	2.87	0.13 (4.3%)
Linear density (Tex)	200	81.75±1.46	109.65±2.40	191.40	8.60 (4.3%)

### 4.2.4 Preforming

#### 4.2.4.1 UD and 3D structure

UD and 3D structure preform with commingled yarns, wrapped yarns and veil were manufactured using a modified table size cartesian coordinate robot developed by the

University of Manchester [52]. The pin frame set on this tow placement was designed to minimise fibre distortion when the final preform is removed from the frame. The UD and 3D [0/90/0/90/0/90/0] structure composites consisted of 7 layers each, and the tow density was 8 tow/cm as following previous researcher [14]. Figure 4-10 shows a 3D structure preforms with commingled and wrapped yarns.

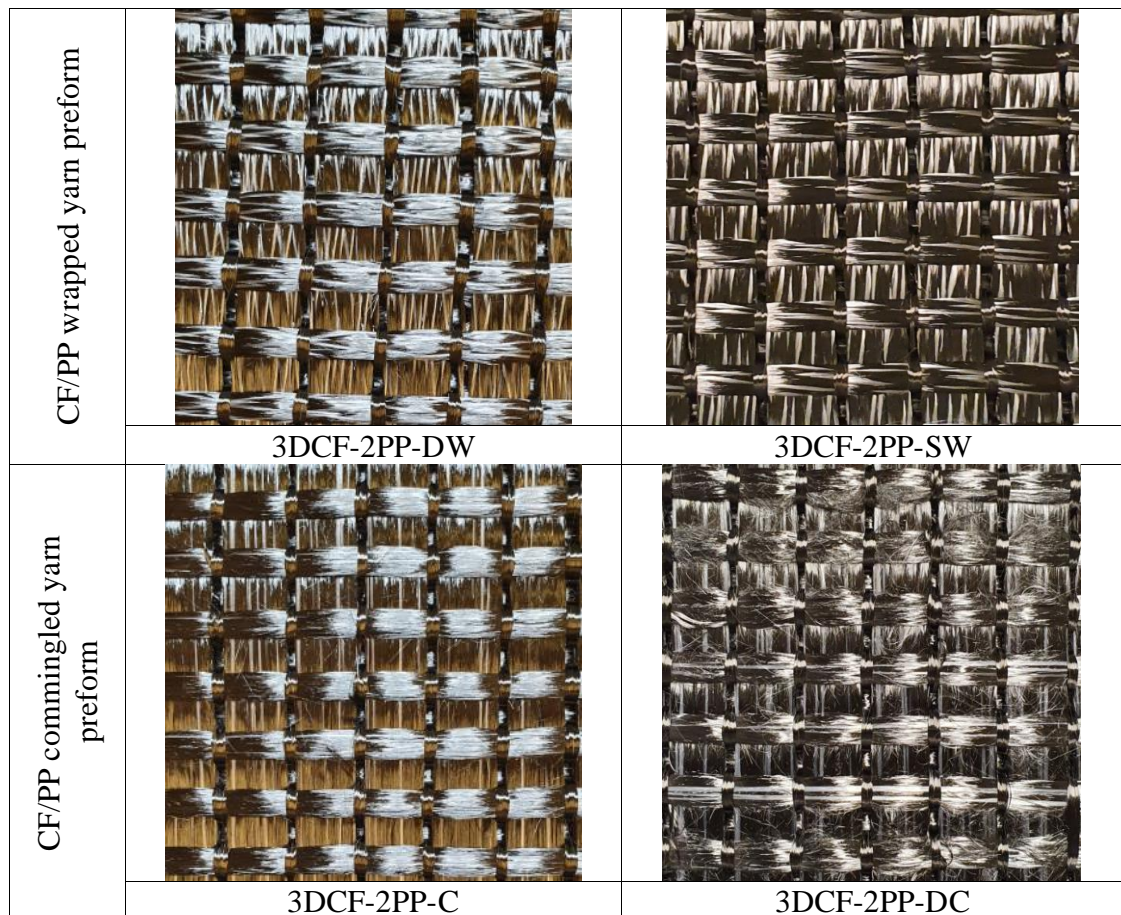


Figure 4-10 Manufactured hybrid yarn 3D structure preforms

#### 4.2.4.2 Micro wrapped yarn preforms

The CF/PP or CF/PPG1.0 wrapped yarns were used to prepare 7 layers of [0/90/0/90/0/90/0] cross-ply laminate preforms (Figure 4-11). The CF/PPG1.0 wrapped yarn was also used to manufacture 3D structural preforms with PPG1.0 fibre through-thickness binder (TT), as shown in Figure 4-12. All preforms are produced on a robotic tow placement, developed by the University of Manchester [91].



Figure 4-11 Cross-ply [0/90] structure preforming on robotic tow placement developed by the University of Manchester

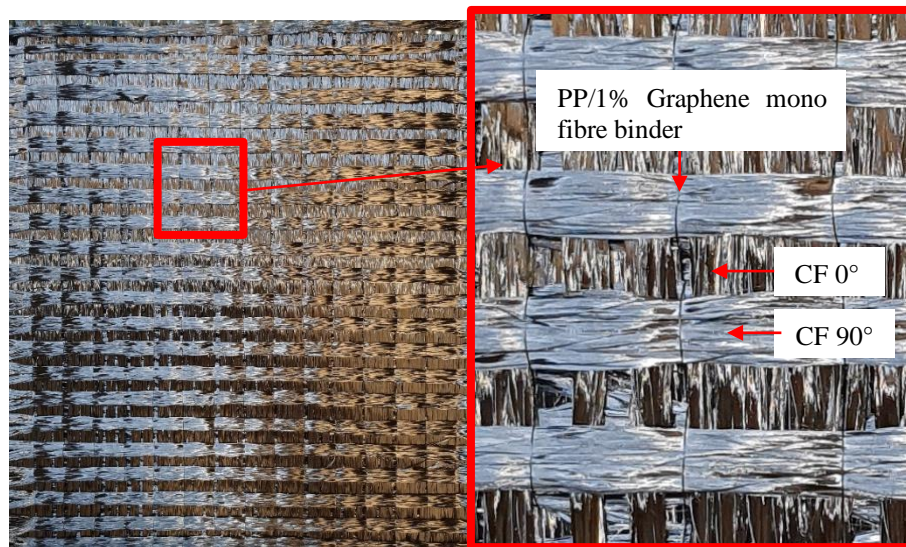


Figure 4-12 Wrapped yarn 3D structure preform with PP/Graphene mono fibre through-thickness binders

#### 4.2.4.3 Carbon fibres and PEI veils preforms

The PEI veil rolls are cut in both 10 mm width and 200 mm width. The 10 mm width of the PEI veil was inserted between 6K carbon fibres (Figure 4-13. a), and the 200 mm width PEI veils were inserted between carbon fibre layers (Figure 4-13. b). And then, UD [0]<sub>7</sub> and 3D [0/90/0/90/0/90/0] structure preforms were prepared, and 6K carbon fibre was used for the through-thickness binder. Every preform was produced on a robotic tow

placement developed by the University of Manchester [91]. Table 4-11 shows the weight and volume fraction of CF and PEI veil.

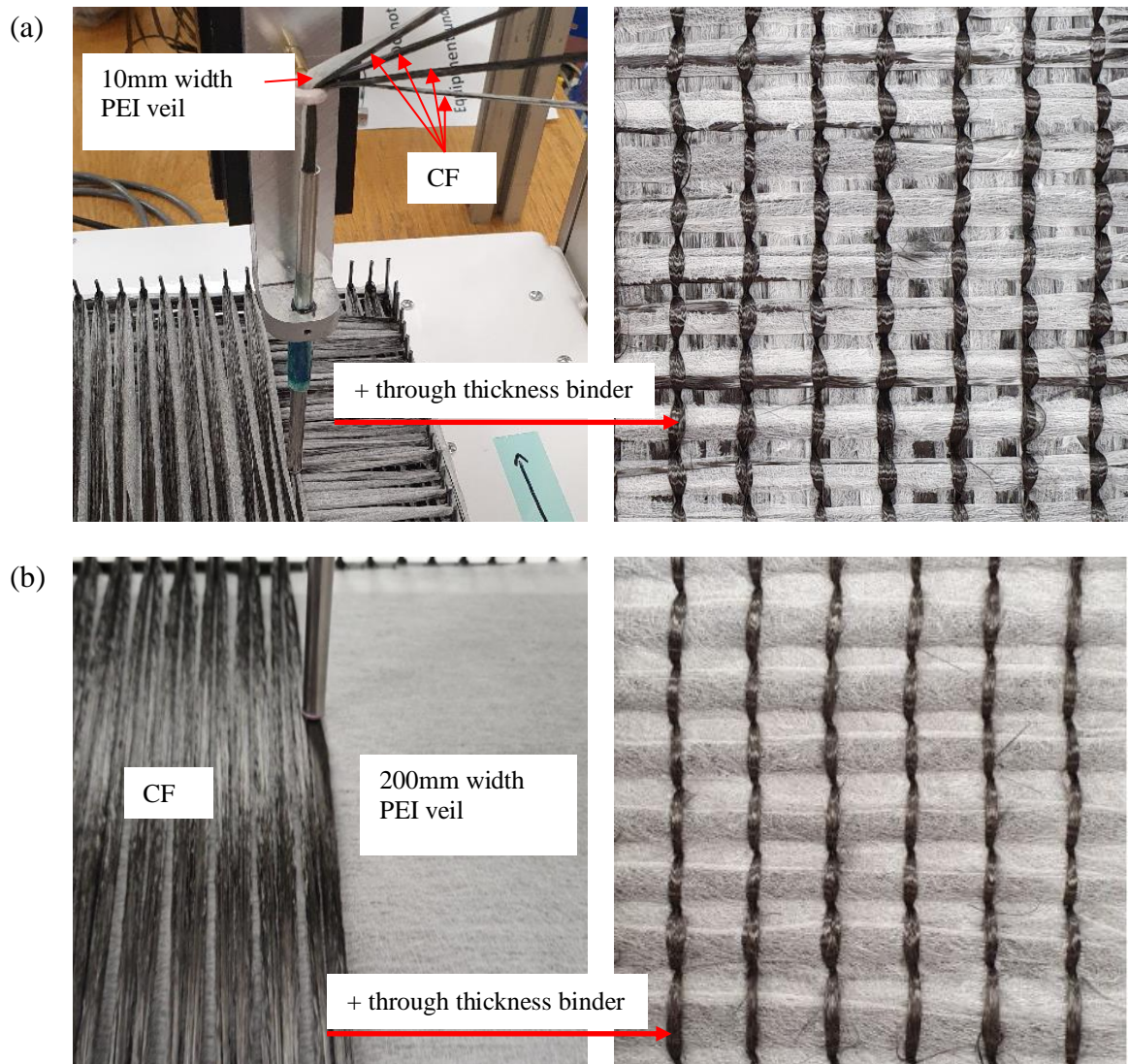


Figure 4-13 PEI veil and carbon fibre lay-up process on the Cartesian coordinate robot; PEI 3D structure of (a) 10mm width, and (b) 200mm width

Table 4-11 Specification of hybrid yarn of PEI veil and carbon fibre

	PEI-10	PEI-200
Carbon fibre (Tex)	400 x1	400 x1
PEI veil width (mm)	10	200
PEI veil length (mm)	-	250
CF weigh fraction	0.88	0.94
TP weight fraction	0.12	0.06
CF volume fraction	0.84	0.91
TP volume fraction	0.16	0.09

### 4.2.5 Composites manufacturing

Composites are produced using the vacuum bagging method. Two metal plates are used to flatten the surface of a specimen to decrease errors during testing. The thickness of the top side of the metal is 2 mm (Figure 4-14).

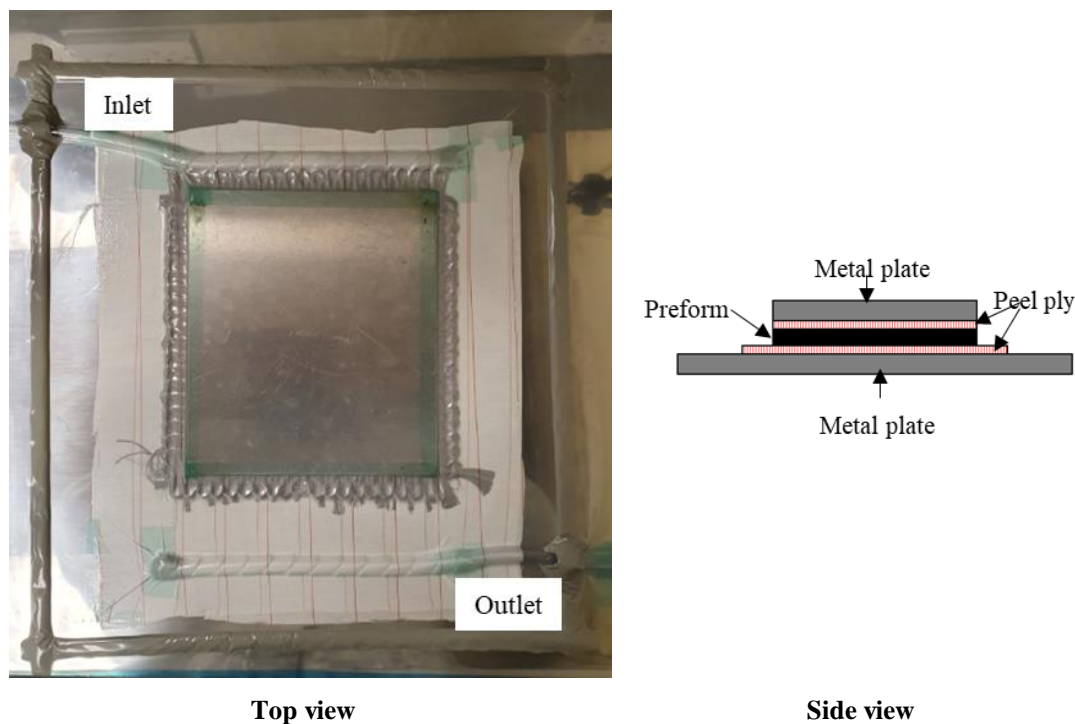


Figure 4-14 Vacuum bagging set-up

The prepared preforms were infused using the vacuumed bagging method with IN2 epoxy resin and AT30 slow epoxy hardener purchased from Easy Composites Ltd, UK. These components were prepared in a weight ratio of 100:30 in separated cups as following the mechanical data sheet, and they were degassed under vacuum for 3hrs. Next, they were mixed for 2 minutes using a glass rod and then degassed again under a vacuum for 15 minutes. Finally, the mixed resin and hardener were delivered into the preform for 0.5-1hr and left for 24hrs at room temperature. Once the resin infusion process was finished, samples were heated in an oven at 60°C for 6 hrs to make fully cured composites. This curing condition followed the technical data provided by the manufacturer [106].

Table 4-12 shows defined composites sample name and their specification. The physical properties of the composite samples are shown in Table 4-13. The composite density to calculate fibre volume fraction (FVF) from the Rule of Mixtures for density (Equation 4-



5 and 6) [107] was measured by the specimen's weight in the air and in distilled water at room temperature following ASTM D792-20 standard test methods [108]. The sample notations and physical properties of composites are presented in Table 4-3.

$$\rho_{comp} = \frac{1}{(w_{CF}/\rho_{CF}) + (w_{TP}/\rho_{TP}) + (w_{epoxy}/\rho_{epoxy})} \quad \text{Equation 4-5}$$

$$V_{void} = \frac{\rho_{comp} - \rho_{exp}}{\rho_{comp}} \quad \text{Equation 4-6}$$

Table 4-12 Details of sample codes

	Sample name	Preform structure	Thermoplastic	Characteristic
Neat carbon fibre composites	UDCF	UD	-	-
	3DCF	3D	-	-
Commingled yarn composites (C)	3DCF-2PP-C	3D	PP fibre 17 tex x 2	
	3DCF-2PP-DC	3D	PP fibre 17 tex x 2	de-sizing PP fibres
Wrapped yarn composites (W)	UDCF-2PP-SW50	UD	PP fibre 17 tex x 2	Single wrapped yarn, 50 w/m
	UDCF-2PP-SW75	UD	PP fibre 17 tex x 2	Single wrapped yarn, 75 w/m
	UDCF-2PP-SW100	UD	PP fibre 17 tex x 2	Single wrapped yarn, 100 w/m
	UDCF-2PP-SW125	UD	PP fibre 17 tex x 2	Single wrapped yarn, 125 w/m
	UDCF-1PP-SW50	UD	PP fibre 17 tex x 1	Single wrapped yarn, 50 w/m
	UDCF-3PP-SW50	UD	PP fibre 17 tex x 3	Single wrapped yarn, 50 w/m

	UDCF-2PP-DW50	UD	PP fibre 17 tex x 2	Double wrapped yarn, 50 w/m
	3DCF-2PP-SW50	3D	PP fibre 17 tex x 2	Single wrapped yarn, 50 w/m
	3DCF-2PP-DW50	3D	PP fibre 17 tex x 2	Double wrapped yarn, 50 w/m
	UDCF-1PA6-SW50	UD	PA6 fibre 23 tex x 1	Single wrapped yarn, 50 w/m
	UDCF-1PA6/G-SW50	UD	PA6/graphene fibre 23 tex x 1	Single wrapped yarn, 50 w/m
Carbon fibre and veil composites	UDCF-PEI-10	UD	PEI veil	Tape type veil (10mm width)
	UDCF-PEI-200	UD	PEI veil	Film type veil (200 mm x 250mm)
	3DCF-PEI-10	3D	PEI veil	Tape type veil (10mm width)
	3DCF-PEI-200	3D	PEI veil	Film type veil (200 mm x 250mm)
Micro wrapped yarn composites	CF	2D	-	
	CF/PP	2D	Drawn PP monofilament	
	CF/PPG1	2D	Drawn PP/graphene 1% monofilament	
	CF/PPG1/TT	3D	Drawn PP/graphene 1% monofilament	Through thickness binder = only drawn PP/graphene 1% monofilament

Table 4-13 Physical properties of composite samples

	Sample name	Thickness (mm)	Density (g/cm <sup>3</sup> )	FVF	
				CF	TP
Carbon fibre composites	UDCF	2.763 (±0.055)	1.488 (±0.003)	0.67	-
	3DCF	3.097 (±0.140)	1.384 (±0.012)	0.60	-
Commingled yarn composites (C)	3DCF-2PP-C	3.391 (±0.070)	1.344 (±0.032)	0.60	0.02
	3DCF-2PP-DC	4.001 (±0.436)	1.330 (±0.005)	0.52	0.02
	UDCF-2PP-SW50	3.275 (±0.007)	1.384 (±0.006)	0.63	0.03
	UDCF-2PP-SW75	3.167 (±0.058)	1.337 (±0.019)	0.67	0.03
	UDCF-2PP-SW100	3.250 (±0.114)	1.369 (±0.016)	0.64	0.03
	UDCF-2PP-SW125	3.083 (±0.120)	1.390 (±0.003)	0.66	0.03
Wrapped yarn composites (W)	UDCF-1PP-SW50	2.813 (±0.055)	1.442 (±0.008)	0.67	0.01
	UDCF-3PP-SW50	3.280 (±0.105)	1.323 (±0.026)	0.64	0.04
	UDCF-2PP-DW50	3.320 (±0.070)	1.396 (±0.035)	0.62	0.03
	3DCF-2PP-SW50	3.523 (±0.246)	1.382 (±0.034)	0.54	0.02
	3DCF-2PP-DW50	3.434 (±0.091)	1.351 (±0.031)	0.56	0.02
	UDCF-1PA6-SW50	3.087 (±0.021)	1.446 (±0.004)	0.62	0.02
	UDCF-1PA6/G-SW50	3.143 (±0.025)	1.472 (±0.009)	0.61	0.02

CF/ veil	UDCF-PEI-10	4.557 ( $\pm 0.075$ )	1.374 ( $\pm 0.014$ )	0.47	0.04
	UDCF-PEI-200	3.677 ( $\pm 0.045$ )	1.412 ( $\pm 0.003$ )	0.55	0.03
	3DCF-PEI-10	4.813 ( $\pm 0.308$ )	1.328 ( $\pm 0.020$ )	0.45	0.04
	3DCF-PEI-200	3.874 ( $\pm 0.358$ )	1.325 ( $\pm 0.007$ )	0.56	0.03
Micro wrapped yarn composites	CF	2.926 ( $\pm 0.150$ )	1.444 ( $\pm 0.01$ )	0.401	-
	CF/PP	3.376 ( $\pm 0.026$ )	1.399 ( $\pm 0.01$ )	0.352	0.065
	CF/PPG1	3.296 ( $\pm 0.029$ )	1.344 ( $\pm 0.01$ )	0.369	0.082
	CF/PPG1/TT	3.812 ( $\pm 0.048$ )	1.347 ( $\pm 0.01$ )	0.354	0.072

### 4.3 Testing

#### 4.3.1 Fibre tensile testing

Single fibre tensile tests of single fibres were carried out using an INSTRON 3344 with 100N load cell at the crosshead speed of 10 mm/min and 1000 mm/min according to the standard ASTM D3379 method (Figure 4-15).

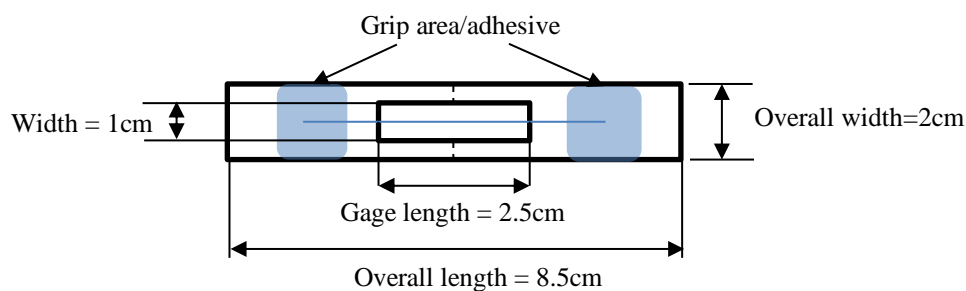


Figure 4-15 Paper card dimension to prepare specimens of single fibre tensile test

The gauge length was 25 mm (Figure 4-16), and raw data were obtained from the Bluehill Universal software. Each sample was repeated five times. The diameter of each fibre was

measured by a 3D digital microscope (VHX-5000, Japan) to calculate stress from the raw data. The peak stress and strain at failure were analysed from stress-strain curves, and Young's modulus was calculated from the slope of the initial linear portion of stress-strain curves.



Figure 4-16 Single fibre tensile test set-up on the Instron 3344 with 100N load cell

### 4.3.2 Composites tensile test

The tensile properties were tested in the warp direction according to the ASTM D3039M-17 method. The samples were cut into 150mm length x 15mm width. End tabs were used on these specimens to avoid premature failure during the testing because specimen dimensions did not follow the recommended size due to the limited size of composites samples. In addition, 50mm length of end tabs of glass fibres were bonded on the specimens using epoxy glue (Huntsman, Araldite 2000 A/B). Testing of prepared specimens was carried out on an INSTRON 5982 Universal Testing Machine with a 100kN load cell, and the loading speed of the upper crosshead was set as 2 mm/min. This tensile test was recorded using an M-lite 5M high-resolution USB camera (LaVision,

Germany) and Strain maps determined with Digital image correlation (DIC) software, Davis 10 software (LaVision, Germany) (Figure 4-17).

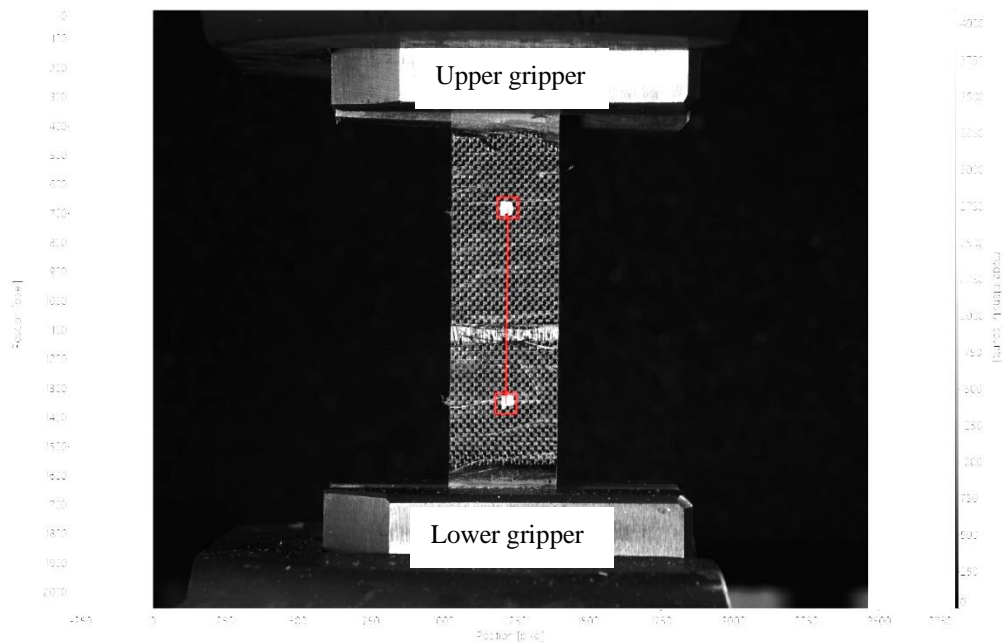


Figure 4-17 Experimental tensile test set-up on DIC normal images

### 4.3.3 Short beam strength test

Short beam strength (SBS) tests have been carried out on an INSTRON 5969 Universal Testing Machine with a 50kN load cell at a 1mm/min crosshead speed. The test set-up and specimen dimension were followed according to ASTM D2344/D2344M-16 standard method [109]. Figure 4-18 presents the test set-up and the dimension of the loading nose and supports. The specimen is put on two supporting cylinders, and testing is monitored by M-Lite 5M high-resolution camera (LaVision, Germany) until the ultimate failure of the specimens happens. Interlaminar shear strength (ILSS) of composites at the SBS test was calculated according to the ASTM standard methods (Equations 4-7) [109].

$$F^{sbs} = \frac{0.75F}{bh} \quad \text{Equation 4-7}$$

$F^{sbs}$  = short beam strength, MPa

$F$  = maximum load observed during the test, N

$b$  = measured specimen width, mm

$h$  = measured specimen thickness, mm

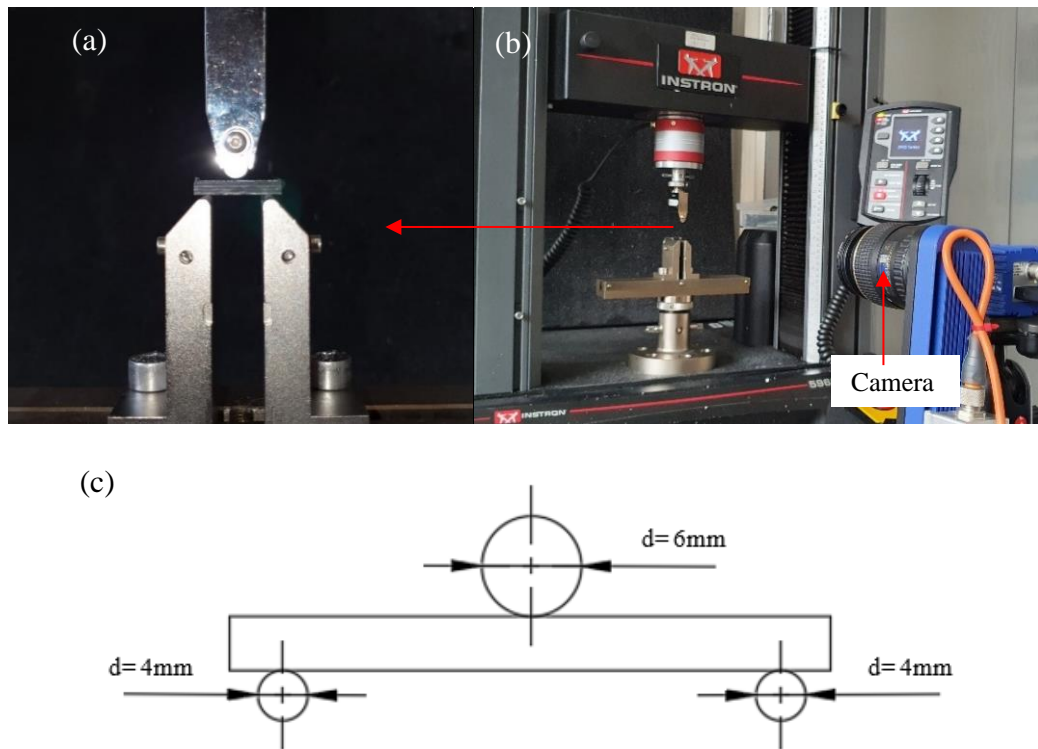


Figure 4-18 (a), (b) Test set-up during the test, and (c) Schematic representation of short beam shear test set-up

#### 4.3.4 Drop-weight impact test

The specimen dimension for drop weight impact tests is 55 (w) x 89 (l) mm, which was modified by Prichard and Hogg for the CAI test [110]. The prepared samples were tested on a CEAAT 9350 drop-weight impact machine which has an anti-rebound system and impactor with a total mass of 2 kg, as shown in Figure 4-19. The hemispherical radius of the impactor head is 20 mm. The specimen was fixed on a fixture to avoid slippage during the testing, and then this fixture was mounted on an impact support fixture. Finally, all composites samples were impacted with 10J and 20J impact energy.

#### 4.3.5 Compression testing

After impact tests, compression tests were processed to analyse the damage tolerance of thermoset composites. An INSTRON 5969 was used for the compression test with a constant displacement of 0.5mm/min and a 100 kN load cell. A modified specimen fixture [110] was used for this research, and samples were mounted vertically and fixed to hold the edges, as depicted in Figure 4-20.

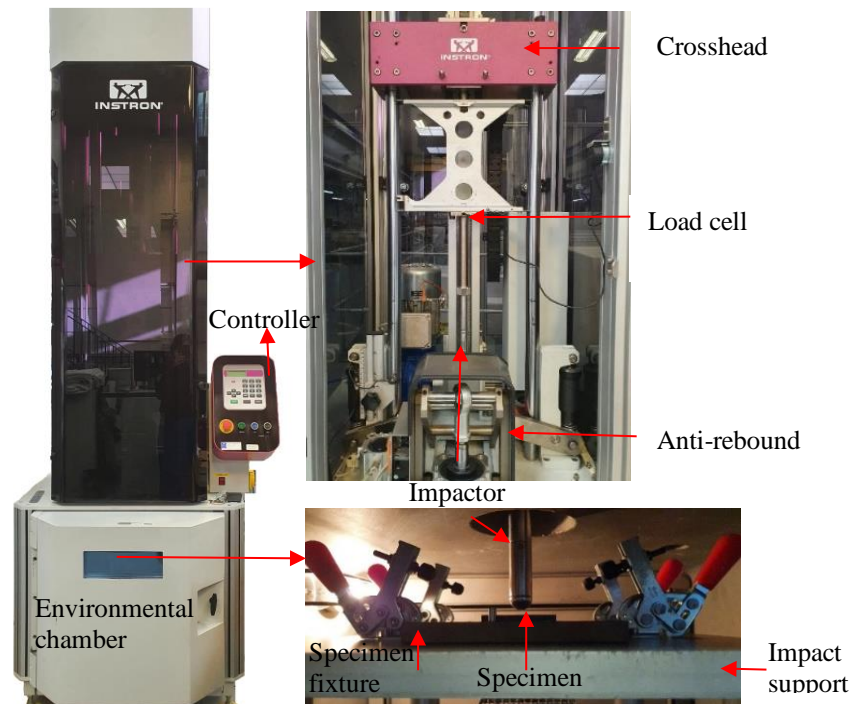


Figure 4-19 Systems of drop weight impact test on a CEAST 9350 machine

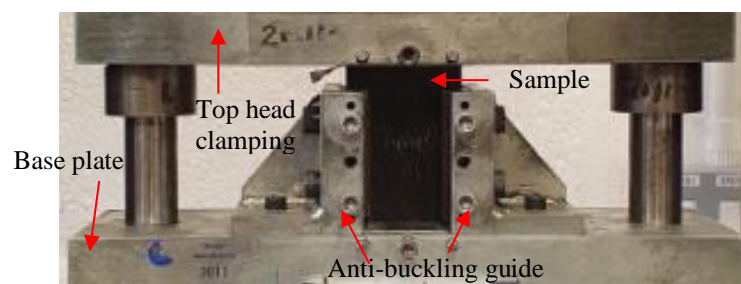


Figure 4-20 CAI test set-up with specimen fixture

#### 4.3.6 Inspection of impact damaged area

The internal damage of composites samples was checked through the Ultrasonic C-Scan manufactured by Midas NDT Ltd. It can assess the damage area with a probe frequency of 1MHz at a scanning speed of 150mm/s. This setting condition was followed from previous study [14]. The damaged area data and images of specimens from C-Scan were obtained by using Zeus v3 software. In addition, dent depth after impact was measured by a digital depth gauge. External damages were observed via 3D digital microscopy (VHX-5000, Japan) and C-scan.



## **Chapter 5.**

# **Impact Damage Tolerance of Thermoset Composites with Carbon and PP Multifilament Hybrid Yarn**

### **5.1 Introduction**

In this research, thermoplastic fibres are used to produce hybrid yarn and to enhance the impact damage tolerance of thermoset composites. Previous research manufactured commingled yarn thermoset composites with glass fibres and polypropylene fibres, and they could check the improvement of impact damage tolerance [14]. However, it is still required to improve the distribution of PP fibres in the hybrid yarn so that mechanical properties can be further increased. Therefore, the commingling process was developed based on the traditional method to improve fibre distribution and decrease the damage of reinforced fibres. The traditional commingling method was used with an air nozzle, but it generated fibre breakages and reduced the mechanical properties of composites. Therefore, to minimise the damage of fibres and increase damage tolerance, the commingling process was developed, and wrapped yarn was introduced to compare the mechanical properties of the commingled yarns.

### **5.2 Results and discussion**

#### **5.2.1 Morphology of hybrid yarn**

Table 5-1 displays cross- and lateral-section images of different types of hybrid yarns obtained by a digital photomicroscope (Keyence, VHX-5000) and their weight and volume fraction are summarised in Table 5-2. The commingled yarn was initially manufactured of carbon fibres and PP multifilament; however, it showed non-homogeneous PP fibres distribution. Therefore, commingled yarn was developed by the de-sizing process to open the filaments and improve fibre distribution. However, this developed yarn still showed that PP fibres are concentrated at one or two sides in the hybrid yarn even though fibre distribution was slightly improved by the de-sizing process. Most of all, the biggest problem was the carbon fibre was broken by the air pressure.

Table 5-1 Cross and lateral section photo-microscopy images of wrapping yarn

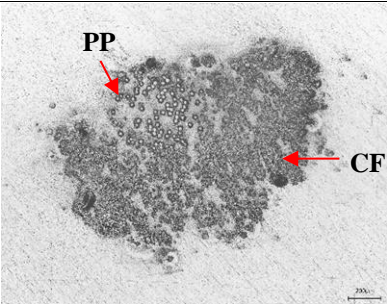
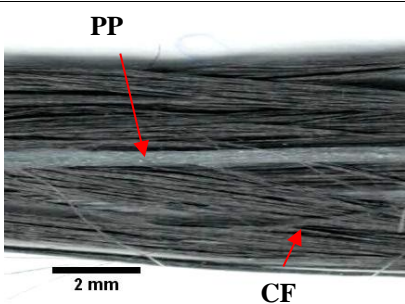
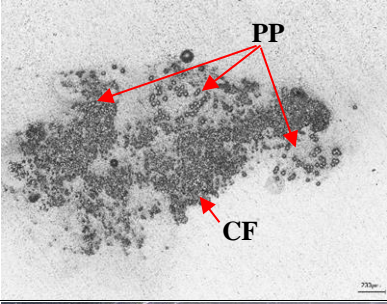
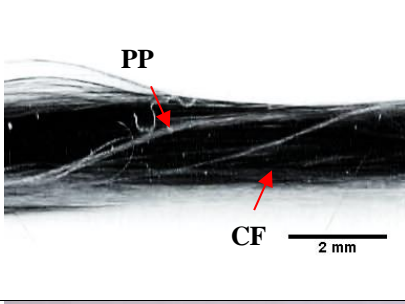
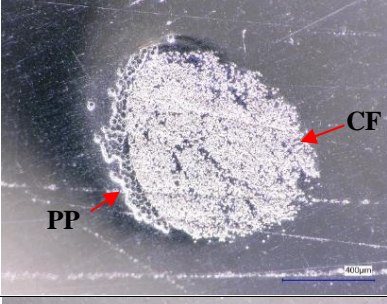
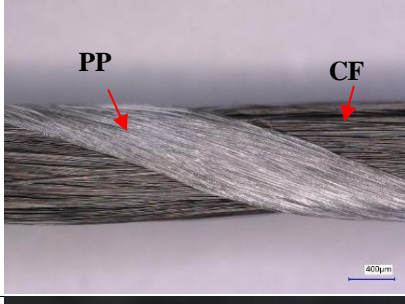
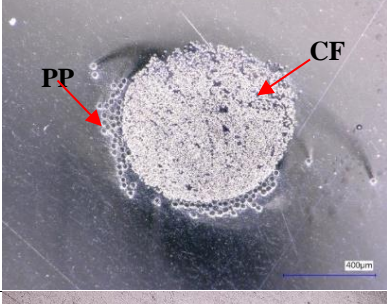
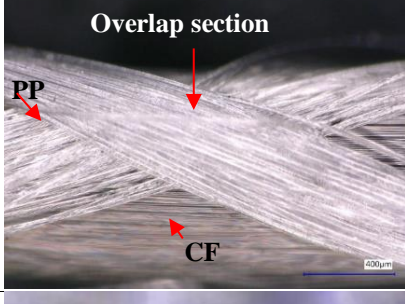
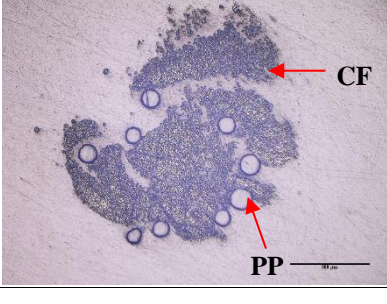
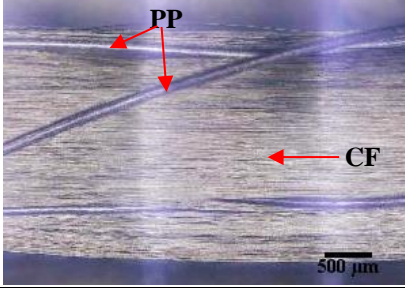
	Cross-section	Lateral-section
Comingled yarn		
Developed comingled yarn		
Single wrapped yarn		
Double wrapped yarn		
Monofilament single wrapped yarn (see Chapter 6)		

Table 5-2 Specification of hybrid yarn samples

To manufacture hybrid yarn without fibre damage, the wrapping process was introduced instead of the mingling process, and single and double wrapped yarns were produced. PP fibres do not mix with carbon fibre, but PP fibres surround carbon fibre, and it is expected that it will protect it from the impact and increase impact damage tolerance. Furthermore, nonhomogeneous PP fibres distribution at commingled yarns could improve through the wrapping process of PP mono microfibre. The microfibre wrapping processes are explained and studied in Chapter 5 separately.

	2PP-SW50	2PP-DW50	2PP-C	2PP-DC
Carbon fibre (tex)	400 x1	400 x1	400 x1	400 x1
Thermoplastic fibre (tex)	17 x 2	17 x 2	17 x 2	12.8 x 2
CF weigh fraction	0.92	0.92	0.92	0.94
TP weight fraction	0.08	0.08	0.08	0.06
CF volume fraction	0.86	0.86	0.86	0.86
TP volume fraction	0.14	0.14	0.14	0.14

## 5.2.2 Polypropylene fibre tensile properties

The tensile test results of PP fibres are shown in Table 5-3, and typical stress-strain curves of PP fibres at 1, 10, and 1000 mm/min loading rates are presented in Figure 5-1. The greater the loading speed, the more tensile strength increased. Also, the modulus at 1000 mm/min loading speed was lower than at the other loading speeds. The peak stress and strain at failure were analysed from stress-strain curves, and Young's modulus was calculated from the slope of the initial linear portion of stress-strain curves.

Table 5-3 Tensile properties data for PP multifilament

Loading speed (mm/min)	Tensile modulus (GPa)			Peak stress (MPa)			Strain failure (%)		
	1	10	1000	1	10	1000	1	10	1000
	3.2 ±0.2	3.7 ±0.1	2.1 ±0.3	236.4 ±49.5	302.3 ±3.2	336.2 ±13.8	-	120.1 ±6.1	30.3 ±1.5

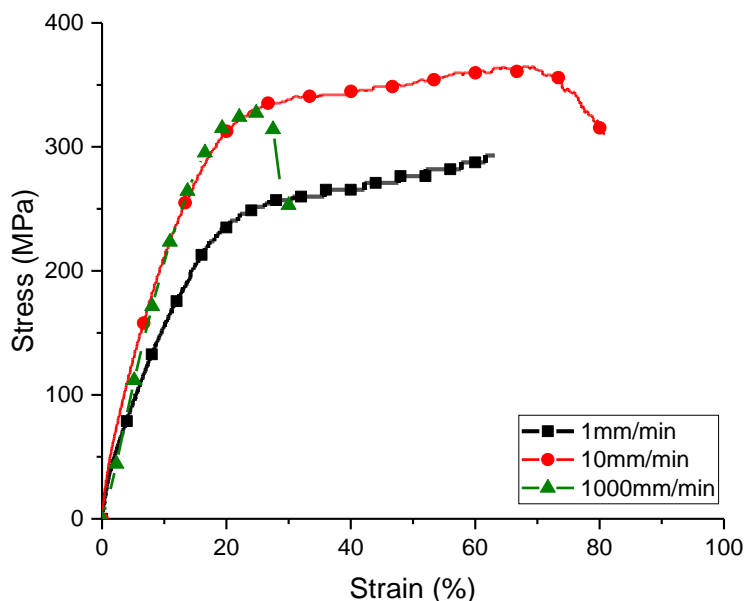


Figure 5-1 Typical stress-strain curves of PP multifilament at 1, 10, 1000 mm/min loading speed

### 5.2.3 Comparison of impact resistance of hybrid yarn composites

The force-displacement impact curves of 3D structure commingled and wrapped yarn composites at 10J and 25J are shown in Figures 5-2 and 5-3, and their impact test results are summarized in Table 5-4. The hybrid yarn composites almost reached up to 5.5kN and 9.0kN at 10J and 25J, respectively, and then the curves reverse after the impactor rebound from the composites.

The peak force and displacement of 3D structure neat CF composite show the highest value among the composite samples in Table 5-4. The absorbed energy of almost of all the samples was similar; however, double wrapped yarn composites show the lowest peak force and rebound energy at 10J and 25J both. The single wrapped yarn composites exhibited relatively smooth impact curves comparison to pure carbon fibre and commingled yarn composites. The degree of load fluctuations reflects the extend of fibre damage of impact loading. It may be concluded that wrapped yarn provides protection during the impact loading in comparison to pure carbon and commingled composites.

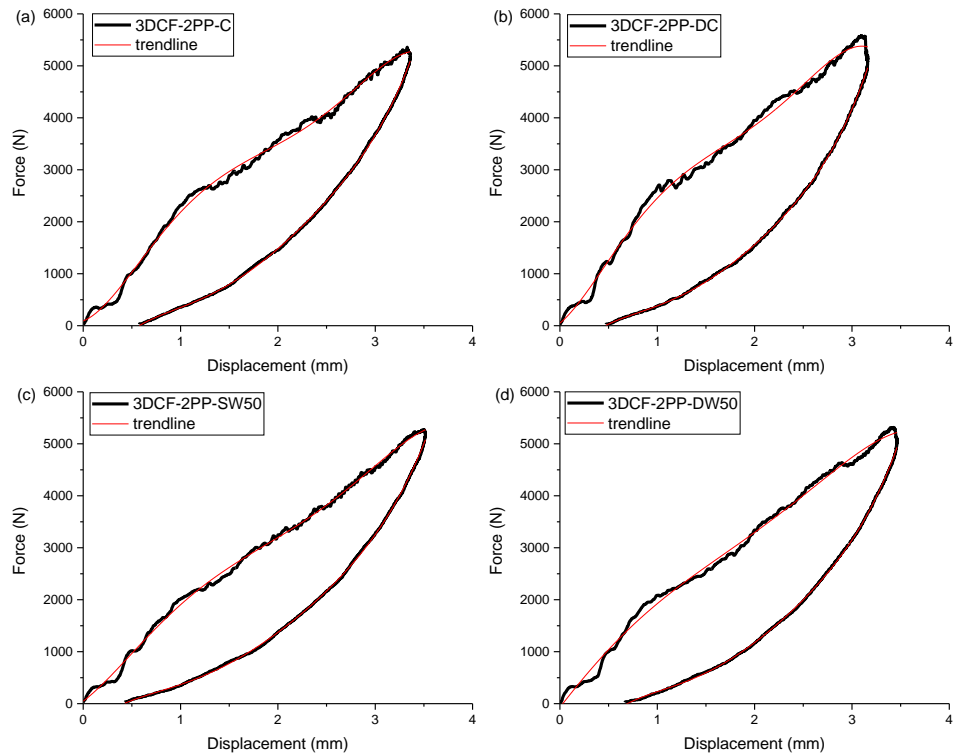


Figure 5-2 Typical force-displacement curves of (a) commingled yarn, (b) developed commingled yarn, (c) single wrapped yarn, and (d) double wrapped yarn composites at 10J impact energy

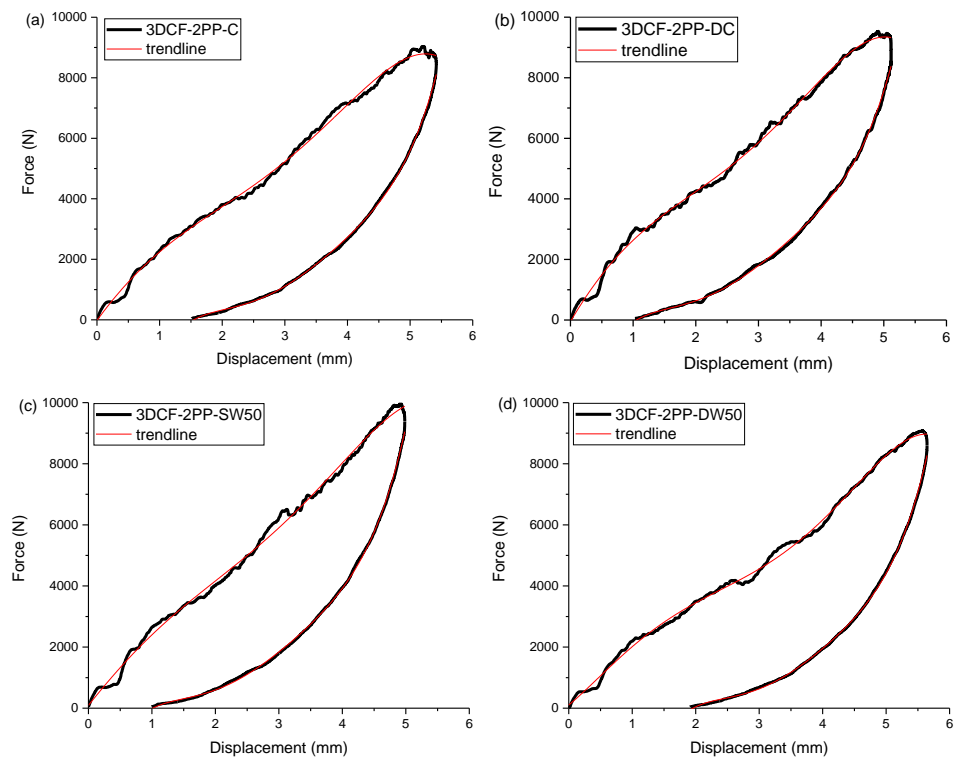


Figure 5-3 Typical force-displacement curves of (a) commingled yarn, (b) developed commingled yarn, (c) single wrapped yarn, and (d) double wrapped yarn composites at 25J impact energy

Table 5-4 Summary of impact test results of 3D structure composites with hybrid yarns at 10J and 25J impact energy

	Sample	Peak force (N)	Peak displacement (mm)	Residual displacement (mm)	Absorbed energy (J)	Recovered energy (J)
10J	3DCF	5524.0 ±64.8	3.6 ±0.1	0.5 ±0.1	4.7 ±0.1	5.3 ±0.1
	3DCF-2PP-C	5460.8 ±117.4	3.3 ±0.1	0.5 ±0.1	5.0 ±0.2	5.0 ±0.2
	3DCF-2PP-DC	5477.5 ±113.6	3.1 ±0.0	0.5 ±0.1	5.5 ±0.2	4.4 ±0.2
	3DCF-2PP-SW50	5498.3 ±204.4	3.3 ±0.2	0.4 ±0.0	4.8 ±0.1	5.2 ±0.1
	3DCF-2PP-DW50	5231.9 ±155.3	3.5 ±0.1	0.7 ±0.1	5.7 ±0.2	4.3 ±0.2
	3DCF	9171.8 ±279.7	5.1 ±0.0	0.9 ±0.3	14.5±1.6	9.0 ±2.5
25J	3DCF-2PP-C	9010.5 ±48.7	5.3 ±0.1	1.4 ±0.1	17.1±0.4	9.4 ±0.3
	3DCF-2PP-DC	9459.3 ±360.7	5.1 ±0.1	1.1 ±0.0	16.6±0.4	10.1 ±0.4
	3DCF-2PP-SW50	9115.1 ±452.1	5.2 ±0.3	1.1 ±0.1	15.3±0.0	10.1 ±0.0
	3DCF-2PP-DW50	9079.1 ±247.1	5.6 ±0.1	1.7 ±0.2	17.2±0.4	8.7 ±0.3

#### 5.2.4 CAI test of commingled and wrapped yarn

The compression test of 3D structure composites was performed after 0J,10J and 25J impact tests. Figure 5-4 illustrates the compressive strength of hybrid yarn composites. Single wrapped yarn shows the highest compressive strength after impact among the composites samples. Compressive strength of commingled yarn and developed commingled yarn composites decreased by 25% and 13% compared to neat carbon fibre composites after the 10J impact test. It may be because of CF damage during production.

A significant difference was found between commingled and wrapped yarn composites. The compressive strength of single-wrapped yarn composites increased by 10% after the 10J impact test. However, double wrapped yarn composites decreased by 27% against neat carbon fibre composites. Therefore, the results suggest that wrapped yarns are effective in improving impact damage tolerance.

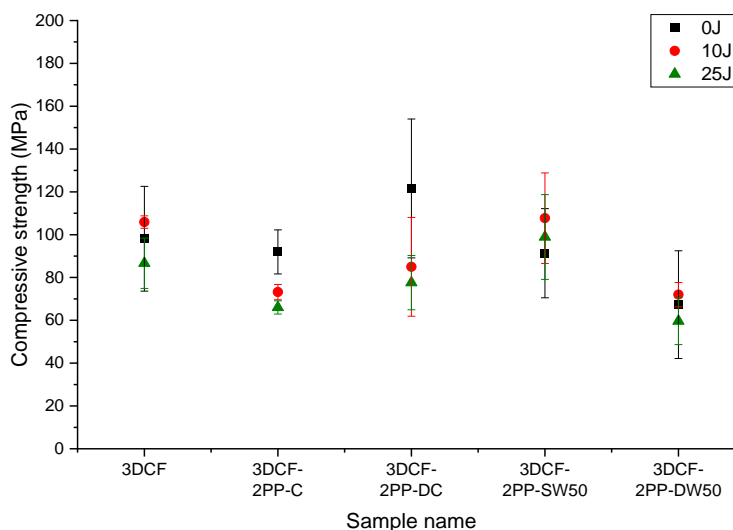


Figure 5-4 Compressive strength of 3D structure hybrid yarn after 0J, 10J and 25J impact test

## 5.2.5 Impact damage tolerance of wrapped yarn composites at different manufacturing conditions

### 5.2.5.1 Effect of wrapping density

Impact test results at 10J are summarised in Table 5-5. All composites at different wrapping densities show a slight difference. UDCF as standard composites showed a slightly higher peak load (4573.9N) and higher recovered energy (4.7J) with respect to wrapped yarn composites, UDCF-50-2PP (4521.9N and 4.5J, respectively). The higher the wrapping density is, the more absorbed energy. Furthermore, the recovered energy is slightly decreased when wrapping density is increased (Figure 5-5). The recovered energy means that the amount of energy is elastically stored by the composites structure and returned after the peak load. Therefore, the highly recovered energy composites have low damage in the composites. Absorbed energy generates damage in the composites, such as matrix cracking, fibre breakage, and delamination [111].

Table 5-5 Summary of impact test results of wrapped yarn UD structure composites at different wrapping density at 10J impact energy

Sample	Wrapping density (w/m)	Peak force (N)	Peak displacement (mm)	Residual displacement (mm)	Absorbed energy (J)	Recovered energy (J)
UDCF	-	4573.9 ±93.7	3.8 ±0.1	0.4 ±0.1	5.2 ±0.1	4.7 ±0.1
UDCF-2PP-SW50	50	4521.9 ±30.8	3.7 ±0.0	0.5 ±0.1	5.5 ±0.2	4.5 ±0.3
UDCF-2PP-SW75	75	4530.4 ±118.2	3.8 ±0.1	0.6 ±0.0	5.4 ±0.2	4.6 ±0.2
UDCF-2PP-SW100	100	4443.4 ±88.8	3.7 ±0.1	0.5 ±0.1	5.5 ±0.1	4.4 ±0.1
UDCF-2PP-SW125	125	4414.3 ±31.5	3.9 ±0.2	0.6 ±0.1	5.6 ±0.1	4.4 ±0.1

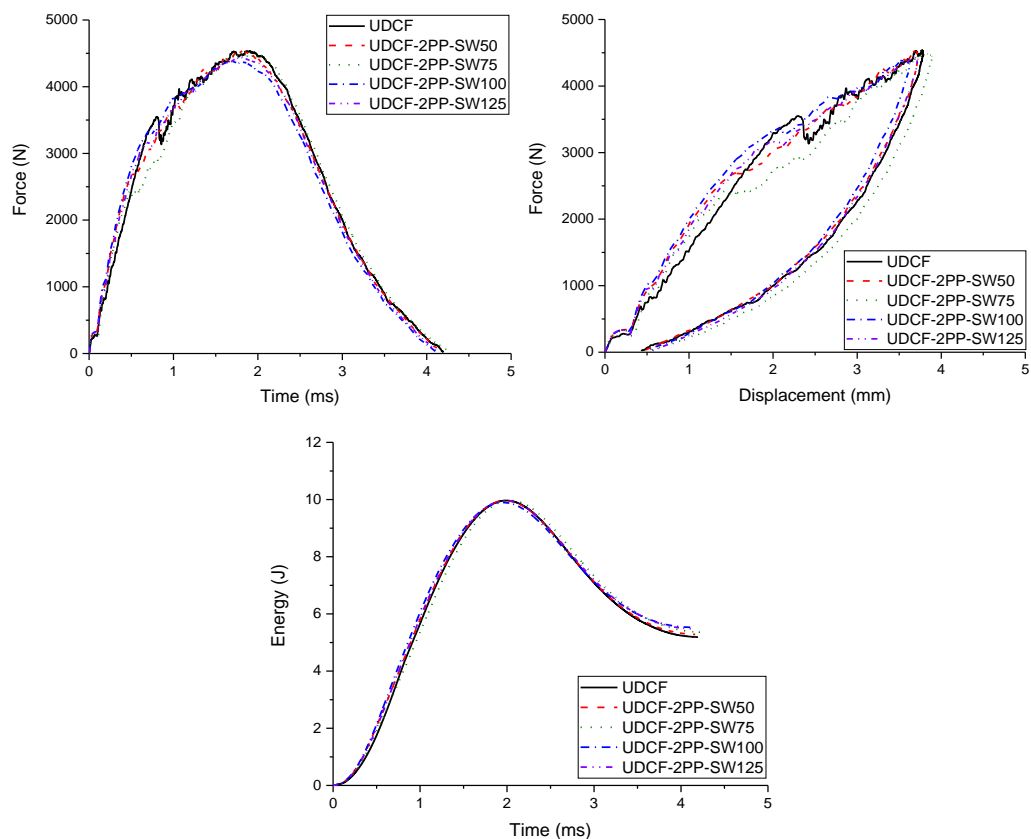


Figure 5-5 Force - displacement and energy - time curve from 10J weight drop test of wrapped yarn composites manufactured at 50, 75, 100, 125w/m



### 5.2.5.2 Effect of the number of PP yarns

The PP yarns influence the impact properties depending on the contents of PP yarns, as shown in Figure 5-6 and Table 5-6. The force-time or displacement curves present that neat carbon fibre composites are damaged more seriously than wrapped yarn composites because force is dropped in while the load is applied. UDCF-50-1PP composites have a higher 4539.9N of peak force and higher 4.7J of recovered energy with respect to UDCF-50-3PP composites (4412.1N and 4.3J, respectively). UDCF-50-1PP and UDCF have similar impact properties. However, the compressive strength of UDCF-50-2PP composites presented the highest values, and UDCF-50-3PP composites were the lowest (Figure 5-7).

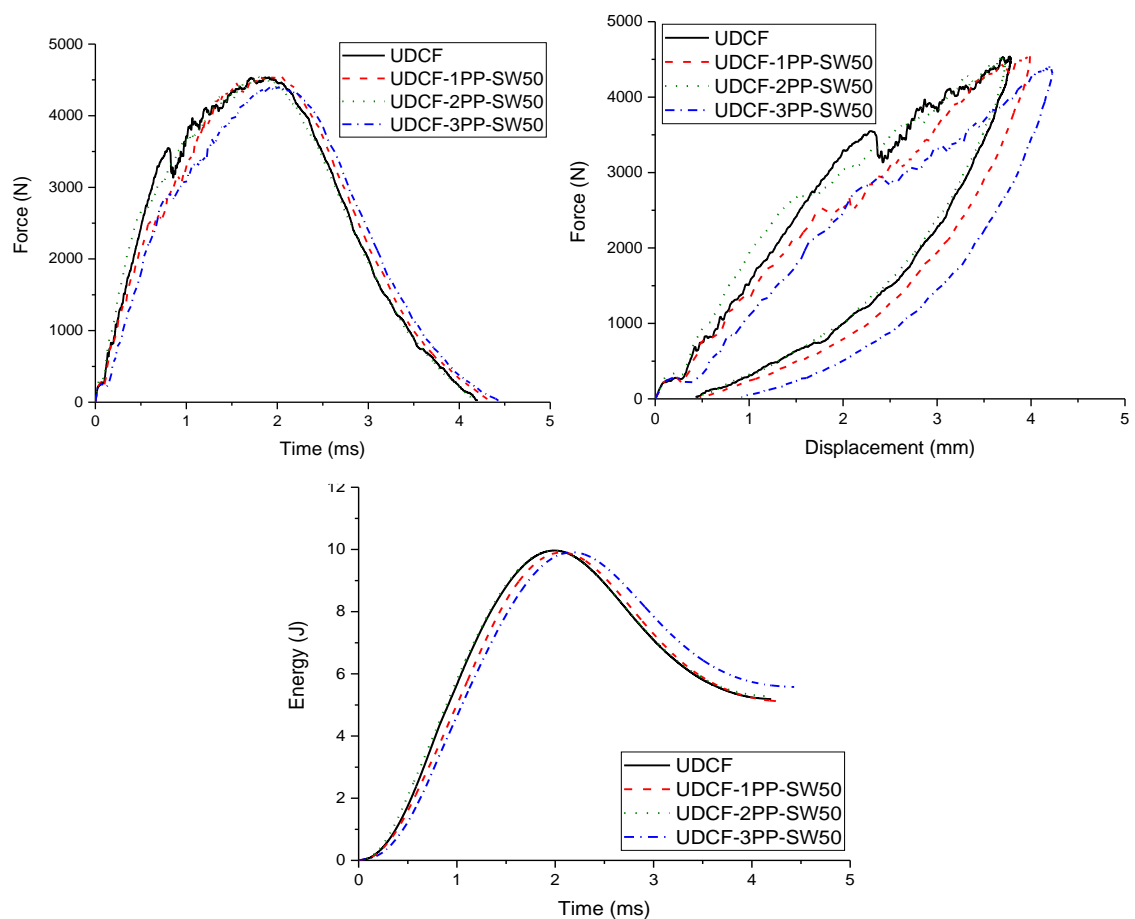


Figure 5-6 Force - displacement and energy -time curve from 10J weight drop test of wrapping yarn composites manufactured by 1PP, 2PP and 3PP yarns

Table 5-6 Summary of impact test results of UD structure wrapped yarn composites at different the number of PP fibres

Sample	Wrapping density (w/m)	Peak force (N)	Peak displacement (mm)	Residual displacement (mm)	Absorbed energy (J)	Recovered energy (J)
UDCF	-	4573.9 ±93.7	3.8±0.1	0.4±0.1	5.2±0.1	4.7±0.1
UDCF-1PP-SW50	50	4539.9 ±13.4	4.1±0.1	0.6±0.2	5.4±0.5	4.7±0.4
UDCF-2PP-SW50	50	4521.9 ±30.8	3.7±0.0	0.5±0.1	5.5 ±0.2	4.5±0.3
UDCF-3PP-SW50	50	4412.1 ±1.3	4.1±0.2	0.8±0.2	5.6±0.0	4.3±0.1

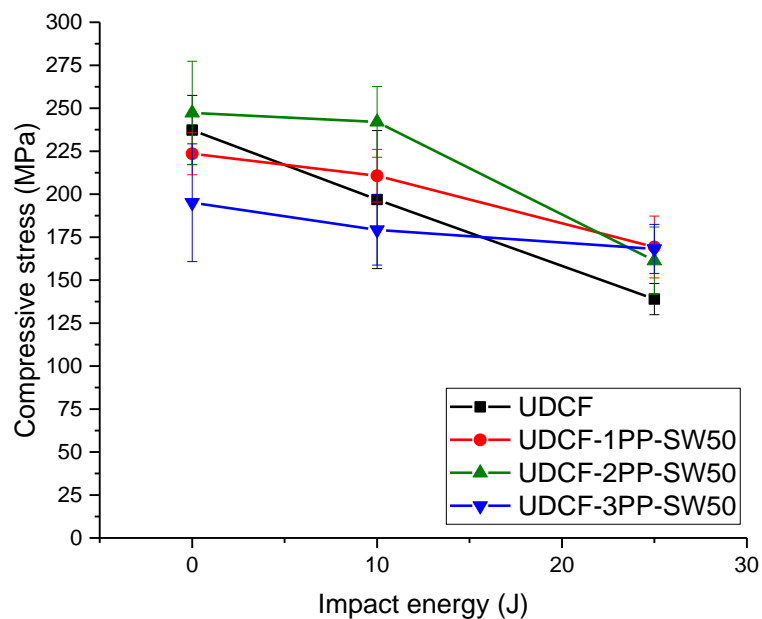


Figure 5-7 Compressive stress versus impact energy curve at different the number of PP multifilament after drop weight impact test

### 5.2.6 UD vs 3D structure hybrid wrapped yarn composites

UD and 3D structure composites were tested on the impact machine at 10J and 25J. The wrapped yarn composites are prepared with 50w/m and 2 x 17 tex PP fibres as following previous results. The 2 x 17 tex fibres were used to manufacture single and double wrapped yarn.

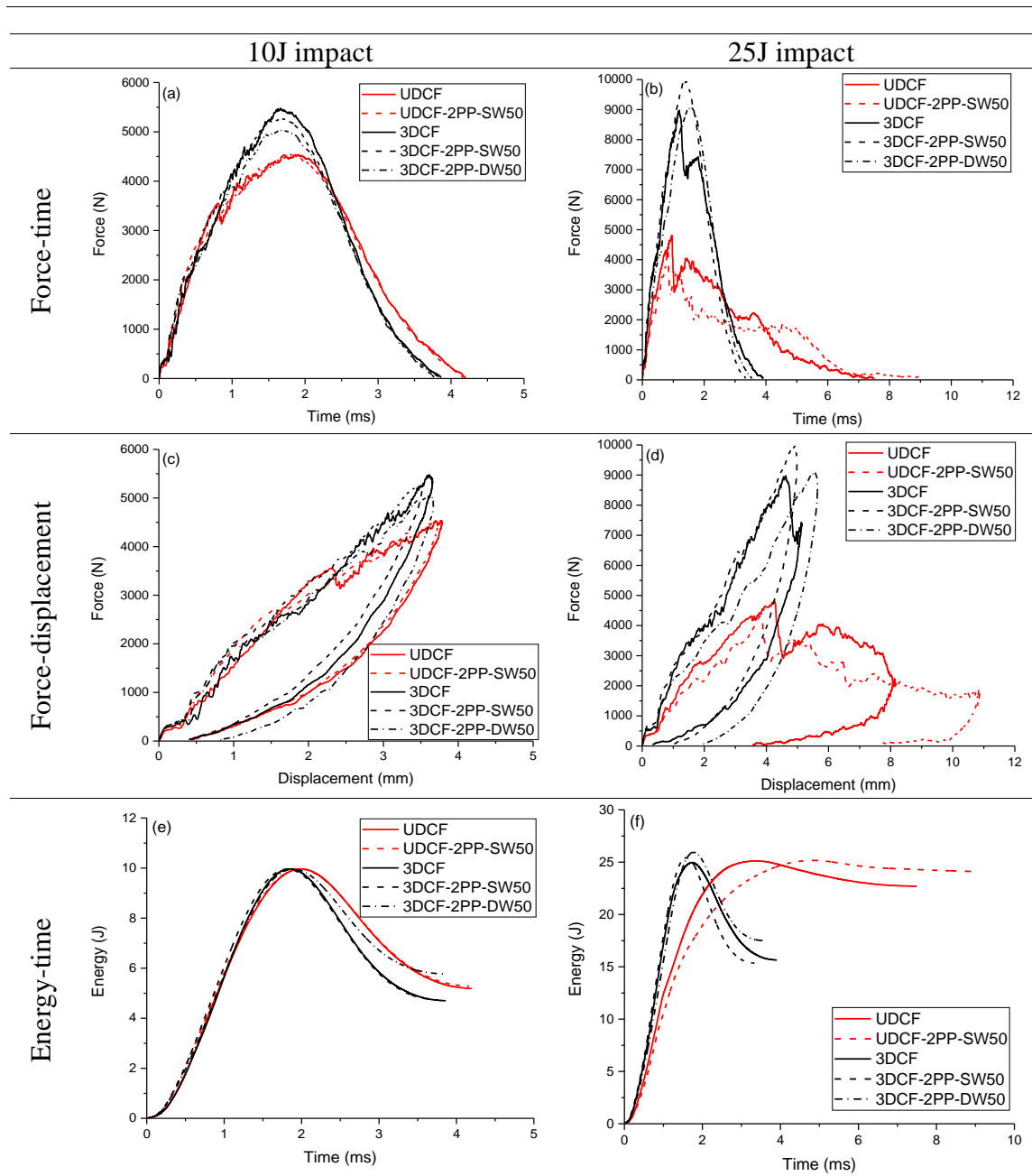


Figure 5-8 Impact test results of UD and 3D structure composites at (a), (c), (e) 10J and (b), (d), (f) 25J. Figure 5-8 shows curves of the impact behaviour, and neat CF composites (3DCF) is shown a highly similar performance with single-wrapped yarn composites (3DCF-2PP-SW50). They exhibit a higher peak force (5524N versus 5498N) and recovered energy (5.3 J versus 5.2 J). The single wrapped yarn composites (3DCF-2PP-SW50) still perform better than double wrapped yarn (3DCF-2PP-DW50) at 10 J and 25 J.

Force-displacement curves present loading curves and unloading curves, and open and close curves are shown depending on the displacement of the unloading curves. If the

displacement of the unloading curve is close to 0 mm, it is called a closed curve. It means composites can still function. On the other hand, if unloading curves are far from 0 displacements, it is called open curves, such as UDCF at Figure 5-8d, and it means that samples are almost penetrated or destroyed by impact [112]. The 3D composites show closed curves at 10 J and 25 J energy impact tests. However, UD composites show closed curves at the 10 J energy impact test and opened curves at the 25 J energy impact test. These findings suggest that 3D composites are available to work under higher impact energy, unlike UD composites. Furthermore, UD and 3D composites with single wrapped yarn absorb 22.4J and 15.3J separately at the 25J energy impact test.

Neat carbon fibre composites show rough loading curves, and load is suddenly dropped compared to wrapped yarn composites, as shown in Figure 5-8. However, the calculated absorbed impact energy from the Figure 5-8 c and d does not show a significant difference between the 3D neat CF (14.5J) and wrapped yarn (15.3J) composites at the 25J impact test. The 3D double wrapped yarn composites are absorbed by 17.2J, the highest impact energy among the 3D structure composites samples at 25J energy impact.

### 5.2.6.1 External damage of composites

From the weigh drop testing, the degree of damage is different according to composites materials and structures. The external damage of composites was studied through the digital indicator and 3D digital microscopy analysis.

In the UD structure, Table 5-7 presents the dent depth of composites after 10J impact in the composites. Dent depth of UDCF-50-1PP, 2PP, and 3PP is 0.35, 0.32 and 0.26mm with respect to UDCF (0.34mm). UDCF-D50-2PP of dent depth at 10J shows the highest depth, 0.37mm. The dent depth of UDCF and UDCF-50-2PP at 25J is 1.07mm and 0.91mm each.

Table 5-7 Dent depth of UD structure composites with different PP contents at 10J

	UDCF	UDCF-1PP-SW50	UDCF-2PP-SW50	UDCF-3PP-SW50	UDCF-2PP-DW50
Dent depth (mm)	0.34±0.03	0.35±0.02	0.32±0.03	0.26±0.03	0.37±0.02

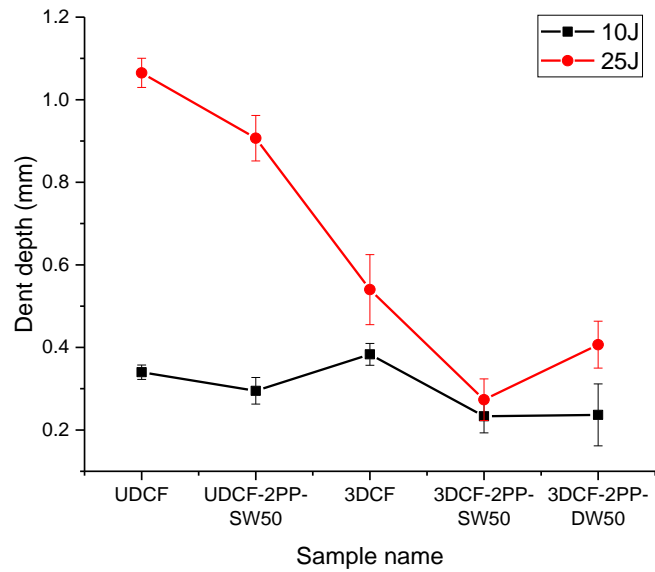


Figure 5-9 Dent depth of UD structure composites at 10J impact

Generally, the PP wrapped yarn composites show less dent depth than neat carbon fibre composites. Moreover, single wrapped composites can have less dent depth than double wrapped yarn composites (Figure 5-9). In 3Dstructure composites, the dent depth of 3DCF (0.54mm) is deeper than wrapped yarn composites that is 3DCF-50-2PP (0.27mm) and 3DCF-D50-2PP (0.41mm) at 25J. The neat carbon fibre composites commonly have deeper dent depth than wrapped yarn composites at 10J and 25J.

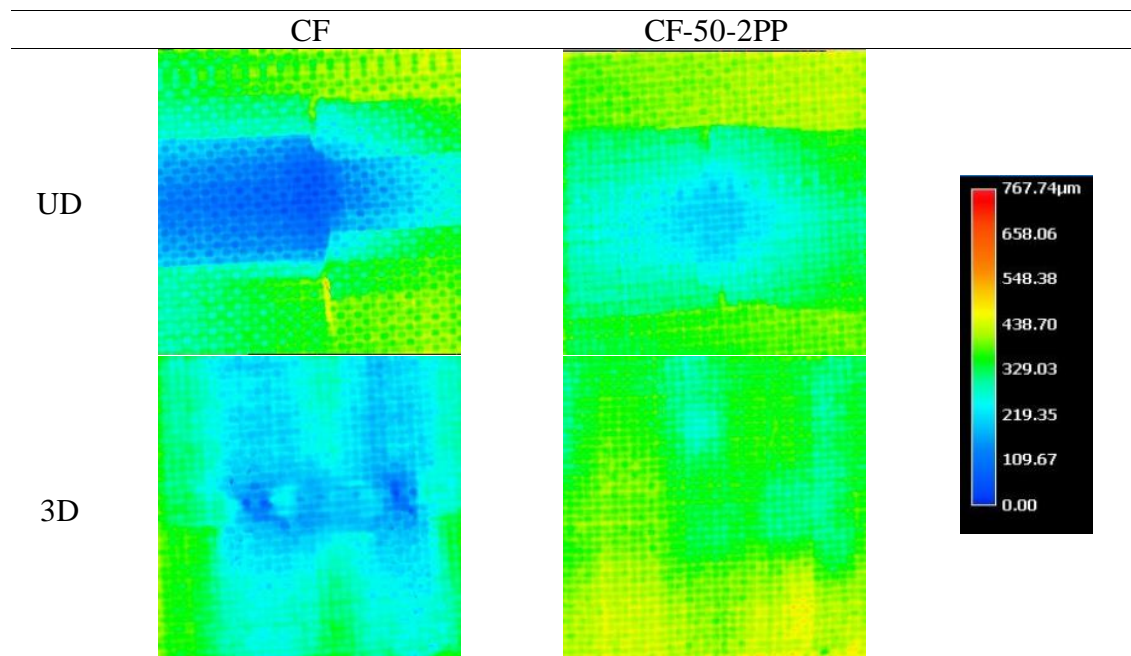
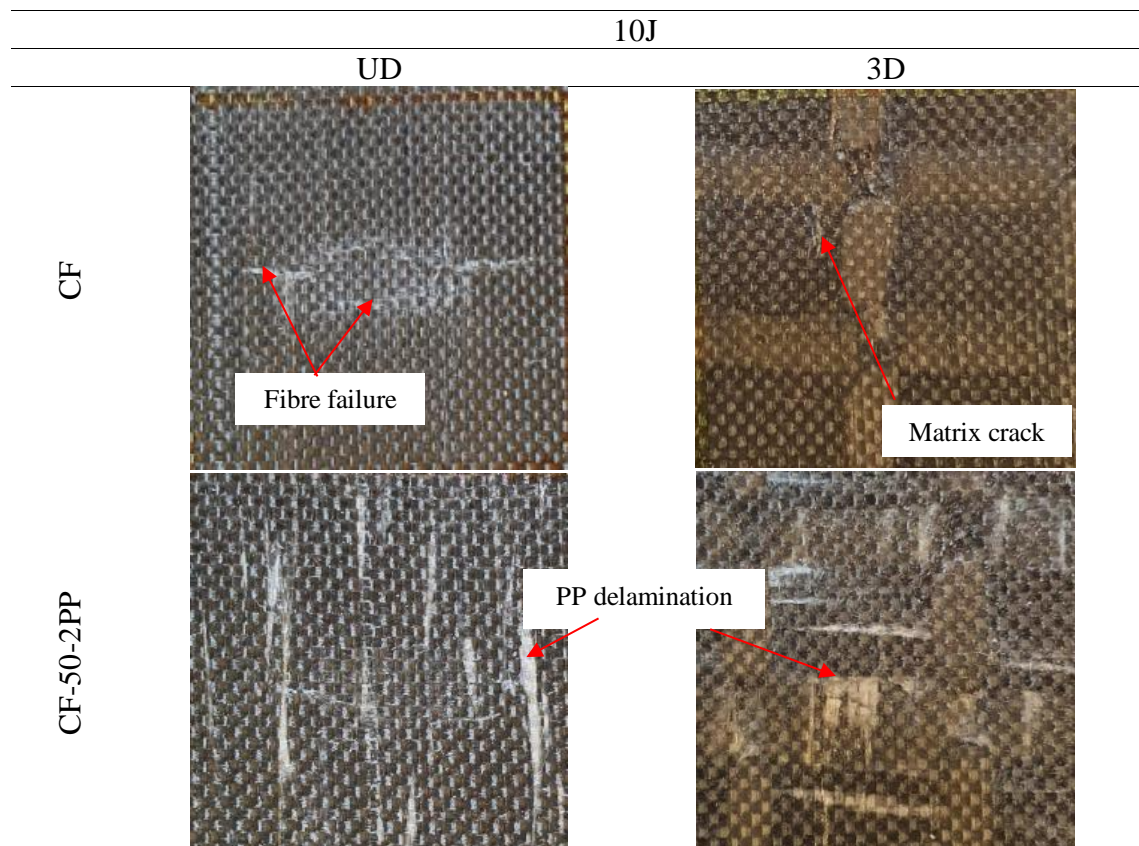


Figure 5-10 3D digital microscopy images of impact depth of UDCF and UDCF-50-2PP composites at 10J impact

Based on Figure 5-9 data, the dent depth of CF and single wrapped yarn composites are analysed by 3D digital microscopy. The dent depth by 10J and 25J energy impact was observed clearly by 3D image analysis as shown in Figure 5-10. UDCF shows deeper dent depth compared to UD single wrapped yarn composites (UDCF-50-2PP). Because composites can decline the dent depth by using a 3D structure, 3DCF shows less dent depth than UDCF. However, 3DCF have a deeper dent depth, shown as a blue colour area compared to 3DCF-50-2PP. Therefore, thermoset composites with PP wrapping yarn can diminish the dent depth with the damaged area from digital depth gauge data and 3D digital image analysis.

Figure 5-11 compares the specimen of CF and wrapped yarn composites between UD and 3D structure from the 10J and 25J impact tests. The crack and fracture of UDCF at 25J can be seen clearly. The composites fracture happens following the fibre direction at 25J. The wrapped yarn composites at UD and 3D structure commonly show the delamination of PP fibres. It can occur because of low compatibility between the epoxy resin and PP [113]. Internal damage of composites.



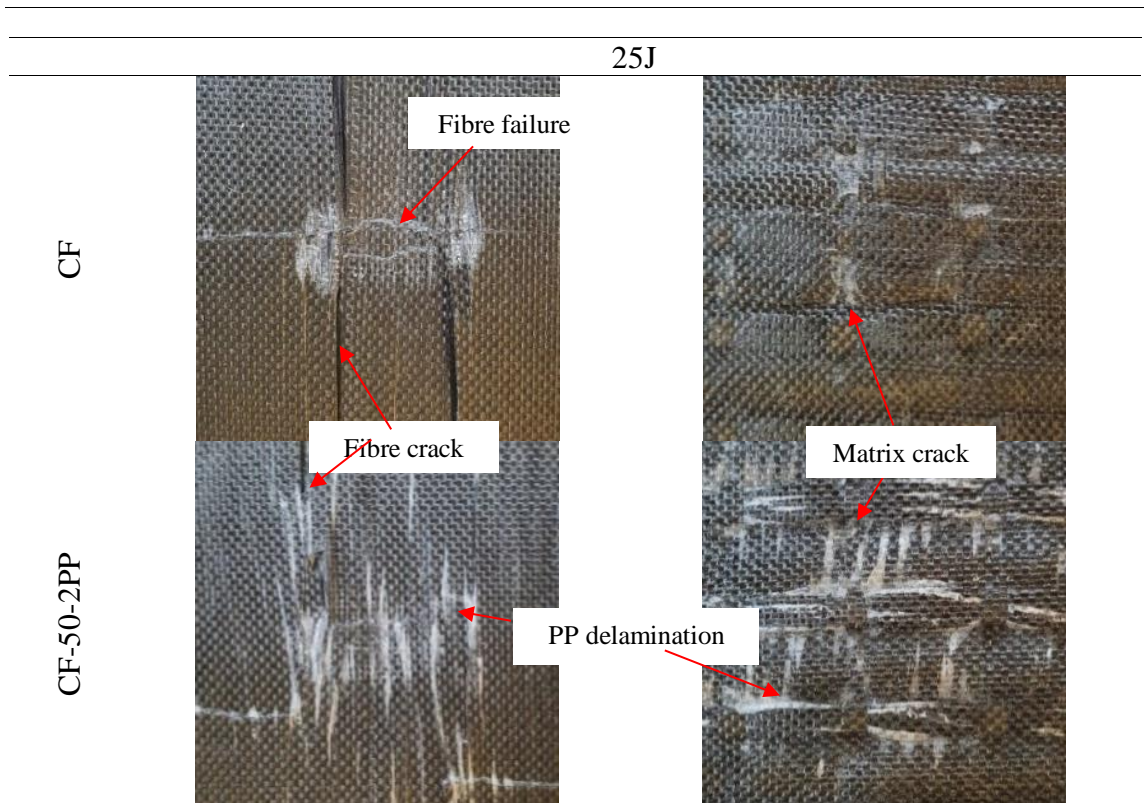


Figure 5-11 CF and wrapped yarn composite specimens after impact test at 10J and 25J energy

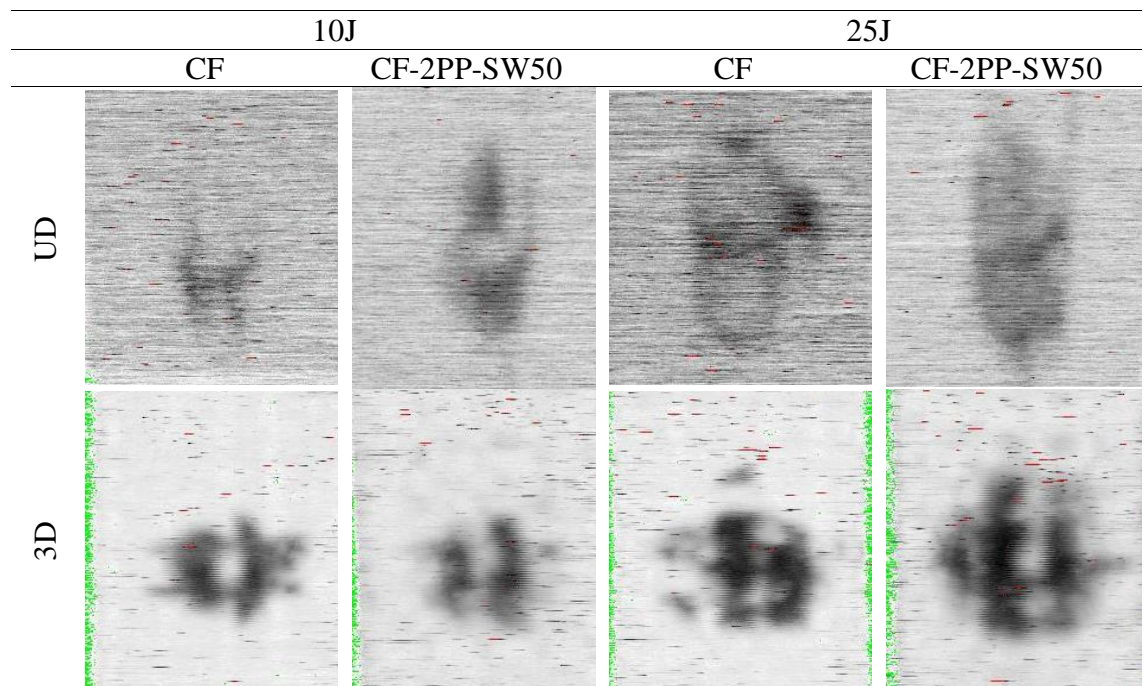


Figure 5-12 C-scan image of carbon fibre and wrapped yarn composites between UD and 3D structure at 10J and 25J

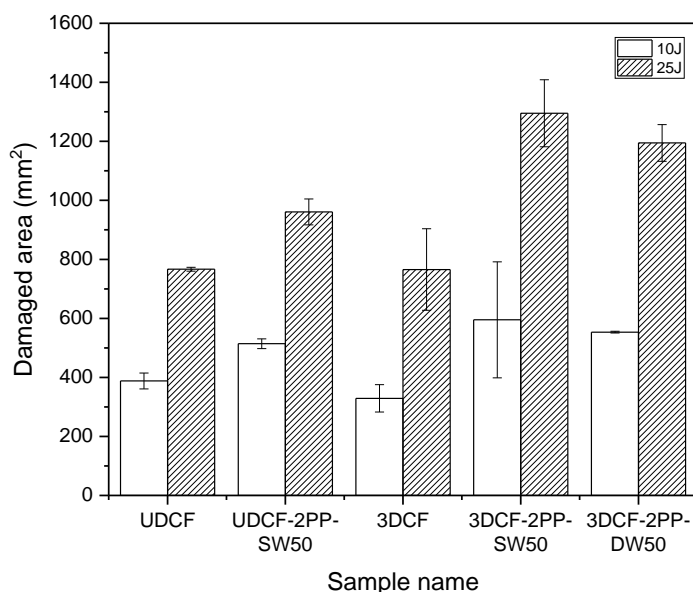


Figure 5-13 Damaged area of UD and 3D structure composites at 10J and 25J

Ultrasonic C-scan, as a non-destructive inspection technique, can analyse damaged areas of composites even inside (Figure 5-12 and 5-13). The damaged area is increased and spread by PP wrapped yarn. UDCF and UDCF-50-2PP have 388mm<sup>2</sup> and 514 mm<sup>2</sup> damaged areas at 10J and 767mm<sup>2</sup> and 961 mm<sup>2</sup> at 25J, respectively. 3D structure composites also show the same trend as UD structure composites. The damaged area analysed by C-scan is increased by wrapped yarn composites at 10J and 25J. The damaged area in the wrapped yarn composites is more expansive, and dent depth is lower than neat carbon fibre composites. Therefore, wrapped yarn composites can spread energy by PP fibre, and it helps its use after impact.

### 5.2.6.2 CAI test

The compression test is carried out after 0J, 10J and 25J impact in the composites. Figure 5-14 shows average compressive strength – impact energy curves of the CAI test for UDCF, 3DCF, UDCF-50-2PP, and 3DCF-50-2PP. The strength of UDCF is lower than UDCF-50-2PP composites. Composite stress of UDCF and UDCF-50-2PP are 197MPa and 242MPa each at 10J and 139MPa and 161MPa at 25J each. Hence, compressive strength is improved by 23% and 16% by wrapped yarn at 10J and 25J separately. 3D structure composites show lower compressive stress because layers consist of 90 (4 layers) and 0 (3 layers) degree directions. Only three layers are aligned in the same direction as



the loading direction. Because of this reason, the 3D structure shows a smaller difference between carbon fibre and wrapped yarn composites than UD (0degree, 7layers) structure composites. 3DCF-50-2PP samples show higher stress than 3DCF.

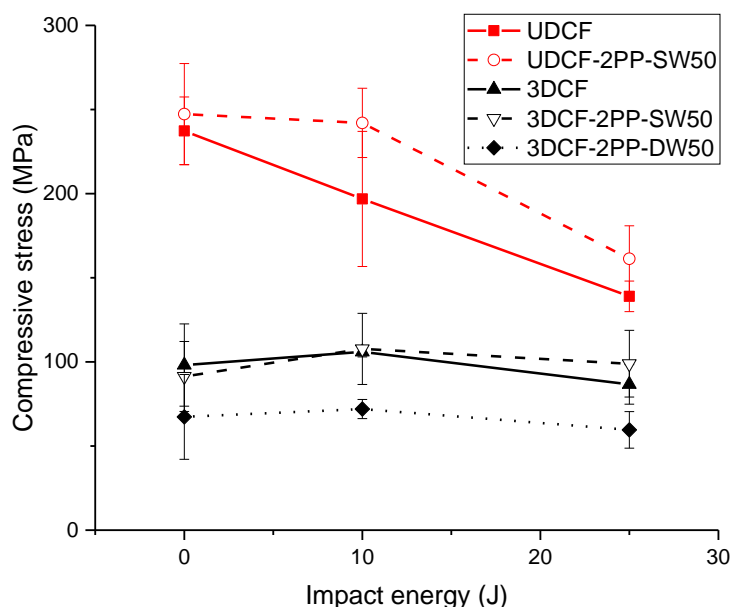


Figure 5-14 Compression strength of UDCF and UDCF-50-2PP composites at different impact energies

### 5.3 Discussion

The most obvious finding to emerge from this study was that carbon fibre (CF) thermoset composites could improve impact damage tolerance with the addition of thermoplastic fibres. In addition, the mechanical properties of the thermoset composites were enhanced through the improved distribution of the fibres. Commingled yarns and wrapped yarns were used to manufacture thermoset composites, and their impact damage tolerance was analysed using the weight drop test and CAI test. The peak force and displacement of neat CF composites afforded the highest values among the composite samples, as determined by the weight drop impact test. It is possible that these results are due to the high fibre volume fraction of neat CF composites. The absorbed energy of almost all samples tested was similar; however, commingled yarns and double-wrapped yarn composites showed a decrease. The rise in absorbed energy by the commingled yarn composites could have been affected by damage from the air nozzle during the manufacture of the hybrid yarns.

Moreover, because double-wrapped yarns include a section of overlap (see Chapter 4.4.1), composites could generate resin-rich areas that are prone to weakness.

Based on the weight drop impact test, no significant differences in the various wrapping densities were observed. However, wrapped yarn composites showed much smoother curves compared to those of CF composites. Absorbed energy was found to increase with an increasing number of PP fibres. And impact damage tolerance was decreased at 1PP and 3PP fibres. It seems that small quantities of PP fibres were not able to protect composites, while too much PP could lead to resin-rich areas, as well as a decrease in the fibre volume fraction of composites.

This study investigated the impact properties between unidimensional (UD) and 3-dimensional (3D) composites with hybrid yarn. The impact damage tolerance of 3D composites was much higher than that of UD composites, even though damaged areas of 3D composites were much wider than those of UD composites. However, because the dent depth of 3D composites was smaller than that of UD composites, 3D composites showed an increased tolerance from impact damage.

## **Chapter 6.**

### **Hybrid Composites with Higher Thermal Performance**

#### **Thermoplastic Fibres**

### **6.1 Introduction**

Fibre-reinforced thermoplastic composites have been applied in aircraft, military, and automobile industries mainly because of their high impact damage tolerance, fire resistance, and recyclability [114]. Thus, thermoplastics have been applied to thermoset composites to improve the impact damage tolerance of thermoset composites. Polyamide 6 (PA6) fibres and polyetherimide (PEI) veil are applied to high-temperature applications as they have excellent thermal stability. They are used to enhance the impact damage tolerance of carbon fibre reinforced thermoset composites in this research. Furthermore, PA6/Graphene nanocomposites fibres were also used to increase the fracture toughness of composites.

### **6.2 Results and discussion**

#### **6.2.1 PA6/Graphene hybrid wrapped yarn composites**

##### **6.2.1.1 Fibre tensile test**

The stress-strain curves of PA6 fibres at 1, 10, and 1000 mm/min loading rates are shown in Figure 6-1, and these tensile test results are summarised in Table 6-1. The tensile test results show that strength is decreased by graphene; however, elongation increases from 25.7 % to 38.5 % at 1000 mm/min loading speed. Elongation can be increased by graphite because of the high concentration of exfoliated graphite, showing more plastic behaviour [115]. Therefore, PA6/Graphene multifilament could decrease tensile strength due to the improvement of plastic properties by Graphene.

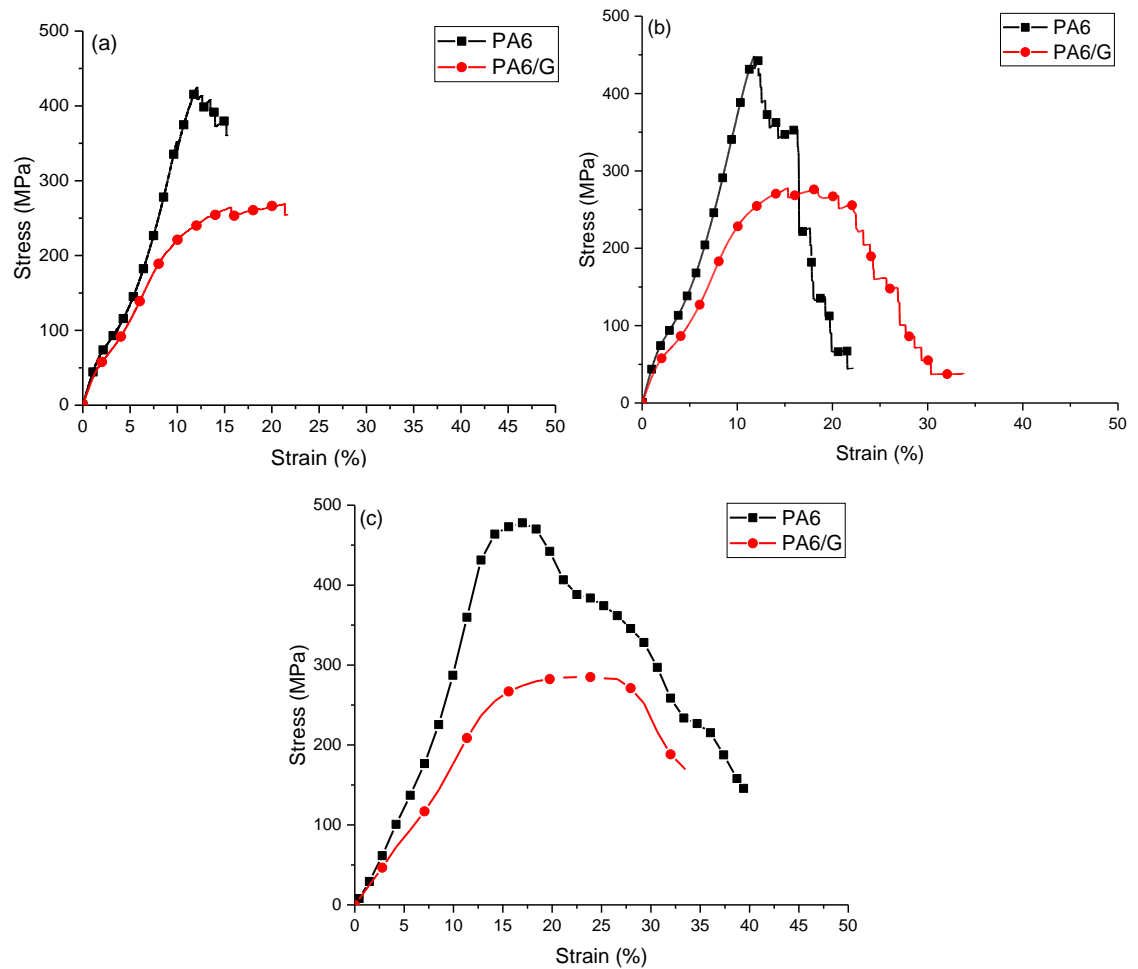


Figure 6-1 PA6 and PA6/Graphene multifilament tensile test results at (a)1 mm/min, (b)10 mm/min, (c)1000 mm/min load speed

Table 6-1 Tensile properties data for PA6 and PA6/Graphene multifilament.

Loading speed (mm/min)	Tensile modulus (GPa)			Peak stress (MPa)			Strain failure (%)		
	1	10	1000	1	10	1000	1	10	1000
PA6	4.5 ±0.2	4.5 ±0.4	4.8 ±0.4	428.3 ±46.8	449.3 ±24.2	490.8 ±39.6	12.0 ±1.6	12.7 ±0.9	14.5 ±1.8
PA6/G	3.8 ±0.1	3.7 ±0.2	2.4 ±0.1	264.5 ±16.2	280.0 ±12.3	282.5 ±14.9	14.7 ±2.5	16.5 ±4.6	18.9 ±3.2

### 6.2.1.2 Drop-weight impact test

The impact behaviour of UD structure CF composites and PA6 wrapped yarn composites were analysed at 10J and 25J. Figure 6-2 presents the impact behaviours of CF/PA6 composites, and the calculated impact properties are summarised in Table 6-2. The UDCF-1PA6-SW50 composite showed a higher peak load (4710 N) with respect to UDCF composites (4574 N) at 10J impact energy, as shown in Figure 6-2a. At the 25J energy impact test, the peak load of PA6 composites and PA6/G composites also increased by 21% and 19% each than neat CF composites (Figure 6-2b). However, no significant differences in absorbed energy and recovered energy were found between composite samples (Figure 6-2e, f). And all samples appear almost open curves at force-displacement graphs at the 25J energy impact test, unlike the 10J energy impact test (Figure 6-2c, d). The open curves can be observed when the specimen is internally damaged and fully penetrated by impact energy. The endpoint of the displacement value of an open curve does not return to zero on the graphs, unlike the closed curve.

Table 6-2 Summary of dynamic impact parameters of CF, PA6, PA6/Graphene wrapped yarn composites at 10J and 25J impact energy

	Sample	Peak force (N)	Peak displacement (mm)	Residual displacement (mm)	Absorbed energy (J)	Recovered energy (J)
10J	UDCF	4573.9 ±93.7	3.8±0.1	0.4±0.1	5.2±0.1	4.7±0.1
	UDCF-1PA6-SW50	4709.6 ±81.2	3.6±0.1	0.5±0.0	5.3±0.2	4.7±0.2
	UDCF-1PA6/G-SW50	4666.7 ±104.9	3.6±0.1	0.4±0.2	5.3±0.2	4.7±0.2
25J	UDCF	5035.7 ±315.8	7.6±0.8	2.5±1.5	22.1±1.0	2.7±1.0
	UDCF-1PA6-SW50	6070.8 ±192.6	6.9±0.3	2.1±0.4	21.3±0.9	3.4±0.8
	UDCF-1PA6/G-SW50	5970.5 ±203.4	7.9±0.7	3.2±0.8	23.2±0.3	2.2±0.4

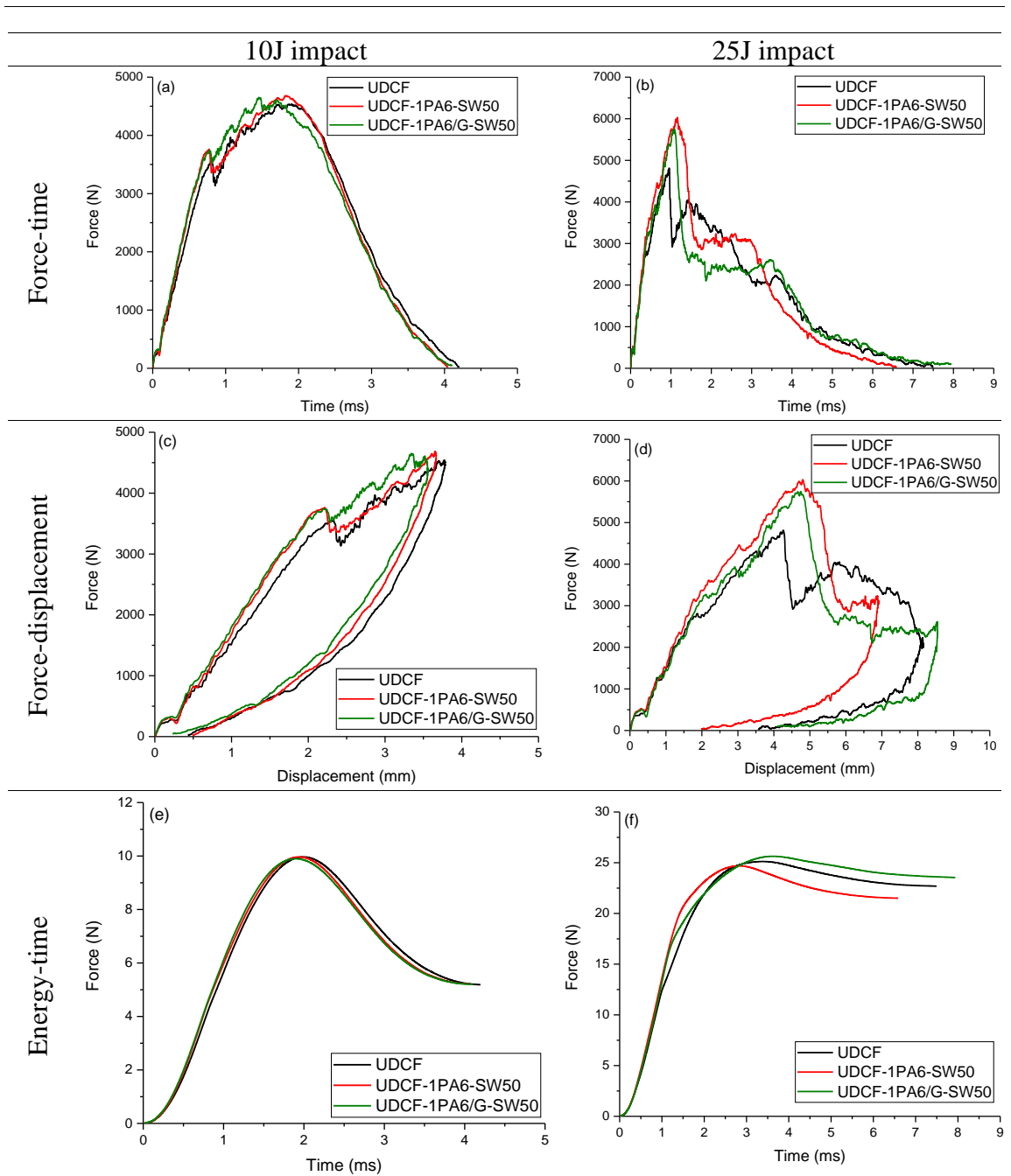


Figure 6-2 Force-time, force-displacement, and force-displacement curves of PA6 and PA6/G wrapped yarn composites at (a), (c), (e) 10J and (b), (c), (f) 25J impact test

### 6.2.1.3 Damaged area

Figure 6-3 shows the damaged area image of PA6 and PA6/G composites on C-scan analysis after the 10J and 25J impact tests. Graphene decreased the damaged area, but the dent depth of CF/PA6G composites was deeper than CF/PA6 composites. PA6/Graphene composites show decreased damaged area. However, the dent depth of PA6/Graphene

composites was 0.02 mm and 0.55 mm deeper than UD structure non-graphene PA6 composites at 10J and 25J impact energy tests, respectively (Figure 6-4.a). Damages were generated along the fibre direction after the impact test.

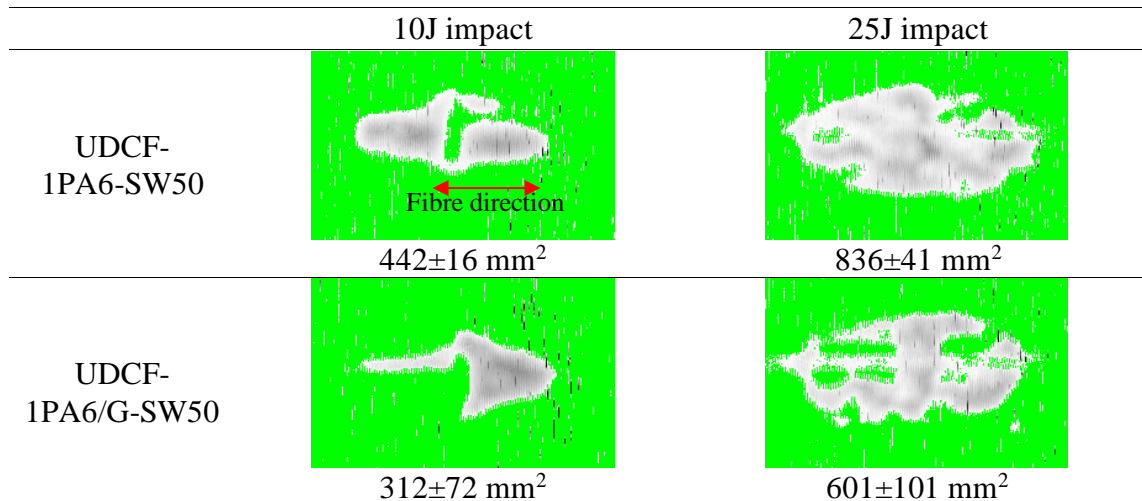


Figure 6-3 C-scan image of UD structure PA6 and PA6/Graphene wrapped yarn composites at 10J and 25J

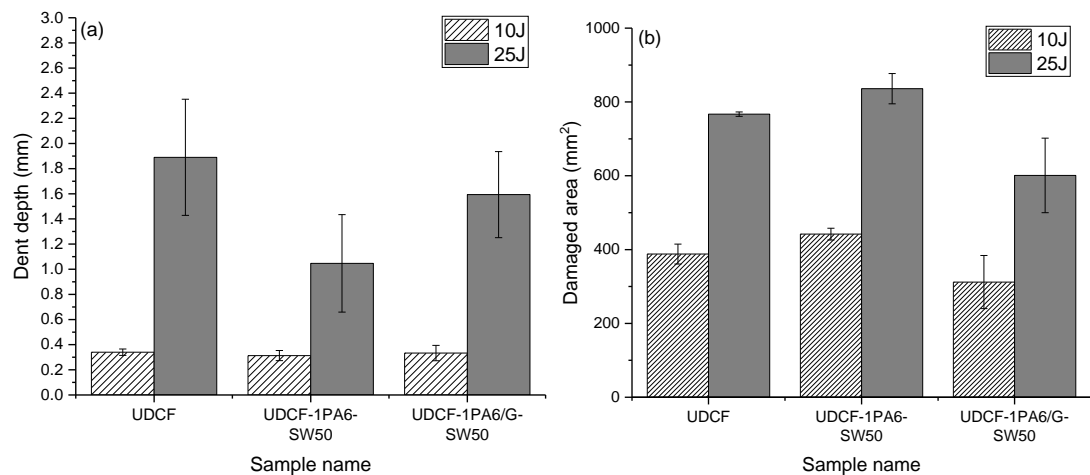


Figure 6-4 (a) Dent depth and (b) damaged are after drop weight impact test of UD structure CF/polyamide 6 hybrid yarn composites

#### 6.2.1.4 Compression after impact test

The compressive strength of PA6 wrapped yarn composites after impact displayed the highest value. The compressive stress of UDCF-1PA6-SW50 and UDCF-1PA6/G-SW50 composites increased by 8.6%, and 3.6% at 10J and 15.1%, and 5.9% at 25J compared

to UDCF composites (Figure 6-5). Composite fractures during the test were generated near the impact area, as shown in Figure 6-6.

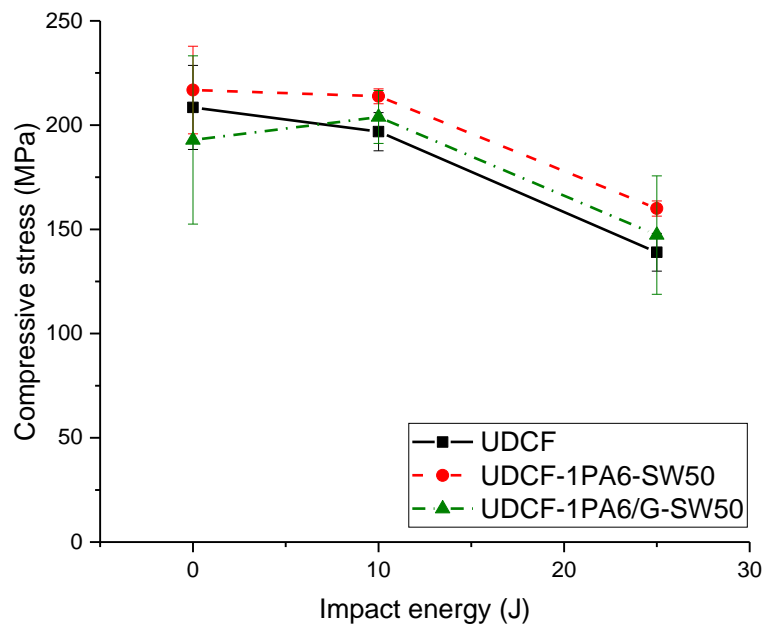


Figure 6-5 Compression strength of UDCF, UDCF-1PA6-SW50, and UDCF-1PA6/G-SW50 composites at different impact energies

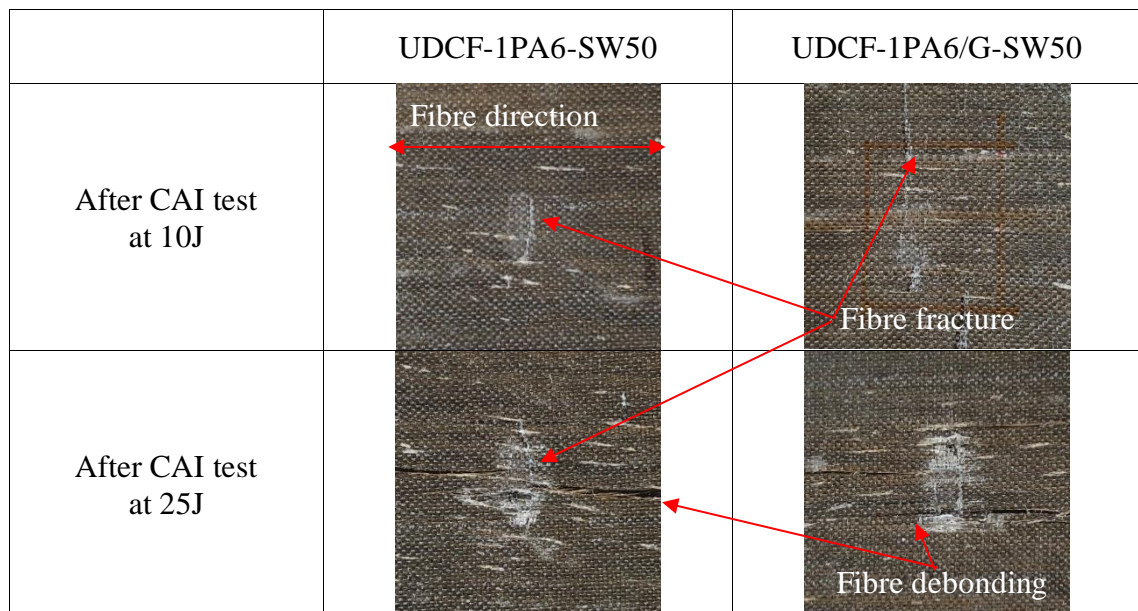


Figure 6-6 3D digital microscopy images of UDCF, UDCF-1PA6-SW50, and UDCF-1PA6/G-SW50 composites at 10J impact and external surface after CAI test at 10J and 25J



## 6.2.2 CF/PEI thermoset composites

### 6.2.2.1 PEI veil tensile test

General stress-strain curves of 10 mm width PEI veils at 1, 10, and 1000 mm/min loading rate are shown in Figure 6-7, and initial modulus, strain at fracture and maximum stress are summarised in Table 6-3. The ultimate tensile strength values of the PEI veil are 4.1 MPa, 8.4 MPa, and 8.7 MPa, separately. Young's moduli of PEI veil at 1, 10 and 1000 mm/min are 0.09 GPa, 0.13 GPa and 0.03 GPa, respectively.

Table 6-3 Tensile properties of thermoplastic fibres and veils at 1, 10, 1000mm/min loading speed

Loading speed (mm/min)	Tensile modulus (GPa)			Peak stress (MPa)			Strain failure (%)		
	1	10	1000	1	10	1000	1	10	1000
PEI veil	0.9 ±0.2	1.3 ±0.2	0.9 ±0.1	40.6 ±8.5	83.8 ±11.3	86.9 ±11.0	-	42.1 ±4.0	41.7 ±1.9

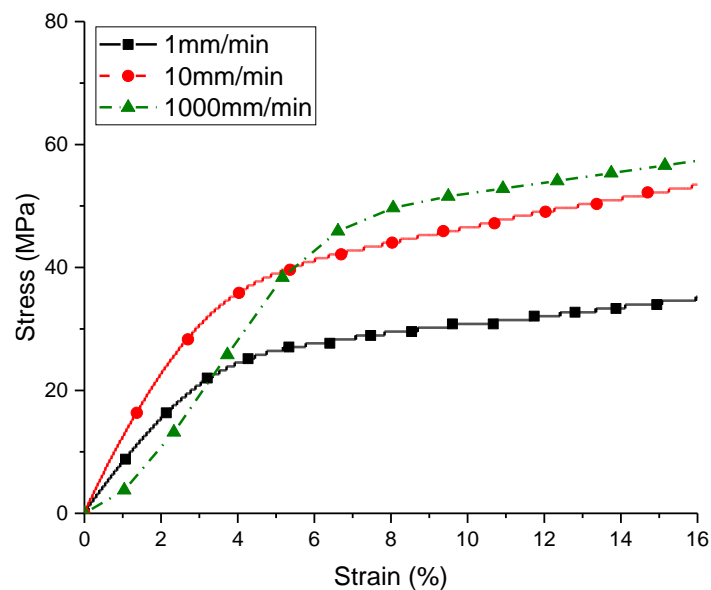


Figure 6-7 PEI veil tensile test at 1, 10, 1000mm/min load speed

### 6.2.2.2 UD structure composites

The laminates response to impact is presented as force-time curves, force-displacement curves, and energy-time curves, as shown in Figure 6-8. These test results are summarised in Table 6-4. The sudden load drop areas are shown at the beginning of the impact (point

A), as shown in figure 6-8a, b. Point A, which is called Hertzian failure, means initial damage such as interlaminar delamination in the composites [116]–[118]. In addition, load oscillations are exhibited as the impact continues (point B). This phenomenon could be caused by damages by impact expansion. The load was decreased suddenly after reaching the peak force (point C). The energy versus time curves provides absorbed and rebounded energy by impact test (Figure 6-8e, and f). The energy-time graphs can be divided into three zones (A-C), as shown in Figure 6-8.e and f. Zone A showed low-level energy because of small dent and deformation generated between impactor and specimen incipiently. And then, the energy is increased (zone B) because of the increased contact area. Zone C showed rebound energy or absorbed energy value [119]. Lastly, force versus displacement graphs provided deformation displacement by energy impact. UDCF-PEI-10 composites showed the lowest peak displacement at both 10J and 25J energy. On the other hand, UDCF composites depicted the highest peak displacement. Thus, CF and PEI hybrid composites exhibit closed curves.

Table 6-4 Summary of dynamic impact parameters of CF and PEI veil hybrid UD composites at 10J and 25J impact energy

	Sample	Peak force (N)	Peak displacement (mm)	Residual displacement (mm)	Absorbed energy (J)	Recovered energy (J)
10J	UDCF	4573.9 ±93.7	3.8±0.1	0.4±0.1	5.2±0.1	4.7±0.1
	UDCF-PEI-10	5433.7 ±310.1	3.3±0.1	0.4±0.0	4.7±0.2	5.2±0.2
	UDCF-PEI-20	5021.8 ±324.1	3.4±0.0	0.4±0.1	5.3±0.3	4.7±0.3
25J	UDCF	5035.7 ±315.8	7.6±0.8	2.5±1.5	22.1±1.0	2.7±1.0
	UDCF-PEI-10	8151.2 ±88.1	5.2±0.2	1.0±0.2	16.3±0.4	9.7±0.3
	UDCF-PEI-20	6632.2 ±129.2	6.4±0.3	1.6±0.3	20.8±2.1	5.5±2.1

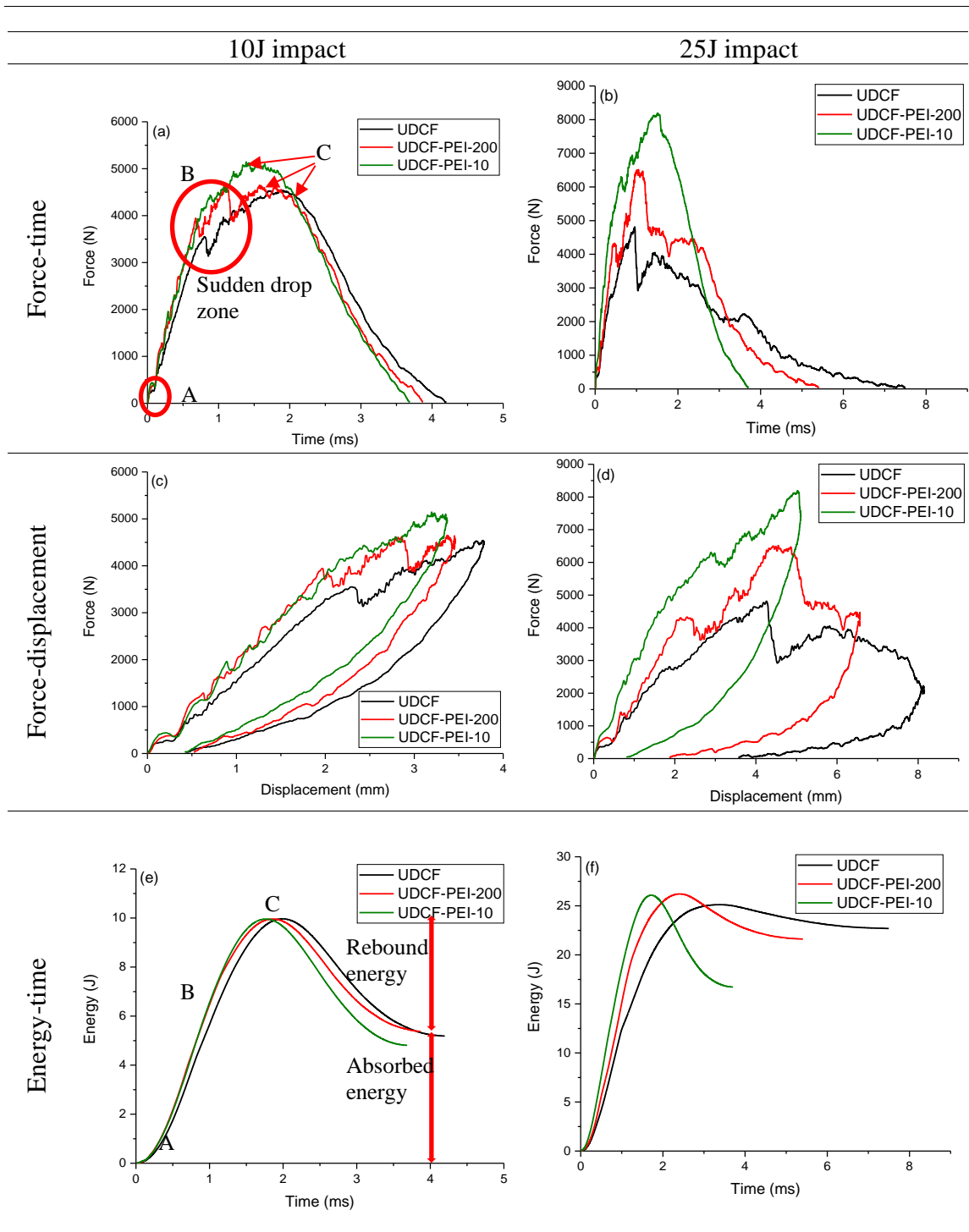


Figure 6-8 Force-time, force-displacement, and force-displacement curves of CF/PEI hybrid composites at (a), (c), (e) 10J and (b), (d), (f) 25J impact test

Figure 6-9 shows the damaged area of UD structure CF/PEI hybrid composites measured by ultrasonic C-scan for the composites. The damaged area of UD structure composites

follows the fibre direction. Dent depth and damaged area were decreased by PEI veils (Figure 6-10).

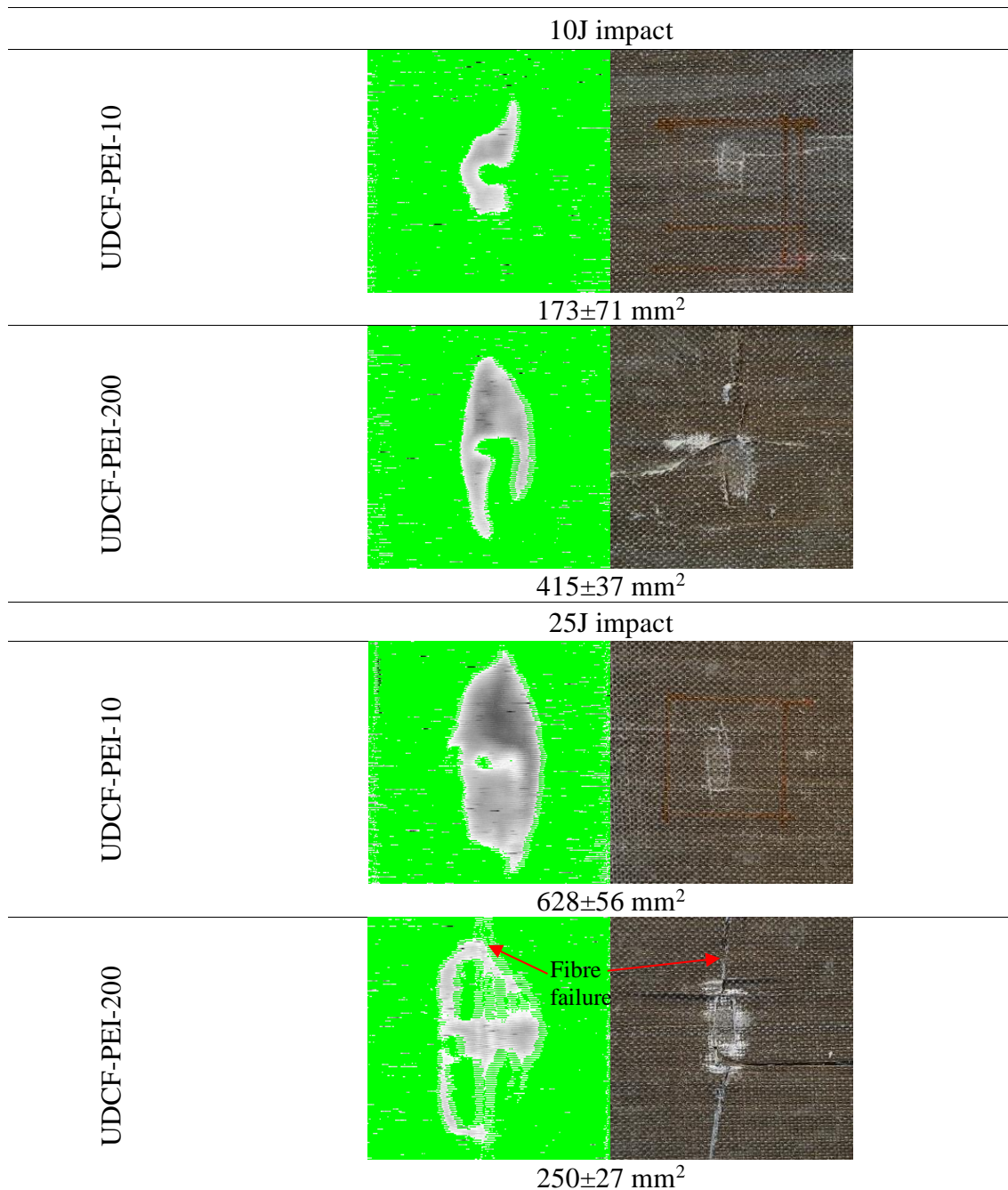


Figure 6-9 Typical c-scan images of UDCF-Tape-PEI and UDCF-Film-PEI composites for UD structure at 10J and 25J

The dent depth of UDCF-PEI-10 composites presents less dent depth than UDCF-PEI-200. It was measured by a digital depth gauge (Figure 6-10.a) and a 3D digital microscope (Figure 6-11), and they show the same results. The damaged area of UDCF- PEI-10 and

UDCF-PEI-200 were more decreased by 55%, and increased by 107% at 10J energy impact respectively and decreased by 18% and 67% respectively at the 25J energy impact test compared to UDCF composites.

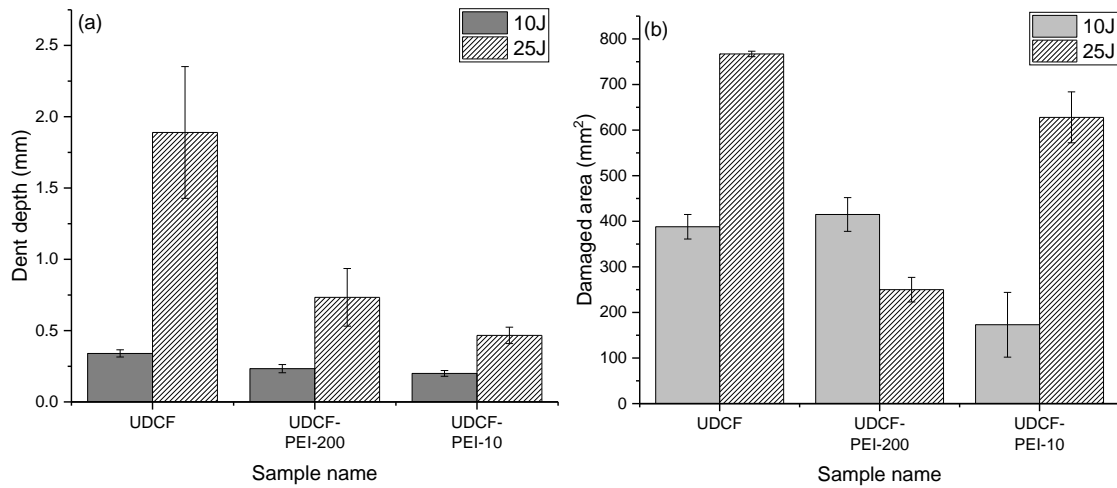


Figure 6-10 (a) Dent depth and (b) damaged area of UD structure PEI composites after 10J and 25J impact test

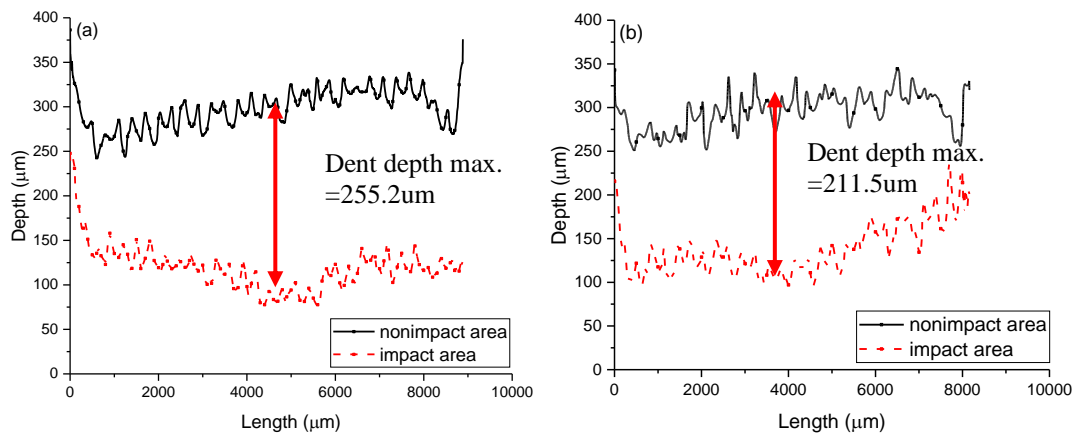


Figure 6-11 Dent depth of (a) UDCF- PEI-200 and (b) UDCF-PEI-10 composites at 10J energy impact. CF and PEI hybridisation epoxy composites did not improve compressive strength. The main problem can be PEI binder material. The binder of the PEI veil is polyester which is not compatible with epoxy resin. In the compression test, especially, UDCF-PEI-200 composites showed much lower strength than UDCF composites, and the UDCF-PEI-10 composites present similar strength with UDCF composites (Figure 6-12).

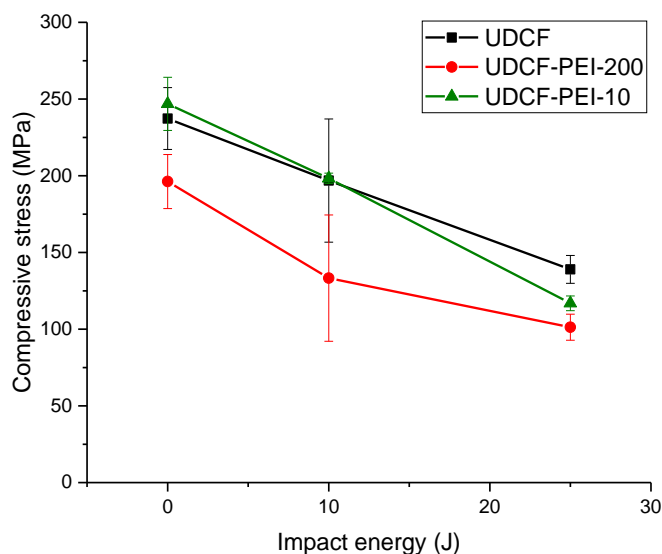


Figure 6-12 Compression strength of UDCF, UDCF-PEI-10, and UDCF-PEI-200 composites at different impact energy

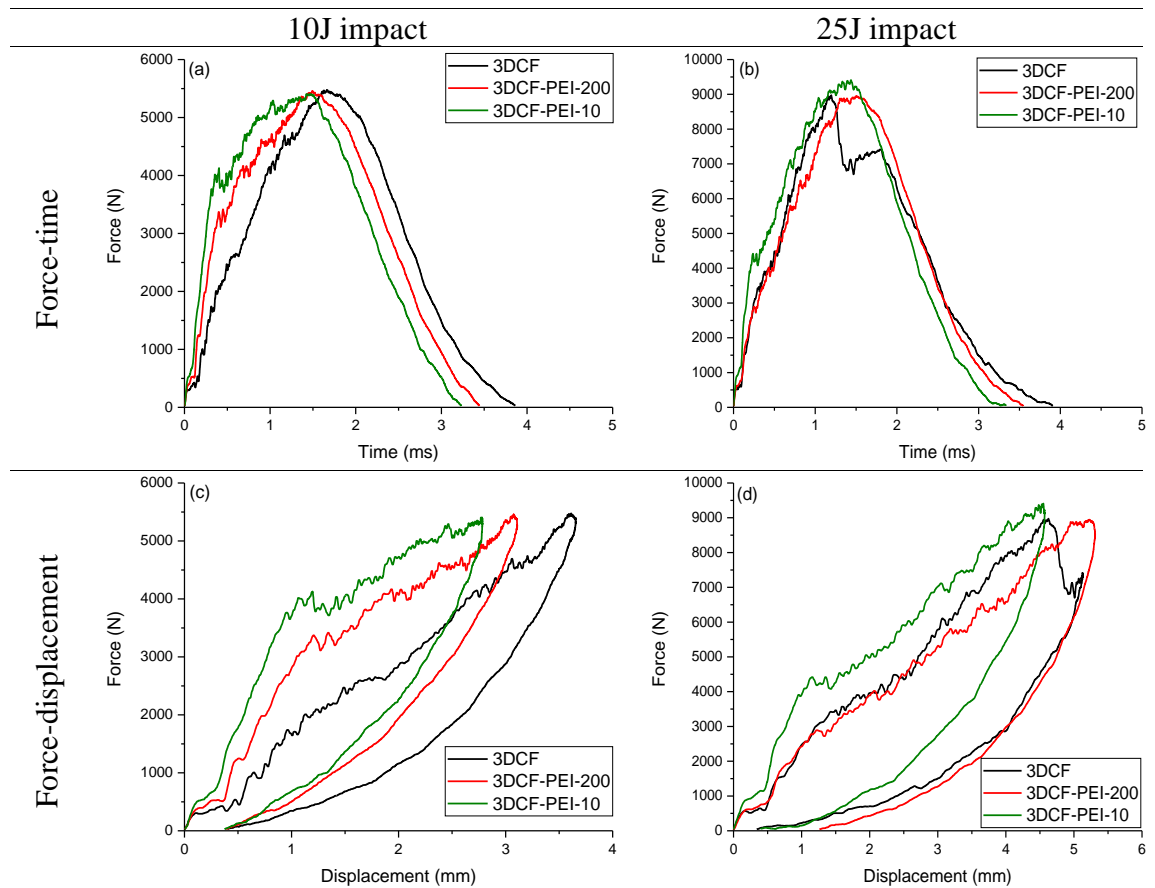
### 6.2.2.3 3D structure composites

The response of laminates to impact is presented as force-time curves, force-displacement curves, and energy-time curves, as shown in Figure 6-13. These test results are summarised in Table 6-5. The force of 3DCF, 3DCF-PEI-10, and 3DCF-PEI-200 were almost reached up to 5.5 kN, 5.5 kN, and 5.4 kN at 10J and 9.1 kN, 9.6 kN, and 8.7 kN at 25J, respectively. The 3D structure of neat CF composites would have been seriously damaged at 25 J impact energy, as the force is clearly reduced compared to the CF/PEI hybrid composite samples in Figure 6-13.b.

The energy versus time curves provides absorbed and rebounded energy by impact test as shown in Figure 6-13. e and f. The rebound energy of all samples is depicted clearly at both 10J and 25J energy impacts. The energy-time curves demonstrated similar curves at 10J and 25J, which is different from UD structure composites. Lastly, force versus displacement graphs provided deformation displacement by energy impact. 3DCF showed the high peak displacement, 3.6 mm, and 5.1 mm at 10J and 25J energy, respectively. On the other hand, 3DCF-PEI-10 composites depicted the lowest peak displacement, 2.8 mm and 4.6 mm, at the 10J and 25J energy impact tests. The recovered energy of CF/PEI composites was less than 3DCF composites at 10J energy impact (Table 6-5).

Table 6-5 Summary of impact dynamic parameters of CF and PEI veil hybrid 3D composites at 10J and 25J impact energy

	Sample	Peak force (N)	Peak displacement (mm)	Residual displacement (mm)	Absorbed energy (J)	Recovered energy (J)
10J	3DCF	5524.0±64.8	3.6±0.1	0.5±0.1	4.7±0.1	5.3±0.1
	3DCF-PEI-10	5521.1±114.6	2.8±0.0	0.4±0.0	5.6±0.0	4.3±0.0
	3DCF-PEI-200	5447.8±123.1	3.2±0.1	0.4±0.0	5.2±0.3	4.8±0.3
25J	3DCF	9171.8±279.7	5.1±0.0	0.6±0.3	14.5±1.6	9.0±2.5
	3DCF-PEI-10	9553.5±151.8	4.6±0.1	0.6±0.2	14.8±0.4	10.2±0.4
	3DCF-PEI-200	8708.1±767.3	5.3±0.1	1.2±0.2	16.1±1.2	9.3±1.3



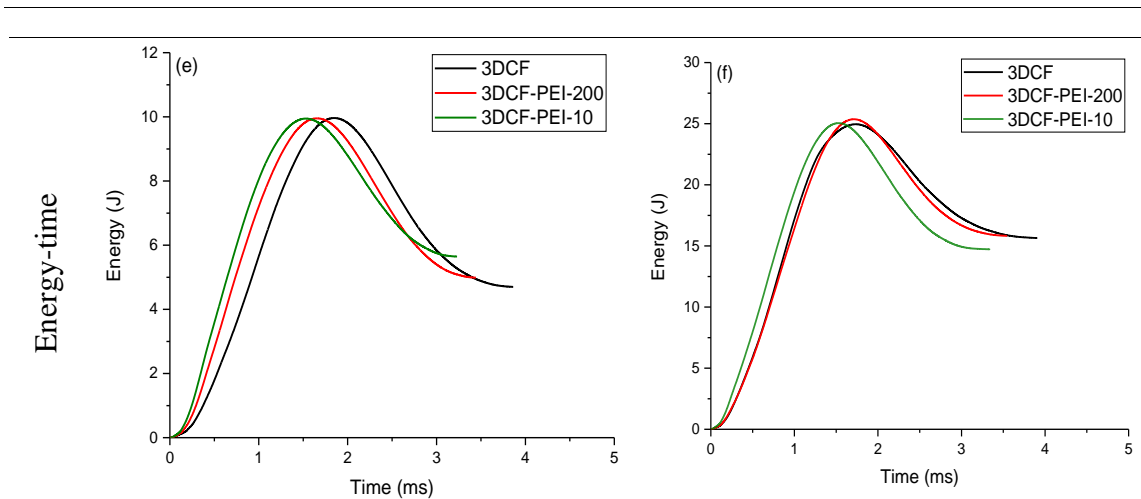


Figure 6-13 Force-time, force-displacement and energy-time curves of 10mm and 200 width PEI veil composites at 10J and 25J

Figure 6-14 shows the damaged area measured by ultrasonic C-scan for the composites. The damaged area of 3D structure composites showed a round shape, unlike UD structure composites. The CF/PEI hybridisation composites could decrease the dent depth in the composites compared to neat 3DCF composites, as shown in Figure 6-15.a.

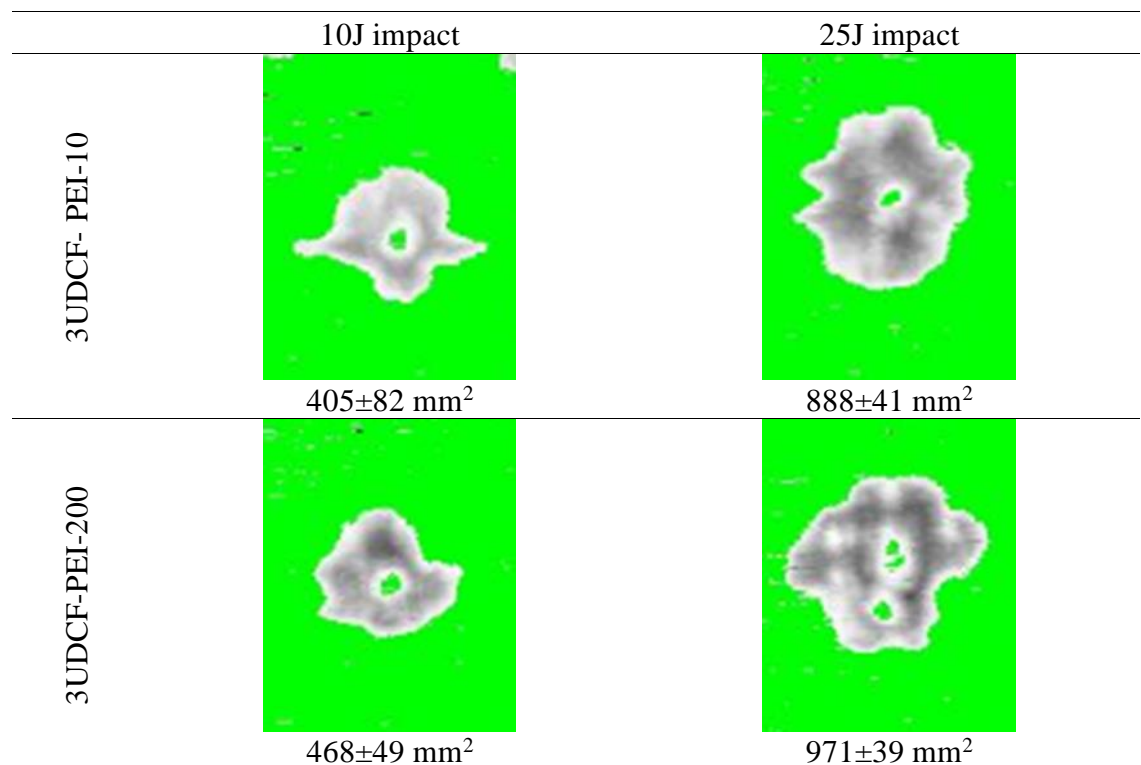


Figure 6-14 C-scan image of 3DCF-Tape-PEI and 3DCF-Film-PEI composites for 3D structure at 10J and 25J



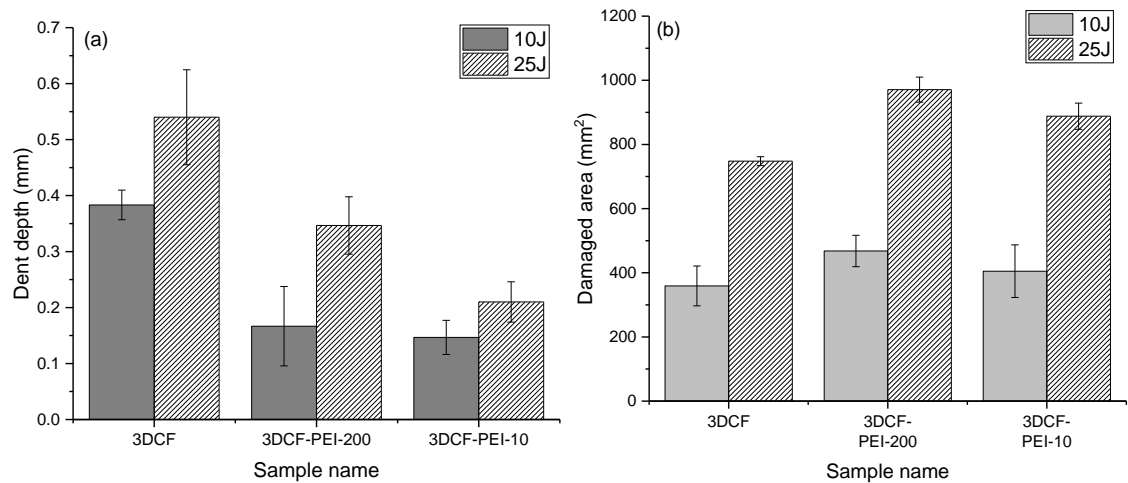


Figure 6-15 (a) Dent depth and (b) damaged area of 3D structure PEI composites after 10J and 25J impact test

On the other hand, the damaged area of 3DCF-PEI-10 and 3DCF-PEI-200 at 10J energy impact was increased by 13% and 30% separately than 3DCF composites. At the 25J energy impact test, the damaged area of tape type and film type was also increased by 19% and 30% each (Figure 6-15.b). The damaged area of 3DCF-PEI-10 is smaller than that of 3DCF-PEI-200 in Figure 6-15. b. A possible explanation for this could be that the impact energy might be able to spread more easily on the film type of PEI in comparison to the tape type of PEI.

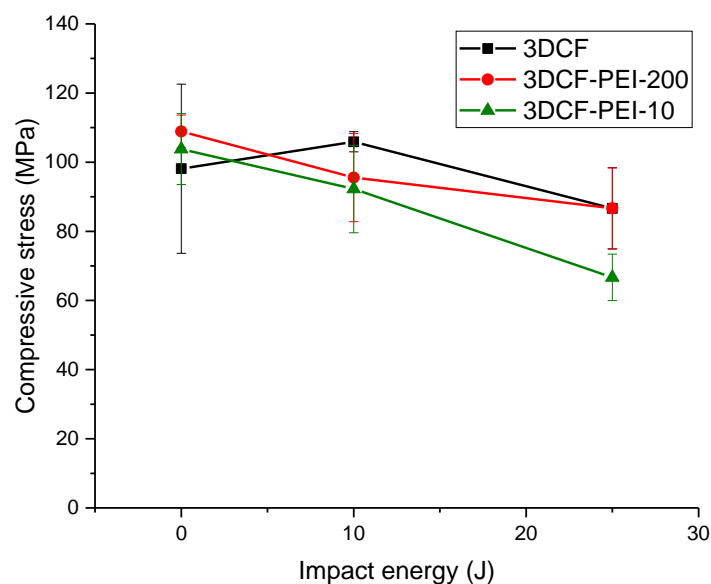


Figure 6-16 Compression strength of 3DCF, 3DCF-PEI-10, and 3DCF-PEI-200 composites at different impact energy

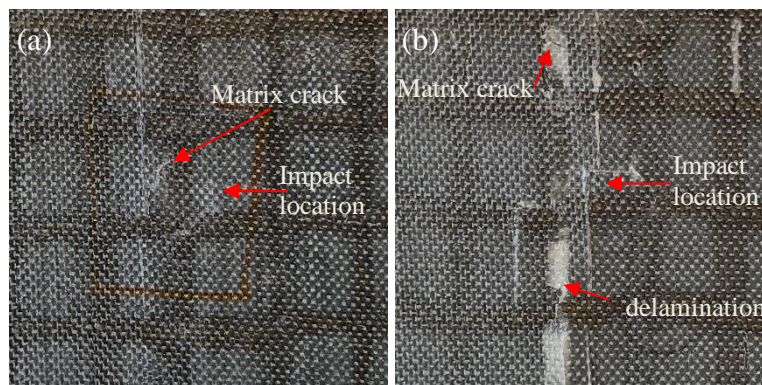


Figure 6-17 Damaged area of 3D structure composites after CAI test with 10J impact energy; (a) 3DCF-PEI-10, and (b) 3DCF-PEI-200

CF and PEI hybridisation epoxy composites showed the deteriorated composites strength through the CAI test (Figure 6-17). The 3DCF-PEI-200 showed lower strength than UDCF composites, and the 3DCF-PEI-10 showed similar strength to UDCF composites. Figure 6-17 shows damaged 3DCF-PEI-10 and 3DCF-PEI-200 composites after the CAI test. The 3DCF-PEI-10 composites showed more serious damage, such as fibre and resin cracks and delamination.

### 6.3 Discussion

The impact damage tolerance of carbon-fibre thermoset composites was improved by PA6 and PA6/graphene nanocomposite fibres. Hybrid CF/PA6 multifilament composites showed increased impact damage tolerance compared to that of hybrid CF/PA6G composites. PA6 hybrid yarn composites demonstrated the highest peak force and rebound energy compared to that of neat CF and PA6/graphene hybrid yarn composites. The most interesting finding in this study was that the impact damage area decreased with graphene nanocomposite fibres. A possible explanation for these results could be that the impact dispersion capability of the graphene nanocomposite fibres was diminished. Thus, while a decrease in the damaged area was observed, dent depth was increased compared to that of neat PA6 hybrid yarn composites.

The damaged area of the composites with a 10 mm wide PEI veil was smaller than that of the hybrid composites with a 200 mm PEI veil. The 10 mm PEI veil showed increased impact resistance compared to that of neat CF composites; however, impact damage tolerance was not improved by PEI hybridisation. The likely reason for this observation

is that the 10 mm wide hybridisation process resulted in thicker preforms, as well as decreased the fibre volume fraction. On the other hand, the impact damage tolerance of CF/PEI hybrid composites showed no improvement compared to that of neat CF composites. Moreover, the 200 mm wide PEI veil showed lower compressive strength than that of the 10 mm PEI veil. A possible explanation for this could be that the PEI binder polyester material decreased the interface force between PEI veils and epoxy resin, such that these veils were inserted between every CF layer.

## **Chapter 7.**

# **Study of Impact Damage Tolerance with Micro-wrapped Carbon Fibres and Polypropylene/Graphene Nanocomposite Fibres**

### **7.1 Introduction**

Fibre-reinforced polymer (FRP) composites have been widely used in the aircraft and automobile industry for their structure because they show superior strength and stiffness properties at low density compared to their metallic parts. Besides, because it is possible to manufacture any shape and size of parts with thermoset resins, which are commonly used in the industry, FRP composite research is getting more critical.

Cost-effective manufacturing methods of thermoset composites are resin infusion (RI), resin transfer moulding (RTM), and vacuum-assisted resin transfer moulding (VARTM) [93]. Instead of two mould tools, the VARTM method uses one side part of the mould tool with a membrane press [93]. However, because thermoset composites are brittle due to high crosslink density, the low damage tolerance of thermoset composites has become an important research topic [35], [93], [120]. Furthermore, as impact damage causes fibre breakage, delamination, and matrix cracking in the composites, the mechanical properties of composites are significantly affected [93]. Therefore, to enhance the post-impact performance of thermoset composites, thermoplastics are used to manufacture thermoset composites because thermoplastic composites show better delamination and less matrix cracking than thermoset composites [120], [121]. There are ways of thermoplastic interleavings, such as co-mingled fibres [8], nanoparticles [10], veils [11], and films [12]. This study chooses polypropylene (PP) fibres to improve impact damage tolerance because PP fibres are a high toughness material, have useful damage tolerance, easy modification in composites, cost-effective and recyclability [122], [123]. Furthermore, Graphene can be incorporated into the PP to improve the mechanical, electrical, and thermal properties of the fibres through the melt extrusion processes because Graphene presents high Young's modulus ( $\sim 1100\text{GPa}$ ), high fracture strength ( $\sim 125\text{GPa}$ ), and

---

superior electrical and thermal conductivity [124]. Even a tiny amount of Graphene can significantly improve mechanical properties in nanocomposite fibres [125]. Wang et al. (2020) determined that the tensile strength and modulus of PP/0.1 wt% GNP fibres are 179.3MPa and 8.05 GPa, 1.6 times and 1.7 times higher than neat PP fibres, respectively [126].

In this study, the required manufacturing processes, such as fibre drawing, splitting and wrapping, are developed and set up. First, the mechanical properties of the extruded PP/Graphene fibres are increased through the drawing process, and then these PP/Graphene fibres wrap carbon fibres to produce hybrid wrapped yarns. Finally, the 3K carbon fibres are split on the lab-scale set-up and used to make wrapped yarn with micro PP/Graphene fibres. These hybrid microfibres wrapped yarns are expected to improve the impact damage tolerance of thermoset composites by enhancing PP fibre distribution in hybrid yarns and their mechanical properties.




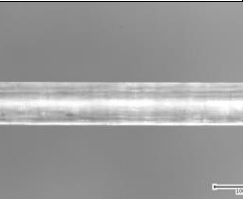
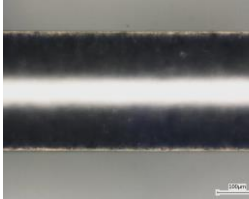


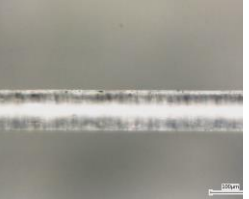
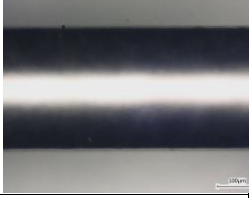
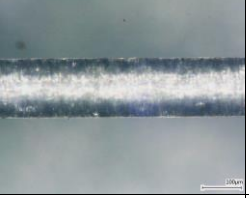
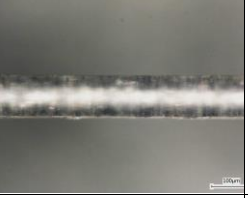
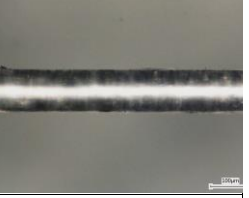
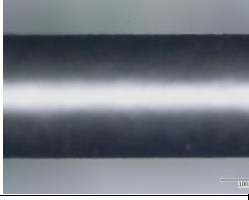

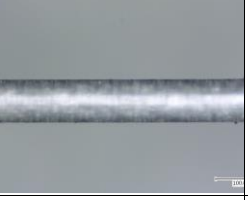
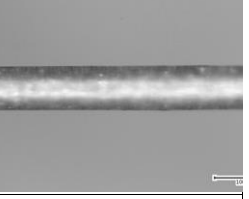
Tensile tests of PP/Graphene (0wt%, 0.25wt%, 0.5wt%, and 1wt%) mono fibres are performed at 10mm/min and 1000 mm/min loading speed each. The mechanical properties of composites are evaluated by tensile test, short beam shear test (SBS), drop weight test, and compression after impact (CAI) test. Damaged areas of specimens after impact are analysed by ultrasonic C-Scan, and the dent depth is measured by a digital depth indicator gauge.

## **7.2 Results and discussion**

### **7.2.1 Dimension of PP/Graphene fibres**

The diameter of the PP/Graphene fibres by 0-3 times the drawing process was observed by optical microscope, and they are illustrated in Table 7-1. The fibre diameter decreased with increasing fibre drawing frequency. However, the diameter of fibres is similar after the two-time drawing. The diameter of neat PP fibre and PP/G1.0 fibre after the first drawing decreased 60% and 57% compared to undrawn fibres. They were then reduced by 4% and 6% more each after the second fibre drawing. The PPG 0.25 and PPG0.5 fibres also experienced the most stretching in the first drawing, as shown in Table 6-5.

Table 7-1 Optical microscope images and fibre diameters of the undrawn and drawn PP/Graphene fibres

	Extruded fibre	1 <sup>st</sup> fibre drawing	2 <sup>nd</sup> fibre drawing	3 <sup>rd</sup> fibre drawing
PP				
	296±23 µm	119±7 µm	107±12 µm	104±6 µm
	58±1.4 Tex	13±0.8 Tex	10.2±0.3 Tex	7±0.1 Tex
PPG0.25				
	287±40 µm	118±6 µm	115±5 µm	105±4 µm
	76±7.3 Tex	12±0.6 Tex	9±0.2 Tex	9±0.1 Tex
PPG0.5				
	326±10 µm	145±8 µm	125±10 µm	120±8 µm
	75±3.2 Tex	15±0.1 Tex	11±0.9 Tex	10±0.4 Tex
PPG1.0				
	320±11 µm	138±5 µm	117±1 µm	114±4 µm
	60±2.8 Tex	11±0.7 Tex	9±0.2 Tex	7±0.6 Tex

### 7.2.2 Fibre tensile test

PP/Graphene single fibre tensile tests were performed separately at 10mm/min and 1000mm/min loading rates. Testing results from stress-strain curves are summarised in Table 7-2, and typical stress-strain curves of single fibres at different drawing repeats (drawing frequencies) are presented in Figures 7-1 (crosshead speed 10 mm/min) and 7-2 (crosshead speed 1000 mm/min loading rate).

Table 7-2 Tensile properties of polypropylene/graphene fibres at the different loading speed

Fibre name	Drawing frequency	10 mm/min loading speed			1000 mm/min loading speed		
		Peak stress (MPa)	Failure strain (%)	Modulus (GPa)	Peak stress (MPa)	Failure strain (%)	Modulus (GPa)
PP	0	28.9 (± 4.8)	1403.2 (± 255.2)	1.0 (± 0.5)	34.9 (± 4.1)	756.3 (± 203.9)	0.9 (± 0.1)
	1	274.1 (± 29.1)	45.3 (± 6.1)	4.8 (± 0.6)	444.4 (± 24.8)	25.5 (± 3.7)	3.4 (± 0.1)
	2	344.3 (± 56.0)	15.1 (± 3.5)	6.0 (± 0.6)	504.8 (± 69.4)	22.4 (± 4.8)	4.0 (± 0.6)
	3	452.9 (± 23.0)	15.3 (± 4.0)	6.6 (± 0.5)	567.6 (± 54.6)	19.6 (± 2.6)	4.5 (± 0.3)
PPG 0.25	0	40.0 (± 1.3)	2130.8 (± 117.6)	1.4 (± 0.1)	38.8 (± 3.2)	8.2 (± 1.2)	0.8 (± 0.1)
	1	383.7 (± 38.1)	49.5 (± 12.6)	5.3 (± 0.5)	390.2 (± 49.9)	24.6 (± 4.1)	3.0 (± 0.5)
	2	409.1 (± 48.6)	39.4 (± 7.1)	6.3 (± 0.8)	471.1 (± 36.6)	21.1 (± 2.8)	4.1 (± 0.4)
	3	493.6 (± 38.4)	18.9 (± 7.1)	8.6 (± 0.7)	505.9 (± 53.4)	15.0 (± 5.0)	5.3 (± 0.4)
PPG 0.5	0	33.7 (± 2.8)	2072.0 (± 194.4)	1.3 (± 0.2)	39.9 (± 1.0)	10.5 (± 1.3)	0.8 (± 0.1)
	1	248.8 (± 19.2)	30.3 (± 2.6)	3.8 (± 0.4)	306.7 (± 48.2)	26.8 (± 1.7)	2.2 (± 0.3)
	2	362.8 (± 68.3)	25.8 (± 3.3)	6.0 (± 1.0)	388.9 (± 47.6)	24.7 (± 1.2)	3.0 (± 0.2)
	3	435.2 (± 84.5)	27.3 (± 3.4)	7.0 (± 0.9)	475.1 (± 47.7)	23.2 (± 2.7)	4.2 (± 0.5)
PPG 1.0	0	31.8 (± 1.1)	1708.6 (± 165.0)	1.5 (± 0.2)	38.4 (± 2.7)	7.2 (± 1.5)	0.9 (± 0.1)
	1	242.2 (± 33.4)	30.9 (± 4.6)	4.9 (± 0.3)	315.0 (± 52.2)	26.6 (± 2.3)	2.5 (± 0.3)
	2	312.4 (± 86.7)	13.7 (± 6.0)	6.4 (± 0.3)	613.4 (± 39.7)	20.9 (± 2.1)	5.1 (± 0.5)
	3	359.3 (± 20.1)	10.3 (± 1.6)	8.1 (± 0.6)	615.6 (± 38.9)	15.7 (± 1.7)	5.7 (± 0.1)

At the slow loading speed (crosshead speed 10 mm/min), tensile strength and stiffness rise with increasing drawing frequency but, strain is decreased by the drawing. Tensile properties are almost similar after the second drawing, as shown in Table 7-2. The stress-strain curves (Figure 7-1) shows a clear trend of increased strength and stiffness and decreased strain rate as drawing frequency increases.

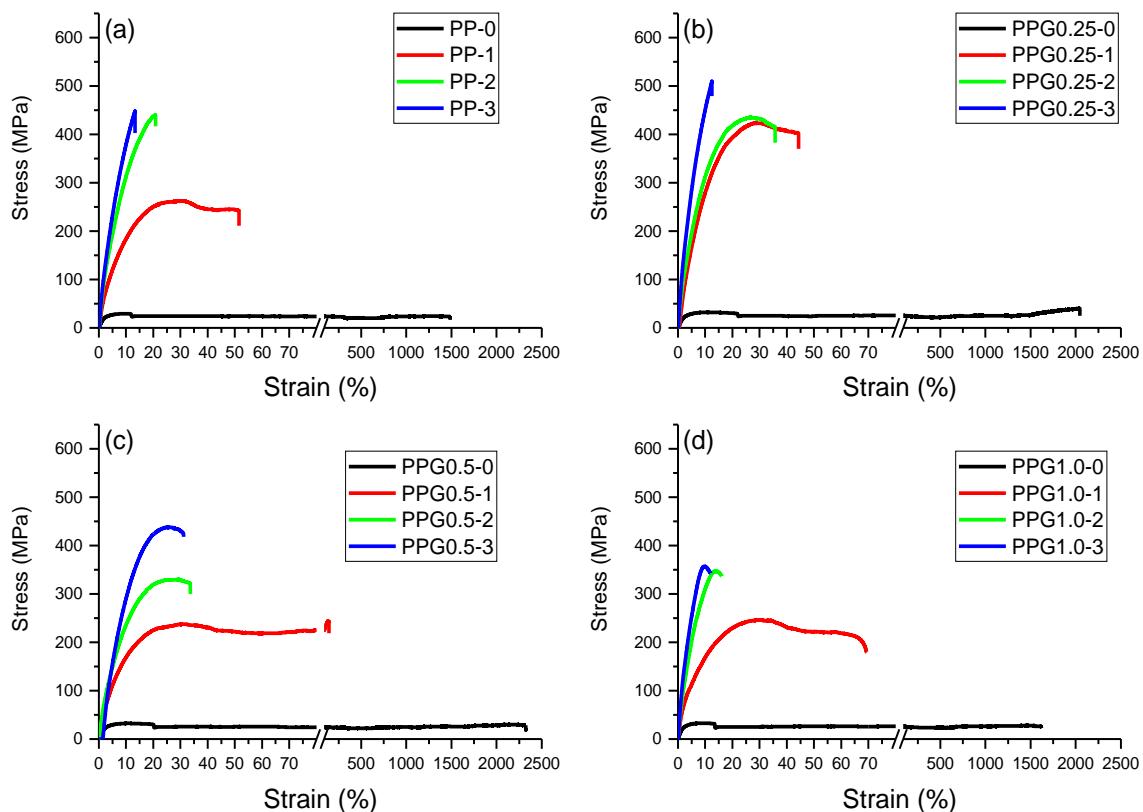


Figure 7-1 Stress-strain curves of drawn fibres at 10 mm/min loading speed

This finding was also reported by other researchers [74]. The fibre drawing process increases crystallisation in the amorphous regions and hence fibre stiffness. Furthermore, yielding phenomena could decline as reorganising macromolecules along the drawing direction [74]. The ductile property worsened after repeated drawing processes, as shown in Figure 7-1.

The PPG0.25 fibres manifest the highest tensile strength and stiffness among the PP/Graphene nanocomposite fibres at a 10mm/min loading speed (Figure 7-1). The tensile strength of neat PP fibre and PPG0.25 fibres by the three times drawing processes averaged 452.9 MPa and 493.6 MPa, which is improved by 9% more than neat PP fibres. The Young's modulus of PP and PPG0.25 is 6.6 GPa, and 8.6 GPa, respectively. The elongation generally decreased with increasing graphene content. These results reflect those of previous researchers [126], who found that low Graphene content improves mechanical properties more than high graphene content fibres because low content graphene (0.25-0.5 vol%) can be dispersed easily in the polymeric matrix. On the other



hand, the high content of Graphene causes much higher agglomerates. This agglomeration of Graphene particles in the polymer can be dispersed by fibre drawing to improve mechanical properties [74], as shown in Figure 7-3.

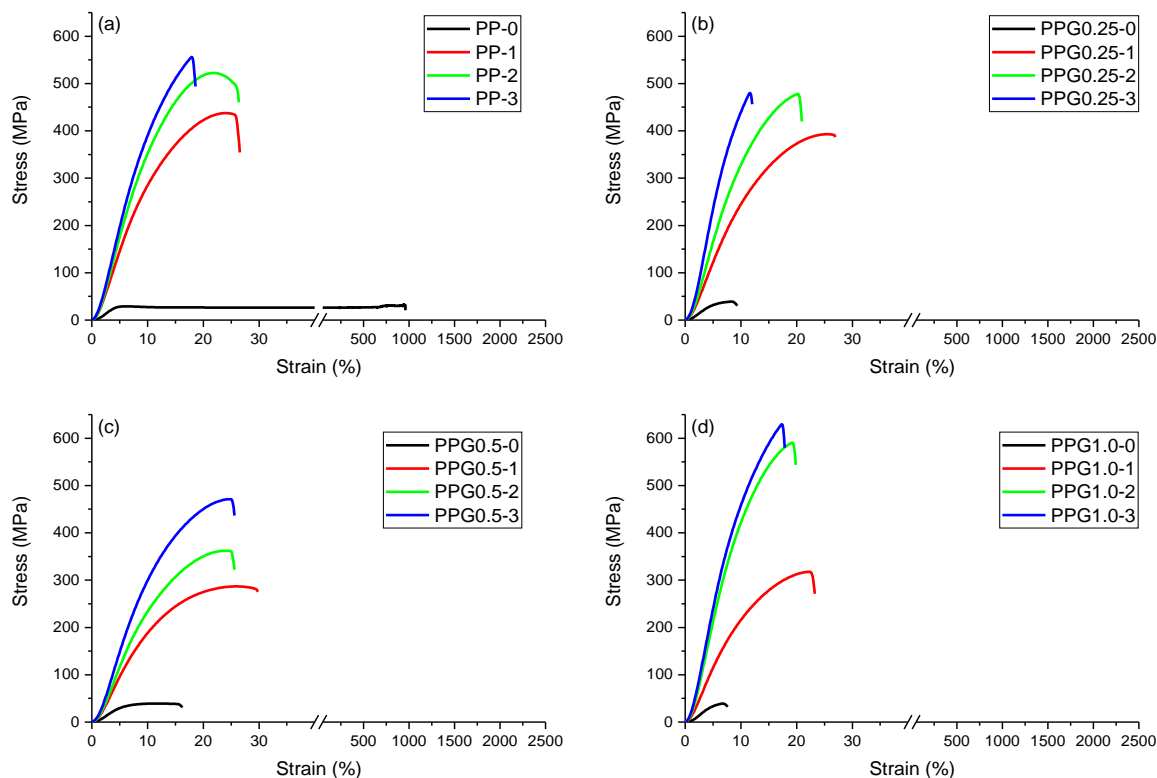


Figure 7-2 Stress-strain curves of drawn fibres at 1000 mm/min loading speed

At the high loading speed (1000mm/min) test, on the other hand, the tensile strength and modulus are enhanced by the drawing process in the same way as the tensile test at 10 mm/min. There is no significant difference between the tensile strength and modulus of the PP/graphene fibres. However, 1 wt% graphene fibres significantly increase in tensile strength and modulus after the second drawing, at 1000 mm/min. It was the highest tensile strength (613 MPa), which increased by 22% more than neat PP fibres at the two times drawing. The PPG0.25 and PPG0.5% fibres dropped by 7% and 23% separately according to neat PP fibres.

Firstly, the strain difference at low and high loading rates may be explained by the fact that PP at low loading speed has qualitatively different areas, such as average molecular weight and degree of mass crystallinity. At high loading speeds, polypropylene presents reduced ductility. Figure 7-3 illustrates PP tensile test specimens of dumbbell shape (EN

ISO 527-2:2012) at low (250 mm/min) and high (1000 mm/min) loading rates after failure. As the low loading rate can produce fibrils (Figure 7-3. a and b), it was able to show high percent elongation. On the other hand, because the surface after fracture was smooth at high loading speed (Figure 7-3.c and d), percent elongation was significantly decreased compared to the slow loading rate tensile test [127]. It also means that the broken surface shows brittleness at high speed because there was no re-crystallinity at high loading speed, especially in undrawn fibres.

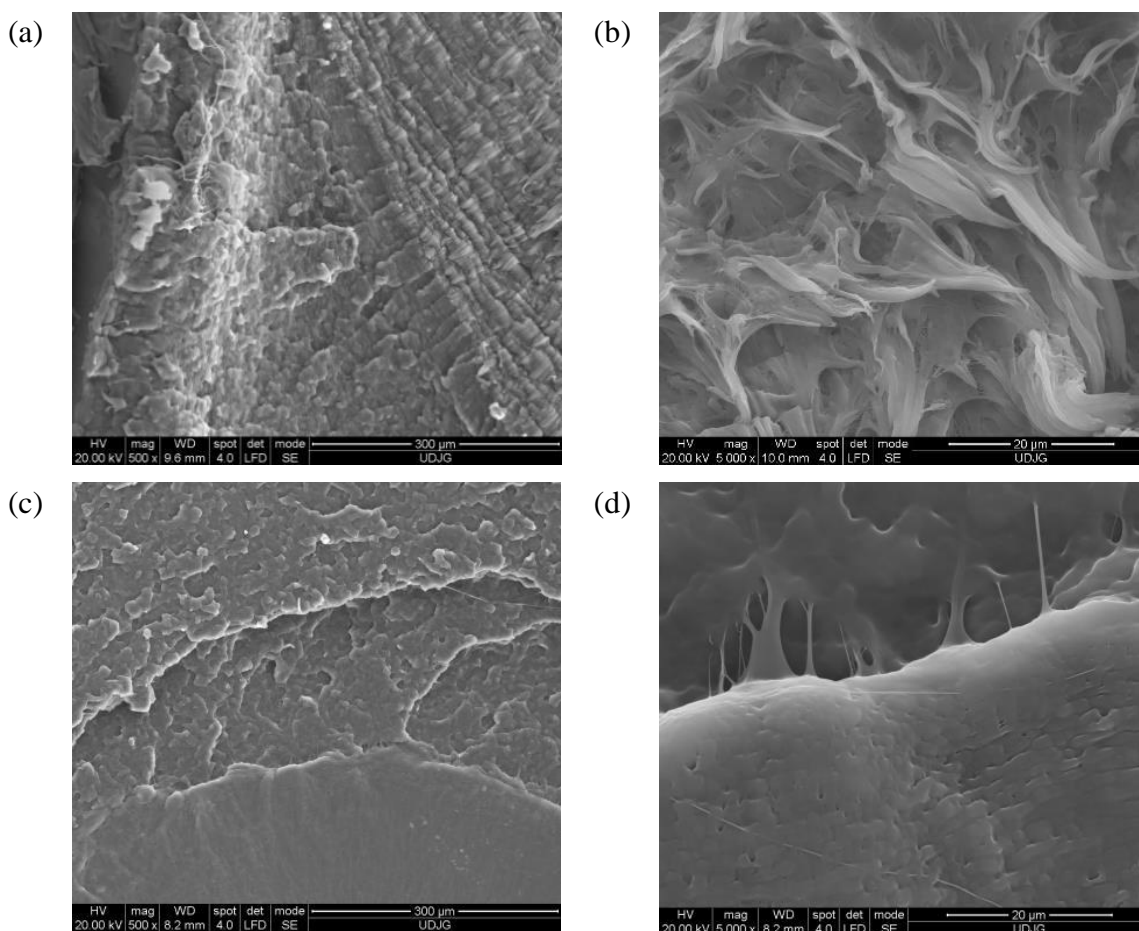


Figure 7-3 Failure surface of polypropylene at different magnifications (a) and (b) at 250mm/min, and (c) and (d) 1000mm/min loading speed tensile tests [127]

What stands out in Figure 7-4 is the increase of strain of Graphene fibres. It shows a different trend compared to the slow loading speed tensile test. The percent elongation of undrawn PP fibre and PPG1.0 fibres is 756% and 7.2% at 1000mm/m loading speed, and they are 26% and 27% after the first drawing separately. All fibre samples show similar strain values after the second drawing. These results show that the strain rate of

PP/Graphene fibres seems not to be affected at the high loading speed once fibres are drawn.

Overall, this study found that tensile strength and stiffness at the low and high loading speeds increased by fibre drawing and adding Graphene. But the tensile strength, modulus, and strain showed different trends depending on the loading rate. This difference can be explained by the fibre drawing process and general polymer properties.

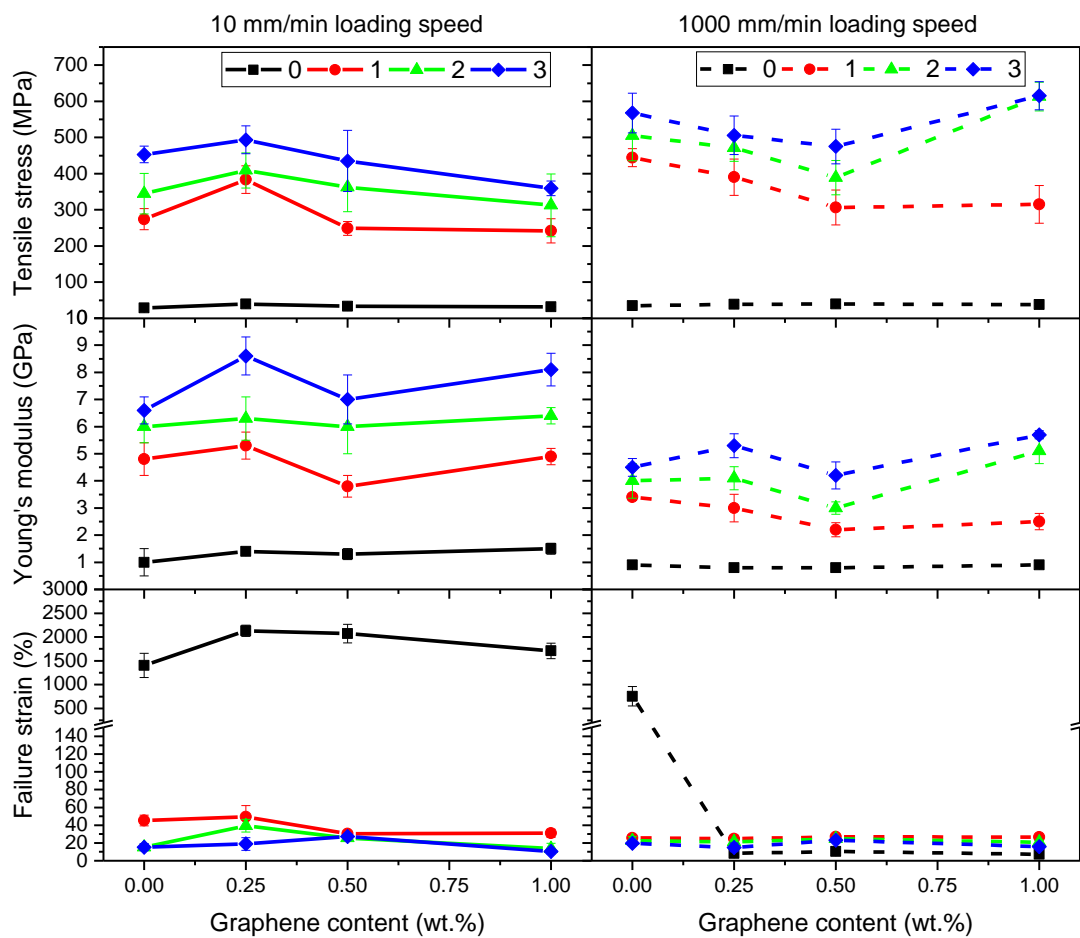


Figure 7-4 Variation of tensile stress, Young's modulus, and failure strain of the PP/Graphene nanocomposites fibres as a function of Graphene content at 10mm/min and 1000 mm/min loading speed

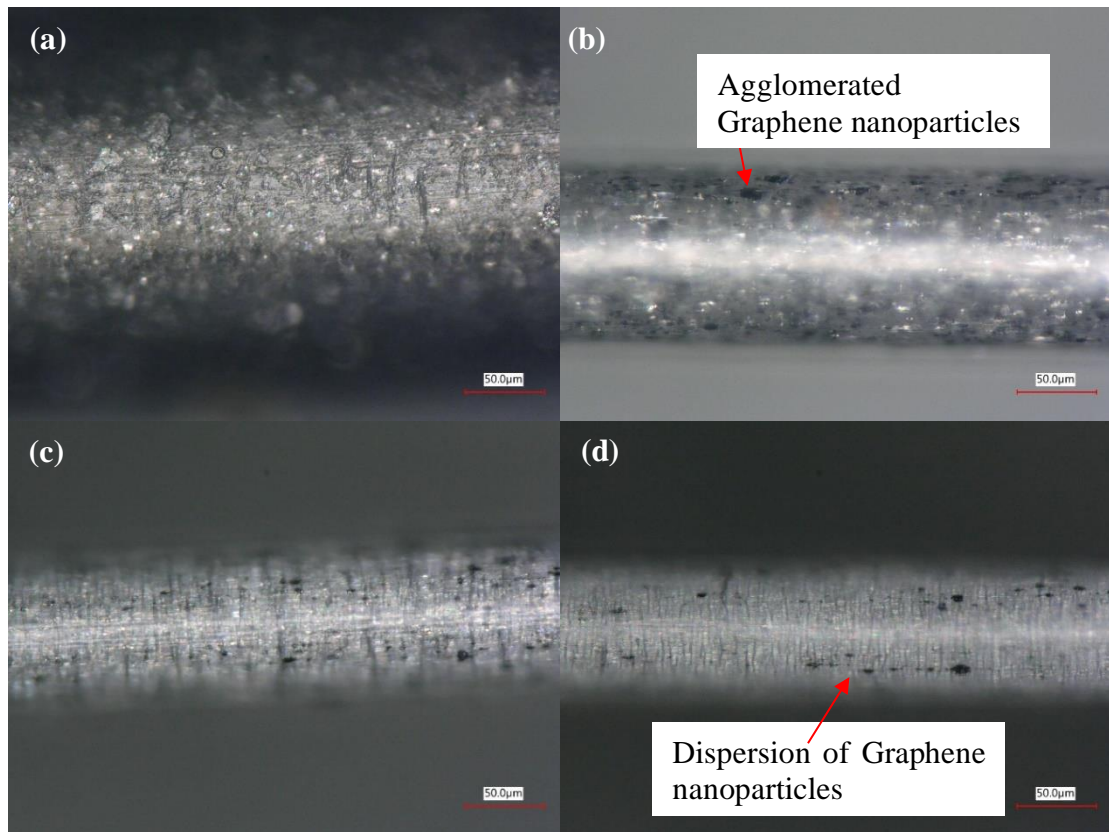


Figure 7-5 Agglomerated graphene particles (black dots) in PPG1 fibres of (a) 300 $\mu\text{m}$  (undrawn fibre), (b) 120  $\mu\text{m}$ , (c) 100  $\mu\text{m}$ , and (d) 90  $\mu\text{m}$  diameter drawn by the supplier

	Low graphene contents	High graphene contents
Low Loading speed	<ul style="list-style-type: none"> <li>• Graphene distribution <math>\uparrow</math></li> <li>• Crystallisation <math>\uparrow</math></li> </ul>	<ul style="list-style-type: none"> <li>• Graphene distribution <math>\downarrow</math></li> <li>• Crystallisation <math>\uparrow</math></li> </ul>
High Loading speed	<ul style="list-style-type: none"> <li>• Crystallisation <math>\downarrow</math></li> <li>• Interface strength between Graphene and PP <math>\downarrow</math></li> </ul>	<ul style="list-style-type: none"> <li>• Crystallisation <math>\downarrow</math></li> <li>• Interface strength between Graphene and PP <math>\uparrow</math></li> </ul>

Figure 7-6 Schematic tensile properties of PP/Graphene nanocomposite fibres at the low and high loading speed

Secondly, because Graphene particles are agglomerated in the fibres, as shown in Figure 7-5, it reduces the mechanical properties of fibres. Agglomerated particles can become close to a homogeneous distribution in the polymer through the fibre drawing process (Figure 7-6). At the high loading speed, 1% graphene fibres presented the highest tensile strength after two times drawing. A possible explanation for this might be that Graphene is used as a bridge at the PP, and it could increase tensile strength as interface strength is improved [128], [129].

### 7.2.3 Composites tensile tests

Typical tensile strain-stress curves of composite laminates with CF and PP hybrid yarn are displayed in Figure 7-7, and those test data are summarised in Table 7-3 with normalised data. The strain was measured from DIC strain mapping methods, and load data was obtained from the Instron mechanical testing machine.

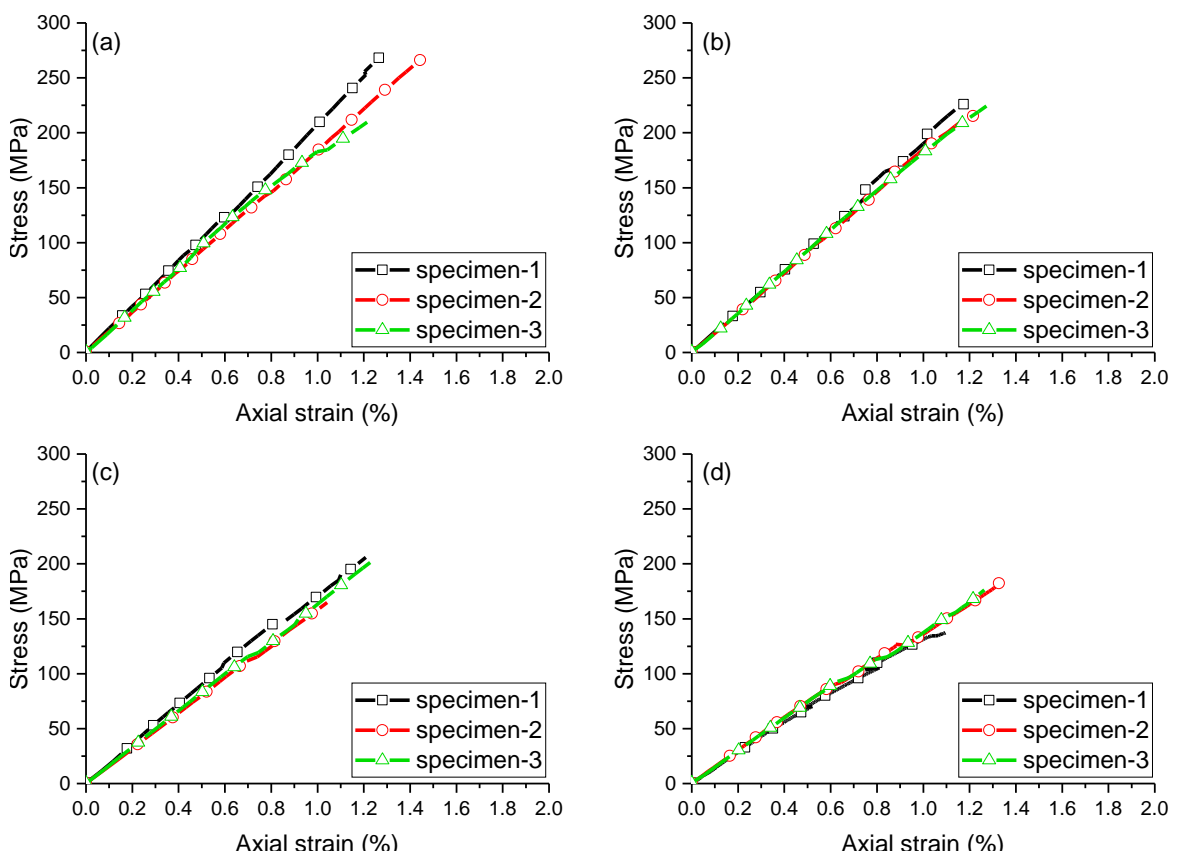


Figure 7-7 Typical stress-strain curves of composites: (a) CF, (b) CF/PP, (c) CF/PPG1.0, and (d) CF/PPG1.0/TT

Table 7-3 Summary of tensile test results of composites

	Experimental data results			Normalised results ( $FVF_{CF}=50\%$ )		
	Peak stress (MPa)	Failure strain (%)	Modulus (GPa)	Peak stress (MPa)	Failure strain (%)	Modulus (GPa)
CF	251.8 ( $\pm 36.5$ )	1.3 ( $\pm 0.1$ )	19.6 ( $\pm 1.0$ )	308.4 ( $\pm 44.7$ )	-	24.0 ( $\pm 1.2$ )
CF/PP	223.7 ( $\pm 8.1$ )	1.2 ( $\pm 0.1$ )	18.7 ( $\pm 0.3$ )	298.2 ( $\pm 10.8$ )	-	24.9 ( $\pm 0.3$ )
CF/PPG 1.0	190.7 ( $\pm 22.5$ )	1.2 ( $\pm 0.1$ )	17.0 ( $\pm 1.0$ )	246.7 ( $\pm 29.1$ )	-	22.0 ( $\pm 1.3$ )
CF/PPG 1.0/TT	165.3 ( $\pm 24.5$ )	1.2 ( $\pm 0.1$ )	14.4 ( $\pm 0.7$ )	220.4 ( $\pm 32.7$ )	-	19.3 ( $\pm 0.9$ )

The experimental data of hybrid wrapped yarn composites show decreased tensile properties against neat CF composites (Figure 7-7). The normalised data at 50% carbon fibre volume fraction shows that the tensile strength of CF/PP and CF/PPG1.0 decreased by 11 % and 24 %, and their moduli also reduced by 5 % and 13 % compared to that of neat CF composites. Between 2D cross-ply structure (CF/PPG1.0) and 3D structure composites (CF/PPG1.0/TT) with PP/Graphene nanocomposite fibres, the tensile strength of 3D structure composites was more decreased than 2D structure composites. The normalised 3D structure tensile properties are decreased by 9% of strength and 12% of modulus by PPG1.0 through-thickness binder compared to neat CF composites.

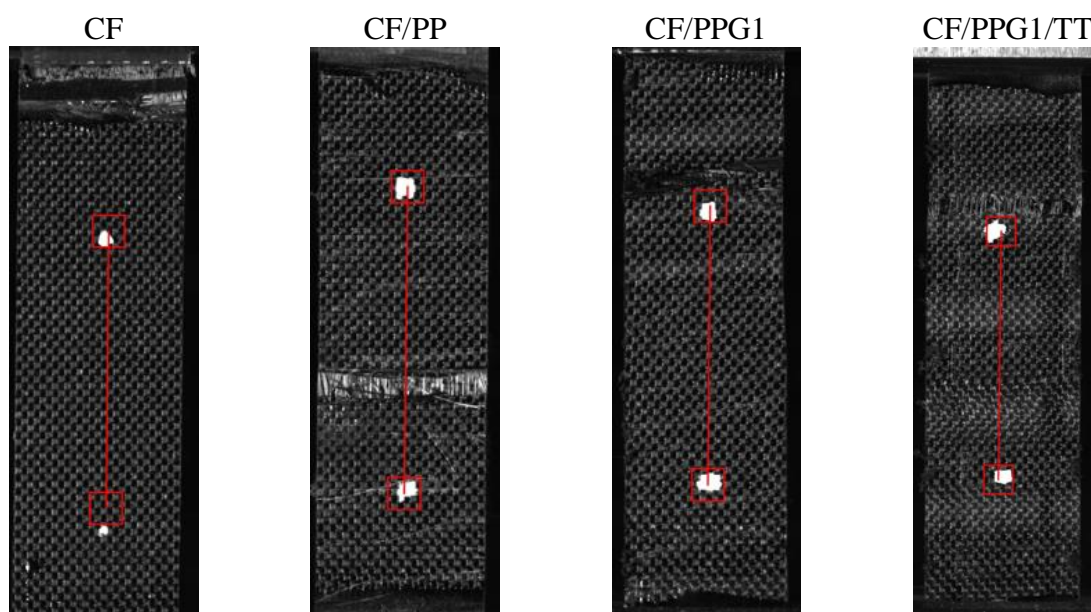


Figure 7-8 General images of CF, CF/PP, CF/PPG1.0, and CF/PPG1.0/TT composite specimens at failure

The decrease in tensile properties can occur due to low carbon fibre volume fraction caused by thermoplastic hybrid yarn and a weak interface between the PP as a non-polar polymer and the epoxy matrix [130].

Figure 7-8 presents general specimen images after tensile failure, and Figure 7-9 shows the DIC contour plot image. This study indicates that a high strain rate is focused on the weft fibres first, which is the weakest direction against the loading direction, and then composite failure occurs. It can be observed clearly through the analysis of the DIC mapping images.

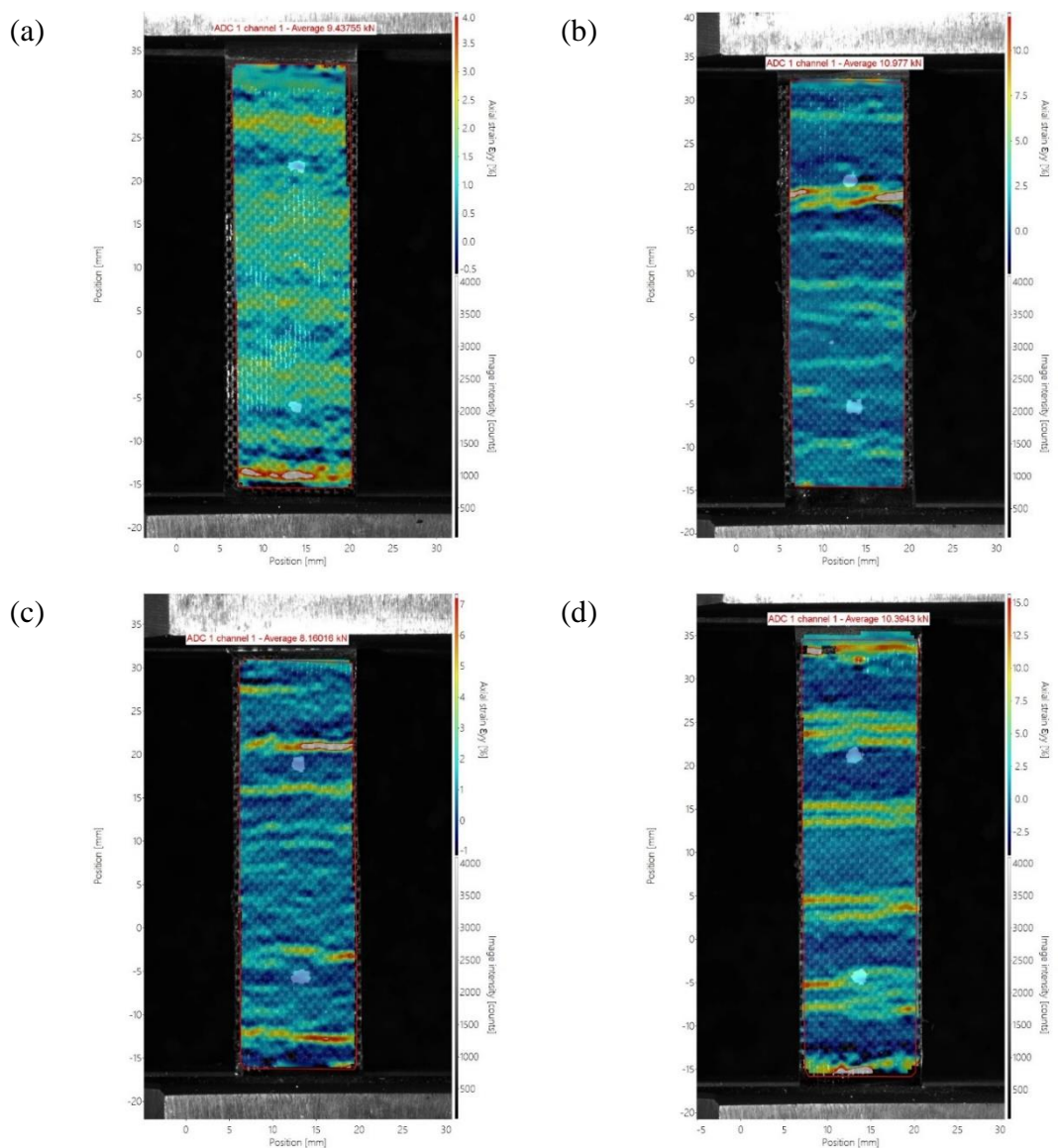


Figure 7-9 Image of DIC method of cross-ply structure composites specimens at maximum load; (a) CF, (b) CF/PP, (c) CF/PPG1.0, and (d) CF/PPG1.0/TT binder composites

### 7.2.4 Short beam strength test

The short beam strength (SBS) test specimen at the transverse direction was performed 4 span length /specimen thickness ratios according to the ASTM D2344 standard method. These results are summarised in Figure 7-10, and the average values of interlaminar shear strength (ILSS) are shown in Table 7-4. The CF/PPG1.0 composites present the maximum interlaminar shear strength of 47.9 MPa, which is improved by 11% more than CF composites. On the other hand, CF/PP cross-ply structure composites are improved by 4%. In the 3D structure composites, the ILSS of CF/PPG1.0/TT composites is 44.3 MPa, slightly improved by 2% more than that of the neat CF composites.

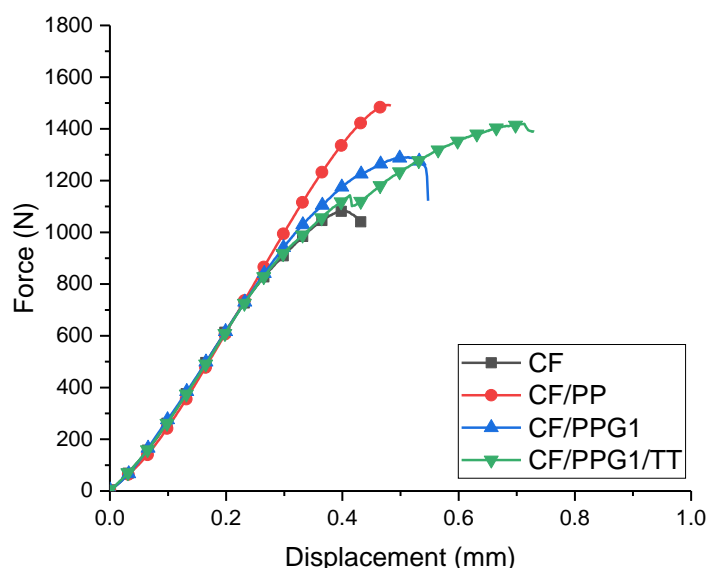


Figure 7-10 Typical force-displacement curves of carbon fibre and PP/Graphene wrapped yarn composites in the short beam strength test

Table 7-4 Summary of dimensions, maximum load and interlaminar shear strength of composites specimens in short beam strength test

	Thickness (mm)	Width (mm)	Peak load (N)	ILSS (MPa)
CF	3.0 (±0.1)	5.5 (± 0.3)	1038.2 (± 53.2)	43.3 (± 2.2)
CF/PP	3.4 (± 0.1)	7.1 (±0.4)	1445.7 (± 116.4)	44.9 (± 3.6)
CF/PPG1.0	3.3 (± 0.1)	6.5 (± 0.2)	1369.1 (± 72.0)	47.9 (± 2.5)
CF/PPG1.0/TT	3.8 (± 0.1)	7.13 (±0.4)	1601.7 (± 113.0)	44.3 (± 3.1)



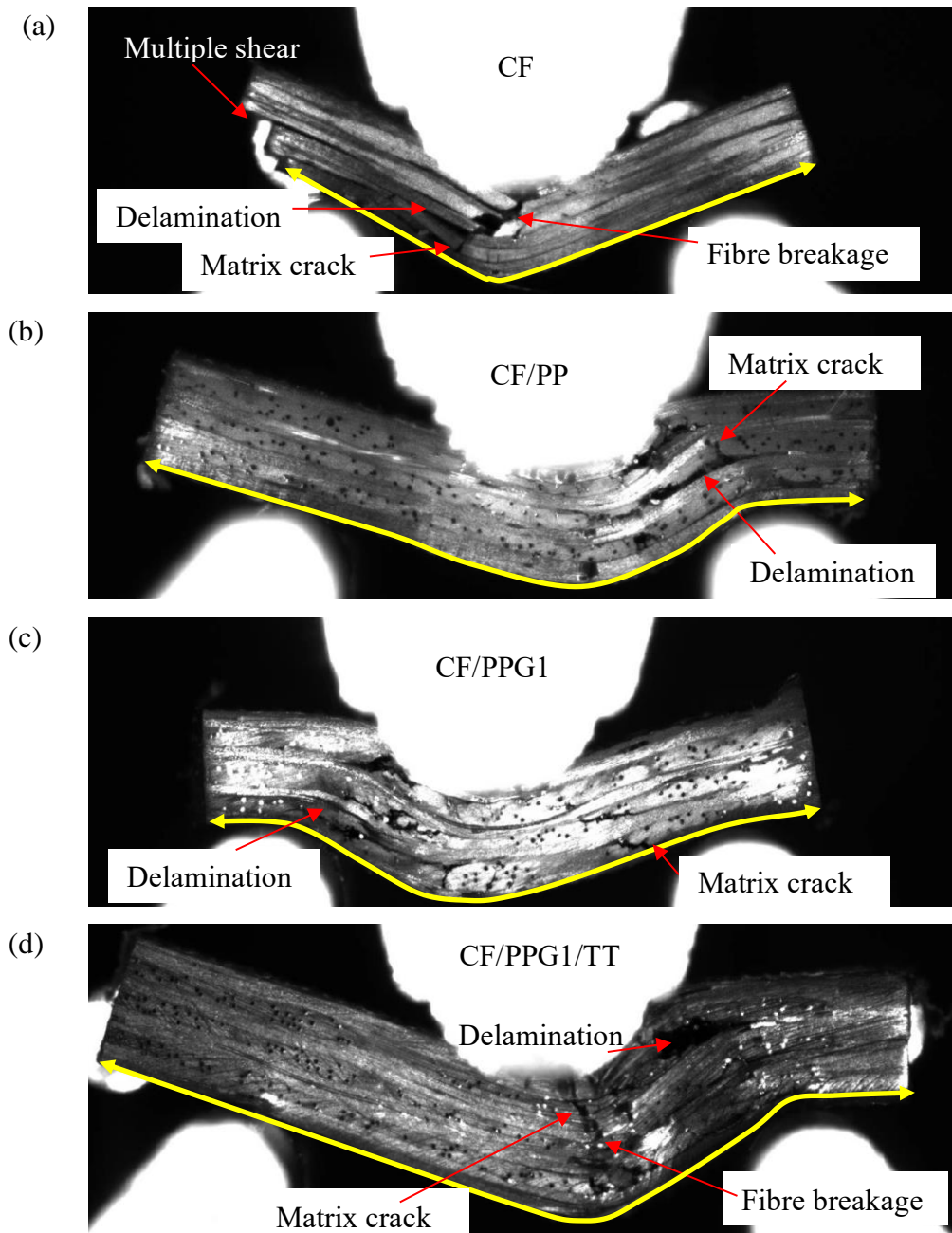


Figure 7-11 Composites specimens after short beam shear test

All composites samples show typical delamination after the fracture, as shown in Figure 7-11. Because of low interlaminar strength, the neat CF composites show failure modes of multi-layer interlaminar failure and fibre breakage. Therefore, CF composites present a V-shaped failure at the bottom of specimens, as shown by the yellow arrows in Figure 7-11. On the other hand, CF/PP and CF/PPG1.0 composites mainly present delamination

and matrix cracks and their ILSS improved by 4% and 11%, respectively, against neat CF composites. The hybrid wrapped yarn composites show deformation failure of an S shape because their interlaminar strength is improved. Among the composites samples, the CF/PPG1/TT composites, which have a through-thickness binder of PPG1.0 fibre, withstood the highest load of 1601 N improvements of 54% against CF and 22% against CF/PPG1.0 composites.

## 7.2.5 Composites impact tests

Force-displacement curves provide information about the response of composites at low-velocity impact. These graphs show open or closed curves depending on the degree of deformation of the specimens [112].

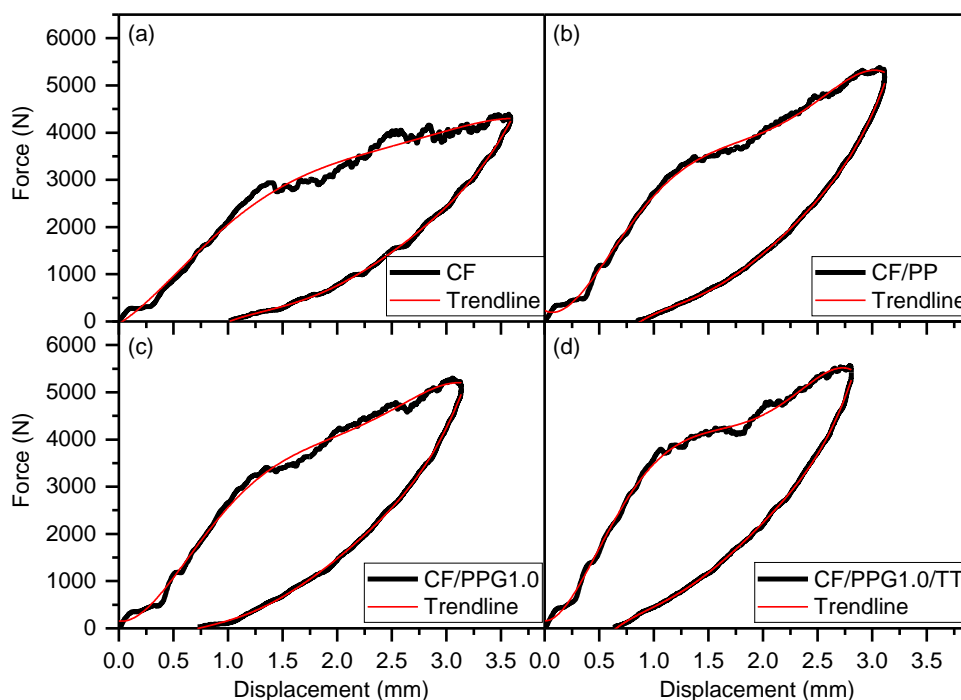


Figure 7-12 Typical force-displacement curves of (a) CF composites, (b) CF/PP composites, (c) CF/PPG1.0 composites, and (d) CF/PPG1.0/TT composites at 10J impact energy

The actual absorption energy due to damage deformation of a specimen can be obtained by calculating the area enclosed by the ascending and descending curves in the graphs [131]. The calculated absorbed energy by trendline is summarised in Table 7-5 with the peak force and displacement. All composites specimens in this research show almost closed curves at 10J and 20J impact energy, as shown in Figures 7-12 and 7-13. No significant differences in the absorbed energy were found between neat CF and hybrid

yarn composites at the 10J impact energy test (Figure 7-14.a). However, CF composites have a peak displacement of 3.7 mm, while hybrid yarn reinforced composites have around 3.0 mm. As a result, the maximum force of 2D cross-ply hybrid yarn reinforced composites (CF/PPG1.0) and 3D structure composites (CF/PPG1.0/TT) increased by 18% and 20%, respectively.

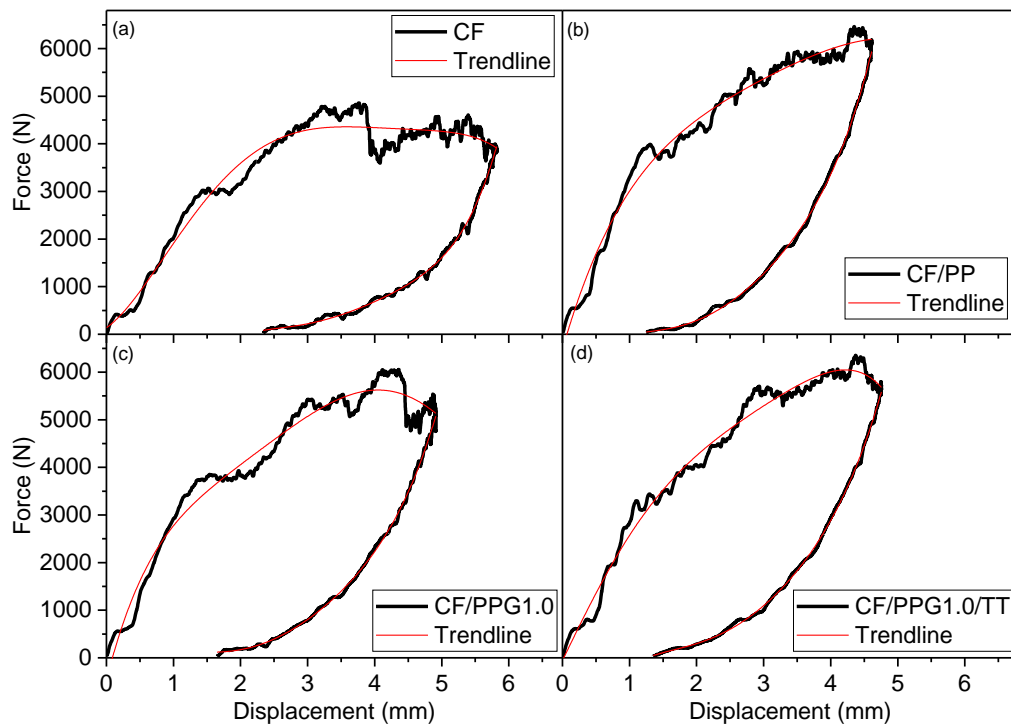


Figure 7-13 Typical force-displacement curves of (a) CF composites, (b) CF/PP composites, (c) CF/PPG1.0 composites, and (d) CF/PPG1.0/TT composites at 20J impact energy

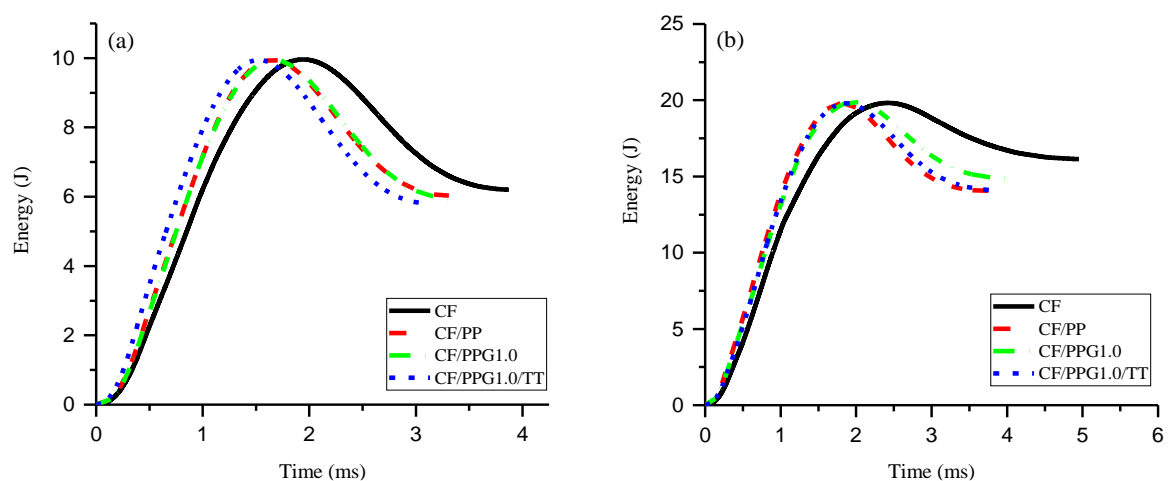


Figure 7-14 Typical energy-time curves of composites at (a) 10J and (b) 20J impact energy

No significant differences in the absorbed energy were found between neat CF and hybrid yarn composites at the 10J impact energy test (Figure 7-14.a). However, CF composites have a peak displacement of 3.7 mm, while hybrid yarn reinforced composites have around 3.0 mm. As a result, the maximum force of 2D cross-ply hybrid yarn reinforced composites (CF/PPG1.0) and 3D structure composites (CF/PPG1.0/TT) increased by 18% and 20%, respectively. The absorbed energy differential between hybrid yarn reinforced composites, and neat CF reinforced composites can clearly be seen from the 20J impact energy test. The better performance is presented by hybrid yarn reinforced composites (Figure 7-14.b). The absorbed energy of hybrid yarn reinforced composites decreased by 11-16% compared to the CF composites.

Table 7-5 Summary of impact test results for cross-ply and 3D structure composites at 10J and 20J impact energy

	Sample	Peak force (N)	Peak displacement (mm)	Residual displacement (mm)	Absorbed energy (J)	Recovered energy (J)
10J	CF	4421.3 ±127.4	3.7 ±0.1	1.0 ±0.1	6.2 ±0.2	3.8 ±0.2
	CF/PP	5212.9 ±281.3	3.1 ±0.1	0.8 ±0.1	6.2 ±0.3	3.8 ±0.3
	CF/PPG1.0	5200.3 ±117.7	3.2 ±0.1	0.7 ±0.1	5.9 ±0.3	4.0 ±0.3
	CF/PPG1.0/ TT	5324.6 ±435.6	2.9 ±0.1	0.7 ±0.1	6.0 ±0.4	3.9 ±0.4
20J	CF	4995.5 ±440.8	6.0 ±0.3	2.2 ±0.2	16.4 ±0.5	3.4 ±0.5
	CF/PP	6440.4 ±328.9	4.7 ±0.1	1.3 ±0.2	14.2 ±0.7	5.6 ±0.7
	CF/PPG1.0	6100.8 ±437.4	4.9 ±0.2	1.6 ±0.1	14.6 ±0.2	5.3 ±0.2
	CF/PPG1.0/ TT	6348.1 ±269.5	4.6 ±0.2	1.1 ±0.2	13.8 ±0.3	6.0 ±0.3

Impact energy in the hybrid yarn reinforced composites could be dissipated by the PP fibres. CF composites have a peak displacement of 2.2 mm, while hybrid yarn reinforced composites have 1.1-1.6 mm. The peak force of CF/PP and CF/PPG1.0 composites increased by 29% and 22%, respectively. The peak force of the 3D structure

CF/PPG1.0/TT composites increased by 27 % compared to the 2D CF composites. These results suggest that a higher contact force absorbs less impact energy and reduces the damage caused to the composites after impact.

### 7.2.6 Inspection of the impact damaged area with C-Scan

C-scan measures the area damaged by the impact test on the X-Y plane of a composite panel. However, it is challenging to know the whole damaged area because the damage data from the Z direction could not be obtained.

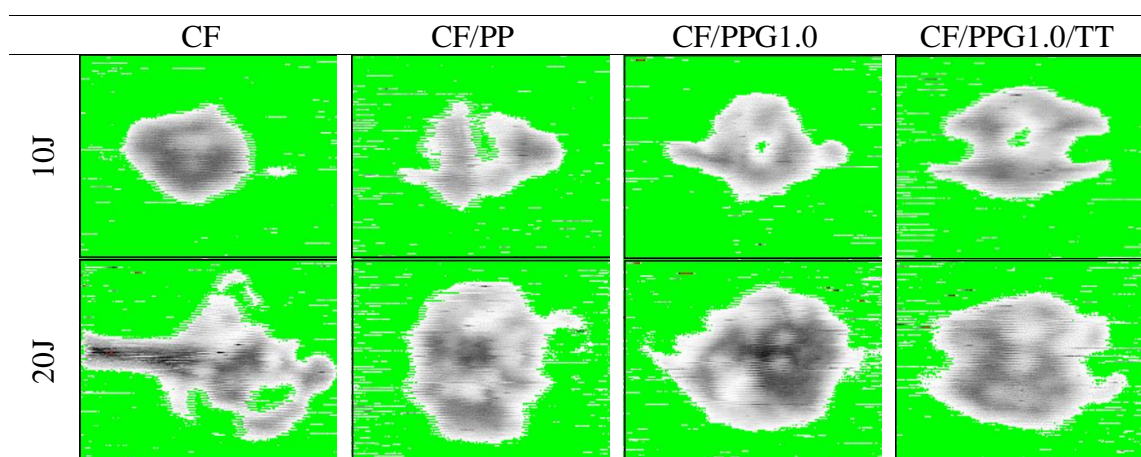


Figure 7-15 C-Scan images of cross-ply and 3D structure composite samples at 10J and 20J impact energy

However, it is enough to analyse the cumulative and expanded damage in the hybrid yarn composites. The images of specimens after impact are shown in Figure 7-15. The accumulative damage extension between the layers has been observed at an incident energy of 10J and 20J (Figure 7-15). The severe delamination of fibres is shown, especially in 2D neat CF composites after 20J impact. Also, there is no significant difference in the damaged areas between the 2D structure composites. However, the damaged area of 3D structure composites (CF/PPG1.0/TT) is 576 mm<sup>2</sup> at 10J and 866 mm<sup>2</sup> at 20J impact energy, which is an increase of 37% and 13% compared to 2D neat CF composites, respectively. But, the dent depth of the 3D structure composites was the lowest at 10J and at 20J impact energy (Figure 7-17). The damaged area increased with hybrid yarn but, the dent depth of all samples decreased with PP or PP/Graphene nanocomposites fibres.

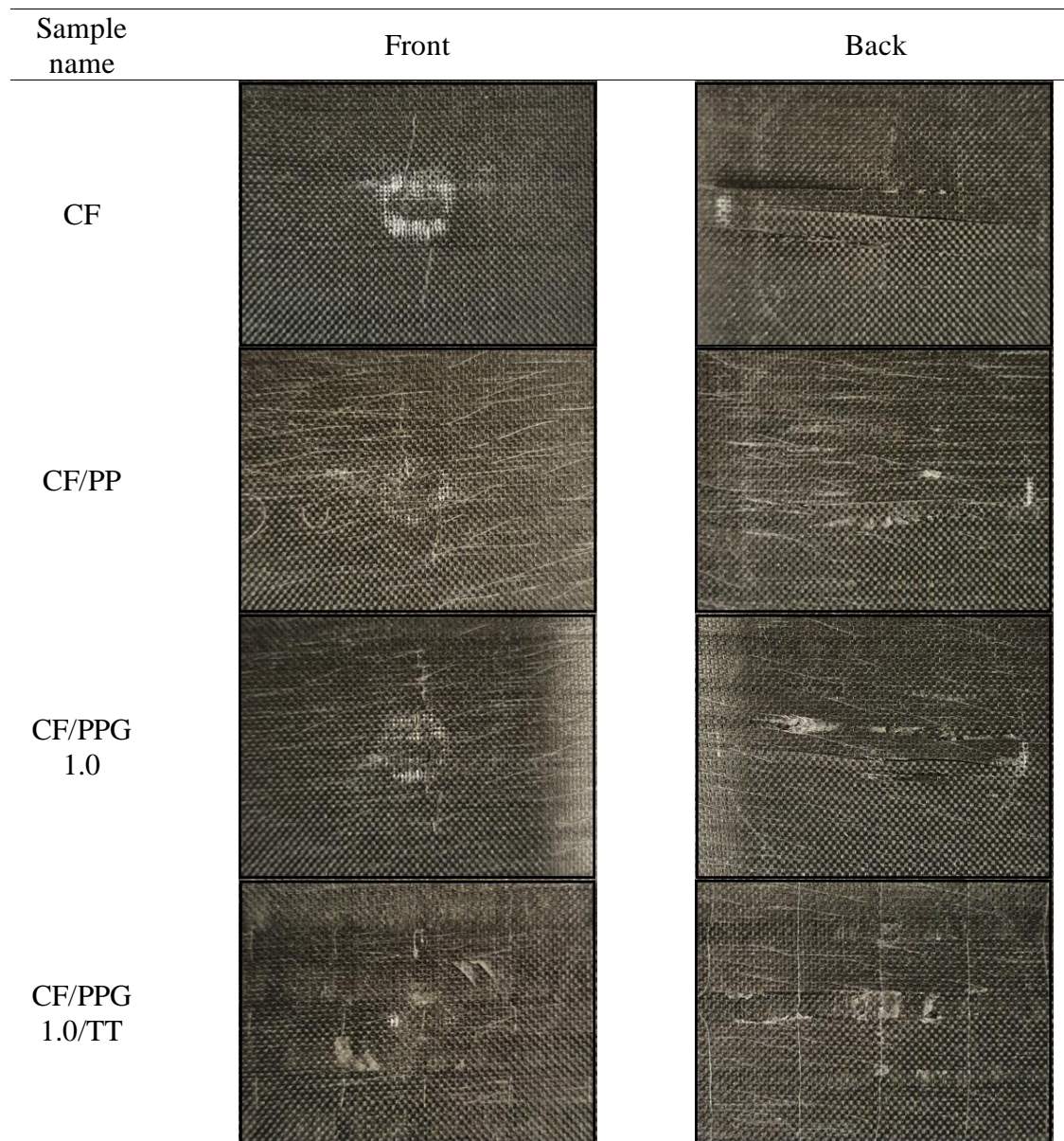


Figure 7-16 Impact damaged area of composites samples after 20J impact test

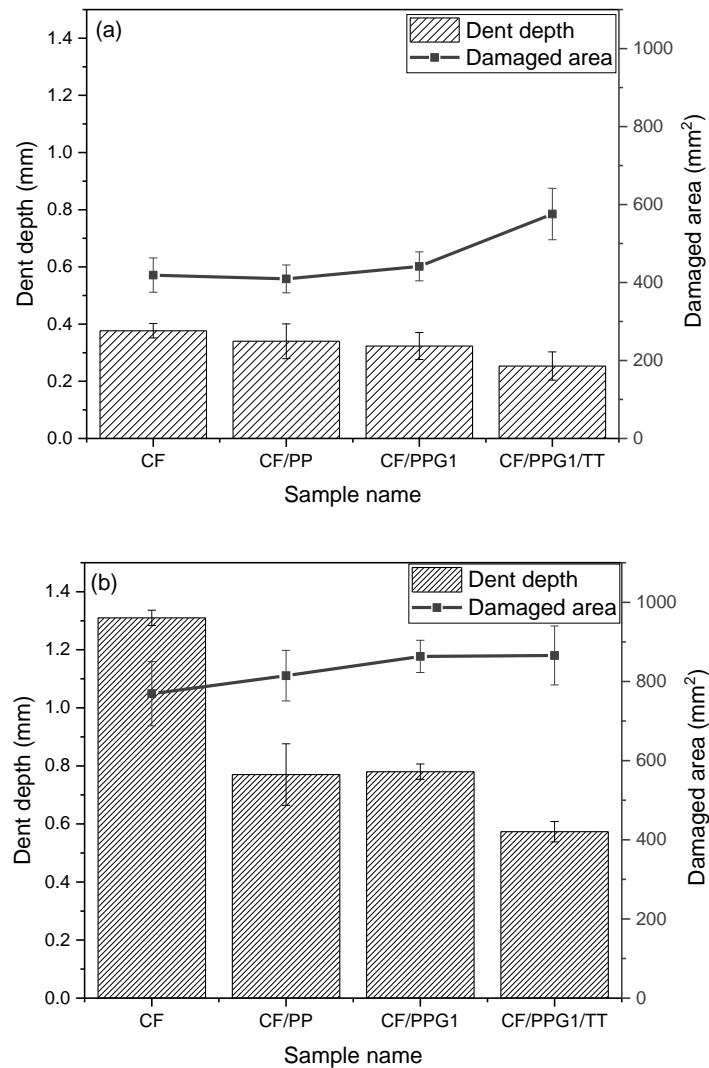


Figure 7-17 Damaged area and dent depth of cross-ply structure and 3D structure composite at (a) 10J and at (b) 20J impact energy

### 7.2.7 Compression test

Figure 7-18 presents the DIC axial strain map images of the unimpacted and impacted samples at 5N (section A), 10N (section B) and maximum load (section C) during the compression test. Section A, B and C are marked in Figure 7-19, the load-extension curves of hybrid reinforced composites obtained from a compression test after a 20J impact test. The failure of specimens after impact started at the impact area, as shown in Figure 7-18.

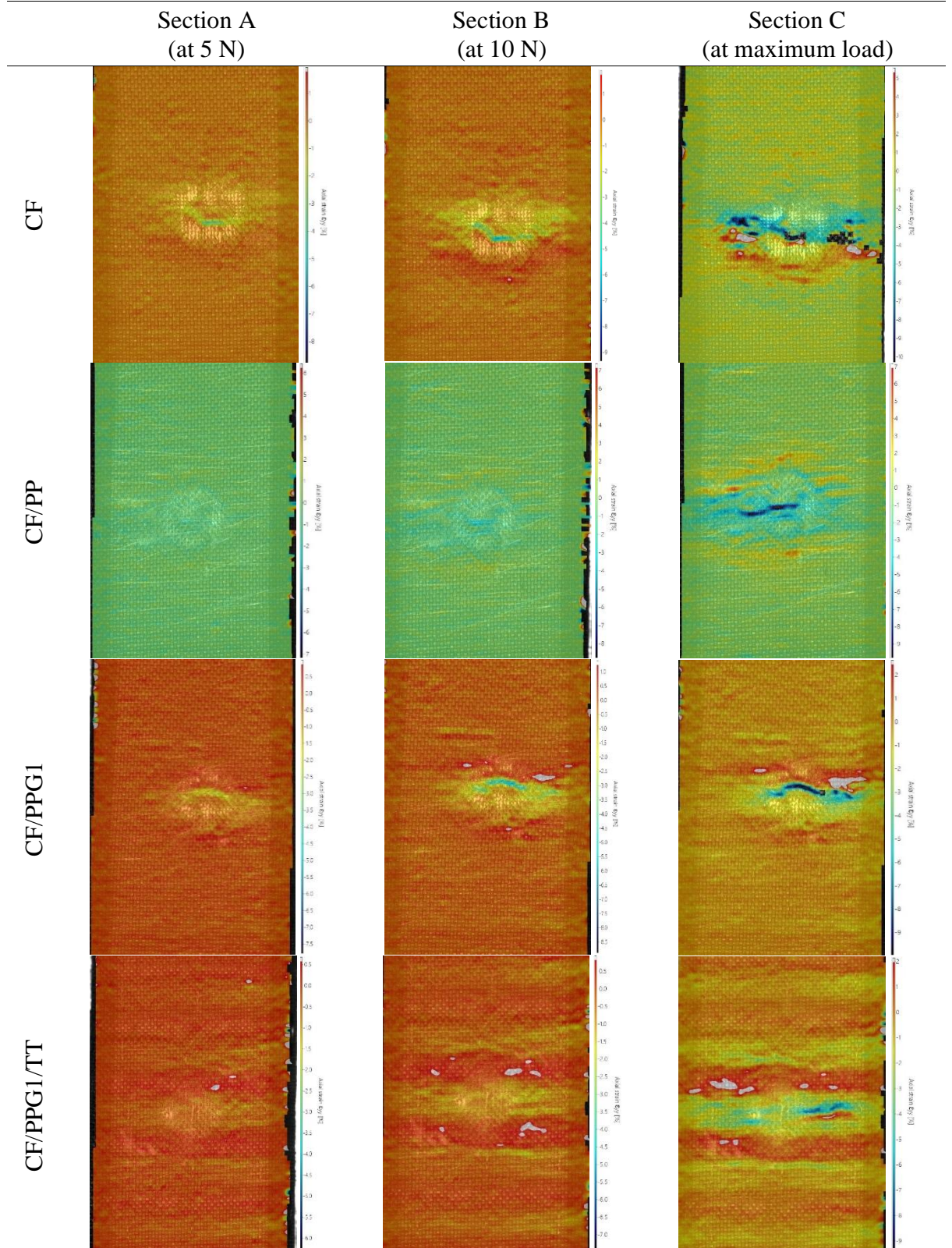


Figure 7-18 Comparison of DIC images of 20J post-impact cross-ply and 3D structure composites during the CAI test



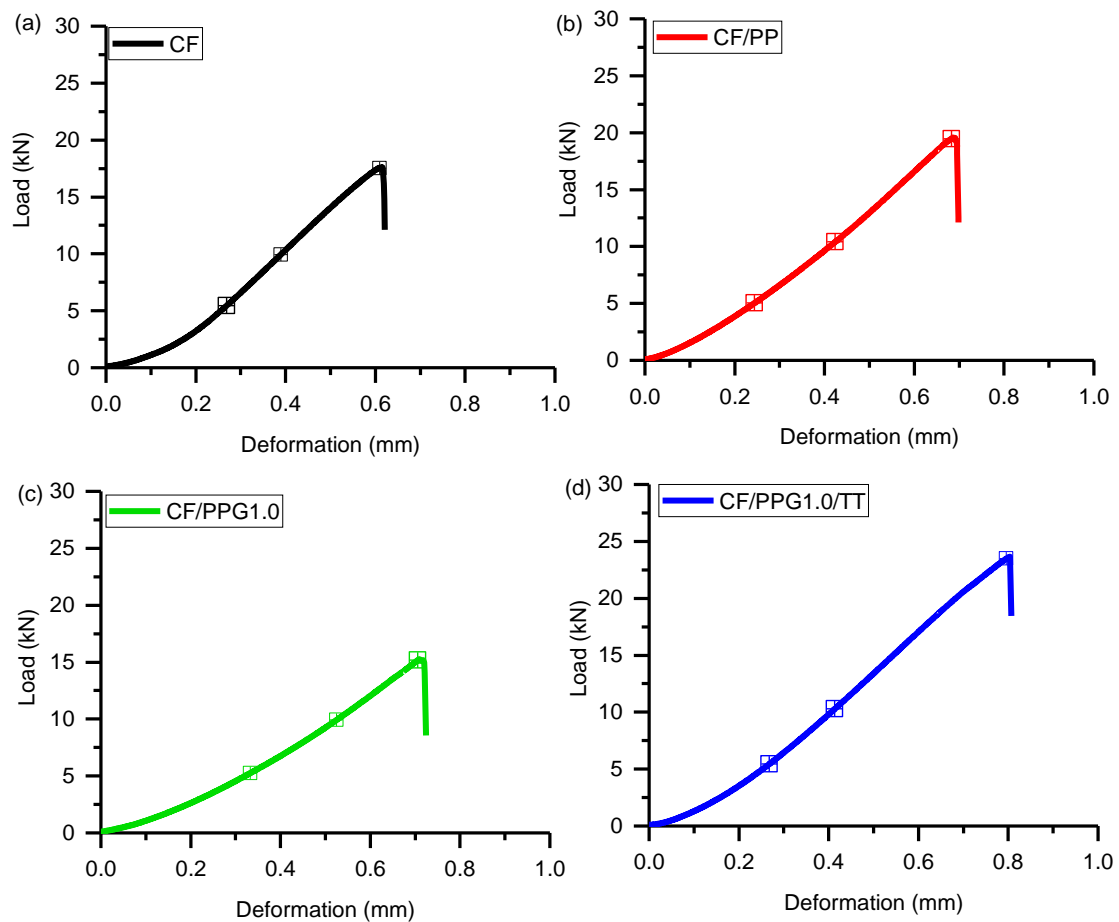


Figure 7-19 Load-extension curves of the hybrid yarn reinforced composites obtained from compression tests

However, because the failure of unimpacted specimens is generated near the boundary of the compression tool, undamaged laminates cannot provide a true measure of compression strength. This research performed a compression test on undamaged specimens at the same test set-up of the CAI test to compare the compressive strength between neat CF composites and hybrid yarn reinforced composites even though it cannot obtain actual values.

The CF/PP composites clearly show less deformation than other 2D composite samples at 10N (Figure 7-18). These results imply an improvement of impact damage tolerance of carbon fibre composites by drawn PP fibres. The 3D CF/PPG1.0/TT composites show small deformation in the DIC strain map; however, compressive strength is reduced by 12% with respect to CF composites.

Table 7-6 compares the compression strength for experimental and normalised data when the carbon fibre volume fraction is 0.5. The normalised strength of CF/PP and CF/PPG1.0 composites increased by 44% and 29% after the 10J energy impact test compared to neat CF composites. CF/PP composites show the highest compressive stress even with 20J impacted specimens. On the other hand, CF/PPG1.0 composite decreased by 1% after the 20J impact test. Overall, graphene fibres can improve impact damage tolerance, but there is no significant difference with CF/PP composites (Figure 7-20).

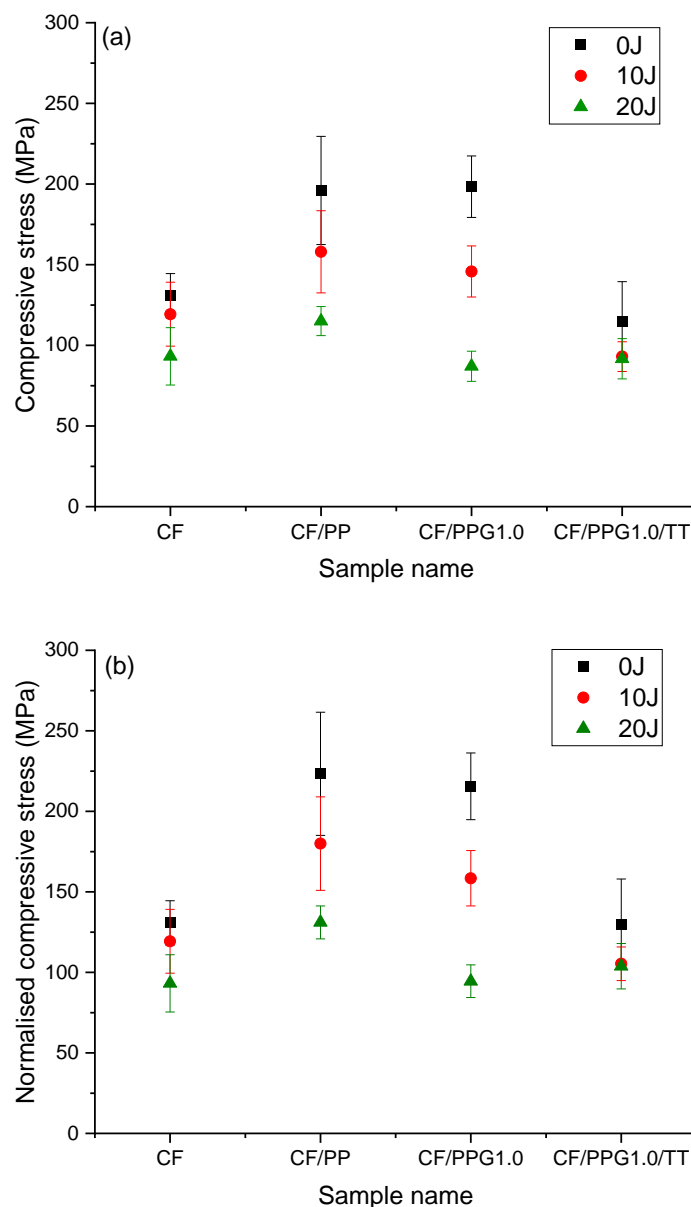


Figure 7-20 (a) Peak compression stress of cross-ply and 3D structure composites samples after 0J, 10J and 20J impact test and (b) normalised data

Table 7-6 Summary of experimental and normalised compressive stress data of hybrid yarn reinforced composites

	Experimental maximum stress (MPa)			Normalised stress (MPa)		
	0J	10J	20J	0J	10J	20J
CF	130.7 (± 13.7)	119.3 (± 19.8)	93.2 (± 17.8)	160.0 (± 16.8)	146.1 (± 24.3)	114.1 (± 21.8)
CF/PP	196.0 (± 33.6)	158.0 (± 25.5)	115.0 (± 9.0)	261.3 (± 44.7)	210.7 (± 34.0)	153.4 (± 12.0)
CF/PPG1.0	198.3 (± 19.1)	145.8 (± 15.8)	87.0 (± 9.3)	256.7 (± 24.7)	188.7 (± 20.5)	112.6 (± 12.1)
CF/PPG1.0/TT	114.7 (± 24.7)	93.0 (± 9.2)	91.7 (± 12.4)	152.9 (± 33.0)	124.0 (± 12.3)	122.2 (± 16.6)

### 7.3 Discussion

This study appears to be the first investigation of the mechanical properties of micro-wrapped yarn by graphene nanocomposite fibres and contributes to our understanding of the impact properties between thermoset composites and thermoplastic. This part of the project was undertaken in order to design wrapped yarn manufacturing of carbon fibre splitting processes and to evaluate the impact damage tolerance of hybrid wrapped yarn composites reinforced with CF/PP/graphene nanocomposite fibres. In addition, this study set out to compare CF/PP hybrid wrapped yarn composites and CF/PP/graphene wrapped yarn composites with a cross-ply structure. Furthermore, PP/graphene nanocomposite fibres were used as a through-thickness binder to produce 3D composites.

This study investigated improvements in the tensile properties of PP/graphene nanocomposite fibres based on graphene content and the number of drawing repeats. The drawn fibres were found to increase the mechanical properties of PP and PP/graphene nanocomposite fibres. Low content graphene fibres showed improvement at low loading speeds, and high content graphene fibres showed the highest tensile properties at high loading speeds. These findings support the premise that low loading speeds increase crystallinity and graphene particle distribution in the PP fibres. In contrast, because crystallinity does not increase at high loading speeds, Young's modulus was lower than that at low loading speeds.

The tensile properties of hybrid yarn composites were decreased due to low fibre volume fraction and poor compatibility between PP fibre and epoxy matrix. Further research is required that examines more closely the links between thermoset composites and thermoplastic fibres. In the CAI test, impact damage tolerance was improved by PP fibres and PP/graphene fibres; however, no improvements with the use of graphene nanocomposite fibre were found in this study. However, the interlaminar shear strength of carbon fibre composites was improved with graphene slightly. 3D composites, with a through-thickness binder of PPG1.0 fibres, exhibited reduced mechanical properties compared to that of cross-ply structure composites in all tests.

## **Chapter 8.**

### **Conclusion and Future Work**

This research aimed to improve the impact damage tolerance of thermoset composites by hybrid yarn. To reach this aim, hybrid yarn architecture, hybrid yarn manufacturing machine, and preform structure have been designed and studied in this research.

#### **8.1 Conclusion**

##### **8.1.1 Hybrid yarn manufacturing machine development**

Machine development successfully manufactured commingled, single wrapped, double wrapped and micro wrapped yarns. Fibre drawing, tow splitting and de-sizing processes have also been installed to solve problems with initial commingled yarns, such as fibre damage and non-homogeneous fibre distribution. The developed machine considered conductive carbon fibre to avoid the electrical cut. Thus, because this bespoke machine is designed and developed for carbon fibre hybrid yarn, it is useful, especially in the composite research area. It is not available in the market.

##### **8.1.2 Thermoplastic fibre drawing**

The thermoplastic fibre was drawn on the developed machine to increase the carbon fibre volume fraction. The diameter of pure PP fibre and PP/G1.0 fibre was decreased by 60% and 57% compared to undrawn fibres after the first drawing. They were then reduced by 4% and 6% more each after the second fibre drawing. Thus, fibre diameter decreased almost by the only one-time fibre drawing process. Peak stress and modulus were increased, and failure strain was decreased with increasing the number of fibre drawings. The maximum stress of non-drawn fibre was 28.9MPa, and its stress increased by 16 times, and the strain was decreased by 92 times more after three times fibre drawing at 10 mm/min loading speed. Tensile modulus also increased by 6.6 times more. Therefore, fibre volume fraction and tensile properties could increase significantly.

### **8.1.3 Graphene loaded fibre**

GNP and PP nanocomposite mono filament was used for the impact damage tolerance. The tensile strength of non-drawing graphene 0.25wt%/PP nanocomposites fibre increased from 28.9MPa to 40MPa, and modulus was enhanced from 1.0 GPa to 1.4GPa by graphene at 10 mm/min loading speed tensile test. Even though there was no significant improvement and difference in mechanical properties (tensile test, short beam strength, and impact test) by using GNP, it can be applied for multifunctional applications.

### **8.1.4 Micro wrapped yarn composites**

Impact energy can be spread efficiently inside tows rather than interlaminar because the micro wrapped yarn is made of fine PP mono fibres. This concept is similar to fracture behaviour in wood. In order to develop micro wrapped yarns, very fine tows that are not commercially available were needed. The cost-effective 1.5K fine carbon tows could obtain in this research as halves split of 3K carbon fibre. The peak force of pure CF and CF/PP micro wrapped yarn composites is 4995.5 N and 6440.4 N at the 20J energy impact test, respectively. The dent depth of composites was decreased, and the damaged area increased by micro wrapped yarn. The normalised strength of CF/PP (210.7MPa) and CF/PPG1.0 (188.7 MPa) composites increased by 44% and 29% after the 10J energy impact test compared to neat CF composites (146.1 MPa).

### **8.1.5 Impact damage tolerance of hybrid yarn composites**

Various hybrid yarns were investigated to improve the impact damage tolerance of thermoset composites. 3D structure commingled yarn and wrapped yarn composites were manufactured. Wrapped yarn composites show improved impact damage tolerance on a CAI test. However, commingled yarn composite decreased compared to neat carbon fibre composites. The compressive strength of commingled yarn composites decreased by 23%, but after PP multifilament de-sizing process, it decreased by 10% compared to neat CF composites at the 25J energy impact test. Single wrapped yarn composites increased by 14%; however, double wrapped yarn composites diminished by 31%. Thus, double wrapped yarn is worst than commingled yarn. These results highlight that hybrid yarn structure can also significantly influence impact damage tolerance.

---

### 8.1.6 UD vs 3D structure composites

UD and 3D structure composites do not show significant differences in the 10 J energy impact test. However, the UD structure was almost destroyed at 25J impact energy. Therefore, 3D structure composites would be useful for applications requiring high impact energy. After the impact test, the dent depth and damaged areas were shallow and wide in 3D composites compared to UD composites. These dent depth and damaged areas were becoming much shallower and wider using hybrid yarn instead of neat CF composites. Dent depth of the wrapped yarn composites was significantly decreased in the 3D composites (UDCF (1.07 mm) > UDCF-50-2PP (0.91 mm) > 3DCF (0.54 mm) > 3DCF-D50-2PP (0.41mm) > 3DCF-50-2PP (0.27 mm)). Therefore, these findings clearly indicate that thermoplastic fibres improve the impact properties of thermoset composites by spreading the impact energy through the composites and creating shallow dent depths.

### 8.1.7 Development of the hybrid yarn manufacturing systems

The fibre commingling, wrapping, and drawing processes were developed based on traditional production lines. The developed machine was designed and programmed to control motor speed, the solenoid air valve, and the temperature controller. Motor speed could be adjusted with a created keyboard or the up and down touch key on an HMI touch screen. It is recommended that the following improvements in the fibre hybridisation machine should be considered for later implementation: 1) not every process could be run at the same time because only one set of winding machinery has been installed. Installation of additional winding machinery would increase productivity; 2) the temperature of the current heating system is limited to a maximum of 232 °C; therefore, research can only be carried out in a limited temperature environment. The reason that this particular heater was chosen was due to the required temperature for PP fibre drawing being a maximum of 180 °C. If higher temperatures are required, the heating element should be replaced after checking the required voltage of the heater; and 3) the movement distance of the linear stroke in this machine was too short for collecting samples on the bobbin. The current linear stroke (325 mm) could be replaced with a longer one, with a total length of up to 600 mm, in order to obtain the samples on a wider bobbin area. The

---

length of the current bobbin is 280 mm, but the samples can only be obtained at a maximum of 100 mm due to the short length of the linear stroke.

### **8.1.8 Hybrid wrapped yarns at different wrapping conditions**

Wrapped yarn with PP multifilament was produced at different wrap densities (50, 75, 100, and 125 w/m), the number of PP fibres (1PP, 2PP, and 3PP), and wrapping types (single- or double-sided wrapping). The impact properties did not show significant differences at different wrapping densities; however, wrapped yarn composites showed much smoother curves than that of CF composites in force-time graphs from the weigh drop test. Absorbed energy increased with an increasing number of PP fibres, but the compression strength of wrapped yarn with two PP fibres showed the highest values (2PP>1PP>3PP). It was apparent that PP fibres at sub-optimal quantities were unable to protect the composites, while an excess of PP fibres resulted in resin-rich areas in the composites and decreased the fibre volume fraction. Finally, the impact properties of the double-wrapped yarn structure composites were considerably decreased due to overlapping sections, which could easily generate resin-rich areas that lead to weakening.

### **8.1.9 CF and high-temperature engineering thermoplastic composites**

Carbon fibre and PA6 or PA6/graphene nanocomposite multifilament were used to manufacture single-wrapped yarns and to produce UD composites. PA6 hybrid yarn composites showed a higher peak force and rebound energy compared to that of neat CF and PA6/graphene hybrid yarn composites, based on the weight drop impact test. The impact damage tolerance of PA6/graphene hybrid yarn composites outdo neat CF composites; however, no significant differences compared to that of neat PA6 hybrid yarn composites were observed. A possible explanation for these results may be that graphene nanocomposite multifilament reduced the impact dispersion ability, such that the damaged area was decreased. However, dent depth was increased compared to that of neat PA6 hybrid yarn composites (CF>PA6/G>PA6 composites).

Two different sizes of PEI veils were prepared at widths of 10 mm and 200 mm. Tapes of 10 mm width PEI composites had a lower carbon fibre volume fraction due to high preform thickness. Furthermore, impact damage tolerance was not improved by PEI



hybridisation. There are several possible explanations for these results. First, because the binder materials of PEI veils do not require compatibility with epoxy resin, damage tolerance of 200 mm width PEI composites was significantly decreased. Second, the 10 mm width hybridisation process resulted in thicker preforms and a diminished fibre volume fraction.

### **8.1.10 Micro wrapped yarn with graphene nanocomposite fibres**

This is the first study to analyse the effects of impact damage tolerance of hybrid yarn epoxy composites, including carbon fibres and PP/graphene nanocomposites fibres. The tensile properties of PP/graphene nanocomposites have shown improvements associated with the number of drawing repeats and graphene contents. The drawing process increased fibre strength and stiffness by increasing the number of drawings. Furthermore, fibres with the lowest graphene content (0.25%) showed improvements at low loading speeds. In contrast, fibres with the highest graphene content (1%) had the highest tensile strength at high loading speeds. This research supports the premise that low loading speeds increase crystallinity and graphene particle distribution in the PP fibres. However, impact damage tolerance of thermoset composites with micro wrapped yarn did not improve with the graphene nanocomposite fibres compared to neat PP hybrid yarn composites.

## **8.2 Future work**

### **8.2.1 Enhancing interface properties of nanocomposites fibres**

It would be interesting to assess the impact damage tolerance of thermoset composites as increasing interface strength between thermoplastic and nanoparticles. In this research, graphene/PP nanocomposite fibres increased the fibre volume fraction and damage tolerance. However, there was no significant difference in mechanical properties between graphene and without graphene fibres. Therefore, to stack the nanoparticles in the polymer more strongly, increasing interface interaction using chemicals is suggested for future work instead of mechanically mixing particles and polymers.

### **8.2.2 Improve micro wrapped yarn**

This research improved the hybrid yarn manufacturing process from commingling and wrapping to micro-wrapping to enhance impact damage tolerance of thermoset composites. It is important to develop fine PP fibre production systems and tow splitting process to improve the quality of the micro-wrapped yarn composites. In this study, the diameter of the drawn fibre is around 100µm. To decrease fibre diameter and increase carbon fibre volume fraction, fine PP production system is required. Furthermore, finer tows are important to increase fibre distribution and spread impact energy in composites efficiently. Because fine carbon tows are highly expensive and cause fibre damage during manufacturing, process development could increase micro wrapped yarn quality.

### **8.2.3 Expansion of research with new air nozzle**

Commingling processes that use an air nozzle are not complex; therefore, they are able to produce large quantities of fibre at a low cost. However, current commingling processes with air nozzles are limited in terms of increases in fibre distribution and cause significant damage to the fibres. Thus, the quality of commingled yarn could be increased by modifying the air nozzle. The proposed design of a potential new air nozzle is shown in Appendix D. An air nozzle can be applied to the fibre drawing process to enhance the crystallinity of polymer fibres by using hot air. The hybrid yarn manufacturing process can be simplified and improved using an air nozzle.

### **8.2.4 Hybrid yarn manufacturing depends on machine setting**

The developed hybrid yarn manufacturing machine can control the temperature, winding speed, and air pressure. Because those parameters influence to mechanical properties of thermoset composites, manufacturing conditions can be studied under more subdivided air pressure and temperature. The fibre damage at different air pressure can be more studied. Furthermore, the crystallinity of thermoplastic fibre at different drawing temperatures can be analysed with DSC (Differential scanning calorimetry) and XRD (X-ray powder diffraction) analysis.

### **8.2.5 Improving the impact behaviour of thermoset composites**

Further work is needed to improve the mechanical properties of hybrid yarn composites. In this study, the tensile strength of CF/PP hybrid yarn thermoset composites was found to be decreased, and CF/PEI hybrid thermoset composites did display decreased compressive strength after impact compared to that of neat CF thermoset composites. These results may be explained by the low carbon-fibre fraction in thermoplastic fibres, as well as the low compatibility between the epoxy resin and thermoplastic fibres. PEI binder materials, such as polyester, are not compatible with epoxy resin. This issue should be further studied, for example, developing CF modification and coating nanoparticles to improve the adhesive strength between the matrix and reinforcement. The impact test of the current hybrid yarn composites showed areas of high damage, including thermoplastic fibre delamination, in particular. Therefore, more research is needed to further elucidate the effects of increased tensile properties and to decrease the amount of damaged areas in hybrid yarns.

---

## References

- [1] G. Zhou and L. J. Greaves, *Damage resistance and tolerance of thick laminated woven roving GFRP plates subjected to low-velocity impact*. Woodhead Publishing Ltd, 2000.
- [2] R. Alagirusamy, “Hybrid yarns for thermoplastic composites,” in *Technical Textile Yarns*, 2010.
- [3] P. Potluri, P. Hogg, M. Arshad, D. Jetavat, and P. Jamshidi, “Influence of fibre architecture on impact damage tolerance in 3D woven composites,” *Appl. Compos. Mater.*, vol. 19, no. 5, pp. 799–812, 2012.
- [4] J. K. Kim, D. B. MacKay, and Y. W. Mai, “Drop-weight impact damage tolerance of CFRP with rubber-modified epoxy matrix,” *Composites*, vol. 24, no. 6, pp. 485–494, 1993.
- [5] N. L. Hancox, *An overview of the impact behaviour of fibre-reinforced composites*. Woodhead Publishing Ltd, 2000.
- [6] A. Duarte, I. Herszberg, and R. Paton, “Impact resistance and tolerance of interleaved tape laminates,” *Compos. Struct.*, vol. 47, no. 1–4, pp. 753–758, 1999.
- [7] S. K. Sharma and B. V. Sankar, “Effect of stitching on impact and interlaminar properties of graphite/epoxy laminates,” *Journal of Thermoplastic Composite Materials*, vol. 10, no. 3, pp. 241–253, 1997.
- [8] P. J. Hogg, “Toughening of thermosetting composites with thermoplastic fibres,” *Mater. Sci. Eng. A*, 2005.
- [9] E. Selver and P. Potluri, “Intra-tow micro-wrapping for damage tolerance,” *Compos. Sci. Technol.*, 2021.
- [10] K. Magniez, T. Chaffraix, and B. Fox, “Toughening of a carbon-fibre composite using electrospun poly(hydroxyether of bisphenol A) nanofibrous membranes

- 
- through inverse phase separation and inter-domain etherification,” *Materials (Basel)*, 2011.
- [11] Z. Lingang, “WITHDRAWN: Investigations on damage resistance of carbon fiber composite panels toughened using veils,” *Chinese J. Aeronaut.*, 2013.
- [12] W. H. Lu, F. S. Liao, A. C. Su, P. W. Kao, and T. J. Hsu, “Effect of interleaving on the impact response of a unidirectional carbon/epoxy composite,” *Composites*, vol. 26, no. 3, pp. 215–222, Mar. 1995.
- [13] H. R. Mankodi, *Developments in hybrid yarns*. Woodhead Publishing Limited, 2011.
- [14] E. Selver, P. Potluri, P. Hogg, and C. Soutis, “Impact damage tolerance of thermoset composites reinforced with hybrid commingled yarns,” *Compos. Part B Eng.*, vol. 91, pp. 522–538, 2016.
- [15] X. Huang and S. Zhao, “Damage tolerance characterization of carbon fiber composites at a component level: A thermoset carbon fiber composite,” *J. Compos. Mater.*, vol. 52, no. 1, pp. 37–46, 2018.
- [16] “Characterization of Thermosets Part 21: Tensile Testing of Polymers; A Molecular Interpretation - Polymer Innovation Blog.” [Online]. Available: <https://polymerinnovationblog.com/characterization-thermosets-part-21-tensile-testing-polymers-molecular-interpretation/>. [Accessed: 11-Nov-2021].
- [17] C. Sonnenfeld, H. Mendil-Jakani, R. Agogué, P. Nunez, and P. Beauchêne, “Thermoplastic/thermoset multilayer composites: A way to improve the impact damage tolerance of thermosetting resin matrix composites,” *Compos. Struct.*, 2017.
- [18] S. Z. H. Shah, S. Karuppanan, P. S. M. Megat-Yusoff, and Z. Sajid, “Impact resistance and damage tolerance of fiber reinforced composites: A review,” *Composite Structures*. 2019.
- [19] N. Țăranu, V. Munteanu, I. Ențuc, and G. Opreșan, “Application of Modern
-

- 
- Polymeric Composite Materials in Industrial Construction,” *Bull. Polytech. Inst. Jassy*, 2010.
- [20] D. Liu and L. E. Malvern, “Matrix Cracking in Impacted Glass/Epoxy Plates,” *J. Compos. Mater.*, 1987.
- [21] “Defects and damage and their role in the failure of polymer composites,” *Fail. Anal. Fractography Polym. Compos.*, pp. 356–440, Jan. 2009.
- [22] P. Bajurko, “Comparison of damage resistance of thermoplastic and thermoset carbon fibre-reinforced composites.”
- [23] H. Liu *et al.*, “The behaviour of thermoplastic and thermoset carbon fibre composites subjected to low-velocity and high-velocity impact,” *J. Mater. Sci.*, vol. 55.
- [24] Y. Huang, W. Wang, C. Liu, and A. J. Rosakis, “Analysis of intersonic crack growth in unidirectional fiber-reinforced composites,” *J. Mech. Phys. Solids*, vol. 47, no. 9, pp. 1893–1916, 1999.
- [25] K. M. Elawadly and M. E.- Sayed, “Crack propagation in unidirectional fiber laminated composites,” 2002.
- [26] A. P. Mouritz, “Tensile fatigue properties of 3D composites with through-thickness reinforcement,” *Compos. Sci. Technol.*, vol. 68, no. 12, pp. 2503–2510, 2008.
- [27] S. Rudov-Clark and A. P. Mouritz, “Tensile fatigue properties of a 3D orthogonal woven composite,” *Compos. Part A Appl. Sci. Manuf.*, vol. 39, no. 6, pp. 1018–1024, 2008.
- [28] A. P. Mouritz and B. N. Cox, “A mechanistic interpretation of the comparative in-plane mechanical properties of 3D woven, stitched and pinned composites,” *Compos. Part A Appl. Sci. Manuf.*, vol. 41, no. 6, pp. 709–728, 2010.
- [29] J. P. Quinn, A. T. McIlhagger, and R. McIlhagger, “Examination of the failure of 3D woven composites,” *Compos. Part A Appl. Sci. Manuf.*, vol. 39, no. 2, pp. 273–
-

- 
- 283, 2008.
- [30] D. Kreculj and B. Rasuo, “7 - Impact damage modeling in laminated composite aircraft structures,” in *Woodhead Publishing Series in Composites Science and Engineering*, M. Jawaid and M. B. T.-S. C. for A. A. Thariq, Eds. Woodhead Publishing, 2018, pp. 125–153.
- [31] A. P. Mouritz, “Mechanics of 3D Fibre Reinforced Polymer Composites,” *Encycl. Contin. Mech.*, pp. 1533–1549, 2020.
- [32] B. Yu, R. S. Bradley, C. Soutis, P. J. Hogg, and P. J. Withers, “2D and 3D imaging of fatigue failure mechanisms of 3D woven composites,” *Compos. Part A Appl. Sci. Manuf.*, vol. 77, pp. 37–49, 2015.
- [33] P. Potluri, P. Hogg, M. Arshad, D. Jetavat, and P. Jamshidi, “Influence of fibre architecture on impact damage tolerance in 3D woven composites,” *Appl. Compos. Mater.*, vol. 19, no. 5, pp. 799–812, 2012.
- [34] K. van Rijswijk and H. E. N. Bersee, “Reactive processing of textile fiber-reinforced thermoplastic composites - An overview,” *Compos. Part A Appl. Sci. Manuf.*, vol. 38, no. 3, pp. 666–681, 2007.
- [35] C. Sonnenfeld, H. Mendil-Jakani, R. Agogu , P. Nunez, and P. Beauch ne, “Thermoplastic/thermoset multilayer composites: A way to improve the impact damage tolerance of thermosetting resin matrix composites,” *Compos. Struct.*, vol. 171, pp. 298–305, 2017.
- [36] P. Merati, C. Davis, K. H. Chen, and J. P. Johnson, “Underhood buoyancy driven flow—an experimental study,” *J. Heat Transfer*, 2011.
- [37] E. Ernault, E. Richaud, and B. Fayolle, “Origin of epoxies embrittlement during oxidative ageing,” *Polym. Test.*, 2017.
- [38] T. A. Sebaey, “Effect of exposure temperature on the crashworthiness of carbon/epoxy composite rectangular tubes under quasi-static compression,” *Polymers (Basel)*, 2020.
-

- 
- [39] Y. Liu, B. Zwingmann, and M. Schlaich, "Carbon fiber reinforced polymer for cable structures-a review," *Polymers*. 2015.
- [40] A. Chilali, W. Zouari, M. Assarar, H. Kebir, and R. Ayad, "Analysis of the mechanical behaviour of flax and glass fabrics-reinforced thermoplastic and thermoset resins," *J. Reinf. Plast. Compos.*, vol. 35, no. 16, pp. 1217–1232, 2016.
- [41] A. Najafi, "A facile and scalable coating technique of carbon fibers with carbon nanoparticles for surface adhesion enhancement of fibers and resin in 2D C/C composites," *Ceram. Int.*, 2017.
- [42] S. Laurenzi, S. Botti, A. Rufoloni, and M. G. Santonicola, "Fracture Mechanisms in Epoxy Composites Reinforced with Carbon Nanotubes," *Procedia Eng.*, vol. 88, pp. 157–164, Jan. 2014.
- [43] F. Lionetto, R. Dell'Anna, F. Montagna, and A. Maffezzoli, "Ultrasonic Assisted Consolidation of Commingled Thermoplastic/Glass Fiber Rovings," *Front. Mater.*, vol. 2, no. April, pp. 1–9, 2015.
- [44] M. M. Gudarzi and F. Sharif, "Enhancement of dispersion and bonding of graphene-polymer through wet transfer of functionalized graphene oxide," *Express Polym. Lett.*, 2012.
- [45] E. Mäder, J. Rausch, and N. Schmidt, "Commingled yarns - Processing aspects and tailored surfaces of polypropylene/glass composites," *Compos. Part A Appl. Sci. Manuf.*, vol. 39, no. 4, pp. 612–623, 2008.
- [46] M. N. Saleh and C. Soutis, "Recent advancements in mechanical characterisation of 3D woven composites," *Mech. Adv. Mater. Mod. Process.*, 2017.
- [47] A. P. Mouritz and B. N. Cox, "A mechanistic approach to the properties of stitched laminates," *Compos. Part A Appl. Sci. Manuf.*, vol. 31, no. 1, pp. 1–27, Jan. 2000.
- [48] A. P. Mouritz, "Ballistic impact and explosive blast resistance of stitched composites," *Compos. Part B Engineering*, vol. 32, no. 5, pp. 431–439, 2001.
- [49] P. Potluri, E. Kusak, and T. Y. Reddy, "Novel stitch-bonded sandwich composite
-



- 
- structures,” *Compos. Struct.*, vol. 59, no. 2, pp. 251–259, 2003.
- [50] L. Tong, A. P. Mouritz, and M. K. Bannister, “Manufacture of 3D Fibre Preforms,” *3D Fibre Reinf. Polym. Compos.*, pp. 13–46, 2002.
- [51] T. Gries, M. Raina, T. Quadflieg, and O. Stolyarov, *Manufacturing of Textiles for Civil Engineering Applications*. Elsevier Ltd., 2016.
- [52] M. Matveev, V. Koncherry, S. S. Roy, P. Potluri, and A. Long, “Novel textile preforming for optimised fibre architectures,” in *IOP Conference Series: Materials Science and Engineering*, 2018.
- [53] G. Dell’Anno, D. D. Cartié, I. K. Partridge, and A. Rezai, “Exploring mechanical property balance in tufted carbon fabric/epoxy composites,” *Compos. Part A Appl. Sci. Manuf.*, vol. 38, no. 11, pp. 2366–2373, 2007.
- [54] V. A. Guénon, T.-W. Chou, and J. W. Gillespie Jr., “Toughness properties of a three-dimensional carbon-epoxy composite,” *J. Mater. Sci.*, vol. 24, no. 11, pp. 4168–4175, 1989.
- [55] A. P. Mouritz, C. Bains, and I. Herszberg, “Mode I interlaminar fracture toughness properties of advanced textile fibreglass composites,” *Compos. Part A Appl. Sci. Manuf.*, vol. 30, no. 7, pp. 859–870, 1999.
- [56] J. Brandt, K. Drechsler, and F. J. Arendts, “Mechanical performance of composites based on various three-dimensional woven-fibre preforms,” *Compos. Sci. Technol.*, vol. 56, no. 3, pp. 381–386, 1996.
- [57] S. Chou, H. C. Chen, and H. E. Chen, “Effect of weave structure on mechanical fracture behavior of three-dimensional carbon fiber fabric reinforced epoxy resin composites,” *Compos. Sci. Technol.*, vol. 45, no. 1, pp. 23–35, 1992.
- [58] A. P. Mouritz, M. K. Bannister, P. J. Falzon, and K. H. Leong, “Review of applications for advanced three-dimensional fibre textile composites,” *Compos. Part A Appl. Sci. Manuf.*, vol. 30, no. 12, pp. 1445–1461, 1999.
- [59] E. Barjasteh, C. Sutanto, T. Reddy, and J. Vinh, “A graphene/graphite-based
-

- 
- conductive polyamide 12 interlayer for increasing the fracture toughness and conductivity of carbon-fiber composites,” *J. Compos. Mater.*, vol. 51, no. 20, pp. 2879–2887, 2017.
- [60] G. J. Ehlert, Y. Lin, and H. A. Sodano, “Carboxyl functionalization of carbon fibers through a grafting reaction that preserves fiber tensile strength,” *Carbon N. Y.*, 2011.
- [61] B.-D. Choi, O. Diestel, and P. Offermann, “Commingled CF/PEEK Hybrid Yarns for Use in Textile Reinforced High Performance Rotors,” *12th Int. Conf. Compos. Mater.*, pp. 796–806, 1999.
- [62] M. Golzar, H. Brünig, and E. Mäder, “Commingled hybrid yarn diameter ratio in continuous fiber-reinforced thermoplastic composites,” *J. Thermoplast. Compos. Mater.*, vol. 20, no. 1, pp. 17–26, 2007.
- [63] B. Lauke, U. Bunzel, and K. Schneider, “Effect of hybrid yarn structure on the delamination behaviour of thermoplastic composites,” *Compos. Part A Appl. Sci. Manuf.*, vol. 29, no. 11, pp. 1397–1409, 1998.
- [64] N. Wiegand and E. Mäder, “Commingled Yarn Spinning for Thermoplastic/Glass Fiber Composites,” *Fibers*, vol. 5, no. 3, p. 26, 2017.
- [65] K. Pietsch and H. Fuchs, *Textile Materials for Lightweight Constructions*. 2016.
- [66] P. Kravaev, O. Stolyarov, G. Seide, and T. Gries, “Influence of process parameters on filament distribution and blending quality in commingled yarns used for thermoplastic composites,” *J. Thermoplast. Compos. Mater.*, vol. 27, no. 3, pp. 350–363, 2014.
- [67] V. Ogale and R. Alagirusamy, “Properties of GF/PP commingled yarn composites,” *J. Thermoplast. Compos. Mater.*, vol. 21, no. 6, pp. 511–523, 2008.
- [68] R. Alagirusamy and V. Ogale, “Development and characterization of GF/PET, GF/nylon, and GF/PP commingled yarns for thermoplastic composites,” *J. Thermoplast. Compos. Mater.*, vol. 18, no. 3, pp. 269–285, 2005.
-

- 
- [69] H. R. Mankodi, *Developments in hybrid yarns*, no. January. 2011.
- [70] Nursyahirah Binti Md Nor, “Effect of rewinding on mechanical properties and filament distribution of commingled yarn,” The University of Manchester, 2017.
- [71] J. Schafer, O. Stolyarov, R. Ali, C. Greb, G. Seide, and T. Gries, “Process-structure relationship of carbon/ polyphenylene sulfide commingled hybrid yarns used for thermoplastic composites,” *J. Ind. Text.*, vol. 45, no. 6, pp. 1661–1673, 2016.
- [72] Z. Xu, M. Zhang, S. H. Gao, G. Wang, S. Zhang, and J. Luan, “Study on mechanical properties of unidirectional continuous carbon fiber-reinforced PEEK composites fabricated by the wrapped yarn method,” *Polym. Compos.*, vol. 40, no. 1, pp. 56–69, 2019.
- [73] B. Baghaei, M. Skrifvars, and L. Berglin, “Manufacture and characterisation of thermoplastic composites made from PLA/hemp co-wrapped hybrid yarn prepregs,” *Compos. Part A Appl. Sci. Manuf.*, 2013.
- [74] I. Dabrowska, L. Fambri, A. Pegoretti, M. Slouf, T. Vackova, and J. Kolarik, “Spinning, drawing and physical properties of polypropylene nanocomposite fibers with fumed nanosilica,” *Express Polym. Lett.*, vol. 9, no. 3, pp. 277–290, 2015.
- [75] W. Zhang, N. Ning, Y. Gao, F. Xu, and Q. Fu, “Stretching induced interfacial crystallization and property enhancement of poly(l-lactide)/single-walled carbon nanotubes fibers,” *Compos. Sci. Technol.*, vol. 83, pp. 47–53, Jun. 2013.
- [76] I. F. of Robotics, “Home - World Robotics 2014,” *International Federation of Robotics(IFR) Statistical Department*, 2014. .
- [77] M. Wilson and M. Wilson, “Chapter 2 – Industrial Robots,” *Implement. Robot Syst.*, pp. 19–38, 2015.
- [78] M. Wilson, “Automation System Components,” *Implement. Robot Syst.*, pp. 39–73, 2015.
- [79] T. Sharif, “Robotic Approach to Low-Cost Manufacturing of 3D Preforms with
-

- 
- Dry Fibres | Research Explorer | The University of Manchester,” p. 195, 2012.
- [80] K. Kozaczuk, “Automated Fiber Placement Systems Overview,” *Trans. Inst. Aviat.*, vol. 245, no. 4, pp. 52–59, 2016.
- [81] “The first composite fuselage section for the first composite commercial jet.” [Online]. Available: <https://www.compositesworld.com/articles/the-first-composite-fuselage-section-for-the-first-composite-commercial-jet>. [Accessed: 07-Jul-2020].
- [82] ASM International, “ASM Handbook Vol 21 Composites,” *Technology*, vol. 2, p. 3470, 2001.
- [83] C. S. Lopes, Z. Gürdal, and P. P. Camanho, “Variable-stiffness composite panels: Buckling and first-ply failure improvements over straight-fibre laminates,” *Comput. Struct.*, vol. 86, no. 9, pp. 897–907, 2008.
- [84] Z. Gürdal, B. F. Tatting, and C. K. Wu, “Variable stiffness composite panels: Effects of stiffness variation on the in-plane and buckling response,” *Compos. Part A Appl. Sci. Manuf.*, vol. 39, no. 5, pp. 911–922, 2008.
- [85] C. S. Lopes, Z. Gürdal, and P. P. Camanho, “Tailoring for strength of composite steered-fibre panels with cutouts,” *Compos. Part A Appl. Sci. Manuf.*, vol. 41, no. 12, pp. 1760–1767, 2010.
- [86] D. S. Cairns, L. B. Ilcewicz, and T. Walker, “Far-field and near-field strain response of Automated Tow-Placed laminates to stress concentrations,” *Compos. Eng.*, vol. 3, no. 11, 1993.
- [87] B. F. Tatting and Z. Guerdal, “Design and Manufacture of Elastically Tailored Tow Placed Plates,” *Nasa Arch.*, no. August, 2002.
- [88] D. S. Cairns, L. B. Ilcewicz, T. Walker, and P. J. Minguet, “Fracture scaling parameters of inhomogeneous microstructure in composite structures,” *Compos. Sci. Technol.*, vol. 53, no. 2, pp. 223–231, 1995.
- [89] M. P. Wiehn and R. D. Hale, “Low cost robotic fabrication methods for tow
-

- 
- placement,” in *International SAMPE Symposium and Exhibition (Proceedings)*, 2002, vol. 47 II, pp. 1842–1852.
- [90] D. C. A. S. S. S. Potluri, Prasad; Kennon, Richard; Jetavat, “Complex Preforming With 3D Weaving and Dry Fibre Placement,” *Compos. week*, no. April 2014, pp. 9–12, 2013.
- [91] V. Koncherry *et al.*, “Novel manufacturing techniques for optimized 3D multiaxial orthogonal preform,” in *ICCM International Conferences on Composite Materials*, 2019.
- [92] X. C. Sun and S. R. Hallett, “Failure mechanisms and damage evolution of laminated composites under compression after impact (CAI): Experimental and numerical study,” *Compos. Part A Appl. Sci. Manuf.*, 2018.
- [93] N. H. Nash, T. M. Young, P. T. McGrail, and W. F. Stanley, “Inclusion of a thermoplastic phase to improve impact and post-impact performances of carbon fibre reinforced thermosetting composites - A review,” *Mater. Des.*, 2015.
- [94] S. Mukhopadhyay, B. L. Deopura, and R. Alagirusamy, “Mechanical properties of polypropylene filaments drawn on varying post spinning temperature gradients,” *Fibers Polym.*, vol. 7, no. 4, pp. 432–435, 2006.
- [95] H. Dalfi, K. B. Katnam, and P. Potluri, “Intra-laminar toughening mechanisms to enhance impact damage tolerance of 2D woven composite laminates via yarn-level fiber hybridization and fiber architecture,” *Polym. Compos.*, vol. 40, no. 12, pp. 4573–4587, 2019.
- [96] R. Perneder and I. Osborne, *Handbook timing belts: Principles, calculations, applications*. 2012.
- [97] R. Alagirusamy, V. Ogale, and M. Bhowmick, “Air flow behaviour in commingling nozzles and their influence on properties of commingled yarns,” *Indian J. Fibre Text. Res.*, vol. 32, no. 4, pp. 414–420, 2007.
- [98] “Toray Composite Materials America, Inc. > Home.” [Online]. Available:
-

- 
- <https://www.toraycma.com/>. [Accessed: 02-Dec-2020].
- [99] “Polypropylene Filament Yarn by Drake Extrusion.” [Online]. Available: <https://www.drakeextrusion.com/filament-yarn.php>. [Accessed: 02-Dec-2020].
- [100] “Bespoke extrusion equipment for the manufacture of absorbable yarns.” [Online]. Available: <https://www.fetuk.com/>. [Accessed: 08-Mar-2021].
- [101] “First Graphene - First Graphene.” [Online]. Available: <https://firstgraphene.net/>. [Accessed: 24-Oct-2020].
- [102] “Technical Fibre Products - Technical Nonwoven Solutions.” [Online]. Available: <https://www.tfpglobal.com/>. [Accessed: 26-Jun-2020].
- [103] “Teijin Carbon – Tenax™ Filament Yarn.” [Online]. Available: <https://www.tejincarbon.com/products/tenaxr-carbon-fiber/tenaxr-filament-yarn>. [Accessed: 09-Aug-2021].
- [104] V. Koncherry, P. Potluri, and A. Fernando, “Multifunctional Carbon Fibre Tapes for Automotive Composites,” *Appl. Compos. Mater.*, 2017.
- [105] M. R. Sloan, J. R. Wright, and K. E. Evans, “The helical auxetic yarn - A novel structure for composites and textiles; Geometry, manufacture and mechanical properties,” *Mech. Mater.*, vol. 43, no. 9, pp. 476–486, 2011.
- [106] “IN2 EPOXY INFUSION RESIN-Technical Datasheet.”
- [107] D. L. Deborah Chung, *3 - Polymer-Matrix Composites: Structure and Processing*, Second Edi. Elsevier Inc., 2017.
- [108] ASTM D 792-20, “Standard Test Methods for Density and Specific Gravity ( Relative Density ) of Plastics,” *Annu. B. ASTM Stand.*, 2020.
- [109] W. S. Precision, “Standard Test Method for Short-Beam Strength of Polymer Matrix Composite Materials,” *Annu. B. ASTM Stand.*, vol. 00, no. Reapproved 2006, pp. 1–8, 2011.
- [110] J. C. Prichard and P. J. Hogg, “The role of impact damage in post-impact
-

- 
- compression testing,” *Composites*, 1990.
- [111] L. Sorrentino *et al.*, “Damage tolerance assessment of the interface strength gradation in thermoplastic composites,” *Compos. Part B Eng.*, vol. 113, pp. 111–122, Mar. 2017.
- [112] S. Fidan, T. Snmazçelik, and E. Avcu, “Internal damage investigation of the impacted glass/glassaramid fiber reinforced composites by micro-computerized tomography,” *NDT E Int.*, vol. 51, pp. 1–7, Oct. 2012.
- [113] R. C. L. Dutra, B. G. Soares, E. a. Campos, and J. L. G. Silva, “Hybrid composites based on polypropylene and carbon fiber and epoxy matrix,” *Polymer (Guildf.)*, vol. 41, no. 10, pp. 3841–3849, 2000.
- [114] N. Dubary, G. Taconet, C. Bouvet, and B. Vieille, “Influence of temperature on the impact behavior and damage tolerance of hybrid woven-ply thermoplastic laminates for aeronautical applications,” *Compos. Struct.*, 2017.
- [115] O. Monticelli, S. Bocchini, A. Frache, E. S. Cozza, O. Cavalleri, and L. Prati, “Simple method for the preparation of composites based on PA6 and partially exfoliated graphite,” *J. Nanomater.*, 2012.
- [116] D. Zhang, Y. Sun, L. Chen, and N. Pan, “A comparative study on low-velocity impact response of fabric composite laminates,” *Mater. Des.*, 2013.
- [117] T. Mitrevski, I. H. Marshall, and R. Thomson, “The influence of impactor shape on the damage to composite laminates,” *Compos. Struct.*, 2006.
- [118] L. S. Sutherland and C. G. Soares, “Impact characterisation of low fibre-volume glass reinforced polyester circular laminated plates,” *Int. J. Impact Eng.*, 2005.
- [119] E. Sevkat, B. Liaw, F. Delale, and B. B. Raju, “Drop-weight impact of plain-woven hybrid glass-graphite/toughened epoxy composites,” *Compos. Part A Appl. Sci. Manuf.*, 2009.
- [120] T. Lu, X. Chen, H. Wang, L. Zhang, and Y. Zhou, “Comparison of low-velocity impact damage in thermoplastic and thermoset composites by non-destructive
-

- 
- three-dimensional X-ray microscope,” *Polym. Test.*, 2020.
- [121] R. Martin and G. Murri, “Characterization of Mode I and Mode II Delamination Growth and Thresholds in AS4/PEEK Composites,” in *Composite Materials: Testing and Design (Ninth Volume)*, 2009.
- [122] R. Várdai *et al.*, “Effect of various organic fibers on the stiffness, strength and impact resistance of polypropylene; a comparison,” 2020.
- [123] M. Nili and V. Afrouhsabet, “The effects of silica fume and polypropylene fibers on the impact resistance and mechanical properties of concrete,” *Constr. Build. Mater.*, vol. 24, no. 6, pp. 927–933, Jun. 2010.
- [124] T. Kuilla, S. Bhadra, D. Yao, N. H. Kim, S. Bose, and J. H. Lee, “Recent advances in graphene based polymer composites,” *Progress in Polymer Science (Oxford)*. 2010.
- [125] D. Galpaya, M. Wang, M. Liu, N. Motta, E. Waclawik, and C. Yan, “Recent Advances in Fabrication and Characterization of Graphene-Polymer Nanocomposites,” *Graphene*, 2012.
- [126] J. Wang, F. Song, Y. Ding, and M. Shao, “The incorporation of graphene to enhance mechanical properties of polypropylene self-reinforced polymer composites,” *Mater. Des.*, 2020.
- [127] G. G. Ojoc, L. C. Titire, A. Maria, M. Boțan, G. C. Cristea, and L. Deleanu, “Mechanical Characterization of two blends PP + PA6 + EPDM . Part 2 . Results of Tensile Tests,” *Preprints*, no. April, 2021.
- [128] Z. Li, X. Li, C. Sun, Y. Shi, Q. Zhang, and Q. Fu, “Effect of nanoparticles on fibril formation and mechanical performance of olefinic block copolymer (OBC)/polypropylene (PP) microfibrillar composites,” *RSC Adv.*, 2016.
- [129] S. Quiles-Díaz *et al.*, “Influence of the chemical functionalization of graphene on the properties of polypropylene-based nanocomposites,” *Compos. Part A Appl. Sci. Manuf.*, 2017.
-



- 
- [130] J. Wang, C. Ma, G. Chen, and P. Dai, "Interlaminar fracture toughness and conductivity of carbon fiber/epoxy resin composite laminate modified by carbon black-loaded polypropylene non-woven fabric interleaves," *Compos. Struct.*, 2020.
- [131] C. Atas and O. Sayman, "An overall view on impact response of woven fabric composite plates," *Compos. Struct.*, vol. 82, no. 3, pp. 336–345, Feb. 2008.
- [132] H. F. AL-Qrimli, F. A. Mahdi, and F. B. Ismail, "Carbon/Epoxy Woven Composite Experimental and Numerical Simulation to Predict Tensile Performance," *Adv. Mater. Sci. Appl.*, 2015.
- [133] K. K. Chawla, *Composite materials: Science and engineering, third edition*. 2012.
- [134] E. Menessier, J. P. Dument, A. Geutte, R. Paillet, L. Rabardel, and R. Naslain, "Axial and Radial Coefficients of Thermal Expansion of Carbon Fibers in the 20°–430°C Temperature Range as Derived from the Thermal Expansion of 1-D-C-SiO<sub>2</sub>(B<sub>2</sub>O<sub>3</sub>) Composites," 2008.
- [135] John B. Wachtman, Ed., *13th Annual Conference on Composites and Advanced Ceramic Materials, Part 2 of 2 - Google Books*, vol. 10. 1989.
- [136] W. J. Shanahan, D. W. Lloyd, and J. W. S. Hearle, "Characterizing the Elastic Behavior of Textile Fabrics in Complex Deformations.," *Text. Res. J.*, vol. 48, no. 9, pp. 495–505, 1978.
- [137] A. K. Kaw, *Mechanics of composite materials, second edition*. 2005.
- [138] M. Nirbhay, A. Dixit, R. K. Misra, and H. S. Mali, "Tensile Test Simulation of CFRP Test Specimen Using Finite Elements," *Procedia Mater. Sci.*, 2014.
- [139] A. Avdic and U. K. Saha, "Simulating a tensile test of a carbon fiber composite test specimen in ABAQUS," University of Skovde, 2011.
- [140] R. Alagirusamy, V. Ogale, A. Vaidya, and P. M. V Subbarao, "Effect of jet design on commingling of glass/nylon filaments," *J. Thermoplast. Compos. Mater.*, vol. 18, no. 3, pp. 255–268, 2005.
-

- 
- [141] R. Alagirusamy and V. Ogale, “Commingled and air jet-textured hybrid yarns for thermoplastic composites,” *J. Ind. Text.*, vol. 33, no. 4, pp. 223–243, 2004.
- [142] H. R. Mankodi, “Effect of Nozzle Design and Processing Parameter on Characteristics of Glass / Polypropylene Hybrid Yarns Effect of Nozzle Design and Processing Parameter on Characteristics of Glass / Polypropylene Hybrid Yarns,” *J. Eng. Res. Appl.*, vol. 4, no. December 2014, pp. 144–149, 2016.
- [143] S. P. Rwei, H. I. Pai, and I. C. Wang, “Fluid Simulation of the Airflow in Interlacing Nozzles,” *Text. Res. J.*, vol. 71, no. 7, pp. 630–634, 2001.
- [144] H. K. Versteeg, M. Acar, and S. Bilgin, “Effect of Geometry on the Performance of Intermingling Nozzles,” *Text. Res. J.*, vol. 69, no. 8, pp. 545–551, 1999.
- [145] R. H. Gong, *Specialist yarn and fabric structures: Developments and applications*. 2011.
- [146] “Flow Regimes – The Physics Hypertextbook.” [Online]. Available: <https://physics.info/turbulence/>. [Accessed: 28-Jun-2020].
- [147] A. K. Coker, “FLUID FLOW,” in *Ludwig’s Applied Process Design for Chemical and Petrochemical Plants*, 2007.
- [148] P. J. LaNasa and E. L. Upp, “2 - Basic Flow Measurement Laws,” P. J. LaNasa and E. L. B. T.-F. F. M. (Third E. Upp, Eds. Oxford: Butterworth-Heinemann, 2014, pp. 19–29.
- [149] P. K. Kundu, I. M. Cohen, and D. R. Dowling, “Chapter 15 - Compressible Flow,” P. K. Kundu, I. M. Cohen, and D. R. B. T.-F. M. (Sixth E. Dowling, Eds. Boston: Academic Press, 2016, pp. 819–879.
- [150] A. Barber, “Valves and Sensors,” *Pneum. Handb.*, pp. 421–473, 1997.
-

## Appendix A. Tensile Test Simulation of Thermoset Composites

The mechanical properties of carbon fibre composites with different fibre directions are observed via simulated tensile tests before the preforms and composites manufacturing. Strength and stiffness were analysed and predicted in a unidirectional (UD) lamina with the simulation software ABAQUS. The constants needed for the simulated tensile test are calculated with the theoretical formulas used for the model [132]. These engineering constants include elastic longitudinal and the transversal moduli ( $E_1$  and  $E_2$ ), Poisson's ratios ( $\nu_{12}$  and  $\nu_{21}$ ), and the shear modulus ( $G_{12}$ ). These constants can be calculated from Equations A-1 to A-11 or obtained experimentally. When the fibres and matrix are perfectly bonded without gaps between interfaces and composites, they have the same Poisson's ratio in unidirectional composites. The longitudinal elongations of the fibre, matrix, and composites are the same. Thus, the strain is also the same for each component, as shown in Equation A-1 [133].

$$\varepsilon_c = \varepsilon_f = \varepsilon_m \quad \text{Equation A-8-1}$$

Because the load ( $P$ ) is applied along the longitudinal direction, it is shared by the fibres and matrix (Equation A-2). The load  $P$  can convert into stress for the cross-sectional areas of each component, as shown in Equation A-3.

$$P_c = P_f + P_m \quad \text{Equation A-2}$$

$$\sigma_c A_c = \sigma_f A_f + \sigma_m A_m \quad \text{Equation A-3}$$

Because the lengths of the layers are the same, Equation A-3 is converted to  $\sigma_c V_c = \sigma_f V_f + \sigma_m V_m$ , where  $V$  is the volume fraction.

$$\frac{\sigma_c}{\varepsilon_c} = \frac{\sigma_f V_f}{\varepsilon_f} + \frac{\sigma_m V_m}{\varepsilon_m} \quad \text{Equation A-4}$$

$$E_c = E_f V_f + E_m (1 - V_f) = E_{11} \quad \text{Equation A-5}$$

$E_{11}$  is the longitudinal elastic modulus of the composite lamina, and  $E_{22}$  is the transverse tensile modulus. They are calculated with the equations given below. Because an even stress is applied to the composites, the stresses on the fibres and matrix are the same. The composite's elongation is the sum of the elongations of the fibre and matrix.

$$\sigma_c = \sigma_f = \sigma_m \quad \text{Equation A-6}$$

$$\delta_c = \delta_f + \delta_m \quad \text{Equation A-7}$$

Therefore, the strain on the composite in the transverse direction  $\varepsilon_2$  presents with the volume fractions of the fibres and matrix.

$$\varepsilon_2 = V_f \varepsilon_f + V_m \varepsilon_m \quad \text{Equation A-8}$$

$$\begin{aligned} E_2 = \frac{\sigma_2}{\varepsilon_2} &= \frac{\sigma_2}{V_f \varepsilon_f + V_m \varepsilon_m} = \frac{1}{\frac{V_f \varepsilon_f}{E_f \varepsilon_f} + \frac{V_m \varepsilon_m}{E_m \varepsilon_m}} = \frac{1}{\frac{V_f}{E_f} + \frac{V_m}{E_m}} \\ &= \frac{E_f E_m}{(E_f V_m + E_m V_f)} \end{aligned} \quad \text{Equation A-9}$$

Next,  $\nu_{12} = V_f \nu_f + V_m \nu_m$ , where  $\nu_f$  is Poisson's rate for the fibre, and  $\nu_m$  is Poisson's rate for the matrix (Equations A-10 and A-11).

$$\nu_{12} = -\frac{\varepsilon_2}{\varepsilon_1} \quad \text{Equation A-10}$$

$$\varepsilon_c = \varepsilon_f = \varepsilon_m$$

$$\varepsilon_2 = V_f \varepsilon_{f2} + V_m \varepsilon_{m2}$$

$$= -(V_f \nu_f \varepsilon_f + V_m \nu_m \varepsilon_m)$$

$$\nu_{12} = -\frac{\varepsilon_2}{\varepsilon_1} = \frac{V_f \nu_f \varepsilon_f}{\varepsilon_f} + \frac{V_m \nu_m \varepsilon_m}{\varepsilon_m}$$

$$= V_f \nu_f + V_m \nu_m$$

$$\nu_{21} = \frac{E_2}{E_1} \nu_{12} \quad \text{Equation A-8-2}$$

The shear moduli  $G_f$  and  $G_m$  are calculated to obtain  $G_{12}$ .

$$\text{Shear Modulus (G)} = \frac{E}{2(1 + \nu)} \quad \text{or} \quad \text{Equation A-8-3}$$

$$\tau_c = G_f \nu_f = G_m \nu_m$$

$$\nu = V_f \nu_f + V_m \nu_m$$

$$G_{12} = \frac{\tau}{\nu} = \frac{1}{\frac{V_f}{G_f} + \frac{V_m}{G_m}}$$

$$= \frac{G_f G_m}{(G_f V_m + G_m V_f)}$$

Unidirectional composites are orthotropic in nature and have the same stiffness properties in the transverse direction, so  $E_{22} = E_{33}$ , and  $G_{13} = G_{12}$ . The fibre and matrix constants are from the supplier.

Table A-1 The general mechanical properties of reinforcements and matrix.

	Carbon fibre	Epoxy
Young's Modulus (GPa)	230	3
Ultimate tensile strength (MPa)	3530	70
Shear Modulus (GPa)	92.74	1.11
Poisson's ratio	0.24 [134][135]	0.35

The engineering constant for a laminate can be calculated to define elastic behaviour via classical lamination theory [136].

$$\begin{bmatrix} \epsilon_1 \\ \epsilon_2 \\ \epsilon_3 \end{bmatrix} = \begin{bmatrix} \frac{1}{E_1} & \frac{-\nu_2}{E_2} & 0 \\ \frac{-\nu_1}{E_1} & \frac{1}{E_2} & 0 \\ 0 & 0 & \frac{1}{G_{12}} \end{bmatrix} \begin{bmatrix} T_1 \\ T_2 \\ T_{12} \end{bmatrix} = \begin{bmatrix} C_{11} & C_{12} & 0 \\ C_{12} & C_{22} & 0 \\ 0 & 0 & C_{33} \end{bmatrix} \begin{bmatrix} T_1 \\ T_2 \\ T_{12} \end{bmatrix}$$

These equations can be transferred to stiffness tensor. The stiffness of the material,  $C_{ij}$ , is calculated by inverting the compliance tensor,  $A_{ij}$ .

$$\begin{bmatrix} T_1 \\ T_2 \\ T_{12} \end{bmatrix} = \begin{bmatrix} \frac{E_1}{1 - \nu_{12}\nu_{21}} & \frac{\nu_{21}E_1}{1 - \nu_{12}\nu_{21}} & 0 \\ \frac{\nu_{12}E_2}{1 - \nu_{12}\nu_{21}} & \frac{E_2}{1 - \nu_{12}\nu_{21}} & 0 \\ 0 & 0 & G_{12} \end{bmatrix} \begin{bmatrix} \epsilon_1 \\ \epsilon_2 \\ \epsilon_3 \end{bmatrix} = \begin{bmatrix} A_{11} & A_{12} & 0 \\ A_{12} & A_{22} & 0 \\ 0 & 0 & A_{66} \end{bmatrix} \begin{bmatrix} \epsilon_1 \\ \epsilon_2 \\ \epsilon_3 \end{bmatrix}$$

For the multi-direction layers of the composite, average values of constant for each layer are needed. When the alignment of the fibres is not in the direction of loading,  $\bar{A}_{ij}$  is

calculated, and then the modulus is obtained with the equations below. Here,  $c = \cos \phi$ ,  $s = \sin \phi$ , and the angle are between the fibre and stress axes.

$$\bar{A}_{11} = A_{11}c^4 + A_{22}s^4 + (2A_{12} + 4A_{33})c^2s^2$$

$$\bar{A}_{12} = A_{12}(c^4 + s^4) + (A_{11} + A_{22} - 4A_{33})c^2s^2$$

$$\bar{A}_{22} = A_{11}s^4 + A_{22}c^4 + (2A_{12} + 4A_{33})c^2s^2$$

$$\bar{A}_{13} = (A_{11} - A_{12} - 2A_{33})c^3s - (A_{22} - A_{12} - 2A_{33})c^3s^3$$

$$\bar{A}_{23} = (A_{11} - A_{12} - 2A_{33})cs^3 - (A_{22} - A_{12} - 2A_{33})c^3s$$

$$\bar{A}_{33} = (A_{11} + A_{22} - 2A_{12} - 2A_{33})c^2s^2 + A_{33}(c^4 + s^4)$$

$[A] = \sum_{k=1}^n [A_{ij}]_k (h_k - h_{k-1})$ ,  $i=1,2,6$ ,  $j=1,2,6$ , and  $h$ =single layer thickness [137].

$$E_x = \frac{1}{hA^{-1}}$$

The rule of mixtures model provides the lamina properties for  $E_{11}$ ,  $E_{22}$ ,  $E_{33}$ ,  $G_{12}$ , and  $G_{13}$ , and they are presented in Table A-2.

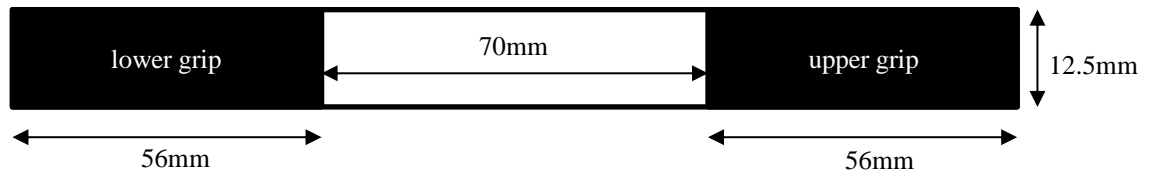


Figure A-1 Dimension of UD composites test coupon

Table A-2 The mechanical properties of unidirectional laminate

Property	CF/epoxy [138]	UD CF/epoxy [139]	Woven CF/epoxy [132]	UD CF/epoxy [This research]
$E_{11}$ (GPa)	146.5	112.3	67	105.15
$E_{22}=E_{33}$ (GPa)	109.62	8.8	5.6	5.40
$G_{12}=G_{13}$ (GPa)	44.29	3.15	5.31	2.00
$G_{23}$ (GPa)	-	-	3.07	-
$\nu_{12}$	0.30	0.30	0.35	0.30

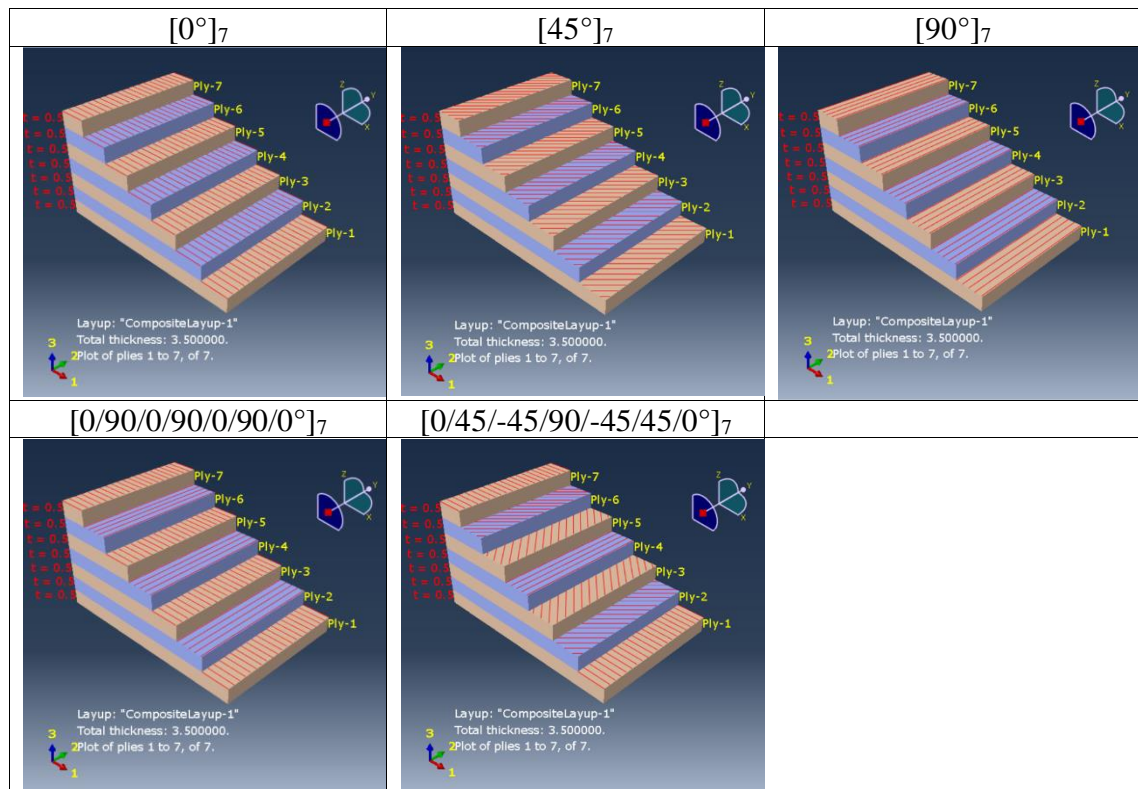


Figure A-2 Fibre direction of each layer for tensile test simulation

Table A-3 Each layer specification of multidirectional laminar for simulation

Ply no.	Material	Thickness(mm)	Orientation (°)				
			1	2	3	4	5
Ply-1	CF/epoxy	0.5	0	45	90	0	0
Ply-2	CF/epoxy	0.5	0	45	90	90	45
Ply-3	CF/epoxy	0.5	0	45	90	0	-45
Ply-4	CF/epoxy	0.5	0	45	90	90	90
Ply-5	CF/epoxy	0.5	0	45	90	0	-45
Ply-6	CF/epoxy	0.5	0	45	90	90	45
Ply-7	CF/epoxy	0.5	0	45	90	0	0

The dimensions of the test specimens are all 118 x 12.5 mm, as shown in Figure A-1, and the designed specimens are created in a shell planer option. To set the shell composites, the material, thickness, and fibre orientation angle are defined (Table A-2, A-3 and Figure A-2). A standard four-node, reduced integration (S4R) shell element is set with 500

elements, and load is applied to the longitudinal direction of a fibre with a 50mm displacement.

The stress-strain curves were obtained from the stress-time and strain-time curves created with simulation (Figure A-3). The curves of different samples are combined according to the fibre direction, as shown in Figure A-4. Young's modulus can be found with the slope of the curve from this graph. The  $[0^\circ/90^\circ/0^\circ/90^\circ/0^\circ/90^\circ/0^\circ]$  lamina composite shows the steepest slope among the samples.

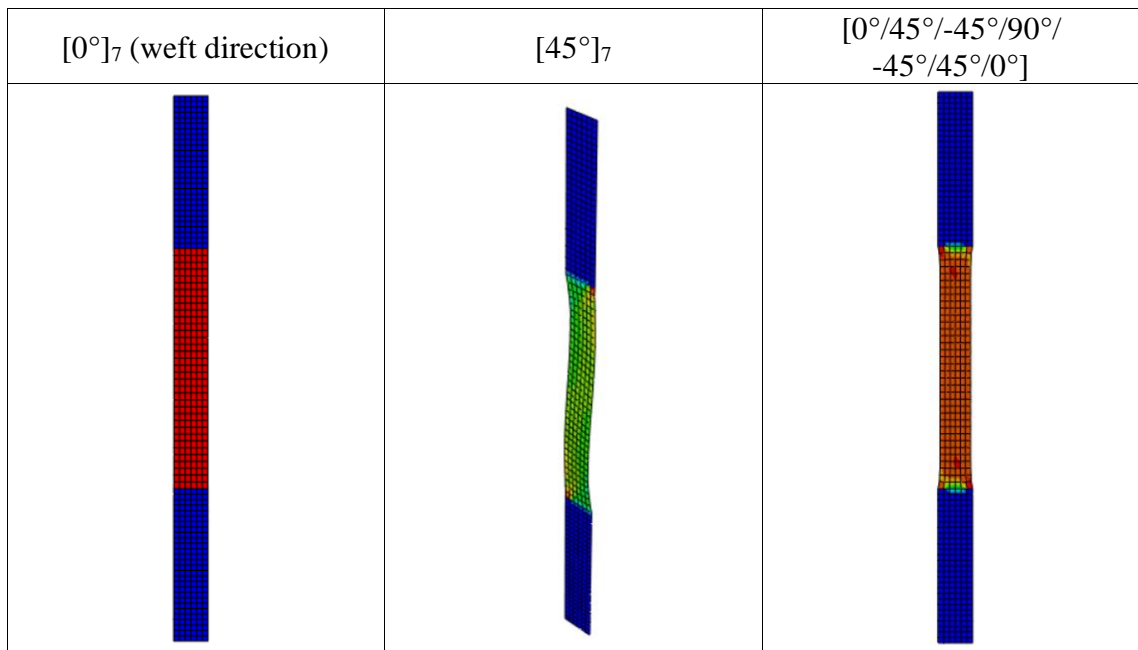


Figure A-3 Tensile test simulation results of carbon fibre composites at different fibre alignment

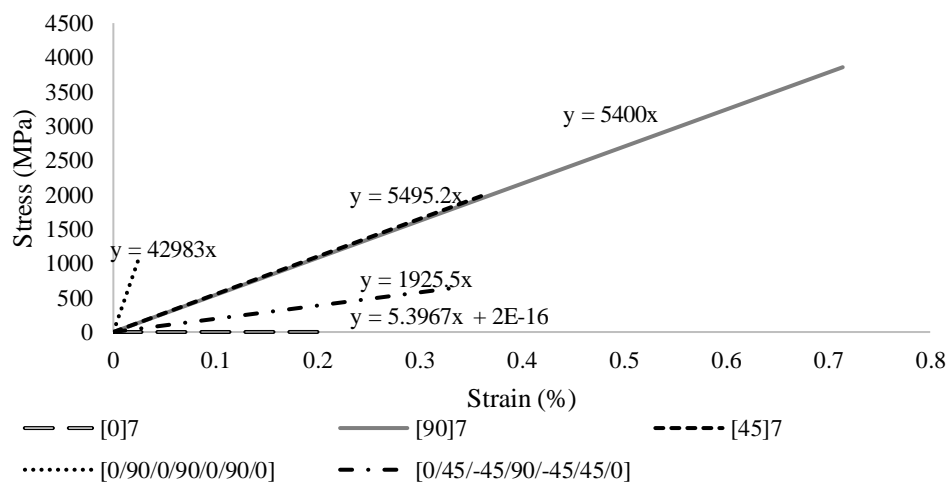


Figure A-4 Calculated stress-strain curves of different fibre directions preform structures



---

## Appendix B. Programing

<INIT>

```

=====
' Customer: University of Manchester
' Application: 5 axis stepper machine demo
' Platform: Trio Motion Coordinator MC4N
'-----
' Version:1.2.0
' Author: S Finnigan
' Revised by J Park
'-----
'           Copyright (c) 2019 Motor Technology Ltd
'           Motec House (Unit one)
'           Chadkirk Business Park.
'           Romiley Stockport SK6
'           Web site: www.motec.co.uk   Email: support@motec.co.uk
'-----
=====
start:
OP(15,ON)
HMI_SET_PAGE("BOOT")
error_check = ON
WHILE VR(1000) <> 3 OR error_check = ON 'check ECAT is "operational" & correct
number axis present
  RESET
  CLEAR
  error_check = OFF

  WDOG = OFF
'ETHERCAT($91,-1,1000500)
  ETHERCAT(1,0)'switch off ethercat
  WA(100)
  ETHERCAT ($E0,0,1) 'disable effect of eroneous ethercat error
  WA(100)

  ETHERCAT(0,0) 'initialise EtherCAT
  WA(100)

  ETHERCAT($06,0,1000) 'check EtherCAT state
  WA(50)
  ETHERCAT ( 3 , 0 , 1001 ) 'check number of slaves
  WA(50)
'ETHERCAT($06,0,-1)

```

---

---

```
'WA(50)
'ETHERCAT ( 3 , 0 , -1 )
'WA(50)
WEND

axis_number = 0
FOR axis_number = 1 TO 5 ' axis set-up
  BASE(axis_number)

  SERVO=OFF
  AXIS_ENABLE = OFF 'disable the AXIS

  UNITS = 1712
  FE_LIMIT = 100000000
  DATUM(0)
  WA(100)
  DEFPOS(0)
  WA(100)

  ACCEL = 1000
  DECEL = 1000
  SPEED = 0

NEXT axis_number

WDOG = ON
WA(10000)

IF WDOG <> ON THEN 'Check ETHERCAT has established without errors
  error_check = ON
  WA(500)
  GOTO start
ENDIF

RUN "SPEED_CONTROL_1",4
WAIT UNTIL PROC_STATUS PROC(4) <>0
RUN "SPEED_CONTROL_2",5
WAIT UNTIL PROC_STATUS PROC(5) <>0
RUN "SPEED_CONTROL_3",6
WAIT UNTIL PROC_STATUS PROC(6) <>0
RUN "POSITION_CONTROL_4",7
WAIT UNTIL PROC_STATUS PROC(7) <>0
RUN "SPEED_CONTROL_5",8
WAIT UNTIL PROC_STATUS PROC(8) <>0
RUN "IO",9
WAIT UNTIL PROC_STATUS PROC(9) <>0
```

---

---

estop: 'emergency stop and system error routine

HMI\_SET\_PAGE("OPERATOR")

IF IN(0)=OFF THEN 'ESTOP Check

STOP "SPEED\_CONTROL\_1"  
STOP "SPEED\_CONTROL\_2"  
STOP "SPEED\_CONTROL\_3"  
STOP "POSITION\_CONTROL\_4"  
STOP "SPEED\_CONTROL\_5"  
STOP "IO"

WDOG=OFF

FOR axis\_number = 1 TO 5 ' axis disabling

BASE(axis\_number)

AXIS\_ENABLE = OFF 'disable the AXIS  
NEXT axis\_number

HMI\_SET\_PAGE("ESTOP")

WAIT UNTIL IN(0)=ON

GOTO start

ENDIF

drive\_fault=0

FOR input\_number = 8 TO 12 ' axis disabling

IF IN(input\_number)=OFF AND IN(0)=ON THEN  
drive\_fault=1  
ENDIF

NEXT input\_number

IF IN(0)=ON AND WDOG<>ON AND drive\_fault=0 THEN

STOP "SPEED\_CONTROL\_1"  
STOP "SPEED\_CONTROL\_2"  
STOP "SPEED\_CONTROL\_3"  
STOP "POSITION\_CONTROL\_4"

---

```
STOP "SPEED_CONTROL_5"  
STOP "IO"  
  
WDOG=OFF  
  
FOR axis_number = 1 TO 5 ' axis disabling  
    BASE(axis_number)  
    AXIS_ENABLE = OFF 'disable the AXIS  
NEXT axis_number  
  
HMI_SET_PAGE("DRIVE_ERROR")  
  
WA(3000)  
  
WHILE drive_fault = 1  
    drive_fault=0  
    FOR input_number = 8 TO 12 ' axis disabling  
        IF IN(input_number)=OFF AND IN(0)=ON THEN  
            drive_fault=1  
        ENDIF  
    NEXT input_number  
WEND  
  
GOTO start  
  
ENDIF  
  
GOTO estop  
  
<IO>  
  
WHILE TRUE  
    IF READ_OP(8) = ON THEN  
        VR(3008) = 1  
    ELSEIF READ_OP(8) = OFF THEN  
        VR(3008) = 0  
    ENDIF
```

---

---

```
IF READ_OP(9) = ON THEN
  VR(3009) = 1
ELSEIF READ_OP(9) = OFF THEN
  VR(3009) = 0
ENDIF

IF READ_OP(10) = ON THEN
  VR(3010) = 1
ELSEIF READ_OP(10) = OFF THEN
  VR(3010) = 0
ENDIF

IF READ_OP(11) = ON THEN
  VR(3011) = 1
ELSEIF READ_OP(11) = OFF THEN
  VR(3011) = 0
ENDIF

IF READ_OP(12) = ON THEN
  VR(3012) = 1
ELSEIF READ_OP(12) = OFF THEN
  VR(3012) = 0
ENDIF

IF READ_OP(13) = ON THEN
  VR(3013) = 1
ELSEIF READ_OP(13) = OFF THEN
  VR(3013) = 0
ENDIF

IF READ_OP(14) = ON THEN
  VR(3014) = 1
ELSEIF READ_OP(14) = OFF THEN
  VR(3014) = 0
ENDIF

IF READ_OP(15) = ON THEN
  VR(3015) = 1
ELSEIF READ_OP(15) = OFF THEN
  VR(3015) = 0
ENDIF

WEND
```

---

---

**<POSITION CONTROL\_4>**

'Position control for motor 1

'Variables from HMI

'VR(2004) enable/disable

'VR(2104) increase speed

'VR(2204) decrease speed

'VR(2304) speed

BASE(4) 'axis number

DECEL=10000

ACCEL=10000

SERVO=ON

enable\_prev=0 'enable check variable, used to ensure only one motion command is sent at a time

inprev\_1=OFF 'limit switch inputs previous states

inprev\_2=OFF

WHILE TRUE 'infinite loop

    SPEED = VR(2304) 'set speed to HMI value

    WA(50)

    IF VR(2004)=1 AND VR(2004)<>enable\_prev THEN 'enable sequence

        enable\_prev=VR(2004)

        FORWARD

        WA(50)

        AXIS\_ENABLE=ON

        WA(50)

    ENDIF

    IF VR(2004)=0 AND VR(2004)<>enable\_prev THEN 'disbale sequence

        enable\_prev=VR(2004)

        CANCEL

        WAIT IDLE

        WA(50)

        AXIS\_ENABLE=OFF

        WA(50)

    ENDIF

    IF VR(2104)=1 THEN 'increase speed

        VR(2304) = VR(2304) + 5

        VR(2104)=0

    ELSEIF VR(2204)=1 THEN 'decrease speed

        VR(2304) = VR(2304) - 5

---

```

    VR(2204)=0
ENDIF

IF IN(1)=OFF OR IN(2)=OFF THEN
    IF IN(1)<>inprev_1 OR IN(2)<>inprev_2 THEN
        VR(2304)=-VR(2304)
        inprev_1=IN(1)
        inprev_2=IN(2)
    ENDIF
ENDIF

WEND

<SPEED_CONTROL_1>

'Speed control for motor 1

'Variables from HMI
'VR(2001) enable/disable
'VR(2101) increase speed
'VR(2201) decrease speed
'VR(2301) speed

BASE(1) 'axis number
SERVO=ON
enable_prev=0 'enable check variable, used to ensure only one motion command is sent
at a time

WHILE TRUE 'infinite loop

    SPEED = VR(2301) 'set speed to HMI value
    WA(50)

    IF VR(2001)=1 AND VR(2001)<>enable_prev THEN 'enable sequence
        enable_prev=VR(2001)
        FORWARD
        WA(50)
        AXIS_ENABLE=ON
        WA(50)
    ENDIF

    IF VR(2001)=0 AND VR(2001)<>enable_prev THEN 'disbale sequence
        enable_prev=VR(2001)
        CANCEL
        WAIT IDLE
        WA(50)

```

---

---

```
    AXIS_ENABLE=OFF
    WA(50)
ENDIF

IF VR(2101)=1 THEN 'increase speed
    VR(2301) = VR(2301) + 5
    VR(2101)=0
ELSEIF VR(2201)=1 THEN 'decrease speed
    VR(2301) = VR(2301) - 5
    VR(2201)=0
ENDIF

WEND

<SPEED_CONTROL_2>

'Speed control for motor 2

'Variables from HMI
'VR(2002) enable/disable
'VR(2102) increase speed
'VR(2202) decrease speed
'VR(2302) speed

BASE(2) 'axis number
SERVO=ON
enable_prev=0 'enable check variable, used to ensure only one motion command is sent
at a time

WHILE TRUE 'infinite loop

    SPEED = VR(2302) 'set speed to HMI value
    WA(50)

    IF VR(2002)=1 AND VR(2002)<>enable_prev THEN 'enable sequence
        enable_prev=VR(2002)
        FORWARD
        WA(50)
        AXIS_ENABLE=ON
        WA(50)
    ENDIF

    IF VR(2002)=0 AND VR(2002)<>enable_prev THEN 'disbale sequence
        enable_prev=VR(2002)
        CANCEL
        WAIT IDLE
```

---



---

```
    WA(50)
    AXIS_ENABLE=OFF
    WA(50)
ENDIF

IF VR(2102)=1 THEN 'increase speed
    VR(2302) = VR(2302) + 5
    VR(2102)=0
ELSEIF VR(2202)=1 THEN 'decrease speed
    VR(2302) = VR(2302) - 5
    VR(2202)=0
ENDIF

WEND

<SPEED_CONTROL_3>

'Speed control for motor 2

'Variables from HMI
'VR(2002) enable/disable
'VR(2102) increase speed
'VR(2202) decrease speed
'VR(2302) speed

BASE(2) 'axis number
SERVO=ON
enable_prev=0 'enable check variable, used to ensure only one motion command is sent
at a time

WHILE TRUE 'infinite loop

    SPEED = VR(2302) 'set speed to HMI value
    WA(50)

    IF VR(2002)=1 AND VR(2002)<>enable_prev THEN 'enable sequence
        enable_prev=VR(2002)
        FORWARD
        WA(50)
        AXIS_ENABLE=ON
        WA(50)
    ENDIF

    IF VR(2002)=0 AND VR(2002)<>enable_prev THEN 'disbale sequence
        enable_prev=VR(2002)
        CANCEL
```

---

---

```
    WAIT IDLE
    WA(50)
    AXIS_ENABLE=OFF
    WA(50)
ENDIF

IF VR(2102)=1 THEN 'increase speed
    VR(2302) = VR(2302) + 5
    VR(2102)=0
ELSEIF VR(2202)=1 THEN 'decrease speed
    VR(2302) = VR(2302) - 5
    VR(2202)=0
ENDIF

WEND

<SPEED_CONTROL_5>

'Speed control for motor 5

'Variables from HMI
'VR(2005) enable/disable
'VR(2105) increase speed
'VR(2205) decrease speed
'VR(2305) speed

BASE(5) 'axis number
SERVO=ON
enable_prev=0 'enable check variable, used to ensure only one motion command is sent
at a time

WHILE TRUE 'infinite loop

    SPEED = VR(2305) 'set speed to HMI value
    WA(50)

    IF VR(2005)=1 AND VR(2005)<>enable_prev THEN 'enable sequence
        enable_prev=VR(2005)
        FORWARD
        WA(50)
        AXIS_ENABLE=ON
        WA(50)
    ENDIF

    IF VR(2005)=0 AND VR(2005)<>enable_prev THEN 'disbale sequence
        enable_prev=VR(2005)
```

---

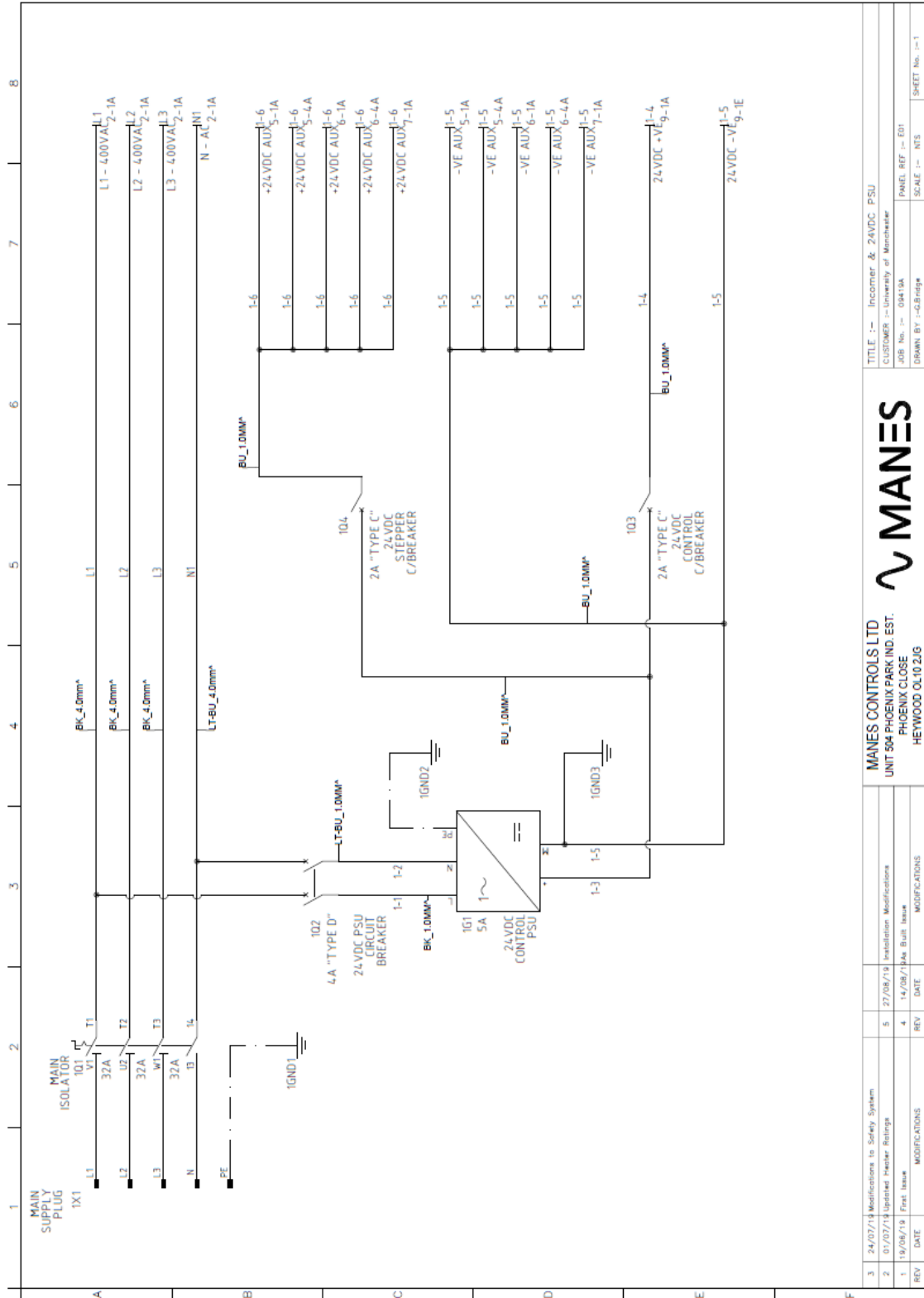
---

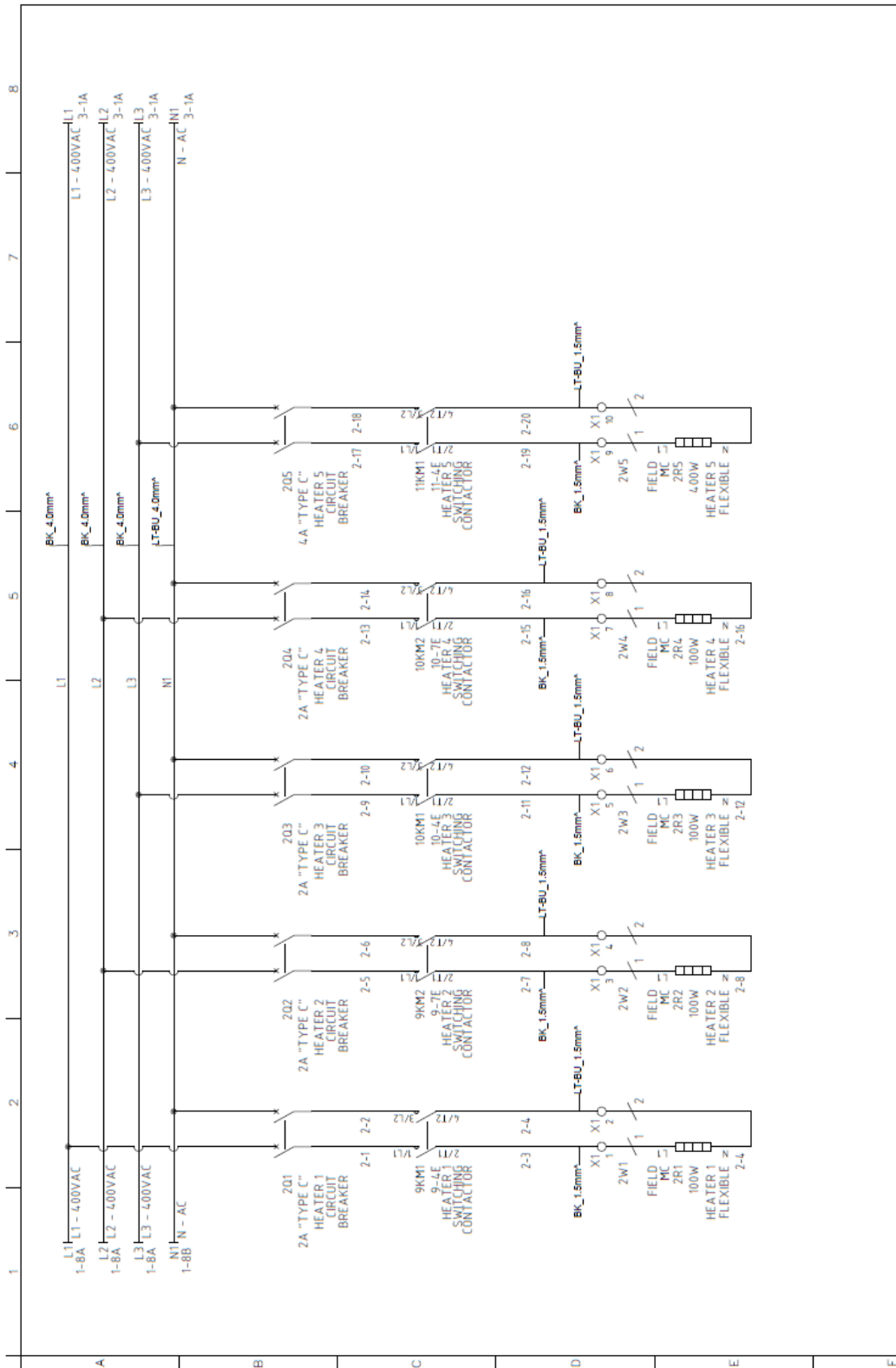
```
CANCEL
WAIT IDLE
WA(50)
AXIS_ENABLE=OFF
WA(50)
ENDIF

IF VR(2105)=1 THEN 'increase speed
  VR(2305) = VR(2305) + 5
  VR(2105)=0
ELSEIF VR(2205)=1 THEN 'decrease speed
  VR(2305) = VR(2305) - 5
  VR(2205)=0
ENDIF

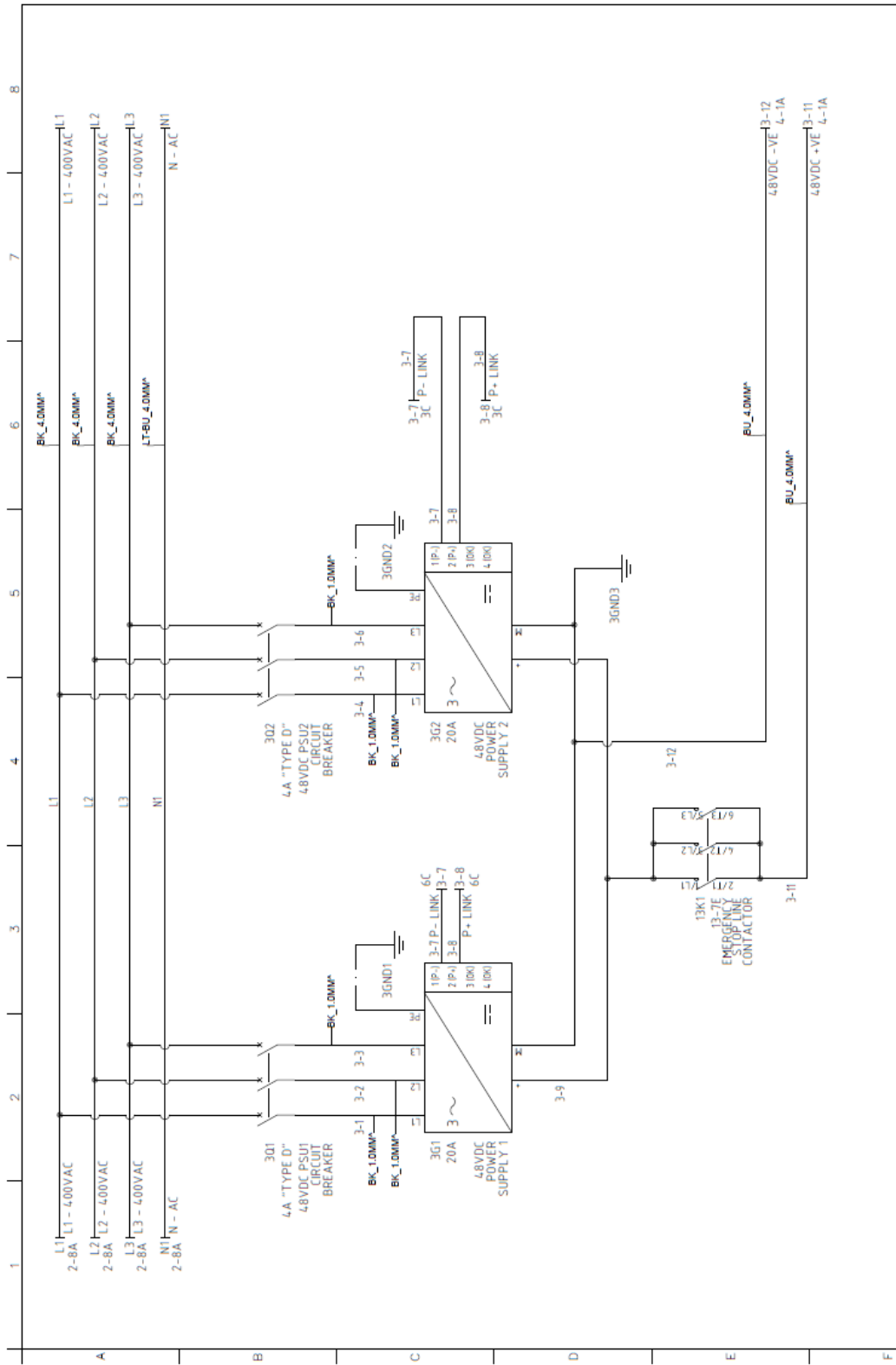
WEN
```

## Appendix C. PLC Electrical Schematics





MANES		MANES CONTROLS LTD		UNIT 504 PHOENIX PARK IND. EST.		HEWWOOD OL10 2JG	
TITLE :- 240VAC HEATERS CUSTOMER :- University of Manchester JOB No. :- 09419A DRAWN BY :- G.Bridge PANEL REF :- ED1 SCALE :- SHEET No. :- 2							
3	24/07/19	Modifications to Safety System					
2	07/07/19	Updated Heater Ratings	5	27/08/19	Installation Modifications		
1	19/06/19	First Issue	4	14/08/19	As Built Issue		
REV	DATE	MODIFICATIONS	REV	DATE	MODIFICATIONS		

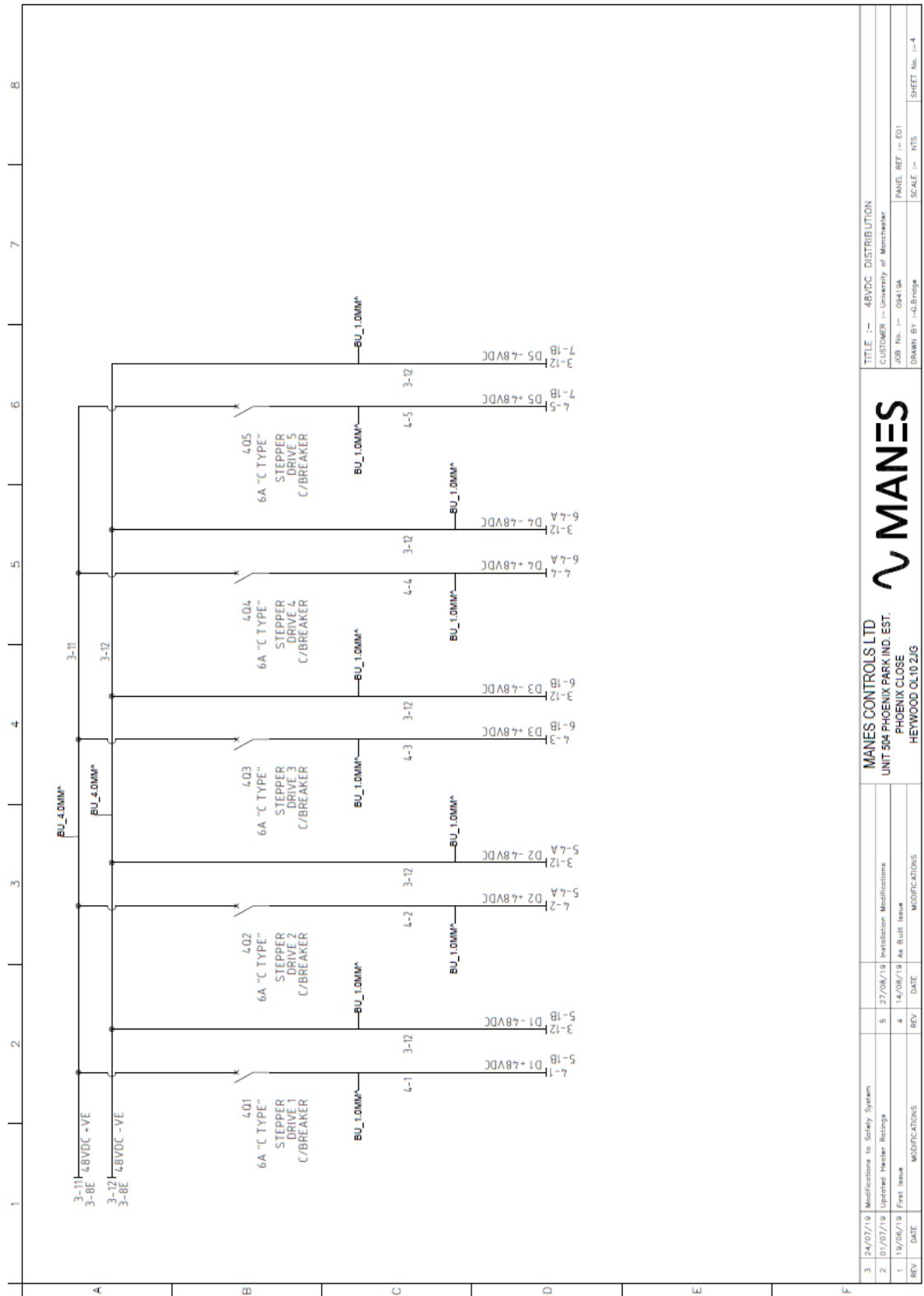


3	24/07/19	Modifications to Safety System	5	27/08/19	Installation	Modifications
2	07/07/19	Updated Heater Ratings	4	14/08/19	As Built	Issue
1	19/06/19	First Issue				
REV	DATE	MODIFICATIONS	REV	DATE	MODIFICATIONS	

MANES CONTROLS LTD  
 UNIT 504 PHOENIX PARK IND. EST.  
 PHOENIX CLOSE  
 HEYWOOD OL10 2JG

**MANES**

TITLE :- 48VDC POWER SUPPLIES  
 CUSTOMER :- University of Manchester  
 JOB No. :- 08419A  
 DRAWN BY :- G.B.Hdg\*  
 SCALE :- NTS  
 SHEET No. :- 3  
 4-1A  
 48VDC -VE  
 48VDC +VE

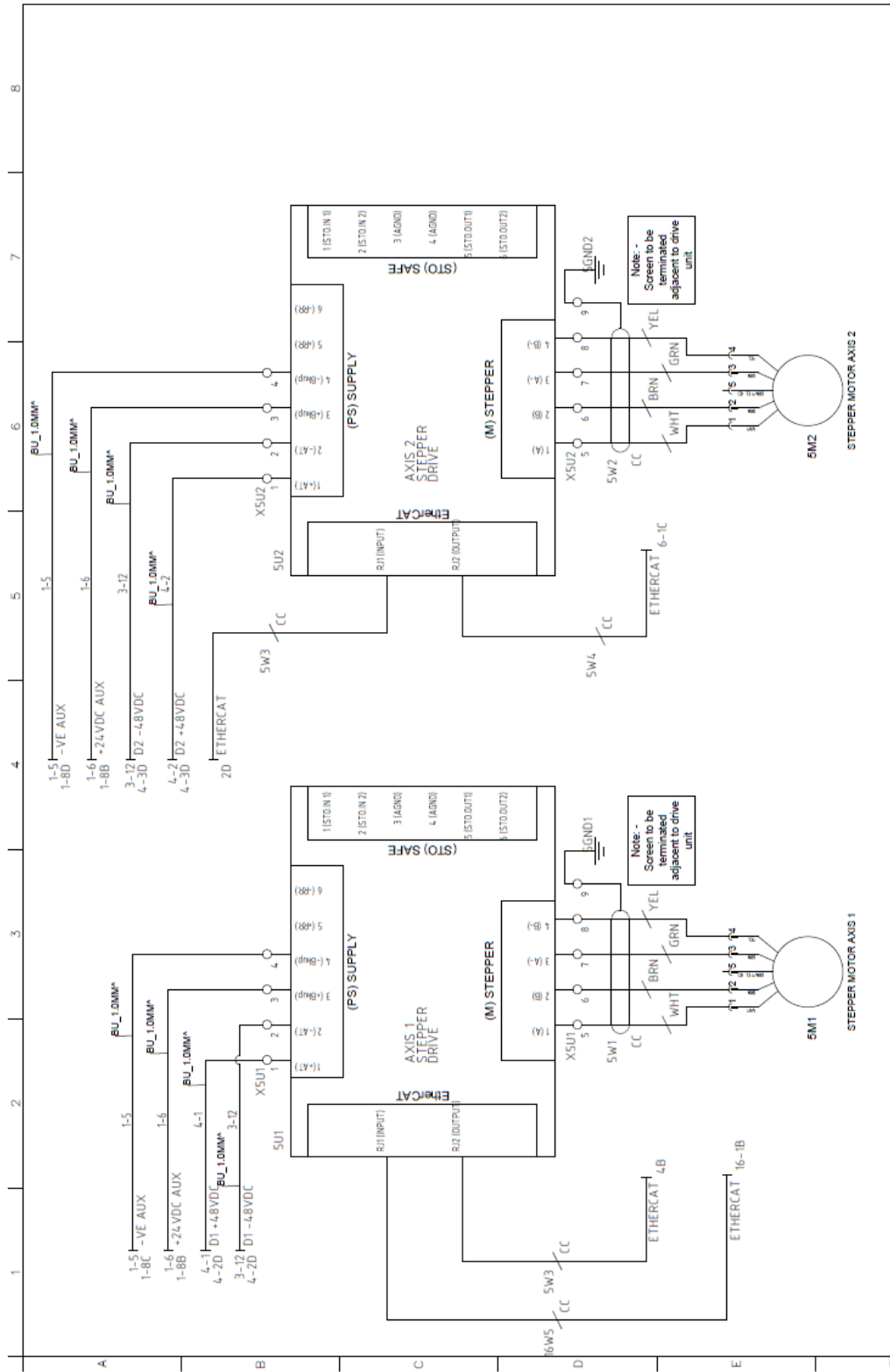


3	24/07/19	Modifications to Safety System	5	27/08/19	Installation Modifications
2	01/07/19	Updated Heater Ratings	4	14/08/19	As Built Issue
1	19/08/19	First Issue			

**MANES**

MANES CONTROLS LTD  
 UNIT 504 PHOENIX PARK IND. EST.  
 PHOENIX CLOSE  
 HEYWOOD OL10 2JG

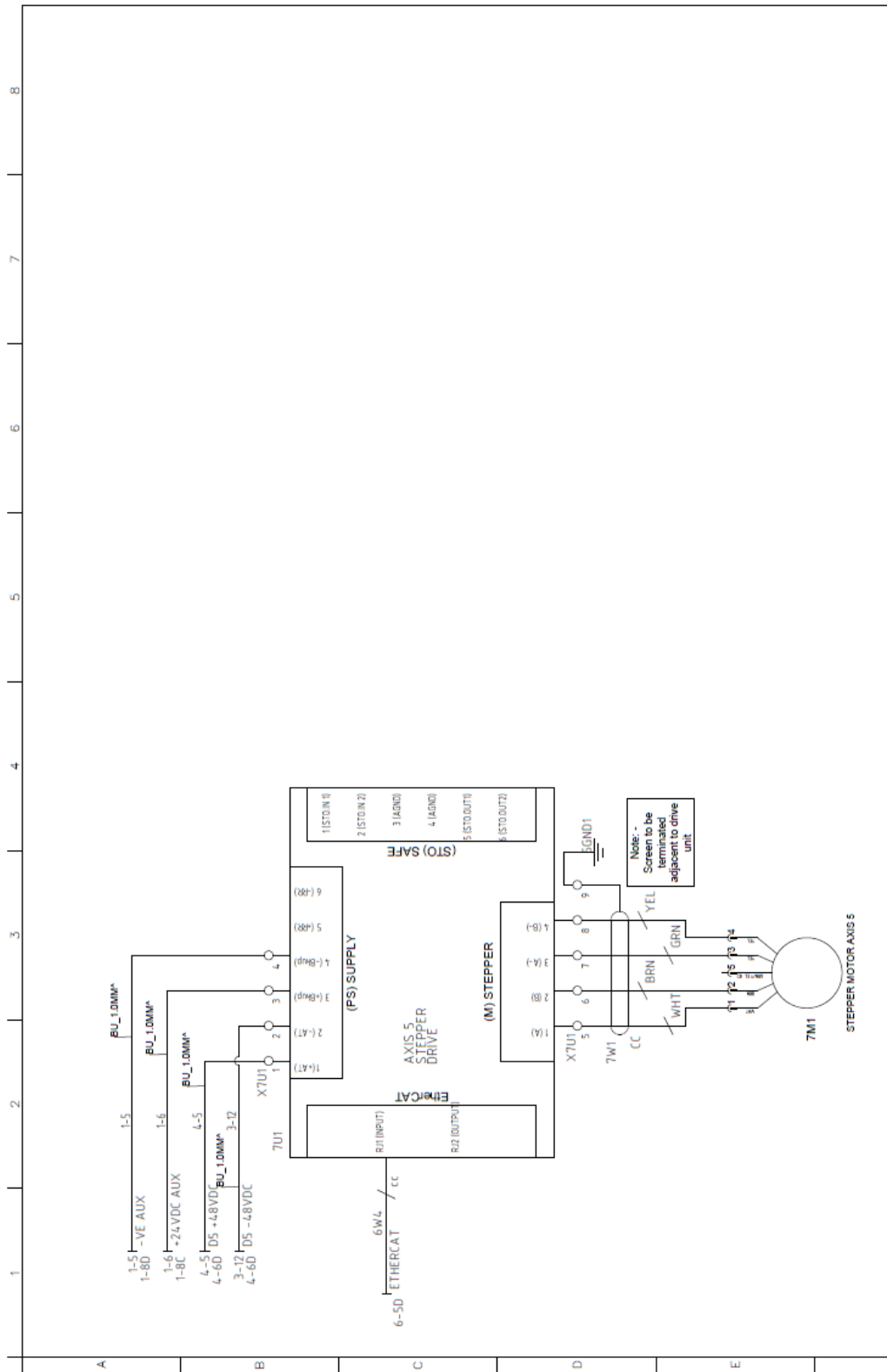
MODIFICATIONS		MODIFICATIONS	
REV	DATE	REV	DATE
2019-08-27			
TITLE :- 48VDC DISTRIBUTION			
CUSTOMER :- University of Manchester			
JOB No. :- 0441A		PANEL REF :- E01	
DRAWN BY :- G.Bridge		SCALE :- NTS	
		SHEET No. :- 4	



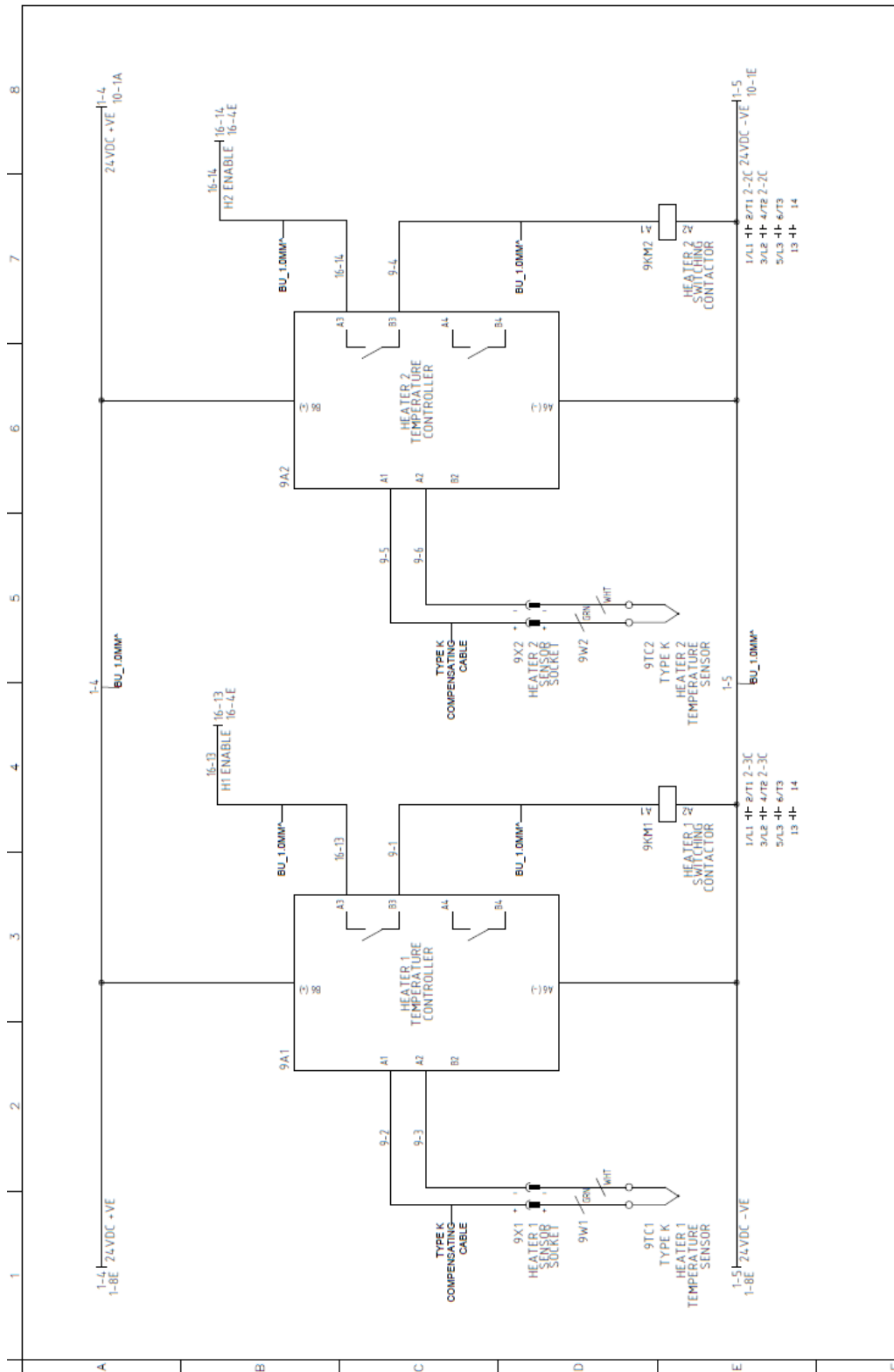
3		24/07/19	Modifications to Safety System	TITLE :- STEPPER AXIS 1 & 2	
2		07/07/19	Updated Motor Ratings	CUSTOMER :- University of Manchester	
1		19/06/19	Final Issue	JOB No. :- 09419A	
REV	DATE	MODIFICATIONS	DATE	SCALE :-	SHEET No. :- 5
MANES CONTROLS LTD UNIT 504 PHOENIX PARK IND. EST. PHOENIX CLOSE HEYWOOD OL10 2JG			DRAWN BY :- G.Bridge		







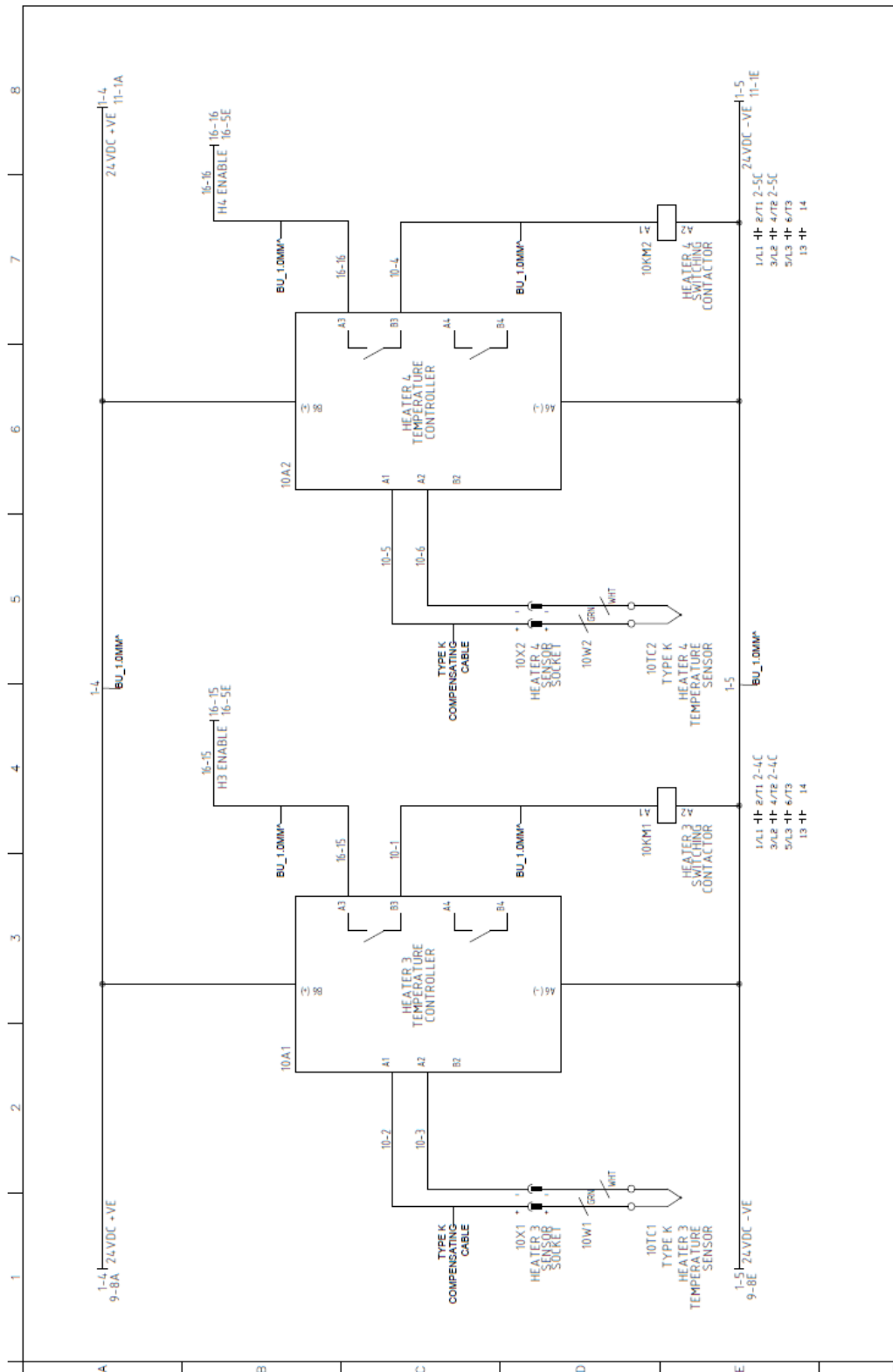
3	24/07/19	Modifications to Safety System	5	27/08/19	Installation Modifications	<b>MANES CONTROLS LTD</b> UNIT 504 PHOENIX PARK IND. EST. PHOENIX CLOSE HEYWOOD OL10 2JG		TITLE :- STEPPER AXIS 5
2	07/07/19	Updated Heater Ratings	4	14/08/19	As Built Issue			CUSTOMER :- University of Manchester
1	19/06/19	First Issue	REV	DATE	MODIFICATIONS	REV	DATE	JOB No. :- 08415A
						DRAWN BY :- G.Bridge SCALE :- SHEET No. :- 7		PANEL REF :- E01
								SCALE :-



REV	DATE	DESCRIPTION	DATE	DESCRIPTION	
3	24/07/19	Modifications to Safety System			
2	07/07/19	Updated Heater Ratings	5	27/08/19	Installation Modifications
1	19/06/19	Final Issue	4	14/06/19	As Built Issue

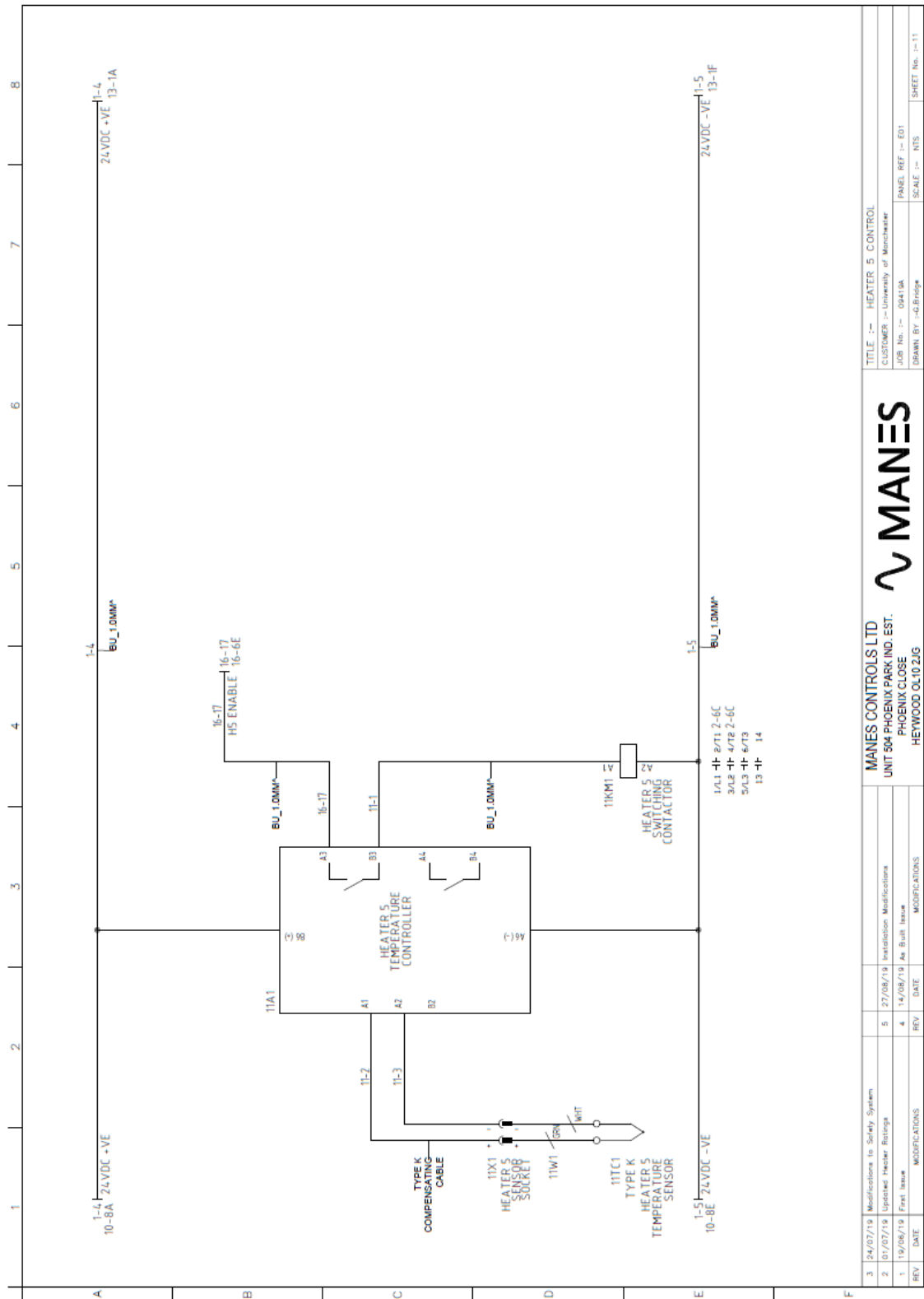
<b>MANES</b> MANES CONTROLS LTD UNIT 504 PHOENIX PARK IND. EST. PHOENIX CLOSE HEYWOOD OL10 2JG		TITLE :- HEATERS 1 & 2 CONTROL CUSTOMER :- University of Manchester JOB No. :- 0415A DRAWN BY :- G.E.Hopps
PANEL REF :- ED1	SCALE :- NIS	SHEET No. :- 9



REV	DATE	MODIFICATIONS	REV	DATE	MODIFICATIONS
3	24/07/19	Modifications to Safety System	5	27/08/19	Installation Modifications
2	07/07/19	Updated Heater Ratings	4	14/08/19	As Built Issue
1	19/06/19	First Issue			

<b>MANES</b> MANES CONTROLS LTD UNIT 504 PHOENIX PARK IND. EST. PHOENIX CLOSE HETWOOD DL10 2JG		TITLE :- HEATERS 3 & 4 CONTROL CUSTOMER :- University of Manchester JOB No. :- 09419A DRAWN BY :- G.R.Hughes
PANEL REF :- E01 SCALE :- NTS SHEET No. :- 10		



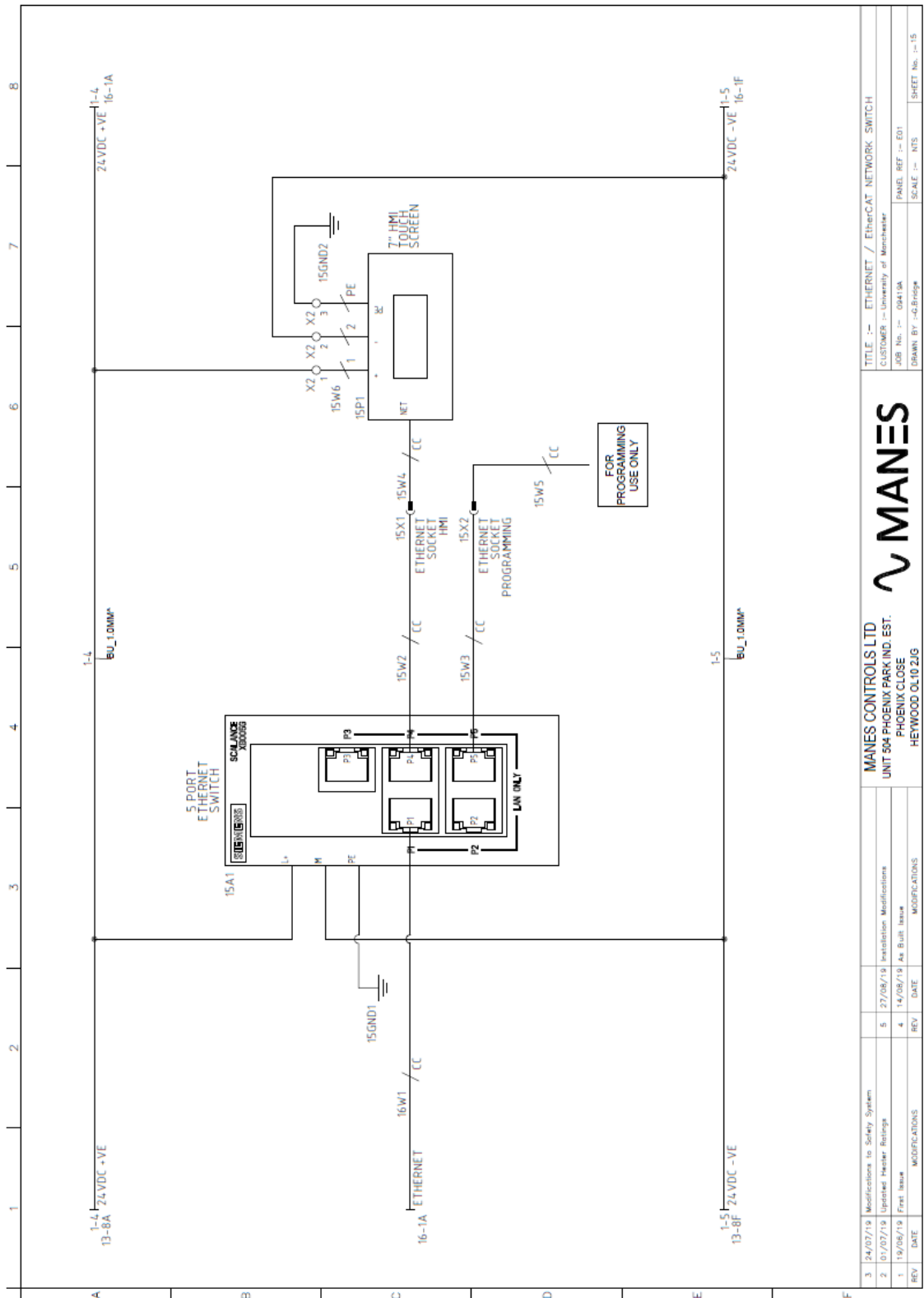
REV	DATE	MODIFICATIONS	REV	DATE	MODIFICATIONS
3	24/07/19	Modifications to Safety System	5	27/08/19	Installation Modifications
2	01/07/19	Updated Heater Ratings	4	14/08/19	As Built Issue
1	19/06/19	First Issue			

MANES CONTROLS LTD  
 UNIT 504 PHOENIX PARK IND. EST.  
 PHOENIX CLOSE  
 HEWOOD OL10 2JG

MANES

TITLE :- HEATER 5 CONTROL  
 CUSTOMER :- University of Manchester  
 JOB No. :- 04419A  
 DRAWN BY :- JB Bridge  
 SCALE :- NTS  
 SHEET No. :- 11





3	24/07/19	Modifications to Safety System	5	27/08/19	Installation Modifications
2	01/07/19	Updated Heater Ratings	4	14/08/19	As Built Issue
1	19/06/19	First Issue			

**MANES**

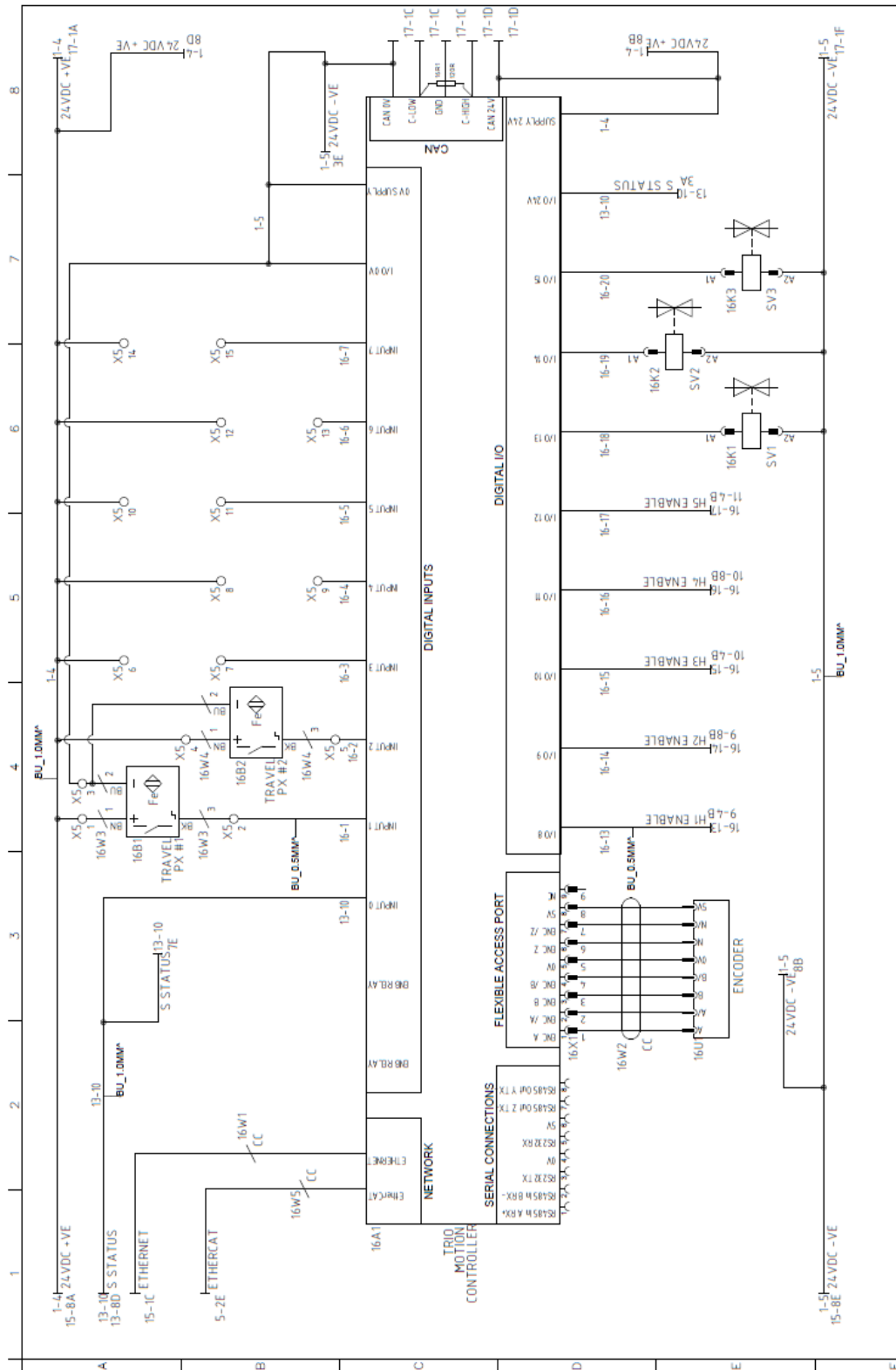
MANES CONTROLS LTD  
 UNIT 504 PHOENIX PARK IND. EST.  
 PHOENIX CLOSE  
 HEYWOOD OL10 2JG

REV	DATE	MODIFICATIONS	REV	DATE	MODIFICATIONS

2019-08-27

09/38

TITLE :-	ETHERNET / EtherCAT NETWORK SWITCH
CUSTOMER :-	University of Manchester
JOB No. :-	0943/A
PANEL REF :-	E01
DRAWN BY :-	G.Bridge
SCALE :-	NIS
SHEET No. :-	15



3	24/07/19	Modifications to Safety System	5	27/06/19	Installation Modifications
2	01/07/19	Updated Header Ratings	4	14/06/19	As Built Issue
1	19/06/19	First Issue			MODIFICATIONS
REV	DATE	MODIFICATIONS	REV	DATE	MODIFICATIONS

2019-06-27

TITLE :- MOTION CONTROLLER & ONBOARD I/O  
 CUSTOMER :- University of Manchester  
 JOB No. :- 00415A  
 DRAWN BY :- G.Bridge



MANES CONTROLS LTD  
 UNIT 504 PHOENIX PARK IND. EST.  
 PHOENIX CLOSE  
 HEYWOOD OL10 2JG

PANEL REF :- ED1  
 SCALE :- NTS  
 SHEET No. :- 18





## Appendix D. New Air Nozzle Design

### <Air Nozzle Design >

Because the quality of commingled yarns varies depending on air nozzle design, the choice of nozzle design should be considered in the design of the manufacturing process, along with the number of air inlets, the degree of the obliquity of the inlet, and the channel's shape and length.

For an air inlet design, two different inlet angles ( $45^\circ$  and  $90^\circ$ ) are required to create homogeneous commingled yarn. The primary role of the  $45^\circ$  inlet is to open filaments and carry them to the nozzle exit side. On the other hand, the role of the  $90^\circ$  inlet is to mix the filaments [68]. Blending quality does not improve when the number of air inlets is increased [35]. A single air inlet can provide better quality in commingled yarns than several inlets [55]. Researchers generally recommend a nozzle designed with two  $90^\circ$  air inlets and one  $45^\circ$  air inlet [140].

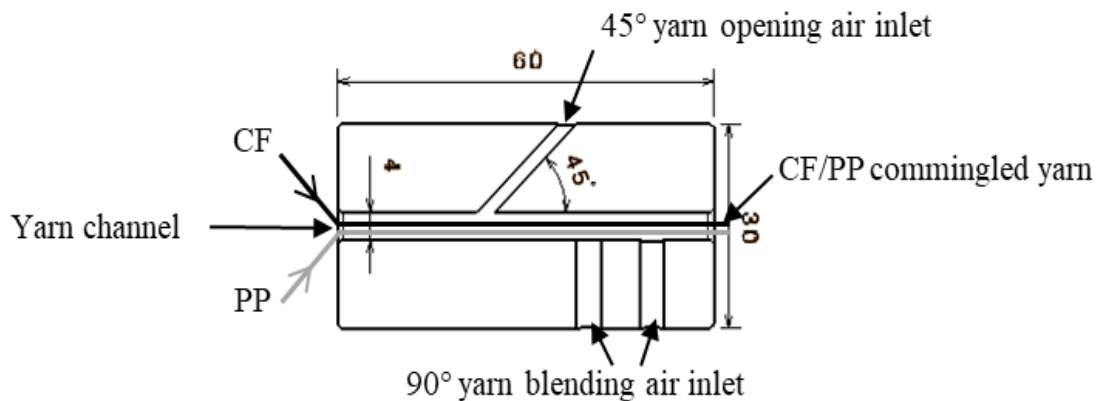


Figure D-1 configuration of general commingling nozzle [14], [68]

Table D-1 Comparing nozzle designs from previous research

Reference	[141]	[68]	[97]	[142]	[14]
The length of the yarn channel	-	60mm	60mm	40mm	60mm
Main channel diameter	-	5mm	4mm	2.5mm	4mm
Air inlet diameter	-	1mm	1mm	1.5mm	1mm
Air inlet degree(°)	90	45, 90	45, 90	15	45,90
The number of inlets	1	1,3,5	2, 3	2	3

Table D-1 shows the dimension of nozzles for different types of fibres, according to different researchers. A nozzle with several inlets cannot mix well, although the inlet number has increased. A nozzle with five inlets cannot blend more than a nozzle with three inlets. According to some studies, the best number of inlets is three [14], [68]. The nozzle channel's shape and size also affect the commingling process. Several researchers insist that the most efficient yarn channel shape for creating a high mingling density is circular, rather than semi-circular or rectangular yarn-channel shapes [143]. However, Bilgin's research [144] identifies the rectangular shape as the most effective. The nozzle channel's shape is applied differently depending on each study's conditions. Furthermore, the nozzle channel length impacts the fibre distribution. When the yarn channel length is increased, the intermingling density improves [140].

#### <Air Flow and Pressure>

The air nozzle channel is a critical element for producing commingled and air-textured yarn. This nozzle forms a turbulent supersonic flow to entangle or blend the fibres [145]. The supersonic nozzle has a Mach number of 1–5 (Ma) [146]. This Mach number is the ratio of the velocity of the gas ( $v$ ) to the speed of sound  $d$  ( $v_s$ ) [147]. The supersonic and turbulent flow can be described by equations D-1 and D-2:

$$Ma = \frac{v}{v_s} \quad \text{Equation D-8-4}$$

The Reynolds number ( $Re$ ) is the ratio of inertial forces to viscous forces (Equation 2) within flowing fluid; it can distinguish between laminar and turbulent flows in a cylinder [148].

$$Re = \frac{\rho VD}{\mu} = \frac{VD}{\nu} \quad \text{Equation D-28-5}$$

$V$  = flow velocity (m/s)

$D$  = Pipe ID (m)

$\rho$  = fluid density ( $\text{kg/m}^3$ )

$\mu$  = fluid viscosity ( $\text{kg/m}\cdot\text{s}$ )

$\nu$  = kinematic viscosity ( $\text{m}^2/\text{s}$ )

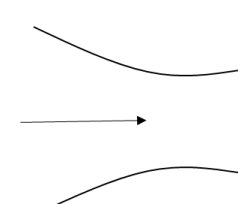
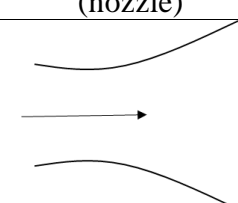
Laminar flow occurs slowly and in straight lines ( $Re < 2000$ ). With laminar flow, it is difficult to mix two different materials. In contrast, turbulent flow – the most common type – uses high velocity and irregular movement ( $Re > 4000$ ) [145]. Therefore, the air nozzle for the commingling process uses a high-velocity flow to mix two different types of fibres.

The relationship of velocity and pressure at the convergent-divergent nozzle is changed along with the entrance area of the nozzle and the Mach numbers, as shown in Table D-2. When airflow direction is from a wide area to a narrow area at subsonic speed ( $Ma < 1$ ), flow speed is increased, and pressure is decreased. On the other hand, the pressure is increased, and flow velocity is decreased at the divergent section [149]. At supersonic speed, velocity and pressure are reversed compared to the subsonic speed nozzle. Velocity is increased, and pressure is decreased at the convergent shape. At the divergent section, velocity is decreased, and pressure is increased.

According to this principle, the mixing quality of commingled yarn can be improved through the development of nozzle design to decrease fibre damage and enhance fibre distribution. Therefore, the yarn entry area and air velocity are considered at subsonic and

supersonic speed, and the entry section has a fast flow velocity and low pressure to diminish the fibre damages and maintain fibre properties.

Table D-2 The relationship between flow velocity and pressure depending on convergent and divergent shapes in subsonic and supersonic regimes [149]

Airflow velocity	$Ma < 1$ (subsonic)	$Ma \geq 1$ (supersonic)
 <p>Convergent section (nozzle)</p>	<p>Velocity increases Pressure decreases</p>	<p>Velocity decreases Pressure increases</p>
 <p>Divergent section (diffuser)</p>	<p>Velocity decreases Pressure increases</p>	<p>Velocity increases Pressure decreases</p>

The divergent area at the new nozzle is referred to in Figure D-2; it passes the EC (European Commission) noise testing criteria that are recommended for deciding the flow rate of compressors (Figure D-3) [150]. From this reference, the divergent area of the new air nozzle is wider than the 4 mm entry by around 4 degrees, as shown in Table D-3.

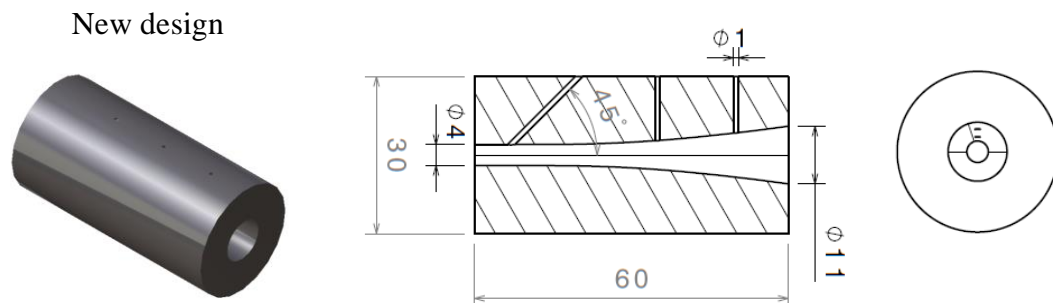


Figure D-2 Developed new nozzle design

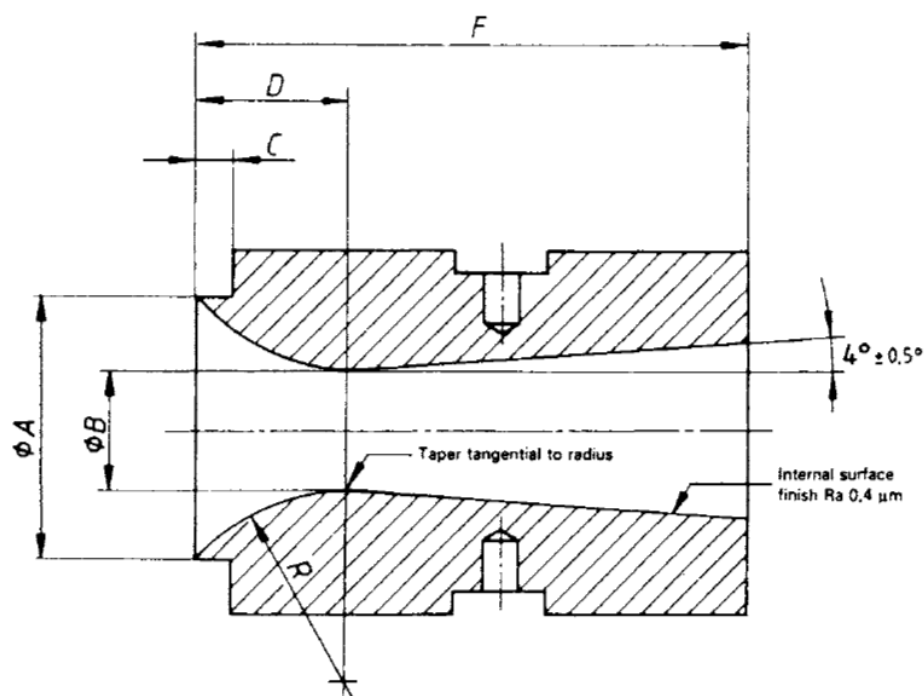


Figure D-3 Cross-sectional diagram of nozzle and dimensions depending on flow rate [150]

Table D-3 Cross-sectional diagram of the nozzle and dimensions depending on flow rate [150]

Flow rate (l/s)	A (mm)	B (mm)	C (mm)	D (mm)	R (mm)	F (mm)
12 - 40	16.00	6.350	2.40	9.96	12.70	60.5
24 - 90	24.00	9.525	3.60	14.95	19.05	91.0
50 - 160	32.00	12.700	4.60	19.93	25.40	121.5
100 - 360	48.00	19.050	7.10	29.89	38.10	182.0
180 - 650	64.00	25.400	9.60	39.85	50.80	243.0
280 - 1000	80.00	31.750	12.00	49.82	63.50	303.5
400 - 1500	95.00	38.100	14.20	59.38	76.20	364.0